AEROTHERMAL AND AEROELASTIC RESPONSE PREDICTION OF AEROSPACE STRUCTURES IN HIGH-SPEED FLOWS USING DIRECT NUMERICAL SIMULATION

BY

CHRISTOPHER MARK OSTOICH

DISSERTATION

Submitted in partial fulfillment of the requirements
for the degree of Doctor of Philosophy in Aerospace Engineering
in the Graduate College of the
University of Illinois at Urbana-Champaign, 2013

Urbana, Illinois

Doctoral Committee:

Professor Daniel J. Bodony, Chair, Director of Research
Professor Philippe H. Geubelle, Contingent Chair
Professor Joanna M. Austin
Professor Carlos A. Pantano-Rubino
Dr. Stephen M. Spottswood

Abstract

Future high-speed air vehicles will be lightweight, flexible, and reusable. Vehicles fitting this description are subject to severe thermal and fluid dynamic loading from multiple sources such as aerothermal heating, propulsion system exhaust, and high dynamic pressures. The combination of low-margin design requirements and extreme environmental conditions emphasizes the occurrence of fluid-thermal-structural coupling. Numerous attempts to field such vehicles have been unsuccessful over the past half-century due partially to the inability of traditional design and analysis practices to predict the structural response in this flight regime. In this thesis, a high-fidelity computational approach is used to examine the fluid-structural response of aerospace structures in high-speed flows. The method is applied to two cases: one involving a fluid-thermal interaction problem in a hypersonic flow and the other a fluid-structure interaction study involving a turbulent boundary layer and a compliant panel.

The coupled fluid-thermal investigation features a nominally rigid aluminum spherical dome fixed to a ceramic panel holder placed in a Mach 6.59 laminar boundary layer. The problem was originally studied by Glass and Hunt in a 1988 wind tunnel experiment in the NASA Langley 8-Foot High Temperature Tunnel and is motivated by thermally bowed body panels designed for the National Aerospace Plane. In this work, the compressible Navier-Stokes equations for a thermally perfect gas and the transient heat equation in the structure are solved simultaneously using two high-fidelity solvers coupled at the solid-fluid interface. Predicted surface heat fluxes are within 10% of the measured values in the dome interior with greater differences found near the dome edges where uncertainties concerning the experimental model's construction likely influence the thermal dynamics. On the flat panel holder, the local surface heat fluxes approach those on the windward dome face due to a dome-induced horseshoe vortex scouring the panel's surface. Comparisons with reduced-order models of heat transfer indicate that they perform with varying levels of accuracy around some portions of the geometry while completely failing to predict significant heat loads in regions where the dome-influenced flow impacts the ceramic panel. Cumulative effects of flow-thermal coupling at later simulation times on the reduction of panel drag and surface heat transfer are quantified.

The second fluid-structure study investigates the interaction between a thin metallic panel and a Mach 2.25 turbulent boundary layer with an initial momentum thickness Reynolds number of 1200. A transient, non-linear, large deformation, 3D finite element solver is developed to compute the dynamic response of the panel. The solver is coupled at the fluid-structure interface with the compressible Navier-Stokes solver, the latter of which is used for a direct numerical simulation of the turbulent boundary layer. In this approach, no simplifying assumptions regarding the structural solution or turbulence modeling are made in order to get detailed solution data. It is found that the thin panel state evolves into a flutter type response characterized by high-amplitude, high-frequency oscillations into the flow. The oscillating panel disturbs the supersonic flow by introducing compression waves, modifying the turbulence, and generating fluctuations in the power exiting the top of the flow domain.

The work in this thesis serves as a step forward in structural response prediction in high-speed flows. The results demonstrate the ability of high-fidelity numerical approaches to serve as a guide for reduced-order model improvement and as well as provide accurate and detailed solution data in scenarios where experimental approaches are difficult or impossible.

To Mom, Dad, Anika, Krista, and Karina.

Acknowledgements

This has been the hardest thing I have ever done, and there are many people without whose help and support I could not have succeeded. First, I thank my advisors, Professor Daniel J. Bodony and Professor Philippe H. Geubelle, for their guidance, endless patience, and friendship. I would next like to thank the rest of my thesis committee, Professor Joanna M. Austin, Professor Carlos A. Pantano-Rubino, and Dr. Stephen Mike Spottswood. I especially appreciate the encouragement and help Dr. Spottswood has given me over the four and a half years I have been working with him.

I am grateful for the support from the U.S. Air Force Research Laboratory Air Vehicles Directorate under contract number FA8650-06-2-3620. Support from the Illinois Space Grant Fellowship Program is also recognized. I acknowledge computational resources provided by the National Science Foundation Teragrid (TG-CTS090004), the DOD Distributed Shared Research Centers at ERDC, ARL, AFRL, and NAVO, and the Computational Science and Engineering Program at the University of Illinois.

I next would like to thank my family, who were always willing to listen to my frustrations and provide loving support. Mom, Dad, Anika, Krista, and Karina: you have all helped me so much, and it would have been impossible without you all. I sincerely thank my grandparents, Baba and Jedo, who are the most generous people I will ever know, and my late grandparents, Noni and Nono, who I miss very much. I am also grateful for the endless support of my close friend, Tim, and my step parents, Liz and Alan.

I would like to thank Michael Campbell for donating so much of his time to helping me over the years. I would have sunk from the start without him. I would also like to thank my friend and lab mate, Mahesh Manchakattil Sucheendran, for the wise advice, the lunches he brought for me, and comforting words. I hope to meet him one day in Zihuatanejo. I thank my lab mates Qi Zhang, Mahesh Natarajan, Ashish Mishra, Nishan Jain, Revathi

Jambunathan, and Ryan Tomokiyo, who have been so kind to me and have cheered me up when I needed it.

I am very thankful to my friend Andy Pukniel for his support and for talking me into going to the Grand Canyon. Thank you Brian and Julia Woodard and Joseph Zimmerman, for your encouragement and for making me laugh. Lastly, I want to thank my roommates: Steve Henry, Emma Berdan, and Claire Baldeck, for keeping me from hanging out by myself too much. I would probably have gotten much weirder without them.

Table of Contents

List of Tables

List of Figures

Chapter 1

Introduction

High-speed flight is accompanied by severe thermal and fluid dynamic loads. A hypersonic vehicle is partially wetted by a turbulent boundary layer that produces severe pressure and thermal fluctuations over the outer skin. Furthermore, these vehicles require powerful propulsion systems that increase the strength of the loading in the engine inlet and exhaust regions. Fig. 1.1 outlines three main fatigue risk areas identified in a National Aerospace Plane (NASP)-era study for a generic hypersonic vehicle [12, 13]; namely (1) the inlet ramp, (2) the exhaust ramp, and (3) the control surfaces. Additionally, such high-speed vehicles are to be lightweight, flexible, and reusable; a set of requirements that vehicles have not satisfied in the past [14]. Such design requirements are commonly satisfied in low-speed applications where the environment and structural response are more easily understood. Extreme loading and more uncertain environmental conditions are typically designed for by increased safety margins in the form of weighty systems and frequent maintenance. Bertin & Cummings [14] give an account spanning the second half of the 20^{th} century littered with attempts to design variants of a NASP-like vehicle. They attribute the many failures of these programs to the rise of "unknown-unknowns," which "are usually discovered during flight tests and could present drastic consequences to the survival of the vehicle or of the crew and lead to unacceptable increases in the costs to develop the vehicle." [14]. Such unknown-unknowns arise due to the inability of traditional design methodologies to account for phenomena present in high-speed environments. A significant source of complexity in the high-speed regime is the presence of fluid-thermal-structural coupling [15].

Current design methodologies use a combination of analytical, experimental and numerical approaches, all utilizing educated assumptions of one form or another. The confidence in the accuracy of the assumptions translates proportionally to the amount of safety margin included in the final design. A successful hypersonic design, the Space Shuttle, reflects the large amount of design margin, in the form of added material, inflexibility, and maintenance, that results from the limited understanding of the operating environment. Figure 1.2(a) shows the extreme thermal loading on the shuttle upon reentry, that requires the use of heavy, inflexible, and frequently maintained tiles on the underside of the vehicle (Fig. 1.2(b)). Large safety factors are warranted, as it was seen that even a small irregularity in the underside of Space Shuttle Discovery caused a local increase in thermal loading (Fig. 1.3). Even considering the extensive precautions taken with the shuttle, unknown-unknowns still exist and, as evidenced by the Space Shuttle Columbia accident in 2003, can have disastrous consequences. The DARPA Falcon (Force Application and Launch from CONtinental United States) program aimed to develop the Hypersonic Cruise Vehicle (HCV) for prompt global strike capability. One stage of the project included two instances of the Hypersonic Test Vehicle 2 (HTV-2), created to test thermal protection and control systems in Mach 20 flight. Both vehicles, flown in 2010 and 2011, failed prematurely in in-flight tests due to unpredicted occurrences. While the results the first flight led to an improvement that was validated in the second flight, incremental advances through flight testing may overextend the budget of these programs, as has been the fate of the majority of hypersonic flight programs in the past.

As demonstrated above, in-flight testing is an effective way to uncover the uncertainties inherent to hypersonic flight. However, modeling techniques are being improved in accuracy and fidelity to reduce the necessity of frequent tests and better utilize testing opportunities. Ground testing is a next step in fidelity; however, due to the increasingly extreme operating conditions, these tests may not be possible. It was concluded in a National Research Council (NRC) report that the lack of ground testing capability at flight-realistic hypersonic conditions was a limiting factor in high-speed vehicle development [16]. Analytical and numerical analysis provide an alternative approach to experiments. Assumptions made in previous analytical models, successful in the design of vehicles for less demanding environments, may not be justified in the hypersonic regime. However, full-order numerical analysis is computationally expensive and may not be feasible for analysis of large components for full vehicle trajectories. Reduced-order models (ROMs) are being developed in order to provide relatively inexpensive numerical solutions. These savings in computational cost are achieved through modeling assumptions about the fidelity and solution accuracy needed to provide vital information. However, without comprehensive experimental data, it is indeterminate whether these assumptions are valid.

1.1 Thesis structure

This thesis consists of two parts. Part I spans Chapter 2 through Chapter 5 and describes the numerical simulation and comparison with an experiment of a fluid-thermal interaction problem in a hypersonic flow. In this part the level of fidelity necessary for accurate aerothermal predictions in hypersonic flows is assessed by measuring lower-fidelity models against our validated high-fidelity approach. Chapter 2 surveys the literature published on studies focused on fluid-thermal interaction. Chapter 3 describes in detail the numerical approach taken in Part I to study the fluid-thermal interaction problem. In Chapter 4, the aerothermal problem setup and the motivating experiment are presented. Part I is concluded with Chapter 5, in which simulation and code validation results are described.

Part II contains Chapter 6 through Chapter 10 and presents the details of a fluid-structure interaction problem between a supersonic turbulent flow and a flexible panel. The key focus of this section is to address how strongly coupled the fluid and structural solutions are by using a high-fidelity approach to investigate the effects that they have on each other. The merit in this approach is that it does not utilize modeling assumptions which might otherwise neglect important aspects of fluid-structure interaction. Chapter 6 gives a literature review of previous fluid-structure interaction work. Chapter 7 presents the numerical approach used in Part II and describes the formulation of a thermomechanical solver developed for the problem. Chapter 8 gives the aeroelastic problem description, and presents a previous numerical study of a compressible turbulent boundary layer [3, 17] that is used as a reference to verify the solution in the fluid domain. In Chapter 9, the generation and analysis of the turbulent boundary layer are discussed and are verified by comparison with the reference solution. Part II ends with Chapter 10, which contains the results from the fluid-structure coupled simulations. Conclusions and suggestions for future work are given in Chapter 11.

1.2 Present approach and key accomplishments

This thesis presents a study on the use of high-fidelity, high-accuracy direct numerical simulations to predict structural response in extreme environments. This approach, based on very few assumptions, serves to provide accurate data in lieu of experimental data in cases where testing may be prohibitively expensive or physically unattainable. Key accomplishments resulting from the work outlined in this thesis are listed below:

- A validated direct numerical simulation of an aerothermal problem involving a relavent 3D thermal structure under a Mach 6+ flow.
- The direct numerical simulation of a compressible turbulent boundary layer over a flexible steel panel and the quantification of the interaction between the turbulent flow and the panel response.
- The use of direct numerical simulation results to evaluate commonly-used reduced-order models for aerothermoelastic design.

Figures for Chapter 1

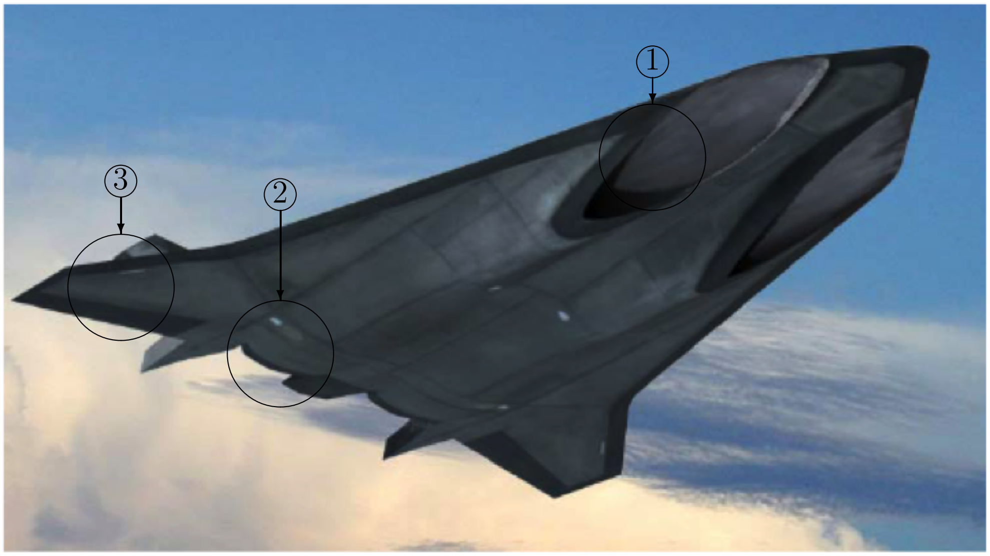

Figure 1.1: Generic hypersonic vehicle showing regions of significant thermoacoustic fatigue risk; (1) engine inlet ramp, (2) engine exhaust, and (3) control surfaces [5].

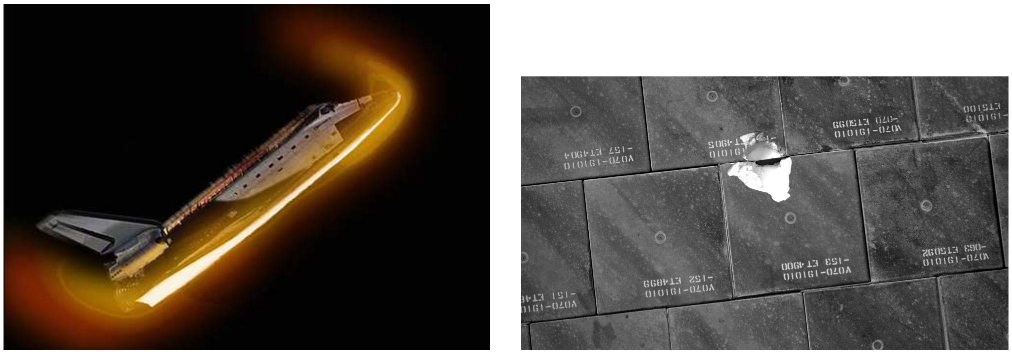

(a) (b)

Figure 1.2: (a) Extreme thermal loading on underside of a shuttle upon atmospheric reentry [6]. (b) A damaged thermal protection tile on the underside of Space Shuttle Endeavor [7].

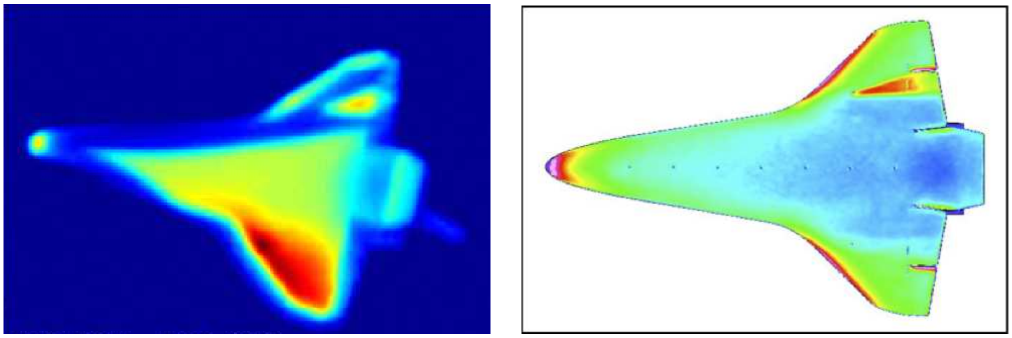

(a) (b)

Figure 1.3: (a) An infrared image of Discovery during reentry showing a 1/4 inch asperity on the wing causing a significant increase in heat load due to boundary layer transition. (b) An infrared image of the asperity on the wing of a space shuttle. [8].

Part I

Direct Numerical Simulation of Fluid-Thermal Interaction in a Mach 6.59 Flow

Chapter 2

Part I Literature Review

At present, full-order coupled analysis in high Mach number flows can be prohibitive due to computational cost, especially when long time records are desired. To mitigate the cost of the coupled approach, various reduced-order models (ROMs) have been used to investigate the effects of coupling, physical loads, and design requirements for hypersonic flight. Several different ROM approaches have been developed, oftentimes using full-order methods for one branch of the coupled analysis and reduced-order methods for the others. For example, Culler & McNamara [18] developed a coupled framework which uses third-order piston theory [19] coupled with Eckert's Reference Enthalpy method [20] to predict fluid aerodynamic pressure and thermal loads, and methods of varying fidelity for the thermal and structural solutions for thin panels. For their flight profile, they found the mutual interaction between structural deformation and aerodynamic heating to be significant, especially over increased time records [18]. They also found that quasi-static, time-averaged dynamic coupling, and instantaneous dynamic coupling yield identical flutter boundaries, but thermal stresses and temperature-varying material properties altered flutter boundaries [15].

Another class of ROMs uses snapshots of full-order steady-state solutions to provide additional information. Crowell & McNamara [21] computed sample steady-state Reynolds averaged Navier-Stokes (RANS) solutions which were then corrected for unsteady flow effects using third-order piston theory. They found that this approach improved predictions significantly when compared to using piston theory or Euler solutions, stressing the importance of viscous effects in hypersonic flows. In the same work, they investigated the use of a database of steady-state computational fluid dynamics (CFD) snapshots to create either an optimal basis of the solution space using proper orthogonal decomposition (POD), or to make approximations to the solution by interpolating between snapshots using kriging. It was found that both approaches yielded average L_∞ errors around 5%, and maximum errors of 10-20%. The kriging models were found to be slightly more accurate, while the POD models were more computationally efficient. Falkiewicz & Cesnik [22] considered the use of POD to provide a reduced-order thermal solution in aerothermoelastic simulations. This approach approximated the full-order solution with an average error of 8.2% when the thermal load on the structure was known *a priori*.

Increasing computational capabilities have enabled full-order coupled approaches to make structural response predictions in hypersonic environments. Dechaumphai et al. [23] used an integrated fluid-thermal-structural approach to analyze the response of a 2D leading edge in a Mach 6.47 uniform flow. They noted that the fluid-thermal coupling from the increase of the leading edge temperature resulted in significant reduction in aerodynamic heating. Thermomechanical results of an engine inlet cowl subject to a prescribed heat load simulating a oblique-shock/bow-shock interference produced severe in-plane stresses, suggesting the need for 3D simulations. In a later work, Dechaumphai et al. [24] investigated the engine inlet cowl while computing the shock-shock interference thermal load using a 2D finite element Navier-Stokes solver. The pressure at the interference location matched experiment, but the heat load, as predicted using a two-point differencing approximation, was only one third of the experimentally measured values, despite a very small wall normal distance of the first element in the fluid domain. Thornton & Dechaumphai [25] used the above mentioned 2D finite element fluid-thermal-structural solver to study hypersonic flow over metallic thin panels in both aligned and inclined configurations with respect to the freestream. Results showed that even very modest deformations altered flow features and introduced shocks, expansions, and recirculation regions that significantly influenced the heat load.

Using a sequential approach in which fluid loads were calculated independent of the structural solution, a numerical simulation of thermal protection system (TPS) panel bowing was performed by Kontinos & Palmer [26]. The semi-empirical methodology used CFD results that were computed *a priori* to form a surface heating distribution function parametrized by dome deflection height. Using this approach, they found that the dome deflection height *did not* change due to the surface heating perturbation caused by the thermal bowing of the dome into the flow. This is contradictory to what Culler

& McNamara [27] found using their more strongly coupled ROM approach. Hassan et al. [28] used 2D coupled CFD, material thermal response, and flight dynamics solvers to study the coupled effects of a non-equilibrium flow on the flight trajectory of a vehicle with an ablating surface. They saw that as the simulation progressed the nosetip blunted due to ablation, affecting the flow and indicating that, after more time, the coupled and uncoupled results would diverge from each other.

Recently, Crowell et al. [29] investigated the fluid-thermal coupling requirements to make heat load predictions on a panel under shock-turbulent boundary layer interactions. Their findings showed that movement of the shock location due to a prescribed panel motion significantly altered the aerothermal load on the panel. Results also suggested that quasi-static fluid-thermal temporal coupling is a viable option for response prediction. Zhao et al. [30] performed a 3D coupled simulation on a leading edge in Mach 6.47 flow using a Riemann solver with a $k-\epsilon-R$ turbulence model coupled with finite element thermal and structural solvers. They showed that a wall normal resolution of $y^+ \leq 5$ was required for accurate prediction of the heat load when compared with experiment, and that the effect of the flow-thermal coupling on the aerodynamic heating was significant.

The collective results of the above studies indicate the significant role that fluid-thermal coupling play in aerothermal response prediction in high-speed flows. In this study a fluid-thermal coupled approach is taken to investigate the aerothermal response of a 3D structure under a Mach 6.59 laminar boundary layer. As discussed in Chapter 3, very few assumptions are made as the full governing equations are solved in the fluid and thermal domains in an attempt to assess the fidelity requirements to make accurate predictions in hypersonic flows. Chapter 4 provides the details of the motivating experiment as well as a background of the simulation details. Chapter 5 focusses on the validation of the method as well as the investigation into the physics of the problem. Results are used to assess the accuracy of the assumptions that go into some common reduced-order approaches.

Chapter 3

Aerothermal Numerical Approach

The numerical formulation described in this chapter is developed to compute the aerothermal heating and thermal response of a high-speed air vehicle (Fig. 1.3). Validation of the coupled fluid-thermal solver is presented in Chapter 5.

3.1 Fluid domain

Our fluid model describes the motion of a fully non-linear, compressible, viscous, calorically or thermally perfect gas. The Navier-Stokes equations describe the conservation of mass, momentum, and total energy and are given as

$$\begin{aligned} \frac{\partial \rho}{\partial t} + \frac{\partial}{\partial x_i}(\rho u_i) &= 0, \\ \frac{\partial \rho u_i}{\partial t} + \frac{\partial}{\partial x_j}\left(\rho u_i u_j + p\delta_{ij} - \tau_{ij}\right) &= 0, \\ \frac{\partial \rho E}{\partial t} + \frac{\partial}{\partial x_j}\left[\left(\rho E + p\right) u_j + q_j - u_i \tau_{ij}\right] &= 0, \end{aligned} \tag{3.1}$$

where the conserved variables, ρ, $\rho \boldsymbol{u}$, $\rho E = p/(\gamma - 1) + \rho \boldsymbol{u} \cdot \boldsymbol{u}$, are the density, specific momentum vector, and specific total energy, respectively. The viscous stress tensor is $\tau_{ij} = \mu(\partial u_i/\partial x_j + \partial u_j/\partial x_i) + \delta_{ij}\lambda\partial u_k/\partial x_k$, where μ, λ, and δ_{ij} are the first and second viscosity coefficients, and the Kronecker delta, respectively. In Eq. (3.1), p is the thermodynamic pressure and $\boldsymbol{q}$ is the heat flux vector. Repeated indices are summed. Non-dimensionalization conventions of Eq. (3.1) are given in Appendix E, and result in the following forms for the Reynolds and Prandtl numbers,

$$\mathrm{Re} = \frac{\tilde{\rho}_\infty \tilde{c}_\infty \tilde{L}}{\tilde{\mu}_\infty},$$

and

$$\mathrm{Pr} = \frac{\tilde{\mu}_\infty \tilde{C}_{p,\infty}}{\tilde{k}_\infty},$$

respecitively, where the tilde denotes a dimensional quantity, subscript ∞ denotes are reference quantity, $\tilde{L}$ is a reference length, and c, k, and C_p are the speed of sound, thermal conductivity, and specific heat at constant pressure, respectively. We solve Eq. (3.1) on a non-uniform, non-orthogonal mesh defined by the smooth mappings

$$\boldsymbol{x} = \boldsymbol{X}(\boldsymbol{\xi}, \tau), \text{ with inverse } \boldsymbol{\xi} = \Xi(\boldsymbol{x}, t),$$

where $\boldsymbol{X}^{-1} = \Xi$, $\tau = t$, and Jacobian $J = |\partial \boldsymbol{X}/\partial \Xi|$. It can be shown that Eq. (3.1) maps into an equivalent conservative form in the computational variables $\boldsymbol{\xi}$ [31].

Finite differences are used to approximate the spatial derivatives in the computational coordinates. We use the summation-by-parts operators [32, 33] which, when coupled to the simultaneous-approximation-term (SAT) boundary conditions [34, 35, 36, 37], yield a provably stable and accurate method [38]. The spatial approximation to $\partial/\partial\xi$ is $P^{-1}Q$, where Q has the property that $Q+Q^T = \mathrm{diag}(-1, 0, \ldots, 0, 1)$. For the SAT formulation, which is a penalization approach, a penalty term is added to the right-hand-side of the governing equations. Following the notation in Svärd & Nordström [36], the penalized equation is

$$\frac{\partial \boldsymbol{q}}{\partial t} = \mathcal{F}(\boldsymbol{q}) + \sigma^{I1} P^{-1} E_1 A^{+}(\boldsymbol{q} - \boldsymbol{g}^{I1}) + \frac{\sigma^{I2}}{\mathrm{Re}} P^{-1} E_1 I(\boldsymbol{q} - \boldsymbol{g}^{I2}), \tag{3.2}$$

where σ^{I1} and σ^{I2} are the penalty parameters for the inviscid and viscous boundary conditions, respectively, and $E_1 = (1, 0, \ldots, 0)^T$. Here $\mathcal{F}(\boldsymbol{q})$ represents the divergence of the fluxes in the governing equations, A^{+} is a Roe matrix to be defined later, and I is the identity matrix. It is known that $\sigma^{I1} \leq -2$ and

$$\sigma^{I2} \leq -\frac{1}{4P(1,1)} \max\left(\frac{\gamma\mu}{\mathrm{Pr}\rho}, \frac{5\mu}{3\rho}\right), \tag{3.3}$$

are required for numerical stability. In the current work, both σ^{I1} and σ^{I2} are set to -2. The boundary data are contained in the vectors $\boldsymbol{g}^{I1}$ and $\boldsymbol{g}^{I2}$. For inviscid flows, one omits the second penalty term and defines the target vector by

$$\boldsymbol{g}^{I1} = \begin{bmatrix} \rho \\ \rho(\boldsymbol{u} - [(\boldsymbol{u}\cdot\boldsymbol{n}) - (\boldsymbol{u}_w\cdot\boldsymbol{n})]\boldsymbol{n}) \\ \rho e + \frac{1}{2}\rho|\boldsymbol{u} - [(\boldsymbol{u}\cdot\boldsymbol{n}) - (\boldsymbol{u}_w\cdot\boldsymbol{n})]\boldsymbol{n}|^2 \end{bmatrix}. \tag{3.4}$$

The matrix $A^+ = \chi\Lambda^+\chi^{-1}$ selects only the incoming characteristic variables $\boldsymbol{R} = \chi\boldsymbol{q}$, where χ transforms the conserved variables $\boldsymbol{q}$ to characteristic variables $\boldsymbol{R}$. For a calorically perfect gas χ is given by Pulliam & Chaussee [39], however, for a thermally perfect gas χ is found numerically. In both cases, χ is evaluated using the Roe average of $\boldsymbol{q}$ and $\boldsymbol{g}^{I1}$. $\Lambda^+ = \Lambda - |\Lambda|$ is a diagonal matrix containing the elements $\Lambda = \mathrm{diag}\{\hat{U},\, \hat{U}, \hat{U}+c, \hat{U}-c\}|\nabla_{\boldsymbol{x}}\xi|$ where $\hat{U}$ is the component of the velocity in the wall normal direction $\boldsymbol{n} = \nabla_{\boldsymbol{x}}\xi/|\nabla_{\boldsymbol{x}}\xi|$. For the viscous penalty term, the target data are

$$\boldsymbol{g}^{I2} = [\rho,\, \rho\boldsymbol{u}_w,\, \rho e(T_w) + \frac{1}{2}\rho|\boldsymbol{u}_w|^2]^T, \tag{3.5}$$

which applies a no-slip, isothermal condition for a moving wall with velocity $\boldsymbol{u}_w(\boldsymbol{x}, t)$ and with temperature $T_w(\boldsymbol{x}, t)$. Additionally, sponge regions, where the forcing term $-\eta(\boldsymbol{q} - \boldsymbol{q}_{ref})$ is added to the right hand side of Eq. (3.1), are employed. The effect is to absorb and minimize reflections from computational boundaries by penalizing the difference between the internal solution, $\boldsymbol{q}$, and a target solution, $\boldsymbol{q}_{ref}$ [40]. The strength of the penalization is controlled by $\eta(\xi) = N\xi^2$, where N is the sponge amplitude and ξ is the distance from the boundary normalized by the sponge length. The effect of the sponge zones can be seen in Fig. 3.1(a). The zones affected by the sponge have been removed from the remaining figures in Part I of this thesis in order to clarify the presentation of the solution (Example: Fig. 3.1(b)).

For the current work, the strong form of the viscous terms is utilized, where spatial second derivatives are approximated by repeated application of first derivative finite difference operators. This method is more computationally efficient than the weak form (expanded second derivatives). However, the strong form of the viscous terms has no numerical damping at the highest wavenumber, which can lead to instabilities in the simulation. The implicit spatial filter presented by Lele [41] is used to provide numerical damping to the solution at each time step. Filtering is accomplished by solving the linear system of equations resulting from the application of Eq. (3.6) to grid points

i in each direction:

$$\alpha_f \hat{f}_{i-1} + \hat{f}_i + \alpha_f \hat{f}_{i+1} = a f_i + \frac{d}{2}(f_{i+3} + f_{i-3}) + \frac{c}{2}(f_{i+2} + f_{i-2}) + \frac{b}{2}(f_{i+1} + f_{i-1}), \tag{3.6}$$

where $(\hat{\ })$ denotes a filtered quantity and a, b, c, and d determine the accuracy of the filter and are functions of α_f. The parameter α_f governs the filter strength, which diminishes as $\alpha_f \rightarrow 0.5$. The value assigned to α_f is 0.499 for the work presented in Part I of this thesis. The transfer function for the 10^{th} order filter using this value of α_f is shown in Fig. 3.2, and the cutoff wavenumber associated with 0.499 is 0.96π, where cutoff is defined as a 3 dB drop in the amplitude of the filtered quantity relative to the unfiltered one. In order to minimize the oscillations due to the presence of shocks in the fluid domain, the shock capturing scheme of Kawai et al. [42] is used. Any direct effect of the scheme on the calculation of heat flux into the thermal domain is removed by allowing only the artificial bulk viscosity to be modified. The shock capturing scheme was found to have no effect on the surface heat flux.

Both calorically perfect (constant specific heat capacities) and thermally perfect (temperature-varying specific heat capacities) gas models are used. The thermally perfect model, which departs from the calorically perfect assumption at high temperatures, is implemented using a user-provided lookup table. For the aerothermal work, the thermal properties of methane-air combustion products were given in Leyhe & Howell [43]. Verification of the implementation of the thermally perfect gas model is given in Appendix A.

The fluids code has been used in a variety of fluid-only problems involving both laminar and turbulent flows [44, 45, 46, 47, 48, 49]. The temporal advancement of Eq. (3.1) is deferred to a later section.

3.2 Thermal domain

The thermal solution in the solid is found by solving the 3D transient heat conduction equation,

$$\rho C_p \frac{\partial T}{\partial t} = \frac{\partial}{\partial x_j}\left(k \frac{\partial T}{\partial x_j}\right), \tag{3.7}$$

using an in-house finite element thermal code fitted with tri-linear basis functions on a hexahedral mesh. The solution is marched implicitly in time using the second-order accurate, unconditionally stable, Crank-Nicholson scheme

[50]. The resulting linear system of equations is then solved iteratively using the Generalized Minimum Residual (GMRES) [51] method provided in the HYPRE [52] suite of parallel linear algebraic solvers. The thermal solver has been verified against classical analytical solutions. The same verification is done for a solver in Section 7.3.1 and is presented in detail there.

3.3 Interface treatment

The individual codes are weakly coupled at the interface where the fluid-thermal interaction takes place. The fluid and thermal solutions are found independently in their respective domains at a given time step $t_m = m\Delta t$. The spatial transfer along the interface is achieved using the common refinement scheme, which provides a conservative and accurate transfer of heat flux across the non-matching discretizations at the interface [53, 54]. The stability benefits of the implicit thermal solver are exploited in the choice of the physical quantities to pass at the fluid-thermal interface. An analysis by Giles [55] showed that numerical stability is increased when temperature is passed from the solid to the fluid while the heat flux is passed from the fluid to the solid. Roe et al. [56] extended this analysis to problems involving moving grids. Thus the thermal solver provides $T_w(\boldsymbol{x}, t)$ to the fluid solver while $q_n = -k\partial T/\partial n$, where $\boldsymbol{n}$ is the unit normal pointing into the fluid from the solid, is determined by the fluid and transferred to the solid thermal solver.

3.4 Temporal solution procedure

One major challenge in fluid-thermal interaction simulations is the impact of the highly disparate time scales involved in fluid and thermal physics. In a preliminary study [57], the fluid solution was seen to recover a state of mechanical equilibrium roughly 1 ms after a boundary condition perturbation. The thermal solution, as presented in the next chapter, changes on the order of 1-10 K/s in the region of interest. This results in an $\mathcal{O}(10^2) - \mathcal{O}(10^3)$ ratio between the thermal and fluid time scales. The computational cost associated with resolving the time scales involved in both disciplines can be prohibitive due to the fact that the transient thermal solution in the solid evolves much more slowly than does the solution in the fluid. This effect is exacerbated in the case where the fluid solution is explicitly advanced in time, in which the coupled system time step is limited by the stability requirements associated with the fluid solution. However, the goal of the current work is to determine the transient thermal response of a structure in the hypersonic environment with a laminar boundary layer. In this situation, it is not necessary to resolve the small time scales in the fluid solution. The transient solution of the fluid-thermal system becomes more tractable if a quasi-static temporal coupling is employed. The time accurate thermal solution at the $m + 1$ time step is found by integrating the solution given the thermal load provided by the fluid solution at time step m. The interface temperature is given as a boundary condition in the fluid domain and the fluid is marched from time step m to the steady-state solution consistent with the $m + 1$ interface temperature.

Since a temporally accurate fluid solution is not required, the equations (Eq. (3.1)) were integrated to steady-state using a less accurate, accelerated five-stage Runge-Kutta (RK5) scheme developed by Jameson [58]. In the RK5 scheme, the viscous fluxes are evaluated at two of the five stages and are frozen for the remaining stages. These schemes were shown by Swanson and Turkel [59] to extend the stability limit significantly while sacrificing temporal accuracy. The variant used in the current work evaluates the viscous terms in the first two stages and is formally first-order accurate in Δt.

Figures for Chapter 3

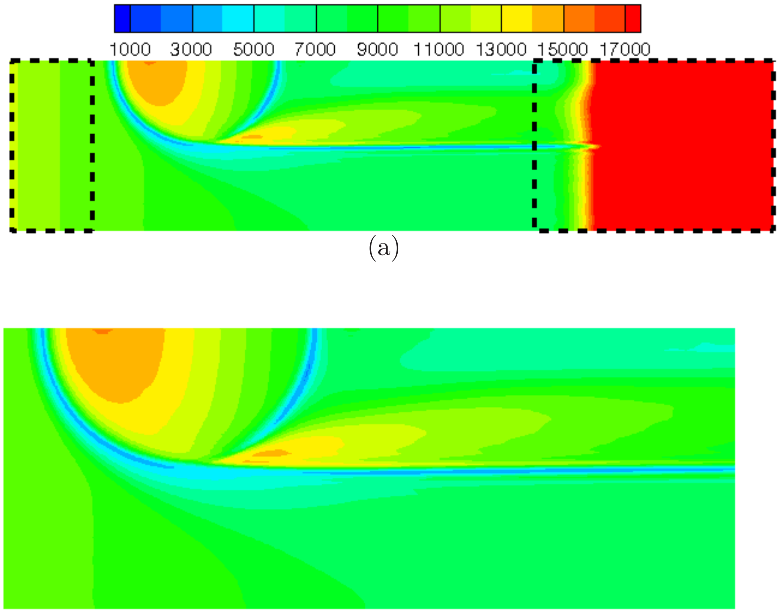

(a)

(b)

Figure 3.1: Surface heat flux (W/m^2) at $t = 1$ s (a) with sponge zones and (b) without sponge zones. Sponge zones are omitted from remaining figures.

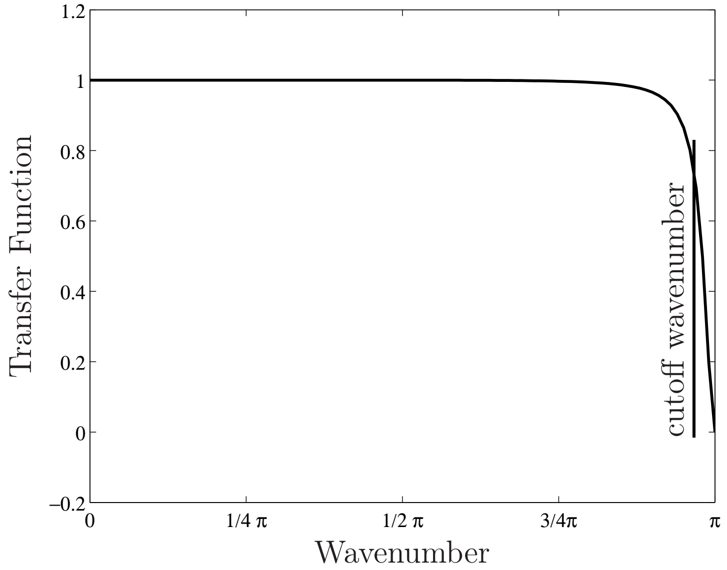

Figure 3.2: Transfer function of the 10^{th}-order implicit filter for filter strength $\alpha_f = 0.499$. The associated cutoff wavenumber of 0.96π is shown with a vertical line.

Chapter 4

Background: Aerothermal Investigation of a Rigid Protuberance in Mach 6.59 Flow

As mentioned in Chapter 1, one key factor that makes simulation of the hypersonic environment so attractive is that it is difficult to run experiments that replicate the desired conditions. Unfortunately, due to this fact, experimental data needed to validate the solutions produced by numerical simulations of extreme environments are limited. However, in the 1980's, researchers at NASA Langley conducted a series of hypersonic wind tunnel experiments that investigated the thermal effects on a NASP-like body panel in a hypersonic flow. The reports [1, 9] involved the insertion of rigid, 3D geometries into hypersonic flows of methane-air combustion products to measure the thermal and structural loads on the models. The motivation for the studies came from the interest in using lightweight, flexible metallic body panels in lieu of heavy, ablative thermal protection system panels. In the presence of high surface temperatures, flexible body panels bow into the flow field due to through-thickness thermal gradients. The rigid, domed protuberance [1] and quilted dome model [9] represented the deformed geometry of such thermally bowed panels. In both reports, surface temperature, surface pressure and heat flux data were taken. In a regime where experimental data are scarce, this series of tests serves as an excellent resource for the validation of the fluid-thermal multi-physics code described in Chapter 3.

4.1 NASA Langley 8-Foot High Temperature Tunnel facility

In order to successfully predict the response of a test article during the experiments, the tunnel conditions first need to be understood. The NASA Langley 8-Foot High Temperature Tunnel (8' HTT) (Fig. 4.1) is a high-energy hypersonic blowdown wind tunnel. Built in the 1960's, it has been used extensively to test various aspects of hypersonic flight vehicles from thermal protection systems to integrated propulsion systems. The tunnel is capable of simulating aerodynamic heating and pressure loading on test articles in a nominally Mach 7 flow at altitudes of 80 to 120 thousand feet (24 km to 36 km). The high-energy freestream flow is obtained by the combustion of methane and air under pressure in a combustion chamber:

$$CH_4 + 2(O_2 + 3.76N_2) + Ar \rightarrow CO_2 + 2H_2O + 7.52N_2 + Ar. \tag{4.1}$$

The combustion products are then accelerated to Mach 7 through a conical nozzle terminated by a constant 8-foot diameter section before entering the test section. The attainable freestream dynamic pressures are within the range of 250 psi to 1800 psi (1.7 MPa to 12.4 MPa), while the total temperatures range from 2400 R to 3600 R (1300 K to 2000 K). The freestream Reynolds numbers range from 0.3 to 2.2×10^6/ft (1.0 to 7.2×10^6/m), and the tunnel can sustain these conditions for 120 seconds.

4.2 Mechanical systems

The test article (e.g., flat plate, spherical protuberance, quilted dome panel) is installed in a cavity of a ceramic flat plate. Initially hidden in a pod below the wind tunnel during startup, the assembly is inserted into the flow in approximately 1.5 seconds using an elevator with a curved strut model pitch system capable of positioning the test article at an angle of attack of $\pm 20°$ [60]. An angle of attack of 5° was used in the experiments of interest.

4.3 Flow conditions

The flow conditions for runs 1 and 14 in the 1986 experiment are given in Table 2 of Glass & Hunt [1] and are reproduced in Tab. 4.1 of this thesis. The tabulated values were not measured directly by Glass & Hunt, but were based on data from previous tunnel surveys. It is noted that the total to static temperature and pressure ratios are those for a thermally perfect gas. Special considerations regarding this fact are discussed below. The freestream properties are dictated by the equivalence ratio of the fuel to oxidizer in the combustor given as

$$\phi = \frac{(n_{CH_4}/n_{O_2})_{actual}}{(n_{CH_4}/n_{O_2})_{stoichiometric}}. \tag{4.2}$$

The equivalence ratios in the combustor were not provided by Glass & Hunt [1].

Table 4.1: Experimental conditions of the 1986 tests [1]. D = dome diameter, H = dome height. Run 1 did not include a dome model.

Run	M	$T_{0,\infty}$ K	$p_{0,\infty}$ kPa	p_{∞} kPa	D m	H mm	δ^{99} mm	Materials	Instrumentation	Boundary layer condition
1	6.55	1872	2961	0.655	N/A	N/A	12.7	Ceramic	Pitot Probe	Laminar
14	6.59	1894	2896	0.648	0.71	19.3	12.7*	Aluminum & Ceramic	Thermocouple	Laminar

4.4 8-Foot High Temperature Tunnel flow conditions

In order to accurately model the flow conditions in the 8' HTT, the gas properties of the methane-air combustion products had to be calculated. However, in order to obtain the needed thermal storage coefficients (specific heat capacities, $C_p(T)$ and $C_v(T)$) and transport coefficients (viscosity, $\mu(T)$ and thermal conductivity, $k(T)$), the composition, and therefore the equivalence ratio of methane and air, had to be obtained. Leyhe & Howell [43] provide empirical data for the specific heats and curves for viscosity and conductivity corresponding to four equivalence ratios: $\phi = 0.7$, $\phi = 0.8$, $\phi = 0.9$, $\phi = 1.0$. As mentioned above, the equivalence ratios for the wind tunnel runs were not given in the Glass & Hunt report and were determined iteratively as follows. First, one of the four ϕ values listed above was selected. Then, given the total temperature and reactant equivalence ratio, a constant pressure combustion calculation using STANJAN [61] was performed to determine the mole fractions of the products in the freestream. Given the mole fractions of the combustion products and the information given on page 26 of Leyhe & Howel [43], a piecewise polynomial for $C_p(T)$ was constructed from the weighted sum of $C_p(T)$ polynomials for all individual species. The freestream ratio of specific heats, γ_∞, total temperature, T_0, and total pressure p_0, were then calculated according to

$$\gamma_\infty = \frac{C_p(T_\infty)}{C_p(T_\infty) - R}, \tag{4.3a}$$

$$\int_0^{T_0} C_p(T)dT = \int_0^{T_\infty} C_p(T)dT + \frac{\gamma_\infty R T_\infty M_\infty^2}{2}, \tag{4.3b}$$

$$p_0 = p_\infty \left[\int_{T_\infty}^{T_0} \frac{C_p(T)}{RT} dT \right]. \tag{4.3c}$$

It was found that an equivalence ratio of $\phi = 0.7$ gave the freestream conditions closest to those presented for the runs in Tab. 4.1. The curves for $\mu(T)$ and $k(T)$ were digitized from Figs. 14(d) and 16(d) on pages 87 and 95 of Leyhe & Howel [43], respectively, and approximated by piecewise polynomials. The representation of the transport coefficient data for the methane-air mixture with polynomials lead to errors under 2% and 5% in the $\mu(T)$ and

$k(T)$ curve fits, respectively. Additionally, the total temperatures and pressures are reported [62] to vary up to 9% and 20% in the horizontal and vertical extremes of a 4-foot by 4-foot box centered at the centerline 18 inches downstream of the nozzle exit. These deviations are attributed to condensation in the expansion section. Note that the test article's area of interest sits within the core flow where the experimental variability is less, on the order of 5%, and is away from the more highly variable flow closer to the tunnel walls.

4.5 Verification of the laminar boundary layer

Runs 1 through 15 of the 1986 experiment [1] involved studying the loads on the spherical dome protuberance due to the presence of a laminar boundary layer in hypersonic flow. The laminar boundary layer was produced over the inclined flat panel with a 3/8-inch radius blunt leading edge (Fig. 4.2(a)). The laminar state of the boundary layer was verified by comparison with an analytically determined boundary layer profile [63]. The experimental boundary layer profile was measured using a boundary layer probe, as shown in Fig. 4.2(b). The use of the boundary layer probe is an invasive measurement. The presence of the probe causes a local bow shock, shown in Fig. 4.3, such that the stagnation pressure measured by the pitot tube is that associated with the post shock flow. To calculate the pre-shock Mach number, Glass & Hunt used the Rayleigh pitot formula

$$\frac{p_{t2}}{p_{fp}} = \left(\frac{(\gamma+1)^2 M_1^2}{4\gamma M_1^2 - 2(\gamma-1)}\right)^{\frac{\gamma}{\gamma-1}} \frac{(1-\gamma)+2\gamma M_1^2}{\gamma+1}, \tag{4.4}$$

which relates the total pressure after the shock (p_{t2}) to the static pressure before the shock (p_{fp}). In supersonic applications, measuring the static pressure upstream of the probe is usually done by placing a static pressure probe flush with the wind tunnel wall in a smooth region of the flow. Glass & Hunt did not use a flat plate pressure that they measured during run time at the location of the probe; instead, a reference flat plate pressure from a previous report [1] at a location downstream of the boundary layer probe was used.

4.6 Initial and boundary conditions

To produce the inflow boundary conditions for the coupled simulation domain, a 2D simulation was run using the commercial software, ANSYS Fluent. The solution of this 2D problem was sufficient to provide the inflow boundary conditions because the geometry up to that point was invariant in the third dimension and edge effects were not capable of affecting the region of interest. The 2D simulation also served to validate that the selection of gas properties was consistent with the Glass & Hunt experiment. The 2D Fluent domain was refined until the solution was determined to be grid independent. It is compared with the coupled simulation fluid domain in Fig. 4.4.

The simulation was run on the 2D Fluent domain using the freestream parameters given in Tab. 4.1 and gas properties consistent with a combustion chamber equivalence ratio of $\phi = 0.7$. The plate had been heated an unknown amount at the time that the boundary layer measurement was taken. It was assumed that the thermal state of the plate was close to its initial isothermal 300 K condition, and that was the value assigned to the plate in the simulation. The results in Fig. 4.5 were post-processed following the procedure used by Glass & Hunt to extract the boundary layer profile. Although the geometry of the probe was not modeled, its presence was simulated by solving for the post shock flow given the unprocessed simulation data. The post shock pitot pressure, p_{t2}, the reference flat plate pressure [9], p_{fp}, and the ratio of specific heats [9], $\gamma = 1.38$, were used to solve for the pre-shock Mach number in the Rayleigh pitot formula (Eq. (4.4)).

It can be seen in Fig. 4.5 that the predicted and the experimentally measured profiles are similar throughout the boundary layer. The simulation slightly underpredicts the Mach number in the entropy layer. The Mach number in this region is very sensitive to the leading edge geometry and boundary conditions, for which the data are not available to be fully confident that the experimental setup was represented exactly. The agreement between the simulation and experiment is sufficiently accurate to validate our assessment of the tunnel flow and gas properties.

4.7 Insertion procedure

In the 8' HTT, test articles were inserted into the initialized hypersonic freestream over a period of 1.5 seconds; before this time they were held below and outside the established freestream. Heating of the panel by the flow occurred during the panel insertion from an angle of attack of 0° to an angle of attack of 5°. In order to accurately model the temperature distribution in the thermal domain at the moment that it reached the 5° position, a fully coupled, transient simulation of the panel insertion would have to be done. A simulated 1D panel insertion was done to estimate the amount of heating that would take place during the insertion time and evaluate the best course of action. The heating of a 1D rod was modeled using a transient finite element code developed in Matlab. The material properties, boundary conditions, and geometry of the rod were chosen to be consistent with the aluminum sheet metal heat flux dome in run 14 of Glass & Hunt [1]. In order to provide the heat flux from the fluid, the compressible self-similar boundary layer equations were solved. The parameters for the flow were chosen to be the post oblique shock flow conditions consistent with the Glass & Hunt scenario at a location similar to that of the heat flux dome. The coupling set up can be seen in Fig. 4.6.

The 1.5 seconds were divided into discrete time steps and at each time step the angle of the flat plate was incremented towards 5°. At each increment, the post oblique shock conditions were calculated and passed along with the plate surface temperature to the boundary layer code to solve. The surface heat flux was taken from the solution of the boundary layer equations and provided as a thermal load on the coupled boundary of the 1D thermal domain. The thermal domain was then integrated one time step and returned a new surface temperature as a boundary condition to the fluid domain. This process was iterated until the heat flux and wall temperature were converged. At the end of the 1.5 second insertion time, with the final angle of attack of 5° attained, the surface temperature at the location of the heat flux dome was estimated to have risen 2 K from the initial temperature of 300 K. This temperature rise was determined to have a negligible effect on the heat flux, and therefore the initial condition of the coupled simulation could be taken as a 300 K isothermal wall boundary condition to the fluid domain and a uniform temperature in the thermal domain.

Figures for Chapter 4

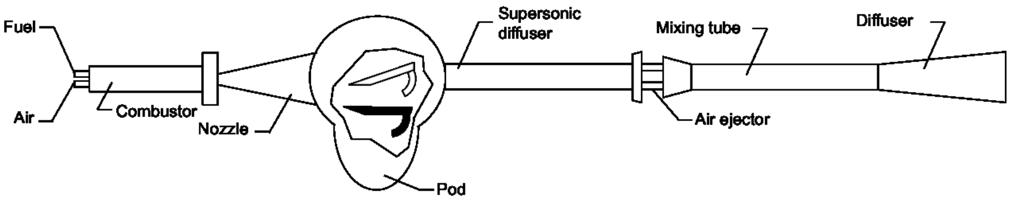

Figure 4.1: The Langley 8-Foot High Temperature Tunnel (Recreated from [9]).

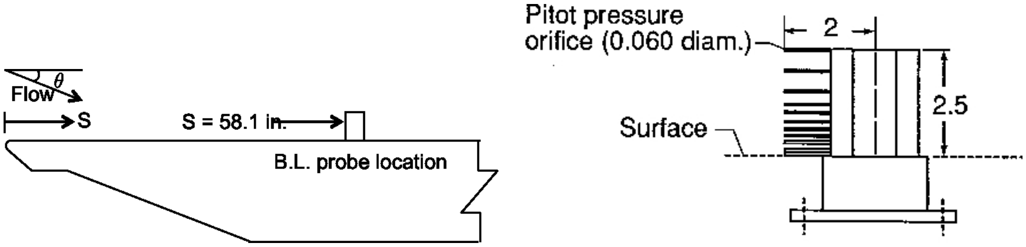

(a) (b)

Figure 4.2: (a) Flat plate panel holder and (b) boundary layer probe schematic. Units are in inches. (Taken from Glass & Hunt [9].)

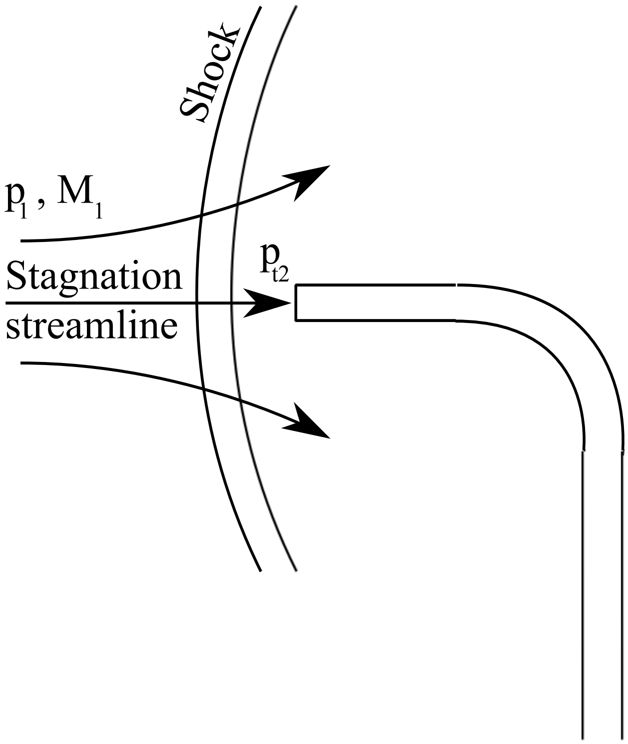

Figure 4.3: Pitot probe in supersonic flow.

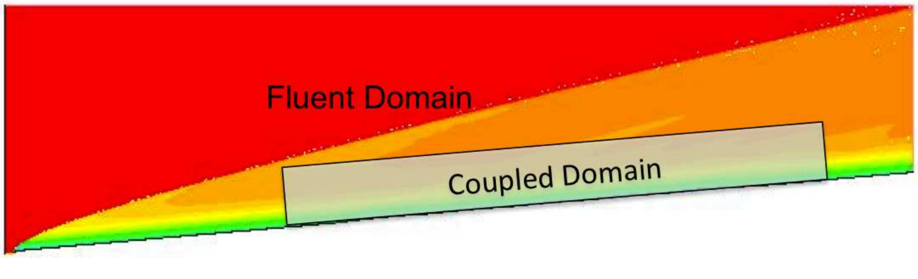

Figure 4.4: 2D Fluent domain with Mach number contours. The coupled simulation uses the Fluent solution to provide boundary conditions and an initial guess for the solution.

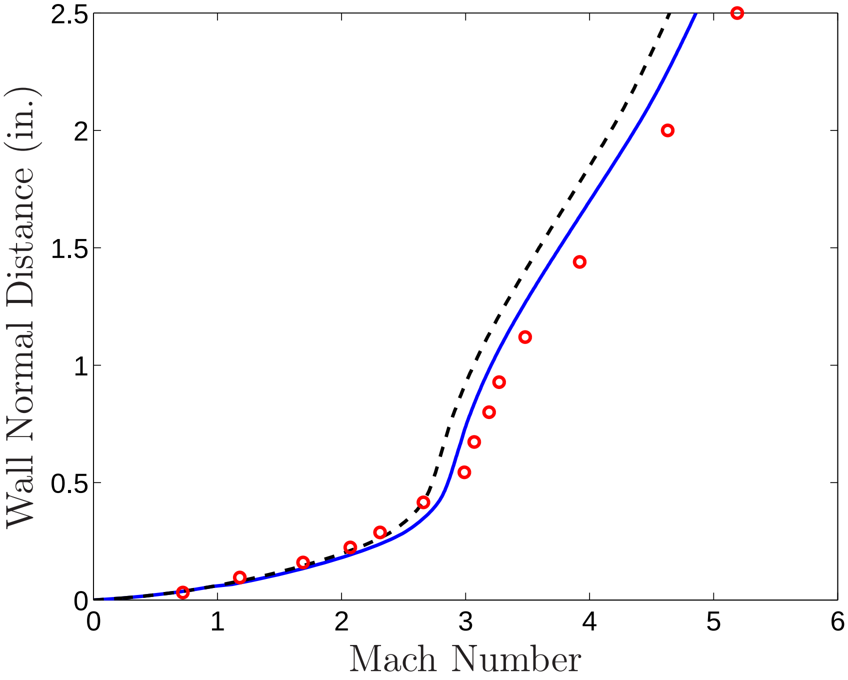

Figure 4.5: Boundary layer profile at $X = 1.476$ m: comparison between numerical results and experimental measurements [1]. Processed simulation data based on Eq. (4.4) (solid line), unprocessed simulation data (dashed line), experiment (circles).

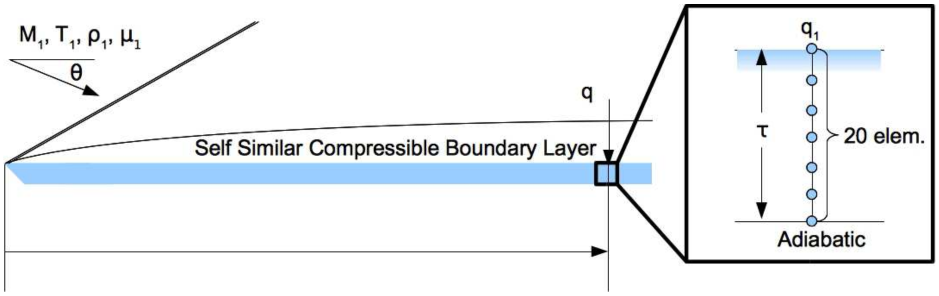

Figure 4.6: 1D fluid-thermal problem to estimate insertion heating. The rise in surface temperature during model insertion was estimated to be 2 K.

Chapter 5

Aerothermal Investigation Results

5.1 Coupled fluid-thermal simulations

The experiment featured in the 1986 report [1] was selected to be the validation case for the fluid-thermal solver. Out of the 33 experimental configurations investigated in the report, run 14 was selected for the present simulation. This particular run featured a single aluminum dome installed in a ceramic flat plate. The 28.6 mm thick flat plate was made from Resco Cast RS-17E refractory ceramic. The aluminum dome was made from 14 gauge sheet metal (1.57 mm thick). The spherical dome had a 3.28 m radius of curvature and a diameter of 0.71 m. The backside of the dome was exposed to an evacuated chamber. Material properties are listed in Tab. 5.1. The assembly was inserted into a Mach 6.59 freestream as described in the above section and shown in Fig. 5.1. Details on the experimental conditions are given in Tab. 4.1.

Fluid and thermal domains

For the coupled simulation, the fluid domain is discretized with a single $288 \times 313 \times 97$ structured grid, totaling over 8.7 million grid points. The grid is designed to have an estimated $y^+ = y/\delta_\nu$ value under 5 for the first wall normal grid point to guide the near-wall resolution, where $\delta_\nu = \nu\sqrt{\rho/\tau_w}$ is the viscous length. It is confirmed by simulation results (Fig. 5.2) that the y^+ value is less than 2 everywhere in the domain. In a later section, a grid convergence study shows this wall normal refinement to be sufficient. The surface grid extends away from the wall with a geometric growth rate under 1%. Fluid grid convergence data are given later in this section.

The thermal domain is meshed with 878,000 linear 8-node brick finite elements and is modeled to represent closely the dome geometry described

Table 5.1: Material properties in thermal domain.

Material	Density ρ, $\frac{\text{kg}}{\text{m}^3}$	Conductivity k, $\frac{\text{W}}{\text{m}\cdot\text{K}}$	Specific heat capacity C_p, $\frac{\text{J}}{\text{kg}\cdot\text{K}}$
Resco RS-17EC	2192	1.07	750
Aluminum (7000 series)	2800	155.0	883

in the 1986 report. As mentioned above, the domain is made up of two parts with different material properties that have to be meshed separately with matching nodes along the material interface. The ceramic flat plate portion has a high mesh density near the surface to capture the thermal gradients at the fluid-structure interface, but then is stretched into the plate. The aluminum dome is meshed with 10 elements through its thickness. This mesh density is shown to produce spatially invariant results for an analogous 1D finite element solution for the present conditions. The spatial resolution of the thermal domain is discussed further in Section 5.2.6. The dome is backed by an evacuated chamber, represented by an adiabatic boundary condition.

Fig. 5.3 shows the orientation and boundary conditions of the two domains. The boundary conditions on the thermal domain are set to adiabatic everywhere except on the interacting surface. The initial condition in the thermal domain is a uniform temperature of 300 K. In the fluid, a symmetry plane bisects the dome while the other spanwise boundary is modeled as a slip wall since edge effects from the panel holder do not influence the region of interest. The inflow, top, and outflow are treated as far field boundaries. The reference solution for the far field boundaries is provided by a target solution generated by an ANSYS Fluent simulation of the complete panel at a 5° incline in the Mach 6.59 freestream flow (Fig. 4.4). The target solution for this simulation is a composite consisting of a refined 2D Fluent solution over the full domain and a coarse 3D Fluent simulation of the full domain. The inflow region is dominated by the 2D solution to provide an accurate and inexpensive estimate for the inflow conditions, while the 3D solution is used in the region above and aft of the dome to provide a reasonable match between a 3D varying internal solution and the fixed boundary conditions. The shaded regions in Fig. 5.3 represent sponges which blend the target solution with the internal solution to promote simulation stability near the boundaries. The target solution also provides a fair initial condition in the fluid domain, which reduces overall the simulation time. All reported results do not include data from the sponge influenced regions.

Fluid steady-state convergence

As mentioned above, the temporal coupling is done in a quasi-static configuration, in which the transient-thermal problem is solved given the heat flux from the steady-state fluid solution at each thermal time step. In a previous paper [64], we considered several definitions of fluid steady-state and found that, for the quantity of interest (heat flux into the thermal domain), the change between fluid iterations in the root-mean-square (RMS) of the heat flux over the interacting surface,

$$\Delta q_{\mathrm{RMS}} = \frac{\sqrt{\sum_{i=1}^{N}(q_{i,k+1} - q_{i,k})^2}}{N},$$

was an appropriate metric, where N is the number of grid points on the interacting surface. Further, through a convergence study, it was concluded that a criteria of $\Delta q_{\mathrm{RMS}} < 1 \times 10^{-3}$ W/m^2 was sufficient to provide accurate results.

Fluid spatial convergence

The primary goal of this study is to simulate the heat flux into the aluminum spherical dome protuberance in the Mach 6.59 flow, for which experimental data are available. To be sure that the predicted heat flux is an accurate solution of the Navier-Stokes equations, grid independence must be verified for the solution on the spherical dome. As the heat flux into the surface is most sensitive to the wall normal resolution of the solution, the grid is designed to be very fine at the wall. The y^+ value is confirmed by a fluid-only simulation to have a maximum value of approximately 1.1 on the dome surface. To ensure that this is sufficient, a homothetic grid refinement by a factor of 2 in the wall normal direction is done, resulting in a $288 \times 625 \times 97 =$ 17.4 million point grid. The solution, after being run to steady-state as defined above, is compared with the solution from the original grid. The maximum y^+ value for the new grid is less than 0.6, and occurs on the flat plate next to the dome. The heat flux into the dome differs from the original results by less than 0.1%. The small difference suggests that the grid point distribution in the wall normal direction in the original grid is fine enough to capture the heat flux into the dome.

To ensure grid independence in the streamwise and spanwise directions, the original, 8.7 million point grid is refined homothetically by a factor of 2 along both directions simultaneously, resulting in a $575 \times 313 \times 193 = 34.7$ million point grid. The resulting steady-state heat flux is again compared to that from the original grid. The change in heat flux on the dome is less than 0.3%, indicating that the 8.7 million point grid is suitable for the coupled fluid-thermal simulation for prediction of heat flux into the dome. However, this refinement shows that the grid requirements *off* the dome are more stringent than those on the dome. Further refinement is done for a fluid-only investigation into the flow features in these regions. The solution on the finest grid is discussed in Section 5.2.4.

5.2 Results

5.2.1 Effect of numerics on surface heat flux

As mentioned in Section 3.1, the viscous terms of Navier-Stokes equations are evaluated in the present work using the strong form due to its computational efficiency. For stability reasons, the strong form requires the use of solution filtering in order to provide numerical damping. Preliminary simulation results indicate that the heat flux calculated at the surface is very sensitive to the level of filtering used. Several small, 2D fluid-only simulations were run over a flat plate at the same freestream conditions in order to understand and avoid the inaccuracies introduced by the filter. The 2D simulations were run on a grid similar to that used in the Glass & Hunt coupled simulation, and extended over the region forward of the dome. The 2D initial and boundary conditions from the Glass & Hunt simulation were used in order to make the results relevant to the 3D simulation. The two filter parameters that affect the solution are the filter strength (α_f) and whether the filter employs biased, high-accuracy stencils as the boundary is approached or centered stencils but with decreasing stencil size and order. Unfiltered solutions using the Cartesian and weak form (not shown) of the viscous terms converge to the same values. The Cartesian and weak forms of the viscous terms use expanded second derivative finite difference operators which provide sufficient numerical dissipation to not require a filter in the current problem. In the strong form simulations using the centered filter, the heat flux very slowly converges to the values found by the unfiltered Cartesian form, significantly underpredicting the heat flux as shown in Fig. 5.4(a). When using the boundary filter, the strong form predictions converge to those of the unfiltered Cartesian form (Fig. 5.4(b)) and was thus used for all simulations in this work. Figure 5.5 shows that the centered filter affects the heat flux by modifying the temperature profile in the boundary. The shallower temperature gradient directly affects the heat flux into the plate.

5.2.2 Assessment of gas thermal model

With the uncertainties associated with the grid and numerics quantified, results are presented from the coupled fluid-thermal simulation of a Mach 6.59 flow over a flat plate with a spherical protuberance. The fluid-thermal solution is advanced to 5 seconds in time in accordance with run 14 of the 1986 Glass & Hunt experiment [1]. The regions of interest are the dome surface and surrounding areas. Results for longer run times are given later in this article.

As mentioned earlier, the flow solver has the capability of simulating a calorically perfect or a thermally perfect gas. It can be seen in Fig. 5.6(a) that the ratios of specific heats ($\gamma = C_p/C_v$) of these two models diverge from each other at higher temperatures. Coupled fluid-thermal simulations are run to 5 seconds using each of the gas thermal models to assess the differences in the resulting heat fluxes and thermal (solid) solution. Referring to Tab. 4.1, the temperature data given in Glass & Hunt [1] is the total temperature based on the 8' HTT combustor conditions. The total temperature and freestream Mach number are used to calculate the freestream static temperature for the inflow boundary condition of the coupled simulations. To be consistent, the calculation of the freestream temperature is calculated by $T_\infty = T_{T,\infty}\left(1 + \frac{\gamma-1}{2}M_\infty^2\right)^{-1}$ in the calorically perfect case, and Eq. (4.3) in the thermally perfect case. The resulting freestream temperatures are 204.73 K and 237.14 K in the calorically and thermally perfect cases, respectively.

Figure 5.7(a) shows the heat flux distribution along the symmetry plane of the dome from the fluid-thermal coupled simulations using both the calorically and thermally perfect gas thermal models. The thermally perfect model consistently predicts higher heat flux values into the dome and flat plate. Interestingly, the variation in heat flux over time is seen to be less in the thermally perfect case. This is due to the increase in C_v with temperature (Fig. 5.6(a)), as given by $C_v = R/(\gamma - 1)$. The boundary layer thickness increases less with temperature as C_v increases, which results in the wall normal temperature gradient being less sensitive to the surface temperature. Therefore, the heat flux decreases less in the thermally perfect case. The resulting surface temperature as the fluid-thermal coupled simulation progresses from 1 to 5 seconds is shown in Fig. 5.7(b). As expected from the heat fluxes, the temperature along the symmetry line is also consistently higher in the thermally perfect case. Although the total temperature of the gas in the two simulations is the same, the total energy in the calorically perfect case is less than that in the thermally perfect case. The difference in total energy is because at $T_{T,\infty} = 1894$ K, the specific heat capacity is higher in the thermally perfect case. When compared to the heat fluxes reported by Glass & Hunt, the values from the thermally perfect simulation are closer than those from the calorically perfect simulation. Unless otherwise stated, all further results represent the thermally perfect gas model. A comparison between solutions from the two models when using identical static freestream conditions is presented in Appendix C.

5.2.3 Surface temperature evolution

Figs. 5.8(a)-(c) show the evolution of the surface temperature at three times during the 5 second coupled simulation. The surface temperature contours give insight into the flow physics. As the time progresses, the largest temperature rise occurs in two regions. While the whole front half of the dome shows an obvious temperature increase, the forward-most portion of the dome exhibits the most elevated temperature. The increased heat flux in this region is due to the flow impinging on the front of the dome. A second region of large temperature increase is located just past the outer spanwise extreme of the dome on the ceramic plate. This is a viscous effect generated by the impingement of vorticity shed off of the dome. Interestingly, the surface temperature in this region is slightly higher than that at the flow impingement region, while Fig. 5.9 shows a larger heat flux at the front of the dome. The relation between surface temperature and heat flux is a function of the thermal properties of the dome (aluminum) and flat plate (ceramic), and will be addressed in Section 5.2.5 below. Another phenomenon, most apparent in Fig. 5.8(c) and Fig. 5.9, is the occurrence of low heat flux regions along the circumference of the dome. The close proximity of high and low heat flux indicates that there is an extreme change in the behavior of the flow in these regions.

5.2.4 Flow solution features

Investigation of the flow behavior at time, $t = 0$ s, at the surface provides information about the mechanisms which lead to the thermal features discussed in the previous section. Fig. 5.10(a) and Fig. 5.10(b) show the surface streamlines, as visualized through the surface shear stresses, along with heat flux and pressure contours, respectively. The shear stress visualization in Fig. 5.10(a) shows that there is a correlation between the flow separation and recirculation and the regions of low heat flux. Fig. 5.10(b) shows the relation between the recirculation regions and the pressure gradients.

In order to investigate the flow features responsible for the high and low surface temperatures that develop on the flat plate in Fig. 5.8, the $575 \times 313 \times 193$ grid is again refined by a factor of 2 in the spanwise direction, producing a $575 \times 313 \times 385$ grid having just under 69.3 million grid points. While the original grid is fine enough to resolve the solution on the dome, surrounding areas on the flat plate are subject to more complex three dimensionally varying flows and require a denser grid in the surface tangent directions. It can be clearly seen in Fig. 5.11 that the region of increased heat flux behind the dome and the long, low heat flux strip are both related to a vortex shed off the dome. The vortex creates the low heat flux strip by lifting the cool gas from the plate surface, decreasing the wall normal temperature gradient. Simultaneously, the vortex forces hot gas from within the boundary layer (Refer to Fig. C.1(b)) to the plate surface, resulting in the high heat flux region aft of the outer side of the dome. A slice of the X-vorticity to the outside of the dome (Fig. 5.12) exposes a counter-rotating vortex pair above the low heat flux strip. As mentioned above, the strong negative vorticity structure is primarily responsible for convecting the hot boundary layer gasses to the plate surface.

A common method for calculating heat transfer is by its relation to the wall shear stress through the Reynolds analogy, which, for compressible flows, takes the form:

$$\frac{C_h}{C_f} = \frac{q_w U_\infty}{2C_p \Delta T \tau_w} = \frac{Pr^{-2/3}}{2} = 0.62,$$

where C_f is the friction coefficient and C_h is the Stanton number. The temperature difference $\Delta T = T_{aw} - T_w$, where the compressible adiabatic wall temperature is given by

$$T_{aw} = T_\infty + r(Pr)\frac{U_\infty^2}{2C_p}, \;\; r(Pr = 0.727) = 0.8519.$$

The Prandtl number for the combustion products of methane and air in the present study is $Pr = 0.727$ in the freestream. The quotient C_h/C_f is calculated from the simulation data to test the validity of the Reynolds analogy over a varying geometry. Fig. 5.13 shows that the Reynolds analogy predictions are low (20% lower than simulation results), but otherwise reasonably estimate the heat flux into the flat plate. However, the analogy breaks down near the compression regions at the front and back of the dome, where it grossly underestimates the heat flux. It is known that in compressible flows with pressure gradients the Reynolds analogy is less useful [11], a fact reflected in Fig. 5.13. Additionally, in flows involving large temperature ranges, this model may be inadequate due to its assumption of a constant Prandtl number. For both the thermally perfect and calorically perfect gas models used in this simulation, the Prandtl number varies significantly over the temperatures present in the flow field (Fig. 5.6(b)). Note that Pr is not constant for the calorically perfect model because of the temperature variation of the methane-air μ and k properties.

5.2.5 Thermal solution

Figs. 5.14(a)-(c) and Figs. 5.15(a)-(c) show the temperature distribution in the thermal domain at three different times during the simulation. It is noted in Section 5.2.3 that the surface temperature at the region aft of the dome is higher than that on the the windward face of the dome where the heat flux is higher. The through-thickness thermal solution reveals that the surface temperature on the flat, ceramic portion of the model is very high in regions, but the temperature quickly decreases with distance into the material. This is very different from the temperature distribution in the aluminum part of the model, where the temperature is lower but nearly constant through the thickness. The reason for this is the large difference in the thermal diffusivities, $\kappa = k/\rho C_p$, of the two materials (aluminum, $\kappa = 6.65 \times 10^{-5}$ m^2/s, Resco RS-17E refractory ceramic, $\kappa = 6.51 \times 10^{-7}$ m^2/s).

5.2.6 Quantitative comparison with experiment

In the experiment, the aluminum dome had 58 thermocouples soldered to its backside. With the time-varying temperature measurements from the thermocouples, the surface heat flux through the aluminum dome was calculated using

$$q = \rho C_p \tau \frac{\Delta T}{\Delta t}. \tag{5.1}$$

The rate, $\Delta T/\Delta t$, was approximated using a central difference over three data points. This value was calculated and reported for only one instant in time, just after the model reached the tunnel centerline. Equation (5.1) is based on several assumptions: (1) the through-thickness temperature is constant, (2) the backside of the dome is perfectly insulated, (3) the specific heat capacity is constant, (4) the heat conduction is 1D, and (5) the thickness of the dome is constant. The temperature contours in Figs. 5.15(a)-(c) and the fact that the backside of the dome is evacuated suggest that the first two assumptions are valid. Assumptions (3) to (5) will be revisited at the end of this section.

In order to compare quantitatively the simulation thermal response predictions with the experimental results, the temperatures over the 5 second run at 13 of the 58 locations are monitored. The temperature and time data at these 13 locations are post-processed using Eq. (5.1) and normalized by the flat plate reference heat flux for run 14 in the report, $q_{ref} = 0.669$ Btu/ft^{2}s (7597 W/m^2). The data are compared at a time shortly after the model insertion, at $t = 0.1$ s, in the simulation. The results of the comparison shown in Fig. 5.16 indicate that the thermally perfect gas model clearly performs better than the calorically perfect model. The more rapidly decreasing heat flux in the calorically perfect case (Figure 5.7) implies that the underpredictions made with the calorically perfect model would worsen over longer time records.

Referring to the thermally perfect model, the simulation and experimental values are within 12% difference at all probes except at 12 and 21, where the heat flux calculated from the temperature probes in the simulation underpredict the heat flux as compared to the experiment. Negative differences of 5% or more are grouped along the periphery of the dome, while positive differences exceeding 5% occur towards the center. This is more easily seen in Fig. 5.18(b). On the edge of the dome, there may be more complicated aspects in the experimental configuration than represented in either Eq. (5.1) or the computer model. Glass and Hunt [1] note that the aluminum dome is secured to the panel with countersunk screws along the perimeter of the dome and there also exists a maximum gap of 0.03 in (0.7 mm) between the dome and flat plate. The fasteners would change both the geometry of the dome (possibly invalidating the constant thickness and 1D heat flux assumptions in Eq. (5.1)) and the local surface topology experienced by the fluid. Also, in the numerical discretization of the thermal domain, the dome/panel interface is modeled to simply be a jump in the material properties. There is no gap or filler material to insulate the dome from the plate. These inconsistencies may contribute to the differences between the numerical and experimental heat flux values near the dome edges.

Glass and Hunt also mention that the assumption made in Eq. (5.1) of constant specific heat capacity may result in $3 - 10\%$ underestimates in the heat flux. They reason that, by normalizing with the flat plate reference heat flux (which also would contain the associated errors), the impact is minimized. The minimization would be least effective in regions of higher heat flux (higher temperatures). This would be one possible reason for the overpredictions made by the simulation toward the center of the dome, where the heat flux is elevated. In a later report [9], Glass and Hunt also state that the uncertainty in the sheet metal dome thickness is approximately 2%. The dome is instrumented with K-type chromel-alumel thermocouples, which can also introduce an uncertainty of $\pm 2.2\%$ [65]. The combined experimental uncertainties in the heat flux measurements are expected thus to be $+4.2\%$ to -14.2%.

The validity of heat flux estimates made with Eq. (5.1) (without the complications of varying material properties and manufacturing defects) is assessed by comparing with the true heat flux calculated at the surface of the dome directly from the fluid solution, $q_n = -k\partial T/\partial n$, where n is the wall normal unit vector. The heat flux values calculated by the two different methods are within 1% of each other, confirming that the assumptions in Eq. (5.1) and the resulting heat flux values are accurate in the numerical model. It should be noted that this is true both for the center and perimeter temperature probes, indicating that the material property jump model of the dome/plate interface does not significantly affect the temperature distribution in the dome, and may not be a contributing factor to the differences seen in Fig. 5.16. In addition, the agreement of Eq. (5.1), which uses data from the thermal solution, with the heat flux calculated directly from the fluid data confirms that the discretization of the thermal domain is sufficient for this problem.

It deserves consideration that thermomechanical deformation of the dome, neglected in the fluid-thermal simulation, may be an additional factor present in the experiment. Such a case would advocate for the need for increased coupling (fluid-thermal-structural) to make reliable predictions in hypersonic environments.

5.2.7 Comparison with a semi-analytical model

A comparison is made between the heat flux from the high-fidelity model with a commonly used semi-analytical model based on third-order piston theory [19] and Eckert's reference enthalpy method [20]. The method, founded on inviscid aerodynamics, is based on the assumption that the freestream Mach number is large and that surface inclination is small enough so that the surface normal velocity component does not exceed the speed of sound. Further, one of the parameters in the Eckert's reference enthalpy method is the distance from the sharp leading edge of a flat plate. As the leading edge of the geometry under consideration is blunt, an effective sharp leading edge is calculated from the streamwise evolution of the boundary layer thickness from the 2D ANSYS Fluent solution using Eq. (5.2), where x_0 is the distance upstream of the blunt leading edge to the effective sharp leading edge and x is the distance from the blunt leading edge to the δ^{99} measurement location,

$$\delta^{99} = \frac{5(x + x_0)}{\sqrt{Re_{x+x0}}}. \tag{5.2}$$

The effective leading edge is found to be 0.15 m forward of the blunt leading edge. Further details on the piston theory/Eckert's reference enthalpy method are given in Appendix B.

A comparison between the heat flux at the surface of the model as predicted by the semi-analytical model and the high-fidelity model shows the similarities and differences between the two approaches (Fig. 5.17). Both methods predict an increased heat flux on the windward face and a decreased heat flux on the leeward face of the dome. However, while qualitative trends in heat loads are similar, a quantitative comparison shows an increased heat load prediction by the simpler approach, with significant features in the heat flux not at all represented.

A comparison of the heat flux over the dome with that measured experimentally by Glass & Hunt (Fig. 5.18) confirms that the semi-analytical model grossly overpredicts the heat flux on the windward side of the dome while underpredicting on the side and back of the dome. The underprediction can be attributed to viscous effects, such as the fact that the boundary layer is thicker on the rear of the dome, making the surface declination of the effective shape less than that of the actual geometry. The high-fidelity model slightly overpredicts at the center of the dome and has both positive and negative differences in isolated locations along the perimeter of the dome. It should be noted that, in Figs. 5.17 and 5.18, the heat flux is calculated directly from the fluid solution, while the values from the experiment were calculated using thermocouples and Eq. (5.1).

5.2.8 Fifty second coupled simulation

As mentioned above, the coupled simulation is continued to a final time of 50 seconds. Glass & Hunt [1] collected 5 seconds of quantitative data during run 14. The modest temperature increase over that time is not sufficient to exhibit the advantages gained by two-way fluid-thermal coupling, as the fluid solution is not altered significantly by the surface temperature increase. However, after 50 seconds, the surface temperature increase is more impressive. As shown in Fig. 5.19(a) and (b), the maximum temperature reaches 465 K and occurs on the windward face of the dome as opposed to the location at 5 seconds on the flat plate where the vortex grazing was seen.

The elevated temperature of the structure affects the flow by decreasing

Table 5.2: Evolution of drag and integrated heat load with time. Drag is calculated assuming both temperature-varying and constant viscosities to demonstrate the effect of boundary layer thickening.

Time s	Drag, $\mu(T)$, N	Drag, $\mu = cst.$, N	Integrated heat load, W
0	14.253	12.632	15341
10	14.122	11.578	14388
30	14.102	11.119	13905
50	14.087	10.821	13556

the density of the gas next to the model, therefore thickening the boundary layer. Fig. 5.20(a) shows the thickening of the boundary layer profile on the windward side of the dome at the symmetry plane as time increases. As a consequence, the effective shape of dome changes, increasing the extent and magnitude of the recirculation region. This is shown in Fig. 5.20(b), where the boundary layer profile shows a taller recirculation region with stronger reversed flow.

The thickening of the boundary layer changes both the velocity and temperature gradients at the surface so that the drag and heat load on the model evolve over time. The sum of the streamwise shear stress and pressure load, integrated over the surface of the model, gives the drag force. As the shear stress is affected by both the velocity gradient and the viscosity, which increases with temperature, the drag is calculated from the same flow field using two different viscosity models to investigate the modification of the flow field by the thermal solution. The baseline drag calculation uses a temperature-dependent viscosity. The drag is again calculated from the same flow field using a constant viscosity model, where the viscosity is held at its freestream value, $\mu = \mu(T_\infty = 237.14 \text{ K})$. The results are shown in Tab. 5.2. The drag is seen to drop with time, but the drop is much smaller in the case of temperature-varying viscosity. The drag reduction with time in the constant viscosity case is due solely to the decreasing velocity gradient, which highlights the affect of the surface temperature on the boundary layer thickness. Also, as expected, the thickening boundary layer and increasing surface temperature cause the integrated heat load to decrease over time. A thermal-only simulation subject to a constant heat load (the initial heat load in the coupled case) yields a maximum surface temperature of 488 K. The temperature distribution on the centerline of the dome is shown in Fig. 5.21 for the two-way coupled and thermal-only simulations. The 23 K difference between the two cases demonstrates the integrated effect of the evolving heat load. The uncoupled peak temperature location also moves upstream relative to the coupled solution.

5.3 Summary of Part I

A high-fidelity coupled fluid-thermal solver was developed for the thermal response prediction of extreme environment structures. For the purpose of solver validation, a hypersonic wind tunnel experiment was studied. The conditions inside the NASA Langley 8-Foot High Temperature Tunnel were reproduced to provide initial and boundary conditions for a coupled simulation. The solution filtering used in the simulation to promote numerical stability was observed to have an effect on the heat load calculation into the solid model. In order to minimize the impact of the filter on the coupled solution, a study was conducted to assess the effects of filtering on heat flux at the boundary of the fluid domain. Following that study, a coupled fluid-thermal simulation of hypersonic flow over a rigid structure was conducted over 5 seconds to compare with experimental data. Comparisons were made between simulations employing both a calorically perfect gas thermal model and a more general thermally perfect model, and the merits of each were discussed. The impact of viscosity on the flow and in particular the surface heat flux resulting from vortical structures in the flow was investigated. The coupled simulation was run until 50 seconds, exceeding the available 5 seconds of experimental data, to evaluate the effect of fluid-thermal coupling on the long-term fluid solution. The results of the simulation were also compared with predictions made using a semi-analytical model to highlight the similarities and differences of the two predictive approaches.

It was found that, if solution filtering is required to ensure numerical stability, the accuracy of the filter at the boundary can significantly affect the heat flux by reducing the temperature gradient in the boundary layer. A comparison between results from our high-fidelity solver and a semi-analytical model based on inviscid aerodynamics and a flat plate boundary layer assumption revealed that while qualitative trends of the heat loads were identified, a quantitative comparison shows a substantial overprediction by the simpler approach, with significant features in the heat flux not at all represented. In particular, a region of substantial heating due to vortex shedding, a viscous effect, was completely neglected. Our simulations showed that the Reynolds analogy, a ‘first-cut’ method for determining heat flux from surface shear stress, provides a fair estimate in hypersonic flows over a flat plate, but the method failed in the presence of pressure gradients. Thermal solution temperatures were found to be a function of heat load, geometry, and material properties. Our high-fidelity, coupled approach incorporated these aspects and produced solutions which were not obvious and may not be predicted by lower-order methods. It was also found that, in flows where there exist even isolated regions of extreme temperatures, the calorically perfect assumption may not be justified, requiring the use of a thermally perfect (or more general) gas model. While changes in the fluid solution were not significant for the 5 second simulations, high temperatures that resulted from long periods of time in hypersonic flow had a noticeable effect on the flow solution in the coupled problem. This led to decreased drag and heat loads on the structure. The coupled solver predictions, using the thermally perfect gas model, were found to be within the experimental uncertainty for points on the dome interior, except for points near the dome periphery where details of the dome geometry were insufficiently described to be captured numerically.

Figures for Chapter 5

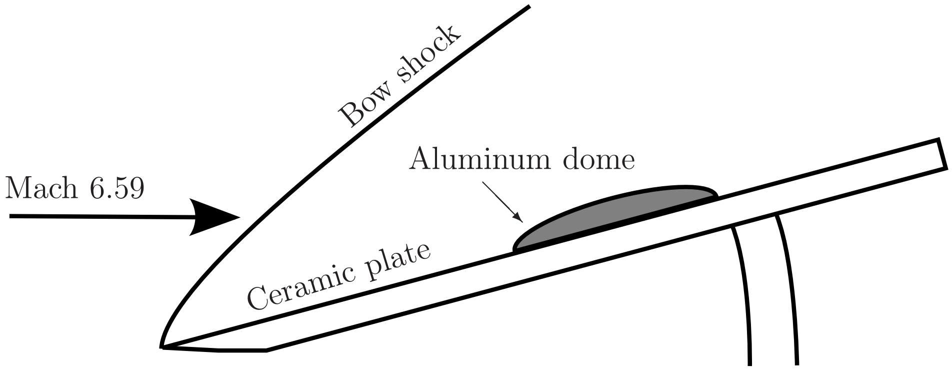

Figure 5.1: Schematic of the ceramic plate and aluminum dome inserted into the Mach 6.59 freestream.

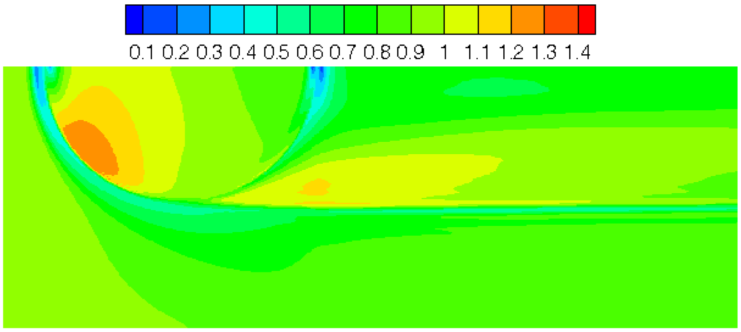

Figure 5.2: y^+ values of the first wall normal grid point at $t = 0$ s.

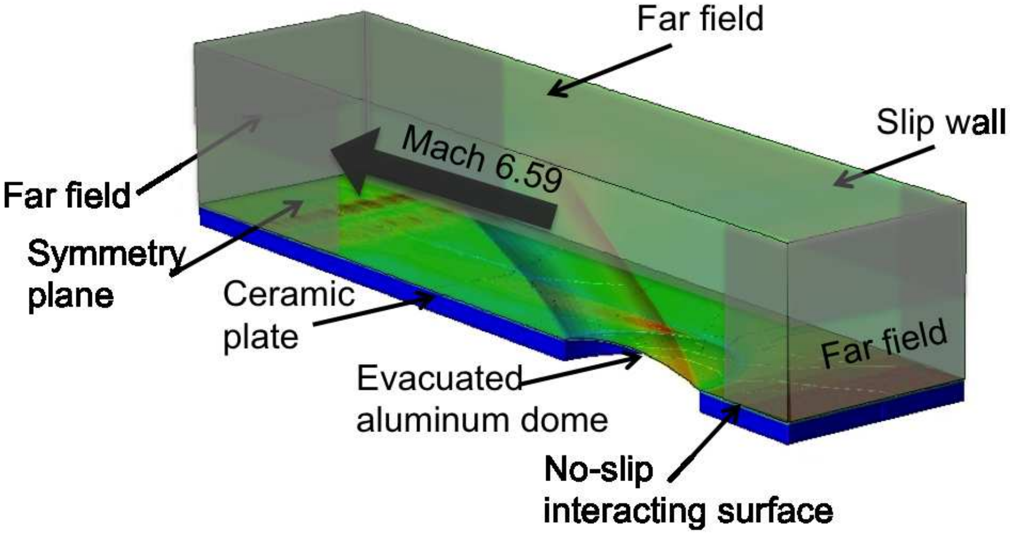

Figure 5.3: Orientation and boundary conditions of the fluid and thermal domains. The sides and back of the thermal domain are adiabatic. An example solution is displayed with temperature contours in the thermal domain and pressure contours in the fluid domain. Shaded regions represent the presence of sponges.

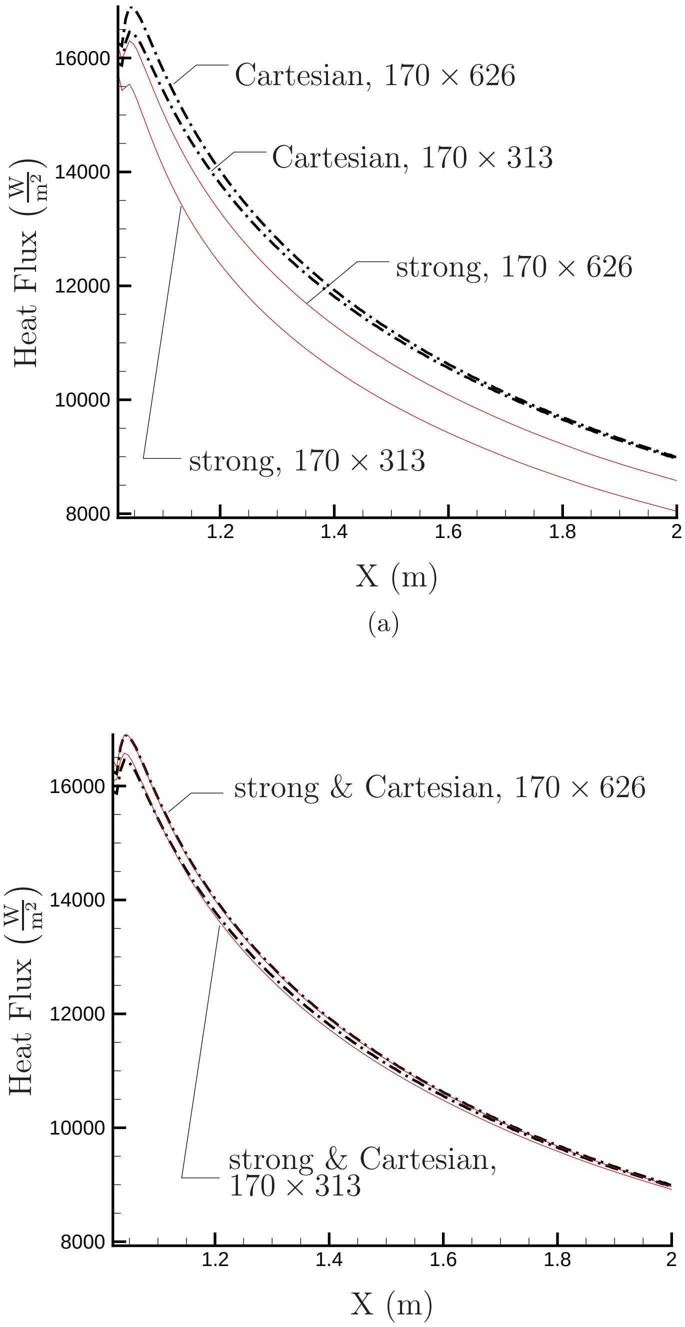

Figure 5.4: Effect of spatial filter boundary schemes on convergence of surface heat flux along the plate. (a) Centered filter, (b) boundary filter. The dashed line corresponds to the unfiltered Cartesian form of the viscous terms while the solid line corresponds to the filtered strong form of the viscous terms.

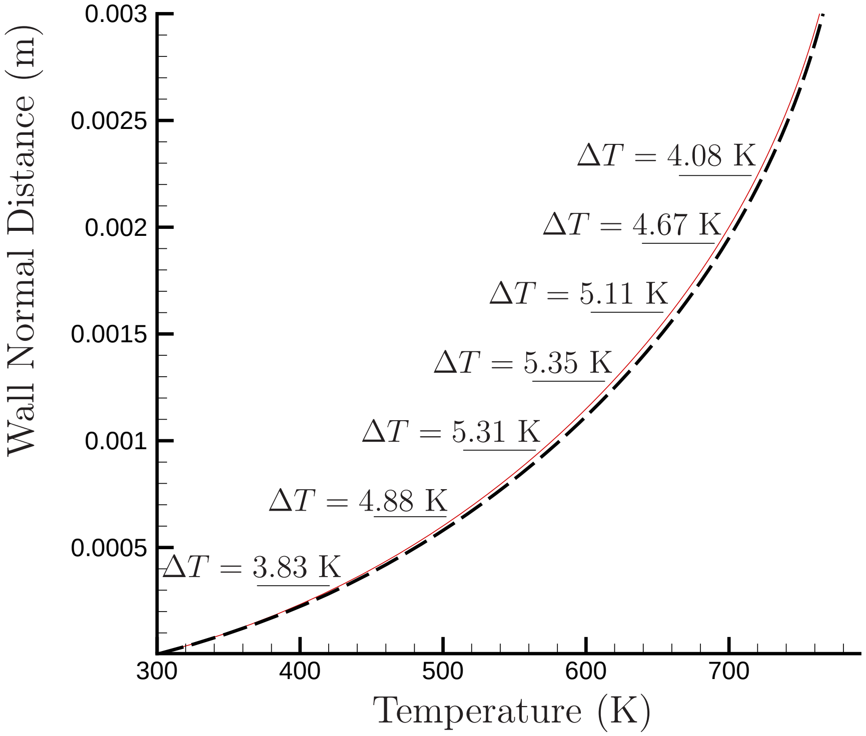

Figure 5.5: Temperature profiles in the boundary layer at $X = 1.58$ m computed using the strong form of the viscous terms with the centered filter (solid line) and the boundary filter (dashed line) on the finer grid (170×626). Temperature differences at several wall normal locations are noted for clarity.

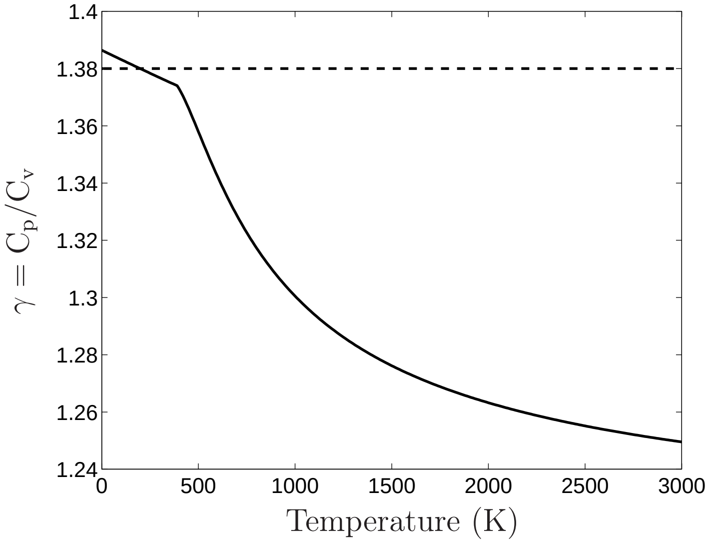

(a)

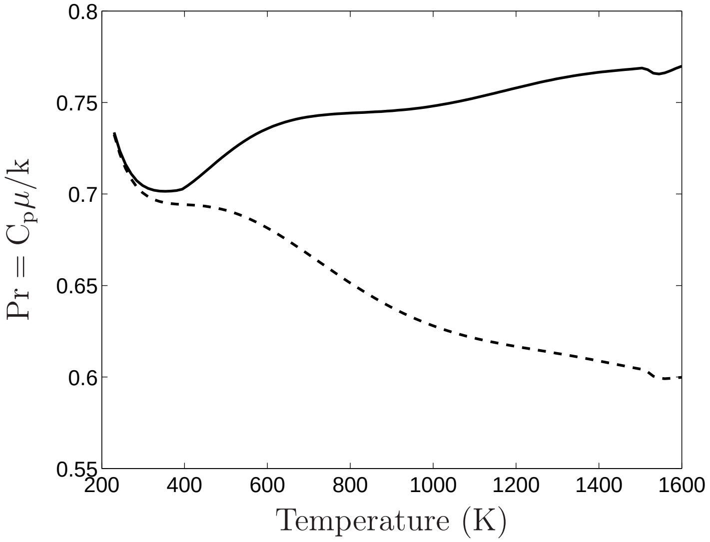

(b)

Figure 5.6: Variation in (a) ratio of specific heats and (b) Prandtl number with temperature. Calorically perfect (dashed line), thermally perfect (solid line).

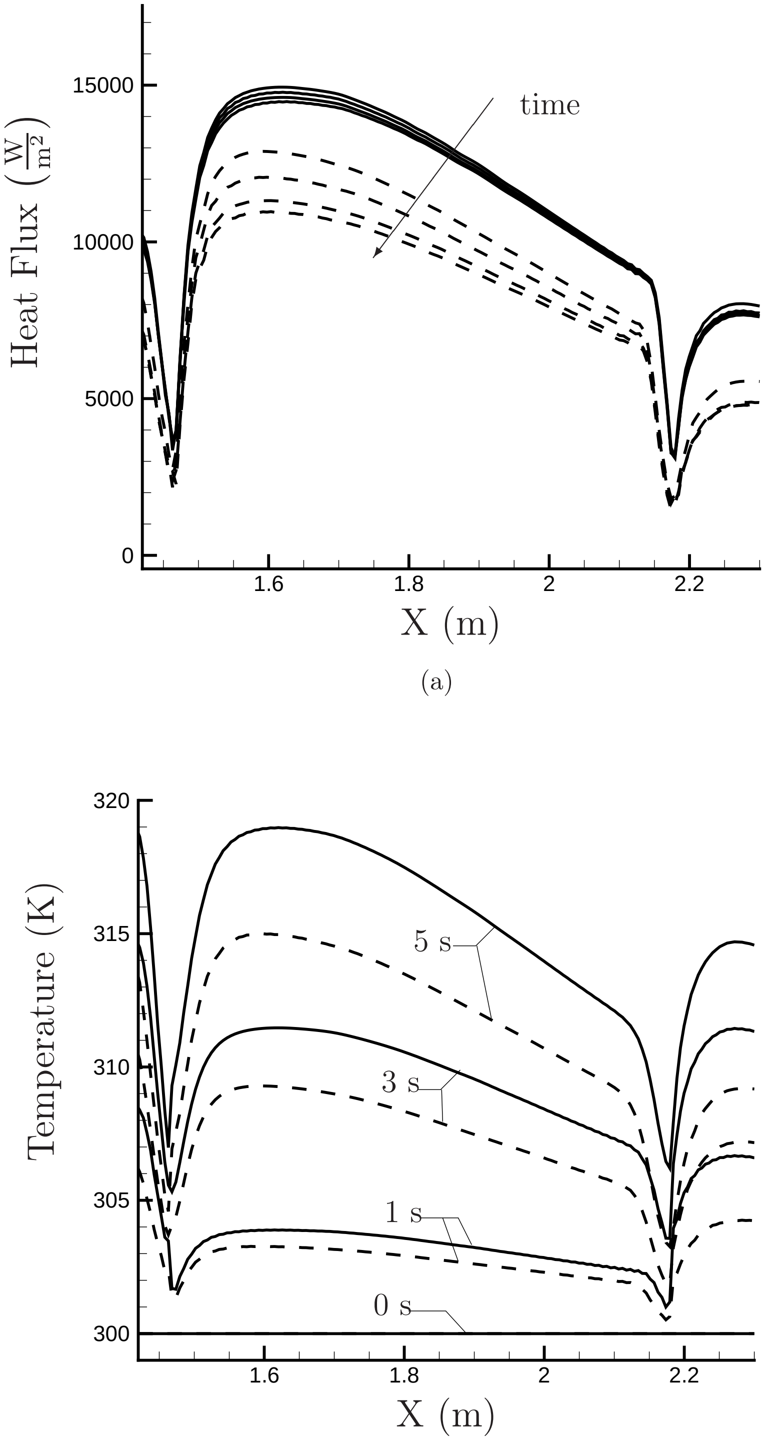

(a)

(b)

Figure 5.7: (a) Heat flux and (b) temperature profiles at the symmetry line for the calorically and thermally perfect gas models at $t = 0$ s, $t = 1$ s, $t = 3$ s, and $t = 5$ s. Calorically perfect (dashed line), thermally perfect (solid line).

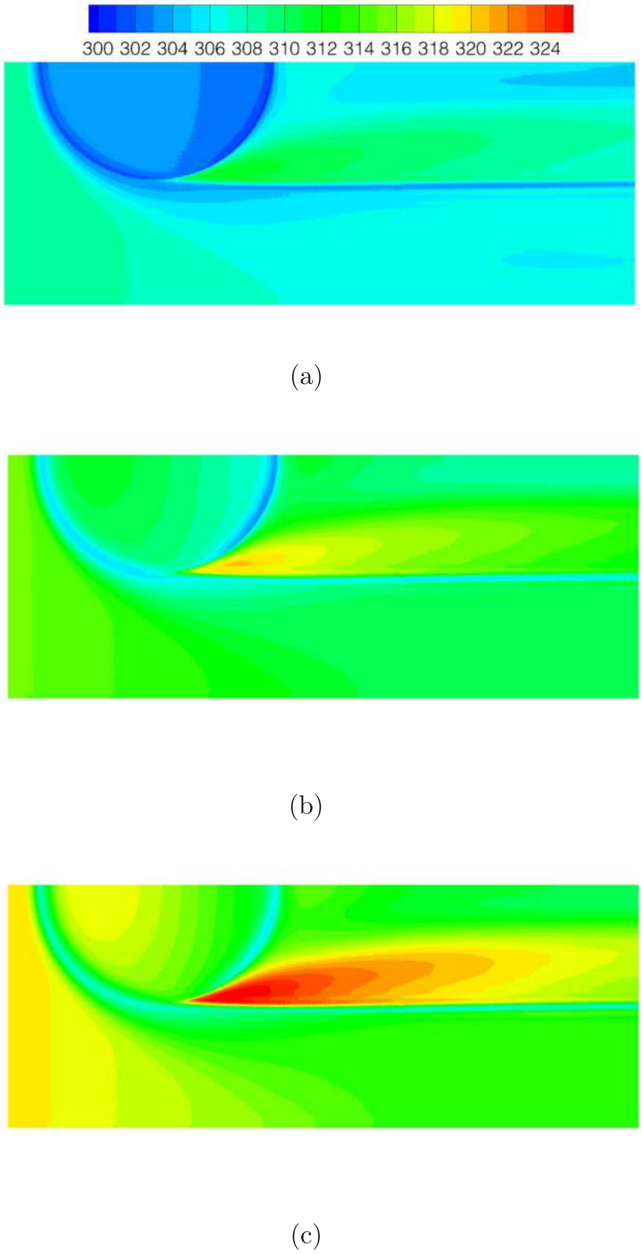

Figure 5.8: Surface temperature (K) at (a) $t = 1$ s, (b) $t = 3$ s, and (c) $t = 5$ s.

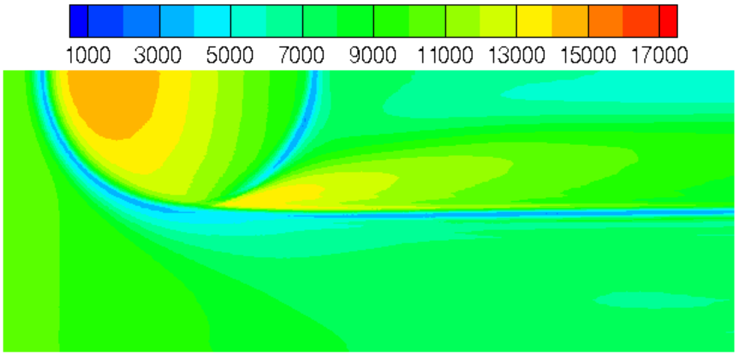

Figure 5.9: Surface heat flux W/m^2 at $t = 1$ s.

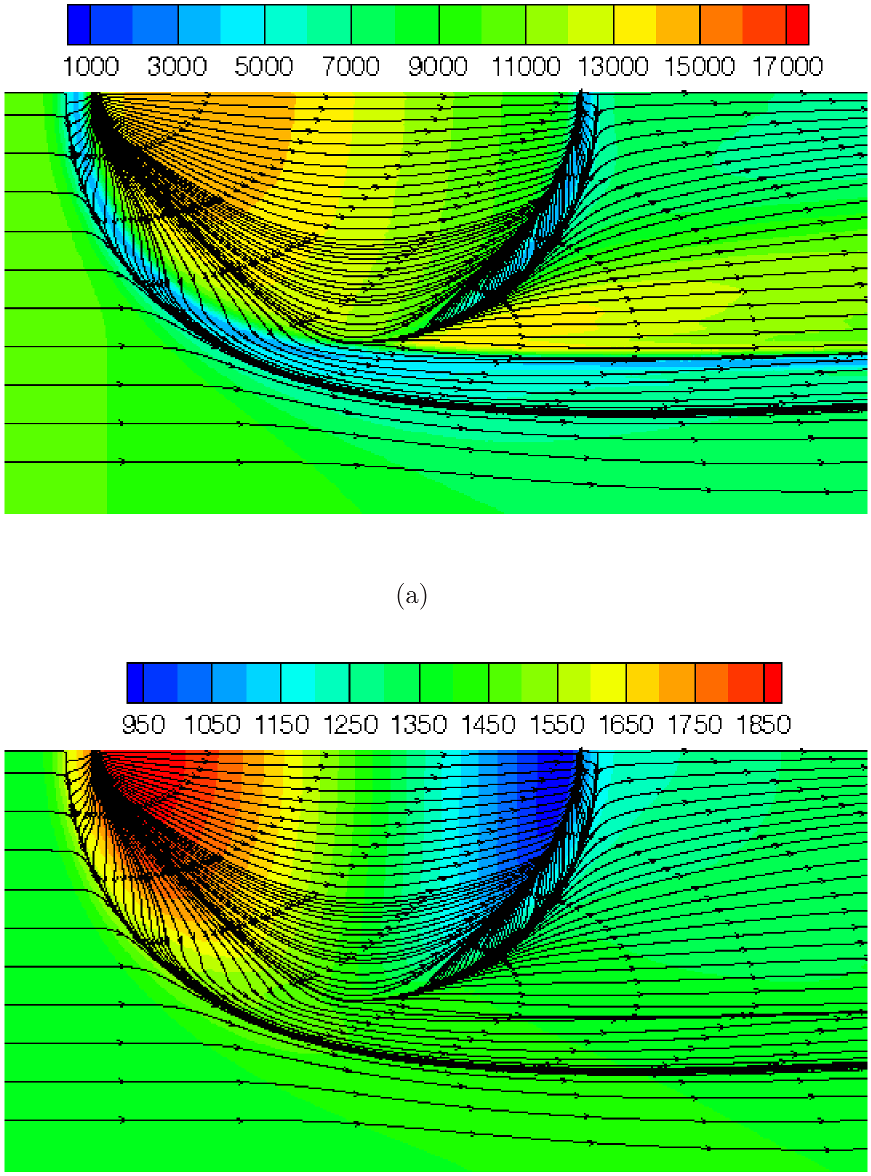

(a)

(b)

Figure 5.10: Shear stress vectors with (a) heat flux (W/m^2) and (b) pressure contours (Pa).

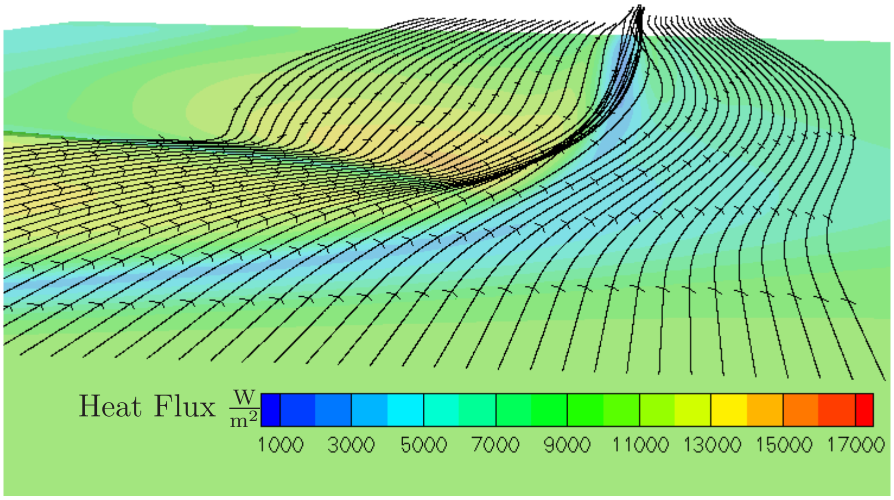

Figure 5.11: Streamlines illustrating a vortex shed off the right side of the dome. Heat flux contours are shown on the thermal domain surface.

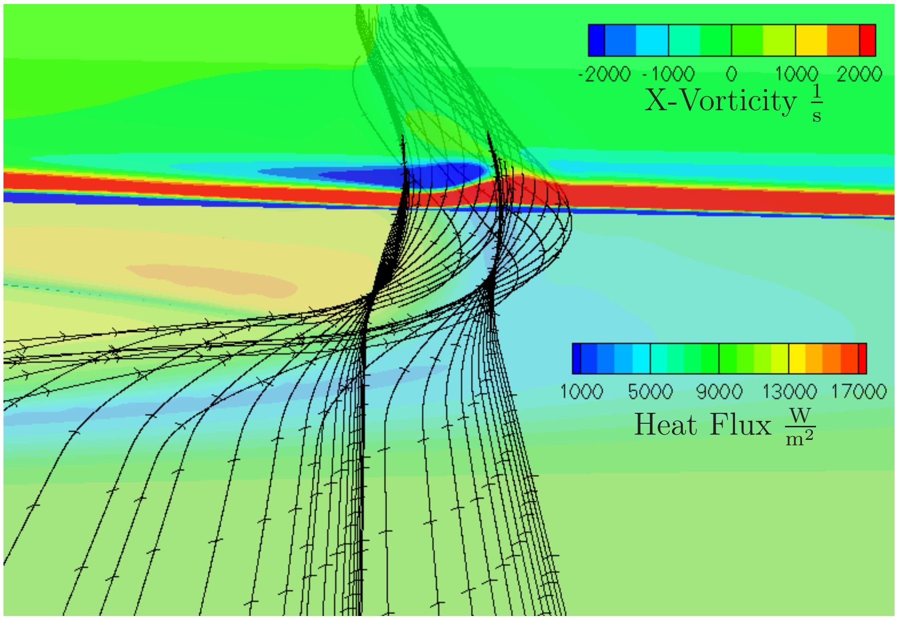

Figure 5.12: Counter-rotating vortex pair grazing the plate on the outside of the dome. Heat flux contours are plotted on the surface. The legend corresponds to the vorticity contours displayed on the vertical slice.

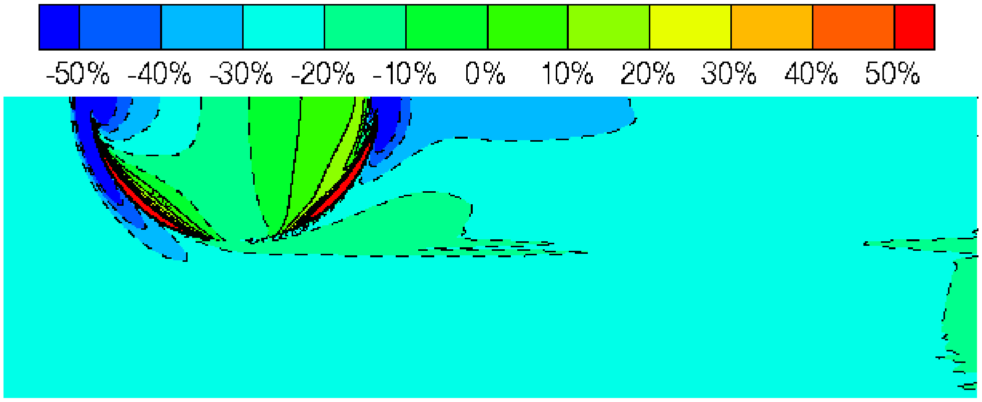

Figure 5.13: Percent difference between value predicted by Reynolds Analogy (0.62) and C_h/C_f calculated over the interacting surface at $t = 0$ s. % Diff. $= \frac{0.62 - C_h/C_f}{C_h/C_f} \times 100\%$

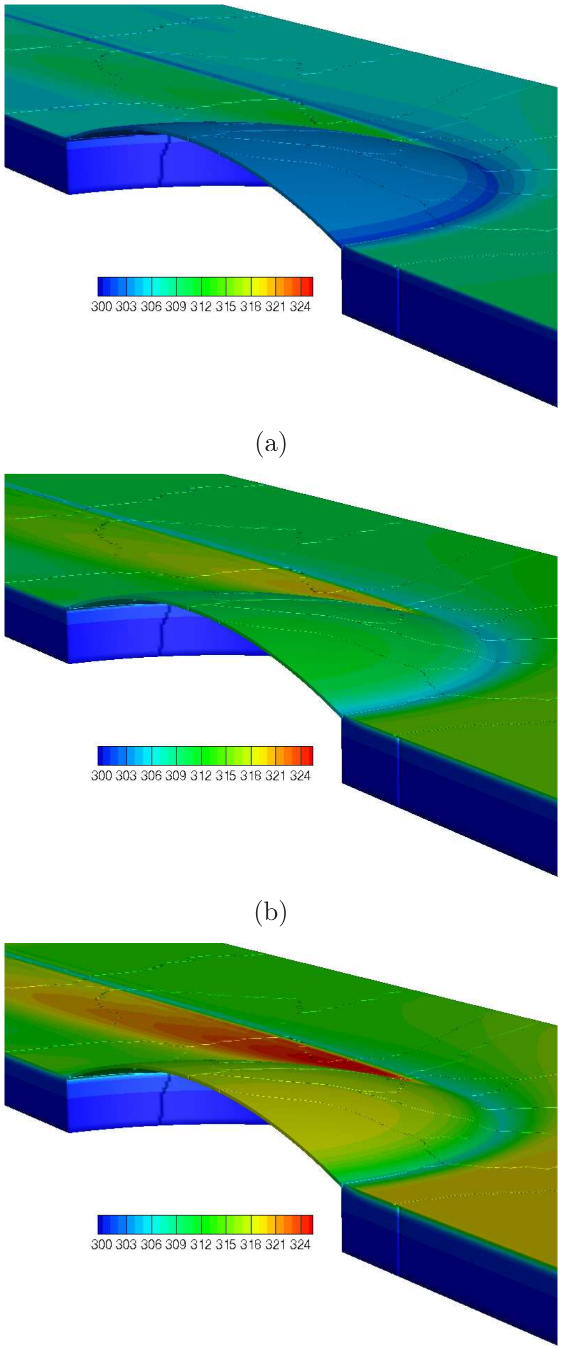

(a)

(b)

(c)

Figure 5.14: Evolution of thermal solution on the windward side of the evacuated aluminum dome at (a) $t = 1$ s, (b) $t = 3$ s, and (c) $t = 5$ s. Temperature contour units are in K. The geometry is scaled by 200% in the vertical direction for clarity. Creases in the images correspond to processor boundaries.

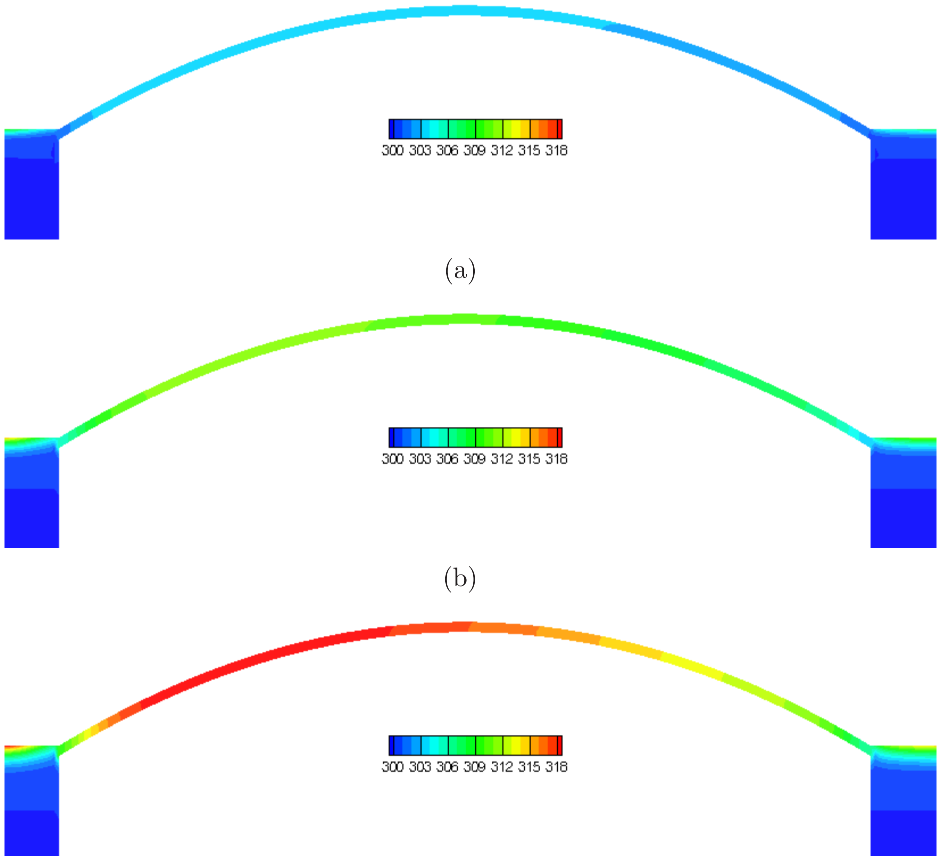

(a)

(b)

(c)

Figure 5.15: Evolution of through-thickness dome temperature (K) at the symmetry plane at (a) $t = 1$ s, (b) $t = 3$ s, and (c) $t = 5$ s. The flow is from left to right.

Thermocouple Number	% Diff. Thermally Perfect	% Diff. Calorically Perfect
2	-7.19 %	-20.29 %
3	-0.91 %	-15.65 %
4	+7.47 %	-9.53 %
7	+11.86 %	-8.11 %
10	+11.01 %	-7.52 %
12	-19.40 %	-31.01 %
19	-1.74 %	-18.62 %
21	-18.96 %	-31.97 %
28	+2.33 %	-16.09 %
30	-5.29 %	-23.04 %
37	+1.26 %	-17.55 %
39	+1.54 %	-18.06 %
41	+4.51 %	-15.10 %

(a)

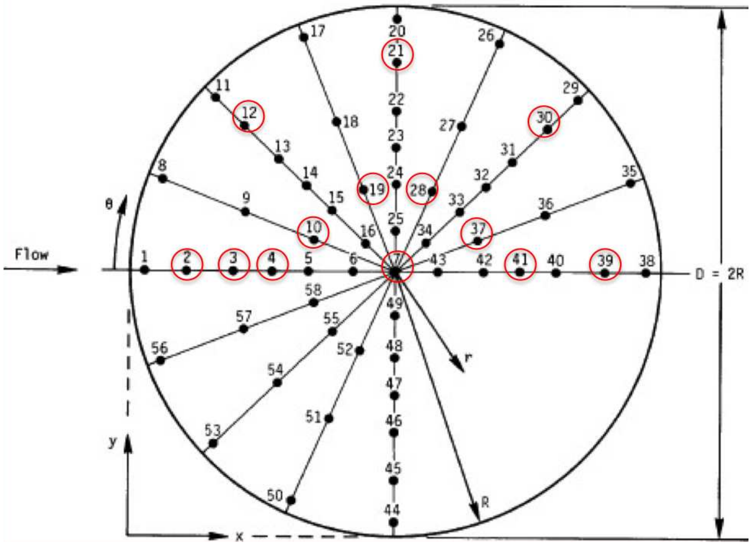

(b)

Figure 5.16: (a) Comparison between experimental and numerical values for heat flux at the thirteen thermocouple locations denoted by circles in (b). % Diff. $= \frac{q_{sim.} - q_{exp.}}{q_{exp.}} \times 100\%$.

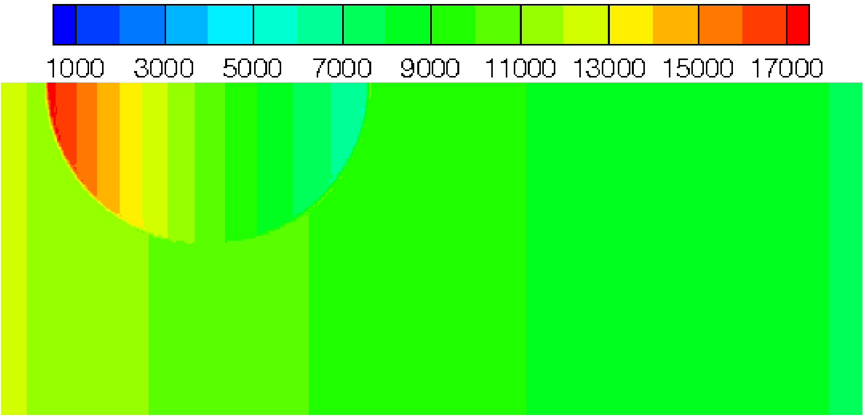

(a)

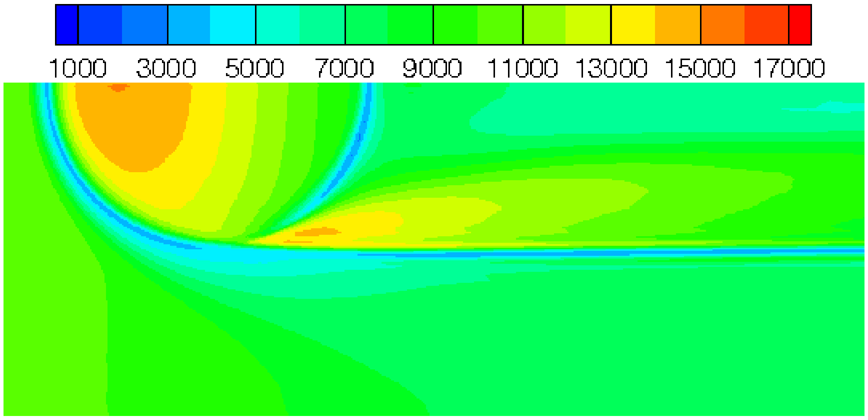

(b)

Figure 5.17: Comparison between heat flux (W/m^2) calculated with (a) piston theory/Eckert's reference enthalpy and (b) the high-fidelity model at $t = 0$ s.

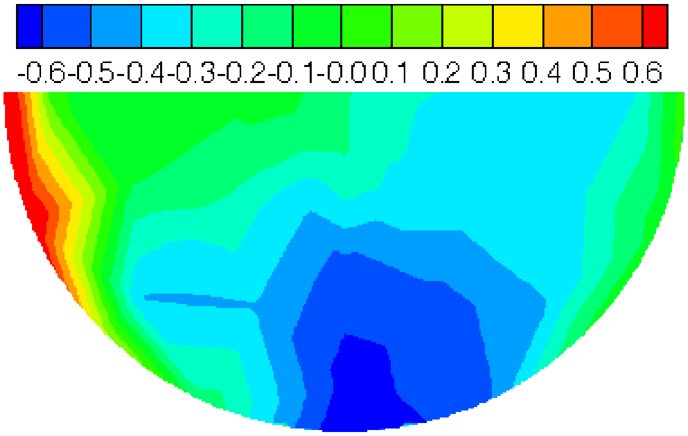

(a)

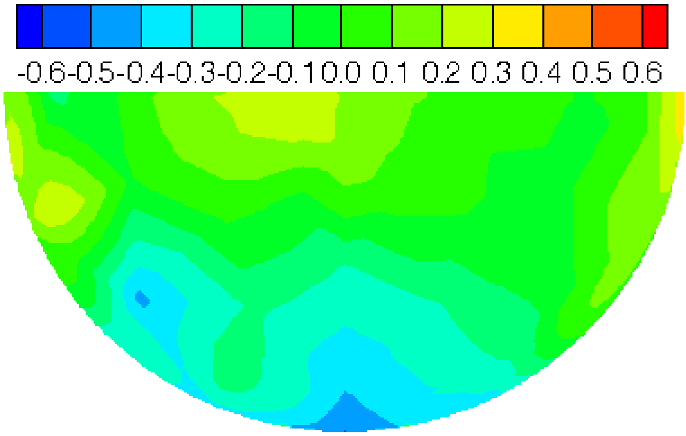

(b)

Figure 5.18: Comparison between heat flux calculated with (a) piston theory/Eckert's reference enthalpy and (b) the high-fidelity model ($t = 0$ s). The contours indicate the difference between the numerical and experimental heat fluxes normalized by the flat plate reference heat flux, $(q_{num.} - q_{exp})/q_{ref}$.

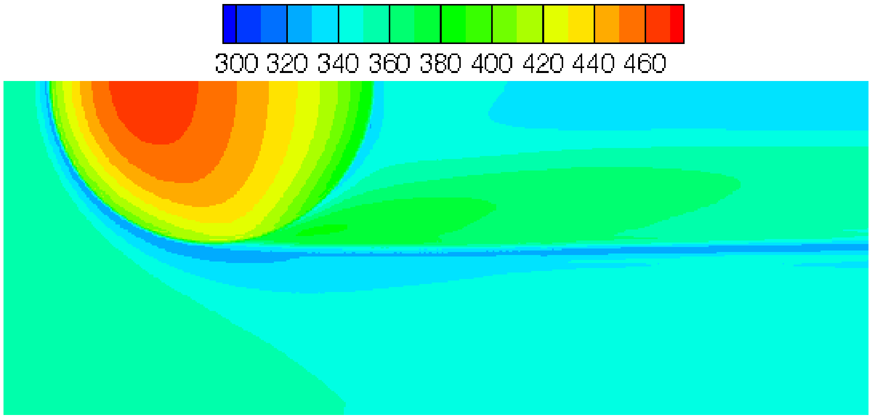

(a)

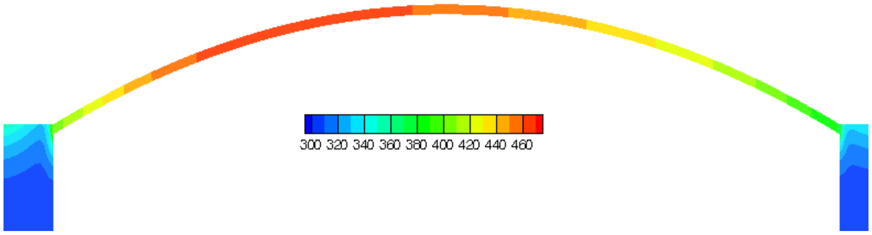

(b)

Figure 5.19: (a) Surface temperature and (b) through-thickness dome temperature at the symmetry plane at $t = 50$ s. Units are in K.

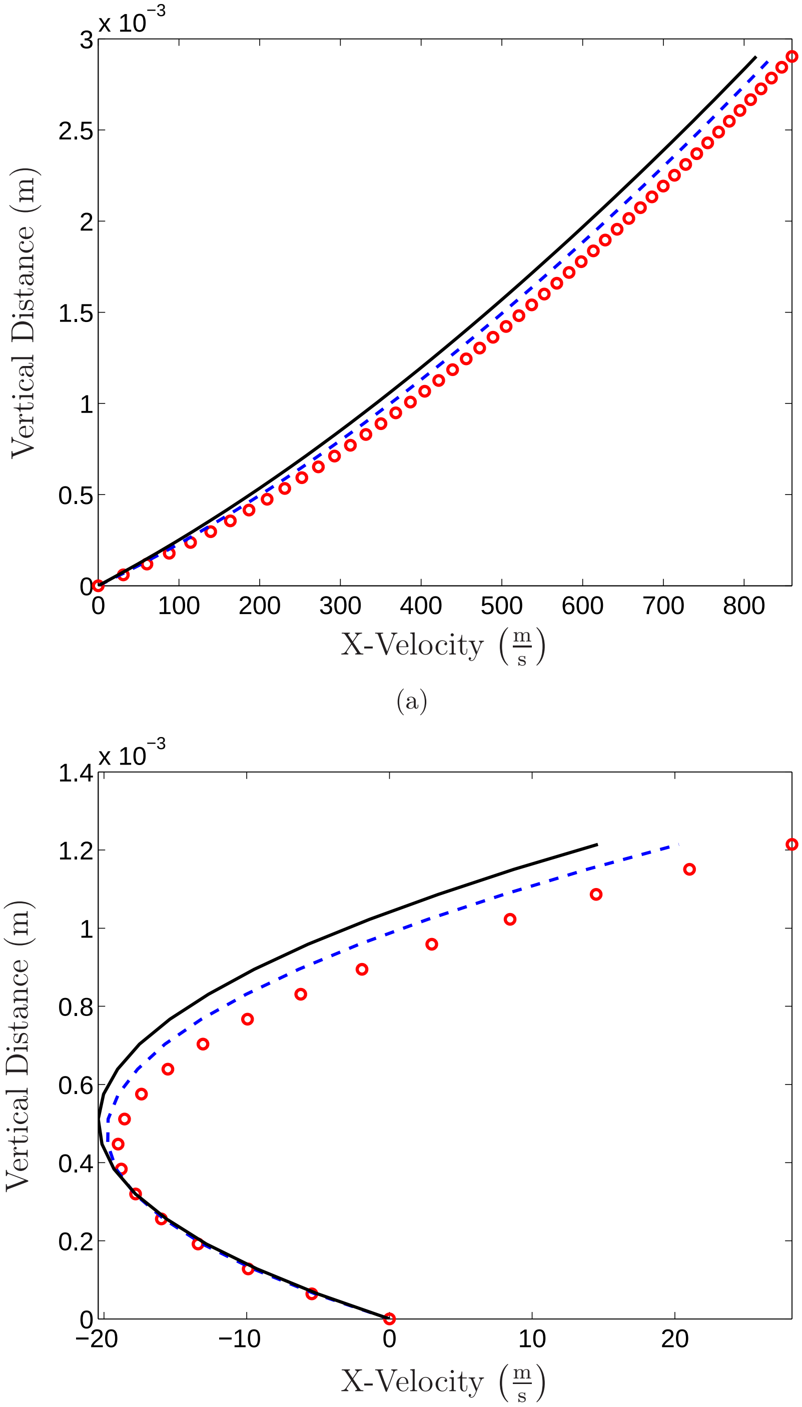

(a)

(b)

Figure 5.20: Boundary layer profile (a) on the windward face of the dome and (b) at the dome leading edge at 10 s (circles), 30 s (dashed line), and 50 s (solid line). The boundary layer thickens and the recirculation region becomes stronger with the increase in surface temperature

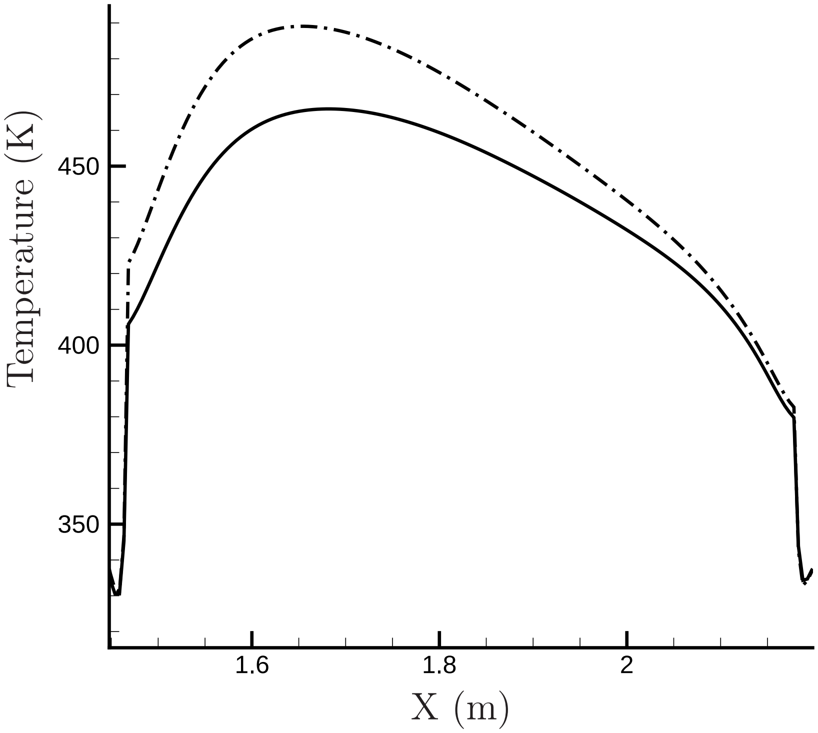

Figure 5.21: Temperature along the centerline of the dome in the two-way coupled (solid) and thermal-only (dashed) simulations. The thermal-only solution predicts the peak temperature to be 23 K higher than the coupled solution.

Part II

Direct Numerical Simulation of Fluid-Structural Interaction of Mach 2.25 Turbulent Boundary Layer Over a Compliant Panel

Chapter 6

Part II Literature Review

We now consider an aeroelastic problem where a compressible turbulent boundary layer (TBL) interacts with NASP-like flexible steel panel to determine the implications of fluid-structural interaction in high speed flows.

A variety of studies involving fluid-structure interaction have been conducted using analytical, numerical, and experimental approaches. Early analytical work on fluid-structural coupling was motivated by noise prediction, coincident with the advent of the jet engine and its impact on air vehicles half way through the 1900's. In 1956, Corcos & Liepmann [66] developed an analytical model based on Lord Rayleigh's theory of sound to study the noise transmission into a fuselage due to a prescribed forcing function representing a boundary layer with turbulence that was random in both space and time. In 1964, Ffowcs Williams [67] studied the effect of turbulence-induced surface deformation on sound radiation from a turbulent boundary layer based on Lighthill's approach. He assumed that surface deformations were sufficiently small to replace the compliant surface by a rigid surface with velocity and stresses equal to those of the moving surface. More recently, Wu & Maestrello [68] extended previous ideas by accounting for structural non-linearities due to stretching and in-plane stress while studying a prescribed turbulent loading on a plate using a forcing function. In their 1993 work [68], they found that acoustic damping of the plate increased linearly with Mach number, while the stiffness increased quadratically, a fact that could lead to instability. When the structural response becomes unstable, the condition referred to as panel flutter results, involving large amplitude, high frequency oscillations of the panel. The fatigue risk associated with this condition can have disastrous results. Furthermore, the interest in high-speed, lightweight vehicles that feature thin body panels subject to high dynamic pressures, conditions promoting panel flutter, make it necessary that flutter be well understood. Flutter analysis has been grouped by Dowel [69] and Cheng & Mei

Table 6.1: Panel flutter analysis categories [2].

Type	Structural theory	Aerodynamic theory	Mach number range	Approach
1	Linear	Linear piston	$\sqrt{2} < M_\infty < 5$	Semi-analytical
2	Linear	Linearized potential flow	$1 < M_\infty < 5$	
3	Non-linear	Linear piston	$\sqrt{2} < M_\infty < 5$	
4	Non-linear	Linearized potential flow	$1 < M_\infty < 5$	
5	Non-linear	Non-linear piston	$M_\infty > 5$	
6	Non-linear	Euler or Navier-Stokes	Transonic, supersonic, or hypersonic	Computational

[2] into five analytical and one computational categories, given in Tab. 6.1, based on the associated requirement of linear and non-linear structural and aerodynamic theories dependent on Mach number range. Early studies focussed on the flutter of simple geometries due to first-order aerodynamic loading models. Degundgji [70] studied the flutter boundaries of rectangular plates by varying aspect ratio, in-plane loads, and the presence of an elastic foundation, and found that the effects of aerodynamic and structural damping were important. Further studies have been extended to more complicated geometries and loading scenarios. Dowell [71] studied the flutter characteristics of curved plates and found that streamwise curvature has a significant effect on the flutter boundary and amplitude. Houbolt [72] took a modal approach to the study of buckling and panel flutter in the presence of a uniform temperature distribution. Hopkins & Dowel [73] used the Rayleigh-Ritz assumed-mode method to study square panels under various temperature differentials, which proved to have a significant influence on the solution. The impact of coupling between aerodynamic heating and structural deformation was extensively studied by Culler in his Ph.D. thesis [74]. He found that the effect of aerodynamic heating can significantly lower the flutter boundary by introducing thermal stresses and material degradation. A review of the above studies shows a trend in the high-speed regime in which increments in modeling fidelity are accompanied by significant changes in predictions, indicating that higher fidelity models are needed to fully understand the environment. While much is learned from analytical approaches such as those

used in the above studies, they are often limited to simplified scenarios involving non-complex geometries and problem specific assumptions.

Historically, experimental approaches to the study panel flutter used wind tunnels with the objective of determining the flutter boundary as a function of dynamic pressure. Typically, a panel is inserted into the flow field at some specified Mach number, stagnation pressure, and temperature. The flutter boundary is sought by increasing the dynamic pressure while holding the Mach number and temperature fixed. Prior to the flutter boundary, random, small amplitude oscillations are observed due to pressure fluctuations present in the TBL. The flutter boundary is marked by the dynamic pressure at which the oscillations become nearly sinusoidal with large amplitudes comparable to the plate thickness [69]. Early studies have been concerned with identification of flutter boundaries. As pointed out in Chapter 1, fluid-structure coupling is expected in future high-speed vehicles, and an understanding of the dynamics of panel motion is necessary. Mei et al. [75] note that "experimental investigations on post or non-linear flutter behavior of panels have been essentially non-existent," citing only one case where Kappus et al. [76] studied panel response far past the flutter boundary. As measurement techniques have advanced, detailed results regarding the panel and fluid dynamics have been sought. Laser vibrometry and accelerometers have been used to gather single point dynamic information about the panel. Recently, full-field digital image correlation have gained interest. From digital image correlation measurements of panel deflections, detailed information about panel strains and stresses can be inferred, but have been restricted in resolution or time record by technological limitations. Recently, at the Air Force Research Laboratory, flexible panels have been inserted in the RC-19 supersonic wind tunnel for aeroelastic testing [77]. Innovative analysis techniques developed by Beberniss et al. [78, 79], are being used to study the response of compliant panels under scramjet inlet loading conditions, for example, using high speed digital image correlation and high speed pressure sensitive paint. Initial results indicate the usefulness of the newly developed techniques and encourage their application to future high-speed fluid-structural interaction experiments.

The computational category in Tab. 6.1 was added by Cheng & Mei [2] in 2004 to account for flow regimes which cannot be modeled by approximate theories, and require the use of Euler or Navier-Stokes solutions. Numerical approaches to fluid-structure interaction overcome some of the limitations that plague analytical and experimental approaches. They are not hampered by the assumptions that are present in analytical formulations and are able to provide detailed information that is unobtainable by current measurement techniques in experiments. However, as the complexity of the problem increases, so do the computational costs. Visbal and Gordinier numerically simulated two-way coupled fluid-structure interaction problems using a high-order Navier-Stokes solver coupled with a non-linear von Karman plate. A 3D simulation [80] of laminar and turbulent boundary layers over a finite plate in both subsonic and supersonic flows showed strong coupling in both flow regimes, in which panel flutter and vortical structures in the unforced boundary layer could be correlated. Later, in a 2D study [81] of a similar configuration, they noted that, due to the coupling, panel flutter was achieved under the boundary layer without any external perturbation and that the boundary layer was left in a transitional state after the interaction. Both studies showed the significant effect of two-way coupling on the fluid solution. The appearance of shock waves is common in high-speed flows, and, in a recent paper, Visbal [82] has studied the 2D interaction of a impinging shock on a flexible panel under an inviscid flow. The presence of the shock lowered the dynamic pressure at the flutter boundary, and the panel motion produced complicated the flow field by modifying the reflected shock and creating additional compression/expansion wave systems at the trailing edge of the panel. The presence of a TBL using a large eddy simulation (LES) approach has been considered by Schäfer et al. [83] in their investigation of a turbulent flow over a thin panel, though they were interested in the acoustics resulting from fluid-structure interaction in low-speed flows. They also conducted accompanying experiments to compare with their simulation results. They found good agreement between numerical and experimental measurements, at least qualitatively.

The above studies indicate the need for accurate information regarding structural response in high-speed flows. Analysis approaches must consider fluid-structural coupling, and increases in model fidelity are often accompanied by new insights into the operating conditions and loading scenarios in the high-speed regime. Results of the highest fidelity are obtainable through experiments, and advances in measurement techniques are allowing more detailed information to been extracted. Numerical approaches have the advantage that they are not constrained by the limitations of available measurement techniques and solution data is easily accessible. Many numerical approaches rely on simplifying assumptions used, for example, in turbulence models and plate theories to reduce the computational cost of simulations. The work in this part presents a study of the interaction between a supersonic TBL and a compliant panel in which no turbulence model or simplifications regarding the structure are made. The approach extends the current state-of-the-art to allow for a detailed investigation of the coupling between a flexible structure and a high-speed TBL. In Chapter 7, the solver is presented, including a detailed formulation of the non-linear thermomechanical solver developed for this work. Chapter 8 introduces the details of the problem to be examined. Chapter 9 discusses in detail the generation, verification, and analysis of a temporal compressible TBL. Part II concludes with Chapter 10 presenting the simulations, results, and analysis of the aeroelastic problem.

Chapter 7

Aeroelastic Numerical Approach

7.1 Fluid domain

The solution in the fluid domain is achieved using the same code described in Chapter 3. Differences between the work in Part II and that presented in Part I are that this problem involves grid deformation and high-accuracy temporal integration. Grid deformation is accomplished using a simple transfinite interpolation scheme, which preserves the arclength-normalized coordinate of each point along its associated grid lines. Details about transfinite interpolation can be found in [84]. An example grid deformation is shown in Fig. 7.1.

Temporal integration in the fluid domain is accomplished using a four-stage Runge-Kutta scheme. While the scheme can achieve $\mathcal{O}(\Delta t^4)$ accuracy with variable time steps (governed by, say, a fixed CFL number), the time step is held constant to accommodate the constant time step requirements of the structural and thermal temporal integration schemes.

The implicit filter described by Eq. (3.6) is again used in Part II of this thesis. However, the filter strength parameter is set to $\alpha_f = 0.490$. The transfer function for the 10^{th}-order filter using this value of α_f is shown in Fig. 7.2, and the cutoff wavenumber associated with 0.490 is 0.90π.

7.2 Solid domain

For the aeroelastic work presented in this thesis, a non-linear thermomechanical finite-element solver was developed. Although the work presented in this thesis utilizes only the structural capabilities of the thermomechanical solver, the thermomechanical formulation is presented below for completeness. Coupling between the thermal and structural solutions is achieved through a multiplicative decomposition of the deformation gradient (Fig. 7.3). As will be shown, this allows the use of a standard constitutive model for computation of the stress field.

7.2.1 Multiplicative decomposition

Consider a deformable body under thermal and mechanical loads. Initially the body is in the reference configuration, B_0, and all points on the body are described by $\boldsymbol{X}$. At some time, t, the body's motion can be described by a transformation, $\boldsymbol{\phi}(\boldsymbol{X}, t)$, such that the position of every particle in the current configuration, B, can be written $\boldsymbol{x} = \boldsymbol{\phi} = \boldsymbol{X} + \boldsymbol{u}$, where $\boldsymbol{u}(\boldsymbol{x}, t)$ is the displacement. The deformation gradient is defined as $\boldsymbol{F}(\boldsymbol{X}, t) = \nabla_{\boldsymbol{X}} \boldsymbol{\phi}(\boldsymbol{X}, t) = \partial \boldsymbol{x} / \partial \boldsymbol{X}$, and the right Cauchy-Green tensor is $\boldsymbol{C} = \boldsymbol{F}^T \boldsymbol{F}$. The Jacobian, $J = \det(\boldsymbol{F})$, represents the volume change between the reference and current configurations. For the thermomechanical formulation adapted in this study, the deformation gradient $\boldsymbol{F}$ is multiplicatively decomposed into a stress-free component, ${}^{\theta}\boldsymbol{F}$, where all deformations are due to thermal expansion/contraction, and an isothermal component, ${}^{e}\boldsymbol{F}$, where deformations produced by the stresses in the elastic body:

$$\boldsymbol{F} = {}^{\theta}\boldsymbol{F}^{e}\boldsymbol{F}. \tag{7.1}$$

Partitioning of the problem in this way is referred to as the isothermal split [85]. Each component of the deformation gradient has an associated Jacobian, ${}^{\theta}J = \det({}^{\theta}\boldsymbol{F})$ and ${}^{e}J = \det({}^{e}\boldsymbol{F})$, which represent the volume changes due to thermal effects and stresses, respectively. It is assumed that the solid is thermally isotropic such that

$${}^{\theta}\boldsymbol{F} = \beta(\Theta)\boldsymbol{I}, \tag{7.2}$$

where $\boldsymbol{I}$ is the identity tensor and $\beta(\Theta)$ is the stretch ratio in any direction due to thermal expansion/contraction.

7.2.2 Isothermal stage

Conservation of linear momentum gives the strong form in the current configuration, B, as

$$\nabla \cdot \boldsymbol{\sigma} + \rho \boldsymbol{b} = \rho \ddot{\boldsymbol{u}}, \tag{7.3}$$

where $\boldsymbol{\sigma}$ is the Cauchy stress tensor, $\boldsymbol{b}$ is a field of body forces, ρ is the density, $\ddot{\boldsymbol{u}} = \partial^2\boldsymbol{u}/\partial t^2$ is the acceleration, and ∇ is the gradient in the current configuration. The corresponding form of the principal of virtual work is

$$\delta W = \int_B (\nabla \cdot \boldsymbol{\sigma}) \cdot \boldsymbol{\delta u}\; dv + \int_B \rho \boldsymbol{b} \cdot \boldsymbol{\delta u}\; dv - \int_B \rho \ddot{\boldsymbol{u}} \cdot \boldsymbol{\delta u}\; dv = \boldsymbol{0}, \tag{7.4}$$

where $\boldsymbol{\delta u}$ denotes the virtual displacement. Rearrangement and application of the divergence theorem $\int_v \nabla \cdot (\cdot) dv = \int_{\partial v} (\cdot) \cdot \hat{\boldsymbol{n}}\; da$ yields the alternative form:

$$\delta W = \int_B \boldsymbol{\sigma} : \nabla \boldsymbol{\delta u}\; dv + \int_B \rho \ddot{\boldsymbol{u}} \cdot \boldsymbol{\delta u}\; dv - \int_{\partial B_{\boldsymbol{t}}} \boldsymbol{t} \cdot \boldsymbol{\delta u}\; da - \int_B \rho \boldsymbol{b} \cdot \boldsymbol{\delta u}\; dv = \boldsymbol{0}, \tag{7.5}$$

where $\boldsymbol{t} = \boldsymbol{\sigma} \cdot \hat{\boldsymbol{n}}$ denotes the traction vector applied along the portion $\partial B_{\boldsymbol{t}}$ of the deformed boundary and $\hat{\boldsymbol{n}}$ is the outward pointing unit normal vector. In order to pull Eq. (7.5) back to the initial configuration, B_0, the following identities are used [86, 87, 88]:

$$\begin{aligned}
\nabla \boldsymbol{\delta u} = \boldsymbol{F}^{-T} \nabla_{\boldsymbol{X}} \boldsymbol{\delta u} = \boldsymbol{F}^{-T} \boldsymbol{\delta F} &= {}^{e}\boldsymbol{F}^{-T\theta} \boldsymbol{F}^{-T} \boldsymbol{\delta F}, \\
dv = JdV = {}^{e}J^{\theta} JdV &= \beta^3(\Theta)^{e}JdV, \\
\boldsymbol{t} da = \boldsymbol{t} J \sqrt{\boldsymbol{N} \cdot \boldsymbol{C}^{-1} \boldsymbol{N}} dA &= \boldsymbol{t}_0 dA, \\
{}^{\theta}\boldsymbol{F} &= \beta(\Theta) \boldsymbol{I}, \\
\hat{\boldsymbol{P}} = \frac{\partial^e W}{\partial^e \boldsymbol{F}} &= {}^{e}J \sigma^{e} F^{-T}, \\
\text{and} \quad \rho_0 &= J\rho.
\end{aligned} \tag{7.6}$$

In Eq. (7.6), dv and dV are infinitesimal volume elements in the current and initial configurations, $\boldsymbol{N}$ is the unit outward pointing normal in the initial configuration, and $\hat{\boldsymbol{P}}$ is the first Piola-Kirchhoff stress tensor representing only stresses due to elastic deformations that take place during the isothermal stage. It is trivial to show that the terms three and four in Eq. (7.5), when pulled back into the reference configuration, are

$$\int_{\partial B} \boldsymbol{t} \cdot \boldsymbol{\delta u}\; da + \int_B \rho \boldsymbol{b} \cdot \boldsymbol{\delta u}\; dv = \int_{\partial B_0} \boldsymbol{t}_0 \cdot \boldsymbol{\delta u}\; dA + \int_{B_0} \rho_0 \boldsymbol{b} \cdot \boldsymbol{\delta u}\; dV.$$

The expression of the first term in the undeformed configuration is derived as follows:

$$\int_B \boldsymbol{\sigma} : \nabla \boldsymbol{\delta u} \, dv = \int_{B_0} J\boldsymbol{\sigma} : \nabla \boldsymbol{\delta u} \, dV = \int_{B_0} J\boldsymbol{\sigma}^e \boldsymbol{F}^{-T} : {}^{\theta}\boldsymbol{F}^{-T} \boldsymbol{\delta F} \, dV$$

$$= \int_{B_0} {}^{\theta}J^e J\boldsymbol{\sigma}^e \boldsymbol{F}^{-T} : {}^{\theta}\boldsymbol{F}^{-T} \boldsymbol{\delta F} \, dV = \int_{B_0} {}^{\theta}J \hat{\boldsymbol{P}} : {}^{\theta}\boldsymbol{F}^{-T} \boldsymbol{\delta F} \, dV$$

$$= \int_{B_0} \beta^3(\Theta) \hat{\boldsymbol{P}} : \frac{\boldsymbol{I}}{\beta(\Theta)} \boldsymbol{\delta F} \, dV = \int_{B_0} \beta^2(\Theta) \hat{\boldsymbol{P}} : \boldsymbol{\delta F} \, dV.$$

The acceleration term is also straightforward:

$$\int_B \rho \ddot{\boldsymbol{u}} \cdot \boldsymbol{\delta u} \, dv = \int_{B_0} \rho_0 \ddot{\boldsymbol{u}} \cdot \boldsymbol{\delta u} \, dV.$$

The principle of virtual work in the reference configuration, B_0, is thus

$$\delta W = \int_{B_0} \beta^2(\Theta) \hat{\boldsymbol{P}} : \boldsymbol{\delta F} \, dV + \int_{B_0} \rho_0 \ddot{\boldsymbol{u}} \cdot \boldsymbol{\delta u} \, dV - \int_{\partial B_0} \boldsymbol{t}_0 \cdot \boldsymbol{\delta u} \, dA - \int_{B_0} \boldsymbol{b}_0 \cdot \boldsymbol{\delta u} \, dV = 0. \quad (7.7)$$

Equation (7.7) shows that using the multiplicative decomposition of the deformation gradient allows for a standard elastic constitutive model to be used to calculate the first Piola-Kirchhoff stress tensor in the isothermal stage. The full expression of the first Piola-Kirchhoff stress tensor is the product $\beta^2(\Theta)\hat{\boldsymbol{P}}$.

Non-linear solution method

In a non-linear problem, if a body with current configuration $\boldsymbol{x}$ does not satisfy $\delta W(\boldsymbol{u}) = 0$, a linear correction is made, i.e., δW is linearized at $\boldsymbol{u}$ and multiplied by a correction $\Delta \boldsymbol{u}$ to achieve $\delta W(\boldsymbol{u} + \Delta \boldsymbol{u}) = 0$

$$\delta W(\boldsymbol{u} + \Delta \boldsymbol{u}) = 0 \approx L[\delta W] = \delta W(\boldsymbol{u}) + D\delta W(\boldsymbol{u})[\Delta \boldsymbol{u}] = 0 \quad (7.8)$$

where $D\delta W(\boldsymbol{u})[\Delta \boldsymbol{u}]$ is the directional derivative of $W(\boldsymbol{u})$ along $\Delta \boldsymbol{u}$. The terms involved in the linearization are the internal stress and traction terms,

$$L[\delta W] = \delta W(\boldsymbol{u}) + D\delta W_{int}(\boldsymbol{u})[\Delta \boldsymbol{u}] - D\delta W_{ext}(\boldsymbol{u})[\Delta \boldsymbol{u}] = 0,$$

which are described below. The corrected configuration $\boldsymbol{u} = \boldsymbol{u}_{old} + \Delta \boldsymbol{u}$ is found by solving for $\Delta \boldsymbol{u}$

$$D\delta W_{int}(\boldsymbol{u})[\Delta \boldsymbol{u}] - D\delta W_{ext}(\boldsymbol{u})[\Delta \boldsymbol{u}] = -\delta W(\boldsymbol{u}), \tag{7.9}$$

and iterating until $\delta W(\boldsymbol{u}) = 0$.

Linearization of δW

The internal virtual work is given by the term

$$\delta W_{int} = \int_{B_0} \beta^2(\Theta) \hat{\boldsymbol{P}} : \boldsymbol{\delta F} dV.$$

The term is linearized by taking the directional derivative along a displacement, $\Delta \boldsymbol{u}$, as

$$D\delta W_{int}[\Delta \boldsymbol{u}] = \int_{B_0} \beta^2(\Theta) \boldsymbol{\delta F} : D\hat{\boldsymbol{P}}[\Delta \boldsymbol{u}] dV. \tag{7.10}$$

Using

$$D\hat{\boldsymbol{P}}[\Delta \boldsymbol{u}] = \frac{\partial \hat{\boldsymbol{P}}}{\partial^e \boldsymbol{F}} : D^e \boldsymbol{F}[\Delta \boldsymbol{u}] = \mathcal{A} : D^e \boldsymbol{F}[\Delta \boldsymbol{u}]$$

and

$$D^e \boldsymbol{F}[\Delta \boldsymbol{u}] = \nabla_{\boldsymbol{X}} \Delta \boldsymbol{u}, \tag{7.11}$$

the linearized term takes the form

$$\int_{B_0} \beta^2(\Theta) \boldsymbol{\delta F} : D\hat{\boldsymbol{P}}[\Delta \boldsymbol{u}] dV = \int_{B_0} \beta^2(\Theta) \boldsymbol{\delta F} : \mathcal{A} : \nabla_{\boldsymbol{X}} \Delta \boldsymbol{u} dV. \tag{7.12}$$

The expressions of $\hat{\boldsymbol{P}}$ and $\mathcal{A}$ for the St. Venant-Kirchhoff and Neo-Hookean constitutive models are given in Appendix Sections D.1 and D.2, respectively. Similarly, the external virtual work term,

$$\delta W_{ext} = \int_{\partial B_0} \boldsymbol{t}_0 \cdot \boldsymbol{\delta u} \, dA,$$

is linearized by taking the directional derivative along $\boldsymbol{u}$ as

$$D\delta W_{ext}[\Delta \boldsymbol{u}] = \int_{\partial B_0} \boldsymbol{\delta u} \cdot D\boldsymbol{t}_0[\Delta \boldsymbol{u}] \, dA, \tag{7.13}$$

where,

$$D\boldsymbol{t}_0[\Delta\boldsymbol{u}] = \frac{\partial}{\partial^e\boldsymbol{F}}\left(\boldsymbol{t}\,{}^eJ\sqrt{\boldsymbol{N}\cdot\boldsymbol{C}^{-1}\boldsymbol{N}}\right) : D^e\boldsymbol{F}[\Delta\boldsymbol{u}] = \mathcal{B} : \nabla_{\boldsymbol{X}}\Delta\boldsymbol{u}, \tag{7.14}$$

where $\mathcal{B}$ is given in Appendix D.3. The resulting linearized equation is given as

$$\begin{aligned} L[\delta W(\boldsymbol{u})] = &\int_{B_0} \beta^2(\Theta)\hat{\boldsymbol{P}} : \boldsymbol{\delta F}\; dV + \int_{B_0} \rho_0\ddot{\boldsymbol{u}}\cdot\boldsymbol{\delta u}\; dV \\ &- \int_{\partial B_0} \boldsymbol{t}_0\cdot\boldsymbol{\delta u}\; dA - \int_{B_0} \boldsymbol{b}_0\cdot\boldsymbol{\delta u}\; dV \\ &+ \int_{B_0} \beta^2(\Theta)\boldsymbol{\delta F} : \mathcal{A} : \nabla_{\boldsymbol{X}}\Delta\boldsymbol{u}\; dV \\ &- \int_{\partial B_0} \boldsymbol{\delta u}\cdot\mathcal{B} : \nabla_{\boldsymbol{X}}\Delta\boldsymbol{u}\; dA = 0. \end{aligned} \tag{7.15}$$

The discretized form for Eq. (7.15) yields

$$\boldsymbol{\delta u}^T\left(\boldsymbol{R}^{int} + \boldsymbol{M}\ddot{\boldsymbol{u}} - \boldsymbol{R}^{tract.} - \boldsymbol{R}^{body} + \boldsymbol{K}\Delta\boldsymbol{u}\right) = \boldsymbol{0}, \tag{7.16}$$

where $\boldsymbol{R}^{int.}$ is the internal load vector, $\boldsymbol{M}$ is the consistent mass matrix, $\boldsymbol{R}^{tract.}$ and $\boldsymbol{R}^{body}$ are the external load vectors due to traction and body forces, respectively, and $\boldsymbol{K}$, the tangent stiffness matrix, represents the linearized internal and external virtual work terms. A detailed description of the spatial discretization can be found in Appendix D.4.

Temporal discretization

The dynamic equilibrium equation at time step $n+1$ is

$$\boldsymbol{R}^{int}_{n+1} - \boldsymbol{R}^{ext}_{n+1} + \boldsymbol{M}\ddot{\boldsymbol{u}}_{n+1} = \boldsymbol{0} \tag{7.17}$$

Newmark's method is used to advance Eq. (7.17) in time, in which the solution at time step $n+1$ is approximated by

$$\begin{aligned} \boldsymbol{u}_{n+1} &= \boldsymbol{u}_n + \Delta t\dot{\boldsymbol{u}}_n + \frac{\Delta t^2}{4}[(1-2\beta)\ddot{\boldsymbol{u}}_n + 2\beta\ddot{\boldsymbol{u}}_{n+1}], \\ \dot{\boldsymbol{u}}_{n+1} &= \dot{\boldsymbol{u}}_n + \Delta t[(1-\gamma)\ddot{\boldsymbol{u}}_n + \gamma\ddot{\boldsymbol{u}}_{n+1}], \end{aligned} \tag{7.18}$$

where $\gamma = 1/2$ and $\beta = 1/4$ are chosen to give an $\mathcal{O}(\Delta t^2)$ accurate, linearly stable scheme. Plugging Eq. (7.18) into Eq. (7.17) and approximating the internal load vector at time step $n+1$ as $\boldsymbol{R}_{n+1}^{int} = \boldsymbol{R}_n^{int} + \boldsymbol{K}\Delta\boldsymbol{u}$ results in

$$\boldsymbol{R}_{n+1}^{ext} - \boldsymbol{R}_n^{ext} + M\left(\frac{4}{\Delta t}\dot{\boldsymbol{u}}_n + 2\ddot{\boldsymbol{u}}_n\right) = \left(\frac{4}{\Delta t^2}\boldsymbol{M} + \boldsymbol{K}\right)\Delta\boldsymbol{u}$$

The solution, $\Delta\boldsymbol{u}$, is used to calculate the solution at $n+1$

$$\begin{aligned}\boldsymbol{u}_{n+1} &= \boldsymbol{u}_n + \Delta\boldsymbol{u},\\ \dot{\boldsymbol{u}}_{n+1} &= \dot{\boldsymbol{u}}_n + \frac{2}{\Delta t}\Delta\boldsymbol{u},\\ \ddot{\boldsymbol{u}}_{n+1} &= \ddot{\boldsymbol{u}}_n + \frac{4}{\Delta t^2}\Delta\boldsymbol{u}.\end{aligned}$$

Newton-Raphson iterations are used until Eq. (7.17) is satisfied to a tolerance of 10^{-5}.

7.2.3 Stress-free stage

The transient heat equation describes the evolution of the thermal state in a solid in the current configuration, B,

$$\rho C_p\dot{\Theta} + \nabla\cdot\boldsymbol{q} = 0. \tag{7.19}$$

where Θ is the temperature, $\boldsymbol{q}$ is the heat flux vector, and C_p and k are the specific heat capacitance and thermal conductivity of the solid, respectively. The weak form is

$$\int_B \rho C_p\dot{\Theta}\delta\Theta dv + \int_B (\nabla\cdot\boldsymbol{q})\delta\Theta dv = 0, \tag{7.20}$$

where $\delta\Theta$ denotes the arbitrary weight function. Using the relation $(\nabla\cdot\boldsymbol{q})\delta\Theta = \nabla\cdot(\boldsymbol{q}\delta\Theta) - \boldsymbol{q}\cdot\nabla\delta\Theta$ and the divergence theorem, Eq. (7.20) is re-expressed as

$$\int_B \rho C_p\dot{\Theta}\delta\Theta dv - \int_B \boldsymbol{q}\cdot\nabla\delta\Theta dv + \int_{\partial B}\boldsymbol{q}\cdot\boldsymbol{n}\delta\Theta da = 0. \tag{7.21}$$

The first term in Eq. (7.21) is readily pulled back into the reference configuration as

$$\int_B \rho C_p \dot{\Theta} \delta\Theta dv = \int_{B_0} J\rho C\dot{\Theta}\delta\Theta dV = \int_{B_0} \rho_0 C_p \dot{\Theta}\delta\Theta dV.$$

For the second term, Fourier's law provides a linear relation between the temperature gradient $\nabla\Theta$ and the heat flux vector

$$\boldsymbol{q} = -k\nabla\Theta. \tag{7.22}$$

The second term in Eq. (7.21) is pulled back into the undeformed configuration as follows:

$$\begin{aligned}\int_B \boldsymbol{q}\cdot\nabla\delta\Theta dv &= \int_{B_0} -Jk\nabla\Theta\cdot\nabla\delta\Theta dV = \int_{B_0} -Jk\boldsymbol{F}^{-T}\nabla_X\Theta\cdot\boldsymbol{F}^{-T}\nabla_X\delta\Theta dV \\ &= \int_{B_0} -Jk\boldsymbol{F}^{-1}\boldsymbol{F}^{-T}\nabla_X\Theta\cdot\nabla_X\delta\Theta dV = \int_{B_0} -Jk\boldsymbol{C}^{-1}\nabla_X\Theta\cdot\nabla_X\delta\Theta dV \\ &= \int_{B_0} \boldsymbol{Q}\cdot\nabla_X\delta\Theta dV,\end{aligned}$$

where $\boldsymbol{Q} = -Jk\boldsymbol{C}^{-1}\nabla_X\Theta$. The third term is found by finding the relation between area elements in the current and reference configurations, da and dA, respectively,

$$da = J\sqrt{\boldsymbol{N}\cdot\boldsymbol{C}^{-1}\boldsymbol{N}}dA. \tag{7.23}$$

The derivation of Eq. (7.23) is given in Appendix D.5. The third term in the reference configuration is thus given as

$$\int_{\partial B} \boldsymbol{q}\cdot\boldsymbol{n}\delta\Theta da = \int_{\partial B_0} \boldsymbol{Q}\cdot\boldsymbol{N}\delta\Theta dA,$$

where

$$\boldsymbol{Q}\cdot\boldsymbol{N} = J\boldsymbol{q}\cdot\boldsymbol{n}\sqrt{\boldsymbol{N}\cdot\boldsymbol{C}^{-1}\boldsymbol{N}}. \tag{7.24}$$

Given a heat flux $\boldsymbol{q}\cdot\boldsymbol{n}$ in the current configuration (e.g. calculated from the fluid solution), $\boldsymbol{Q}\cdot\boldsymbol{N}$ is calculated with Eq. (7.24) to be applied to the reference configuration. The final expression of Eq. (7.21) in the reference configuration is thus

$$\int_{B_0} \rho_0 C_p \dot{\Theta} \delta\Theta dV + \int_{B_0} Jk\boldsymbol{C}^{-1}\nabla_X\Theta \cdot \nabla_X \delta\Theta dV = -\int_{\partial B_0} \boldsymbol{Q} \cdot \boldsymbol{N} \delta\Theta \, dA. \quad (7.25)$$

The discretized for of Eq. (7.25) yields

$$\boldsymbol{C}_{th}\dot{\boldsymbol{\Theta}} + \boldsymbol{K}_{th}\boldsymbol{\Theta} = \boldsymbol{R}_{th}, \quad (7.26)$$

where $\boldsymbol{C}_{th}$ and $\boldsymbol{K}_{th}$ are the thermal capacitance and thermal stiffness matrices, respectively, and $\boldsymbol{R}_{th}$ is the thermal load vector. A detailed description of the discretization can be found in Appendix D.6.

Temporal discretization

In this work, the heat equation in advanced in time using Crank-Nicholson scheme. The thermal state at step $n+1$ is approximated by

$$\boldsymbol{\Theta}_{n+1} \approx \boldsymbol{\Theta}_n + \Delta t \left((1-\beta)\dot{\boldsymbol{\Theta}}_n + \beta \dot{\boldsymbol{\Theta}}_{n+1} \right) \quad (7.27)$$

Adding Eq. (D.22), written at $n+1$ and n, multiplied by β and $(1-\beta)$, respectively, yields

$$\begin{aligned}(1-\beta)\left(\boldsymbol{C}_{th,n}\dot{\boldsymbol{\Theta}}_n + \boldsymbol{K}_{th,n}\boldsymbol{\Theta}_n\right) + \beta\left(\boldsymbol{C}_{th,n+1}\dot{\boldsymbol{\Theta}}_{n+1} + \boldsymbol{K}_{th,n+1}\boldsymbol{\Theta}_{n+1}\right) \quad (7.28)\\ = (1-\beta)\boldsymbol{R}_{th,n} + \beta\boldsymbol{R}_{th,n+1}\end{aligned}$$

The choice of $\beta = 1/2$ is referred to as the trapezoidal rule, and is the value used in this work. Furthermore, the choice of $\beta = 1/2$ gives an $\mathcal{O}(\Delta t^2)$ accurate scheme and is unconditionally stable for linear problems. Using Eq. (7.27) and $\boldsymbol{K}_{th,n+1}\Theta_{n+1} \approx \boldsymbol{K}_{th,n}\Theta_n + \boldsymbol{K}_{th,n}\Delta\Theta$, where $\Delta\Theta = \Theta_{n+1} - \Theta_n$, and noting that $\boldsymbol{C}_{th,n+1} = \boldsymbol{C}_{th,n} = \boldsymbol{C}_{th}$, gives

$$\left(\frac{2}{\Delta t}\boldsymbol{C}_{th} + \boldsymbol{K}_{th,n}\right)\Delta\Theta = \boldsymbol{C}_{th}\dot{\Theta}_n - \boldsymbol{K}_{th,n}\Theta_n + \boldsymbol{R}_{th,n+1}. \quad (7.29)$$

7.2.4 Evolution of coupled equations

In order to integrate the coupled equations Eq. (7.3) and Eq. (7.19) in time, a two-stage staggered approach based on the isothermal split is taken. The in the first stage, the mechanical phase (Eq. (7.17)) is solved with a fixed temperature, and, in the second stage, the thermal phase (Eq. (D.22)) is solved on the fixed, current configuration, $\boldsymbol{x}(\boldsymbol{X}, t)$. The resulting structural and thermal solutions are $\boldsymbol{x}_{n+1}^{k}$ and Θ_{n+1}^{k}, respectively, where n is the time step index and k is the subiteration index. The two solutions are iterated on at time step n until the desired convergence for both solutions is achieved, which for the mechanical and thermal phases are

$$\mathcal{S}_u = \frac{||\boldsymbol{x}_{n+1}^{k+1} - \boldsymbol{x}_{n+1}^{k}||}{||\boldsymbol{x}_{n+1}^{1} - \boldsymbol{x}_n||},$$

and

$$\mathcal{S}_\Theta = \frac{||\Theta_{n+1}^{k+1} - \Theta_{n+1}^{k}||}{||\Theta_{n+1}^{1} - \Theta_n||},$$

respectively. Upon satisfaction of $\mathcal{S}_u \leq \epsilon$ and $\mathcal{S}_\Theta \leq \epsilon$, the structural and thermal solutions at $n+1$ are $\boldsymbol{x}_{n+1} = \boldsymbol{x}_{n+1}^{k+1}$ and $\Theta_{n+1} = \Theta_{n+1}^{k+1}$, and the code proceeds with the next time step.

7.3 Solver verification

As mentioned in Chapter 3, the fluids code has been verified and used in a number of previous investigations. Verification of the thermomechanical solver is presented here.

7.3.1 Dynamic thermal verification

The dynamic thermal solver is verified by comparison with the analytical solution of a structurally rigid beam, insulated on the sides, and with isothermal 0 K temperature imposed on the ends. The beam is given an initial condition of a "triangular" temperature variation (Fig. 7.4),

$$\Theta(x,0) = \begin{cases} \dfrac{2x}{L}\Theta_{max} & \text{for} \quad x \leq \dfrac{L}{2} \\ 2\dfrac{L-x}{L}\Theta_{max} & \text{for} \quad x > \dfrac{L}{2}. \end{cases} \tag{7.30}$$

The analytical solution for the temperature field in the beam is given by

$$\Theta(x,t) = \sum_{n=1}^{n_{max}} B(n) \sin\left(\frac{n\pi x}{L}\right) \exp\left[-\eta_{th}\left(\frac{n\pi}{L}\right)^2 t\right], \tag{7.31}$$

where

$$B(n) = \begin{cases} \dfrac{8L\Theta_{max}}{n^2\pi^2} & \text{for} \quad n = 1, 5, 9... \\ -\dfrac{8L\Theta_{max}}{n^2\pi^2} & \text{for} \quad n = 3, 7, 11... \\ 0 & \text{for} \quad n = \text{even}, \end{cases}$$

and the thermal diffusivity, $\eta_{th} = k/\rho C_p$. For the verification, arbitrary material properties and problem parameters were chosen to be

$$\rho = 400 \, \frac{\text{kg}}{\text{m}^3}, \quad C_p = 500 \, \frac{\text{J}}{\text{kg} \cdot \text{K}}, \quad k = 100 \, \frac{\text{W}}{\text{m} \cdot \text{K}}, \quad L = 1 \text{ m}, \quad \text{and} \quad dt = 1 \text{ s}.$$

The numerical solution obtained with a uniform mesh composed of $N_x \times N_y = 10 \times 1$ quadratic elements closely matches the analytical solution as shown in Fig. 7.5.

7.3.2 Steady-state structural verification

For geometrically non-linear problems, considerable difficulty exists in finding an analytical solution. In lieu of an analytical solution, a reference solution from the commercial finite element analysis tool Abaqus [89] is used. The verification problem is a beam, pinned at the bottom corners with a uniform pressure load on the underside, as shown in Fig. 7.6. For the verification, a 2D beam with $N_x \times N_y = 10 \times 4$ quadratic elements was modeled in simulations using both the in-house code and Abaqus. The beam dimensions and material properties are

$$L = 25.4 \text{ mm}, \ \tau = 0.15 \text{ mm}, \ E = 200 \times 10^9 \text{ Pa}, \ \nu = 0.27, \ \text{and} \ p = 10^5 \text{ Pa}.$$

A similar simulation based on a square panel with pinned edges was also used to verify the 3D solver. The present solver and Abaqus predicted identical center point displacements of 0.343 mm and 0.275 mm in the 2D and 3D cases, respectively. It is noted that these displacements are well over the beam/plate thickness, placing the solution in the geometrically non-linear regime.

7.3.3 Dynamic structural verification

For verification of the dynamic structural solver, the beam in Fig. 7.6 was initially undeformed and subject to a pressure load on one side, placing it out of equilibrium. The same problem parameters are used as in the steady-state verification problem. Additional dynamic parameters were

$$\rho = 8000\ \frac{\mathrm{kg}}{\mathrm{m}^3},\ \text{and}\ dt = 5.0\ \mu\mathrm{s}.$$

As shown in Fig. 7.7, the solutions between the two solvers match, and oscillate about the static displacement of 0.343 mm found above.

7.3.4 Thermomechanical coupling verification

To verify the the coupling between the thermal and structural solutions (accomplished with the isothermal split in Eq. (7.1)), a problem similar to the one used for the structural verification is solved. The pressure load is replaced with a heat load applied along the top of the beam (Fig. 7.8), and the static deflection and temperature of the center of the beam are compared between the current solver and Abaqus. The discretization and mechanical properties are the same as in the structural verification problems. The additional thermal parameters are

$$k = 16.26\ \frac{\mathrm{W}}{\mathrm{m}\cdot\mathrm{K}},\ \alpha_{th} = 5.33\times10^{-6},\ \text{and}\ q = 25.0\times10^{3}\ \frac{\mathrm{W}}{\mathrm{m}^2}.$$

The results of the comparison are given in Tab. 7.1. In the thermomechan-

Table 7.1: Verification of the thermomechanical coupling. Solution values at $x = L/2$, $y = \tau$ from the in-house code and Abaqus.

Solver	Temperature (K)	% Difference	Deflection mm	% Difference
In-house	831.208	9.92×10^{-2}	0.890	0.61
Abaqus	830.384	*N/A*	0.884	N/A

ical comparison between the current solver and Abaqus, some discrepancy is expected. In the current code, both the structural and the thermal solutions discretized with quadratic elements, whereas Abaqus uses quadratic elements in the structural solver and linear elements in the thermal solver. The slightly higher temperature predicted by the current solver produces an equally small increase in the lateral deflection of the beam. Nevertheless, the two solutions are sufficiently close to each other to verify the current thermomechanical implementation. It is also noted that deflections are very large ($\sim$6 times the beam thickness), as illustrated in Fig. 7.9.

7.3.5 Spatial convergence rate

To verify the convergence rate of the quadratic elements, the steady-state problem in Fig. 7.10 is solved with $N_x = 85$ elements along the length of the beam and through thickness discretizations progressively doubled from $N_y = 2$ to $N_y = 64$. Due to the difficulty of obtaining an analytical solution to the geometrically non-linear problem, the solution on a $N_x \times N_y = 85 \times 150$ mesh serves as the reference. The beam dimensions, material properties, and load are

$$L = 50.1 \text{ mm}, \ \tau = 0.15 \text{ mm}, \ E = 200 \times 10^9 \text{ Pa}, \ \nu = 0.27, \text{ and } p = 10^4 \text{ Pa}.$$

The results, shown in Fig. 7.11, confirm the quadratic spatial convergence in the current implementation.

7.4 Interface treatment

The individual fluid and structural solvers are weakly coupled at the interface where the fluid-structural-thermal interaction takes place. The fluid and thermomechanical solutions are found independently in their respective domains at a given time step $t_n = n\Delta t$. The spatial coupling is achieved through matching nodes at the interface. Dirichlet quantities (displacement, temperature) are passed from the solid to the fluid while the Neumann quantities (traction, heat load) are passed from the fluid to the solid. Giles [55] showed that numerical stability at the interface is increased for the thermal problem when information is passed in this manner. Furthermore, it is shown in Appendix D.3.1 that it is less cumbersome to pass the Cauchy stress tensor, $\boldsymbol{\sigma}$, from the fluid solution to the solid domain, instead of the traction, $\boldsymbol{t} = \boldsymbol{\sigma} \cdot \hat{\boldsymbol{n}}$. This approach therefore taken in the current work.

One major challenge in fluid-structural-thermal interaction simulations is the impact of the highly disparate time scales involved in the three physical problems. The computational cost resulting from trying to resolve the time scales involved in all disciplines can be prohibitive due to the fact that the transient thermal solution in the solid evolves much more slowly than does the structural solution, which still evolves slower than the solution in the fluid. This effect is exacerbated in the case where the fluid solution is explicitly advanced in time, in which the coupled system time step is limited by the stringent stability requirements associated with the fluid solution. To efficiently advance the coupled system while minding the stability and accuracy requirements of the solvers, different time step sizes are taken in the fluid, thermal, and structural solution stages. The flow of information can be seen in Fig. 7.12. This method is $\mathcal{O}(\Delta t_c)$ accurate, where Δt_c is the coupling step size.

As indicated, it is likely that the time step size would increase from the fluid solver to the structural solver to the thermal solver. Information is linearly interpolated between time steps when needed. Due to the prohibitive cost of the fluid solution, subiteration is not employed between the fluid solution and the other two solutions. The time step ratios are chosen so that their effect on the solution is minimal. To determine appropriate time step ratios, a 2D simulation of a laminar Mach 2.25 boundary layer over a structurally compliant 2D beam was conducted. The beam was initially excited in the 10^{th} beam mode so that it would deform into and interact with the flow. The simulation was conducted with three different time step ratios: $\Delta t_{solid}/\Delta t_{fluid} = 1/1$ (lock-step), $\Delta t_{solid}/\Delta t_{fluid} = 10/1$, and $\Delta t_{solid}/\Delta t_{fluid} = 100/1$. It was found that the change in the fluid vertical velocity, taken at a location above the beam after one mode 10 period, differed from the lock-step case by $6.7 \times 10^{-4}\%$ and $1.2 \times 10^{-1}\%$ for the $\Delta t_{solid}/\Delta t_{fluid} = 10/1$, and $\Delta t_{solid}/\Delta t_{fluid} = 100/1$, respectively. A time step ratio of $\Delta t_{solid}/\Delta t_{fluid} = 10/1$ is used in this study.

Figures for Chapter 7

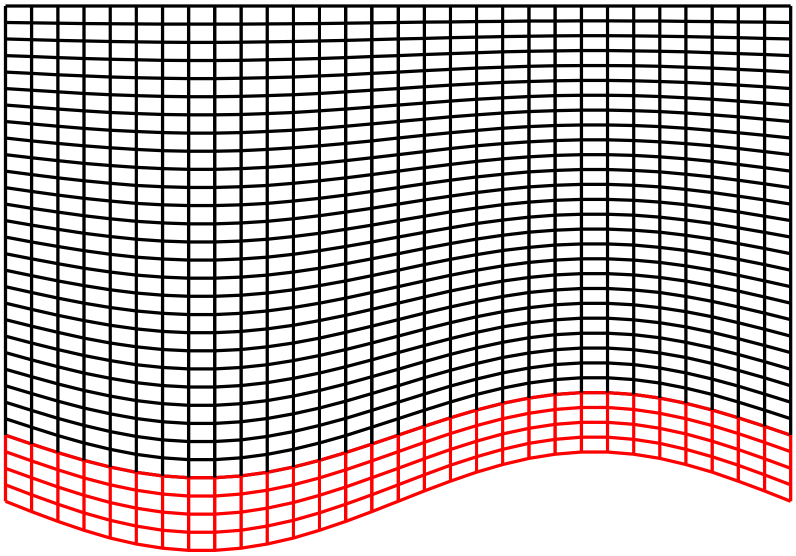

Figure 7.1: A 2D illustration the fluid grid (black) conforming to the motion of the solid grid (red) using transfinite interpolation.

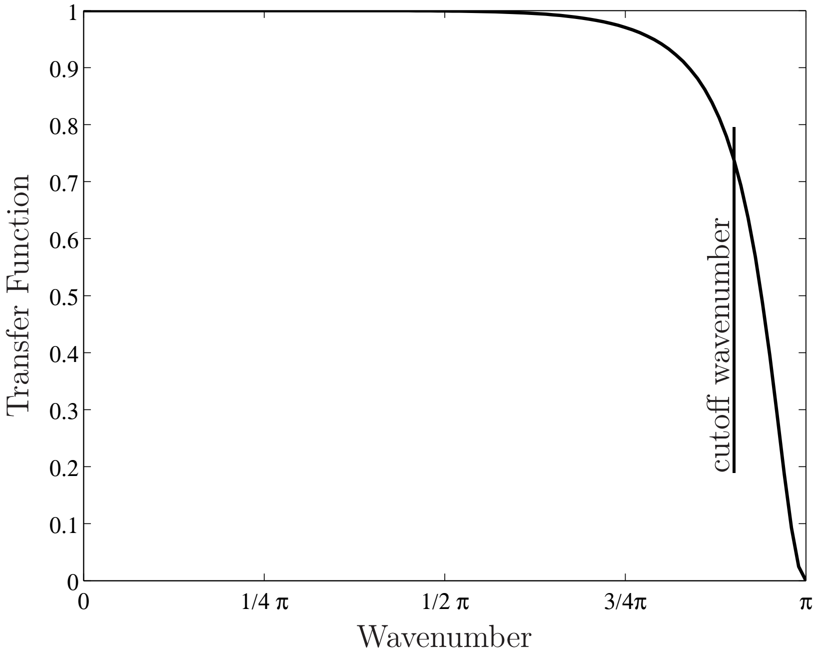

Figure 7.2: Transfer function for the 10^{th}-order implicit filter for filter strength $\alpha_f = 0.490$. The associated cutoff wavenumber of 0.90π is shown with a vertical line.

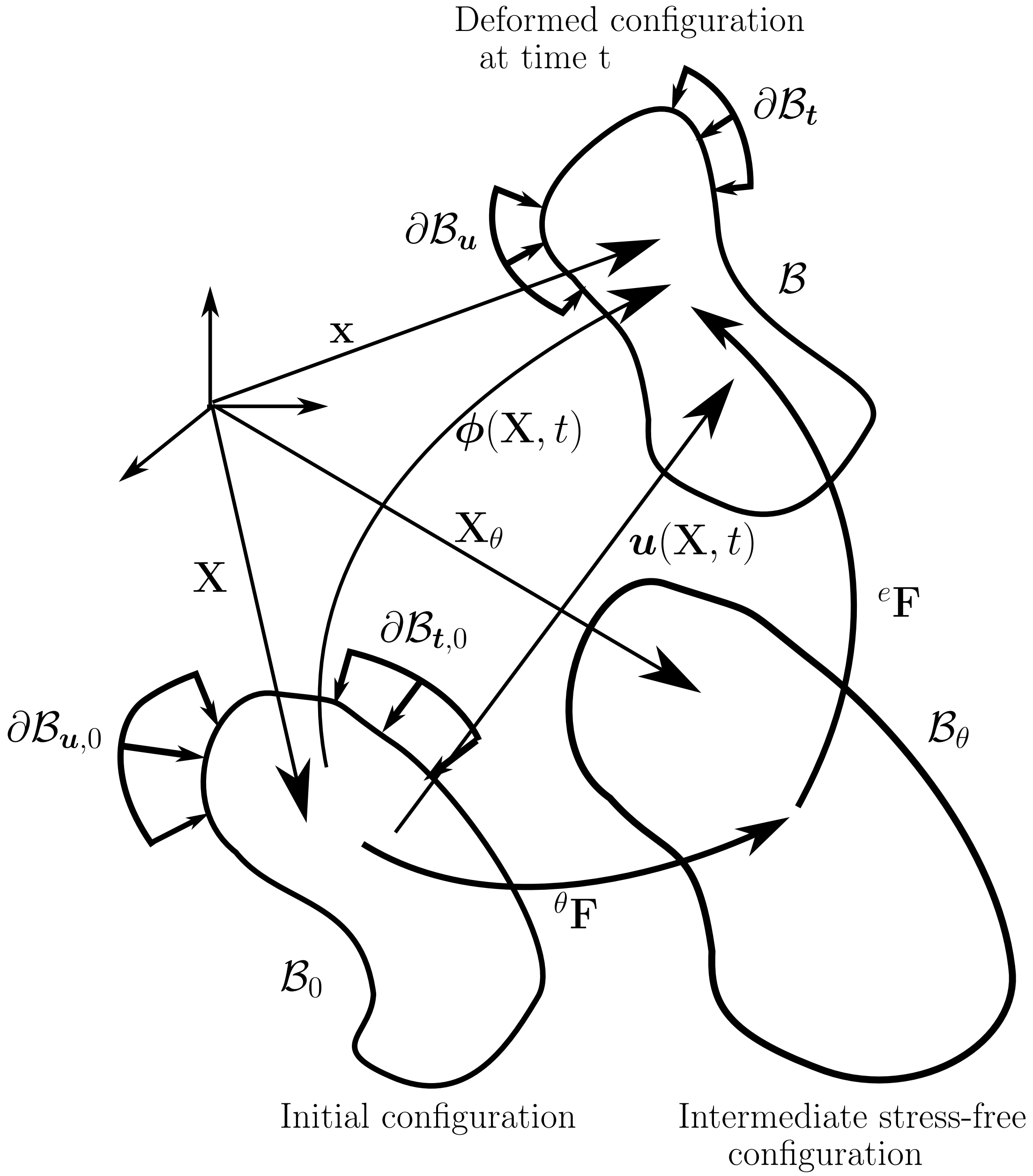

Figure 7.3: Schematic of the isothermal split of the deformation gradient.

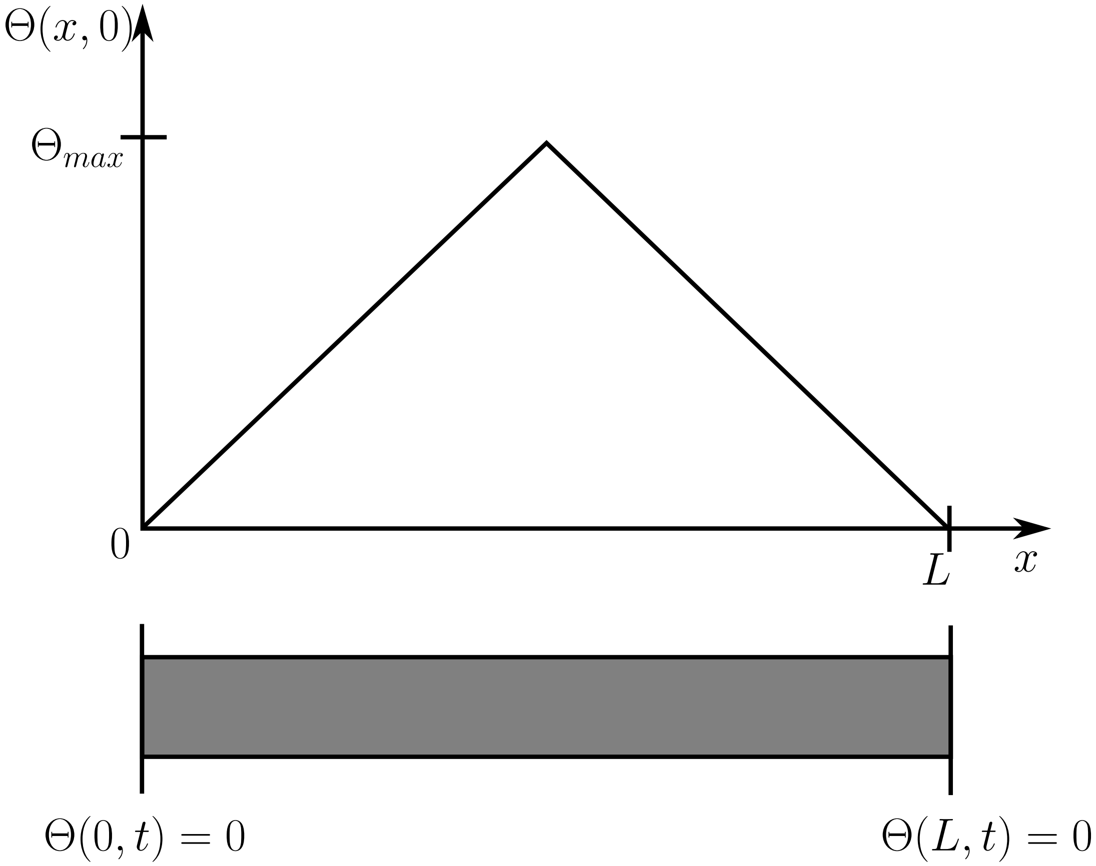

Figure 7.4: Initial condition for dynamic thermal verification problem.

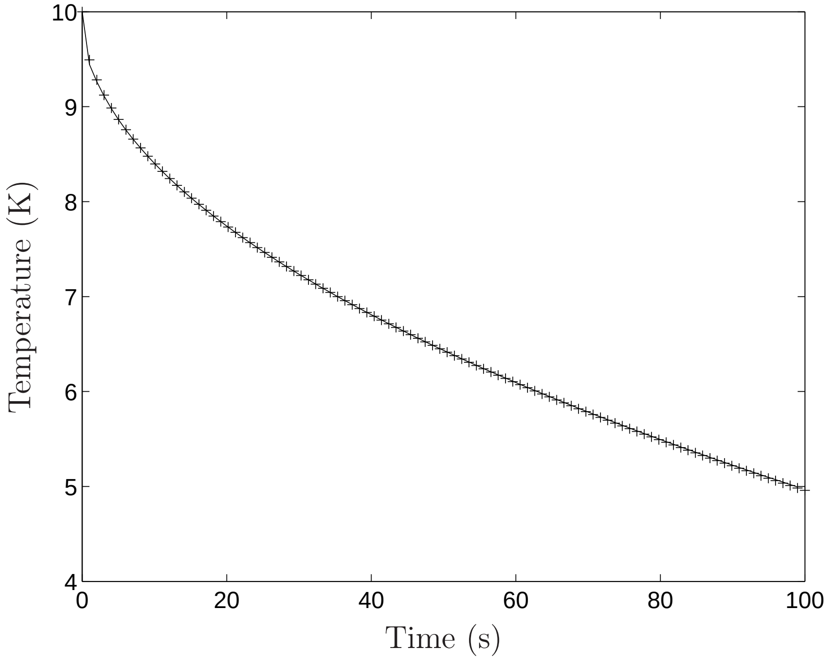

Figure 7.5: Comparison of temperature at x = 0.5 m between the analytical (symbolds) and numerical (solid line) solutions.

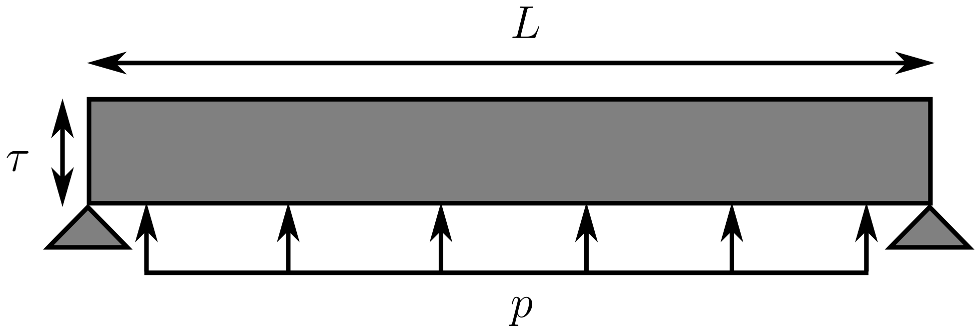

Figure 7.6: Verification problem for the structural solver.

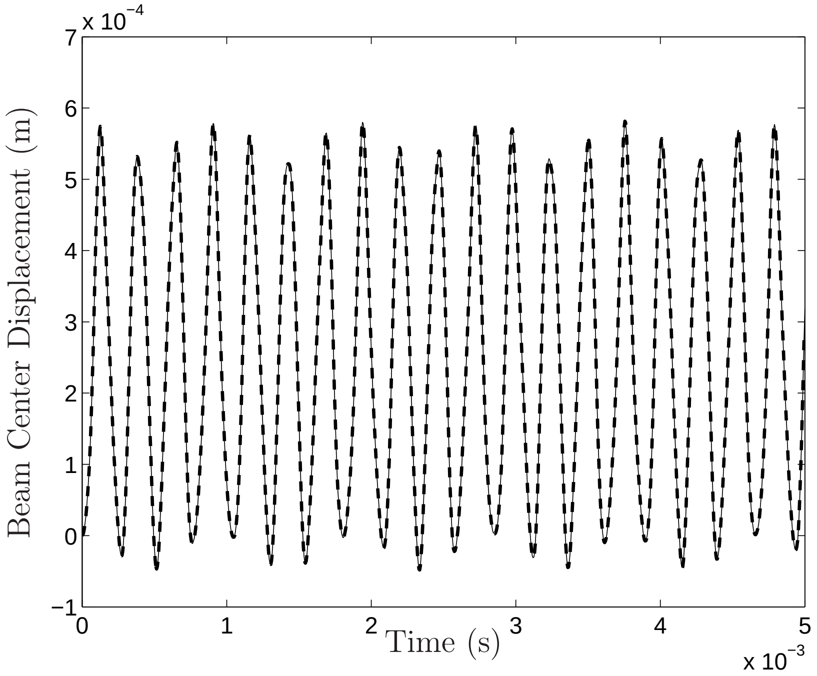

Figure 7.7: Verification problem for the dynamic structural solver. Current solver (solid), Abaqus solution (dashed).

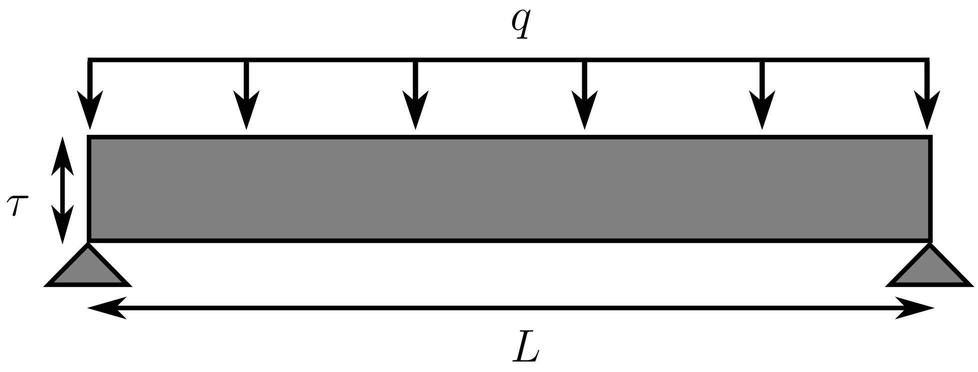

Figure 7.8: Verification problem for the thermomechanical coupling.

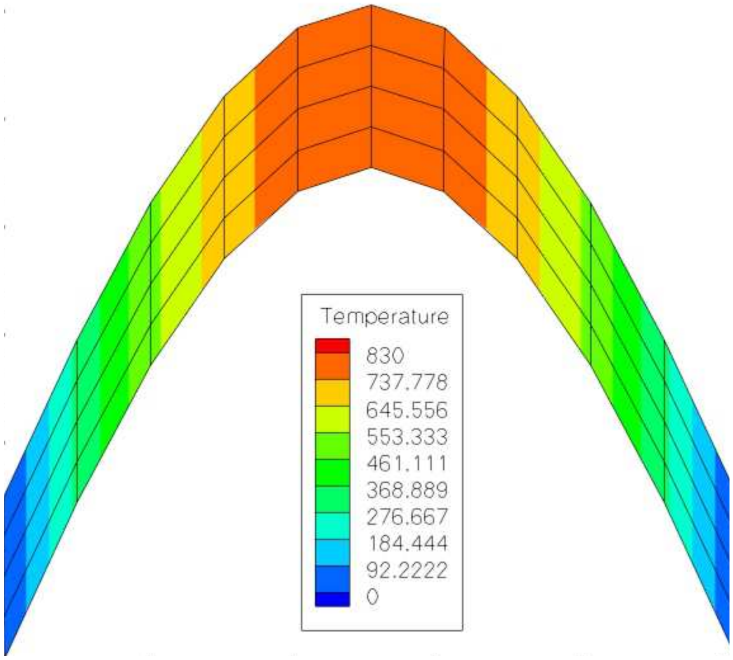

Figure 7.9: Thermomechanical coupling verification problem solution.

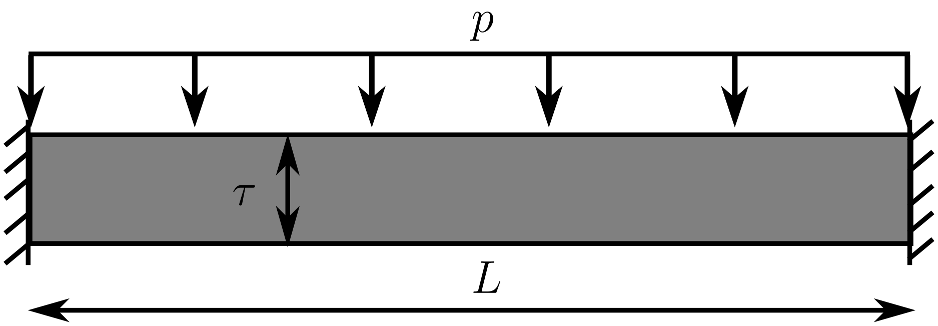

Figure 7.10: Verification problem for the spatial convergence of the quadratic elements.

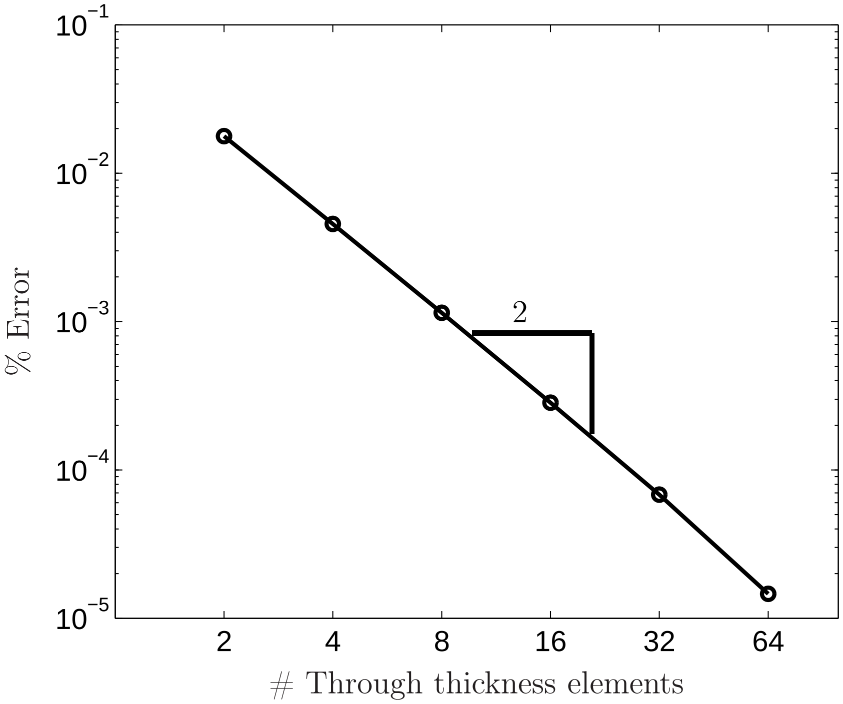

Figure 7.11: Verification problem for the spatial convergence of the quadratic elements. % Error $= \frac{|w - w_{ref}|}{w_{ref}}$, where w_{ref} is the center displacement of the beam with 150 through thickness elements.

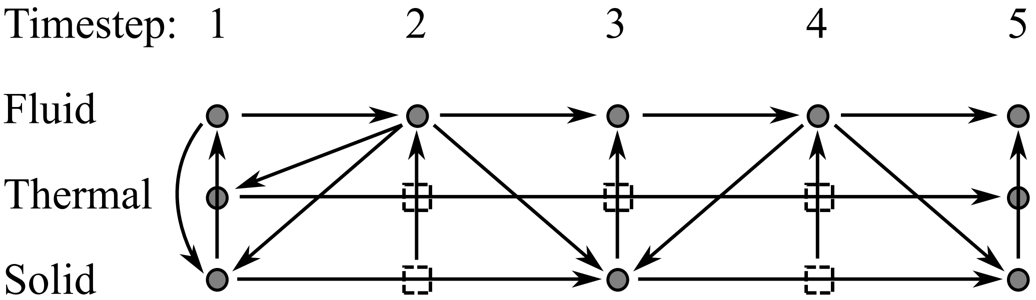

Figure 7.12: Flow of information between the solvers in the case where the structural and thermal time steps are 2× and 4× the fluid time step, respectively. Dashed boxes indicate interpolated data.

Chapter 8

Background: Aeroelastic Investigation of a TBL Over a Compliant Panel in Mach 2.25 Flow

In the work presented in Part I, the aspect of fluid-thermal coupling was addressed while structural deformation was avoided by choosing to solve a problem over a nominally rigid geometry. However, depending on the conditions and structure under consideration, mechanical deformation can significantly alter the solution. As evidenced by the situation that motivated the Glass & Hunt work [1], a deformed body panel can create a shock, local changes in surface heating, and can alter the flow field. In the following, a deformable structure under a high-speed flow is studied to better understand the consequences of fluid-structure coupling.

8.1 Compressible turbulent boundary layer data

The goal of this investigation is to study the interaction of a flexible panel with a high-speed turbulent boundary layer (TBL). Prior to the fully coupled simulation, the fluid solution must be initialized with a TBL. While turbulence is present in the majority of flows in nature, numerical generation of a TBL is not a trivial task. Furthermore, once it is generated, verification that it has reached a fully turbulent state is necessary. A good comparison with previously gathered true data, experimental or otherwise, provides confidence in the numerically generated TBL.

8.2 Problem definition

The current work features a Mach 2.25 turbulent boundary layer wetting a (initially) flat isothermal no-slip surface. A section of the surface is composed of a structurally compliant panel, while the remaining surface area is left structurally rigid (Fig. 8.3(a)). Temporally and spatially varying tractions from the supersonic turbulent boundary layer cause changes in the structural state of the panel. The design of the simulations are guided by physical and computational considerations.

8.2.1 Fluid domain

Temporal DNS

Consider a TBL over a flat plate with fixed freestream conditions. A laminar boundary layer begins to develop at the leading edge of the plate and grows with distance in the streamwise direction. At some point, depending on the environmental conditions, the boundary layer begins to transition from a laminar to turbulent state. The growth rate of the boundary layer changes significantly during transition and settles to a new rate once the boundary layer becomes turbulent. To capture this process in a simulation requires a domain long enough to simulate all stages of boundary layer development. This can be especially expensive considering the number of grid points needed to accurately simulate a turbulent boundary layer. In addition, use of a monolithic, structured grid would lead to a waste of computational resources, as the grid would be unnecessarily fine in the laminar region to accommodate for the turbulent region downstream. Use of a multiblock grid allows the use of fewer grid points in the laminar region, but requires interpolation and an *a priori* knowledge of the transition location. In any case, the simulation of a spatially developing boundary layer, or SDNS, is an expensive endeavor. Various methods have been developed to shorten the required domain in a SDNS [90, 91, 92].

The growth of a boundary layer, whether in the laminar or turbulent regime, is generally slow. It has been common practice to exploit this slow streamwise growth by neglecting it entirely. The flow is assumed to be homogeneous in the streamwise direction thus allowing periodic boundary conditions to be used. The resulting temporal DNS (TDNS) features a boundary layer that is homogeneous in both the spanwise and streamwise directions and grows with time, not space. This allows a significant reduction in the streamwise extent of the computational domain while enabling simulations of boundary layers from their early laminar to fully developed turbulent stages. Xu & Martin [93] state that "The usage [of periodic boundary conditions] is proved to be valid by many numerical experiments, though it may not be well justified physically." In that same work, they consider a method called extended TDNS (ETDNS), first developed by Meader et al. [94], where the governing equations are modified by the addition of forcing terms to achieve stationary mean flow and non-decaying turbulence (two issues that plague TDNS). Xu & Martin show good comparison between TDNS and ETDNS results and reason that, two criteria need to be satisfied for TDNS to be valid: "(i) the turbulence can be considered quasi-steady, i.e., it adjusts itself to local conditions much faster than the mean profile develops; and (ii) for the purpose of gathering statistics, the sampling time is shorter than the time scale of the mean profile development." They later state that the first condition satisfies the second. The first condition is quantified as follows. They state that if the time scale of the boundary layer growth,

$$t_g = \left(\frac{1}{\delta^*} \frac{d\delta^*}{dt} \right)^{-1},$$

is much larger than the timescale associated with turbulence adjustment, i.e., the eddy turnover rate, δ_0/U_e, then the first criterion is satisfied. An *a posteriori* calculation from a TDNS in this study confirmed that the ratio $t_g/(\delta_0/U_e)$ remained in the range of 12 to 22 over the length of the simulation. While the fluid solution requires a higher spatial resolution than the structural solution, the use of a TDNS leads to a better balance in computational resources between the two problems.

Flow properties and domain discretization

The flow properties in the current work are chosen to be similar to those in Pirozzoli & Grasso [3]. At the measurement location, their boundary layer had a momentum thickness Reynolds number of $\mathrm{Re}_\theta = 4263$. The plate was an isothermal 322 K (the recovery temperature to approximate an adiabatic wall) no-slip boundary. In their work, the boundary layer was simulated from a laminar state to a fully turbulent state, utilizing a section of blowing/suction to induce transition. The flow properties are determined from the information given in [3], which included the freestream temperature T_∞, Mach number M_∞, and unit Reynolds number Re_∞. The freestream viscosity was computed assuming Sutherland's law,

$$\mu_\infty = \mu_{ref} \left(\frac{T_\infty}{T_{ref}} \right)^{1.5} \frac{T_{ref} + S}{T_\infty + S},$$

where the reference values are given in White [11] as $S = 111$ K and $T_0 = 273$ K*. Given the above information, the density could be found as

$$\rho_\infty = \frac{\mathrm{Re}_\infty \mu_\infty}{M_\infty \sqrt{\gamma R T_\infty}},$$

where $R = 286.9$ J/kg $\cdot$ K is the specific gas constant for air. The resulting flow properties are presented in Tab. 8.1.

Table 8.1: Flow conditions in the Pirozzoli & Grasso simulation [3].

Re_∞ 1/m	M_∞	T_∞ K	μ_∞ kg/m $\cdot$ s	ρ_∞ kg/m^3
25×10^6	2.25	169.44	1.1489×10^{-5}	0.4893

To spatially resolve their TBL at the measurement location ($\mathrm{Re}_\theta = 4263$), Pirozzoli & Grasso performed a grid convergence study resulting in a 29.5×10^6 point grid, referred to here as the PnG domain. The dimensions are given is given in Tab. 8.2. The large streamwise extent of their domain is due to the requirement that the boundary layer be simulated through the laminar, transitional, and turbulent stages. The only requirement on the spanwise extent was that the turbulent structures be sufficiently decorrelated to justify the use of periodic spanwise boundaries.

Table 8.2: Pirozzoli & Grasso simulation domain.

Total Points	$N_x \times N_y \times N_z$	$L_x \times L_y \times L_z$ mm×mm×mm	$\Delta x^+ \times \Delta y^+_{wall} \times \Delta z^+$
29,488,200	$2065 \times 56 \times 255$	$439.420 \times 12.700 \times 4.445$	$14.50 \times 1.05 \times 6.56$

---

*Sutherland's law is 2% accurate for air in the temperature range 170 K to 1900 K

The domain given in Tab. 8.2 is unsuitable for the current simulation for the following reasons: 1) the spanwise dimension is not sufficient to accommodate the 2 in. × 1 in. panel in the coupled simulations, 2) the large streamwise extent needed for the SDNS is unnecessary in a TDNS, and 3) the streamwise distribution of grid points is not uniform.

To verify our TBL methodology against the Pirozzoli & Grasso data, a new simulation domain was created which is referred to here as the PnG2 domain (Tab. 8.3). The PnG2 domain has several differences from the PnG domain. The streamwise length of the domain is shorter in the PnG2 domain, while the number of streamwise points is greater. This is due to the fact that, in the PnG domain, the domain is split into three zones in the streamwise direction. The first zone is reserved for the blowing/suction strip and transition to turbulence and has a large spacing of $\Delta x = 0.17$ mm. The second zone in the PnG grid encompassed the region of interest where the turbulence develops and is studied. Consequently, it has fine grid point spacing of $\Delta x = 0.039$ mm with $\Delta x^+ = 14.50$. The third zone is progressively coarsened toward the outflow with an average $\Delta x = 2.7$ mm. The uniform grid requirement of TDNS gives the the PnG2 domain constant $\Delta x = 0.053$ mm and a corresponding $\Delta x^+ = 21.29$. In this work, it was found that numerical stability issues required a larger number of points in the wall normal direction in the PnG2 domain when compared to the PnG domain. Results from the comparison are shown in Section 9.1.4 and, despite the differences in resolution, there is good agreement between the current work and reference solution. Schematics of the two domains are given in Fig. 8.1 and Fig. 8.2.

Table 8.3: TDNS domain for simulation for comparison with reference solution. The viscous-length normalized values are valid at the time of comparison with the reference solution (Section 9.1.4).

Total Points	$N_x \times N_y \times N_z$	$L_x \times L_y \times L_z$ mm×mm×mm	$\Delta x^+ \times \Delta y^+_{wall} \times \Delta z^+$
50,182,800	2698 × 100 × 186	142.800 × 12.700 × 4.445	21.29 × 1.42 × 9.66

We now discuss the domain required for the coupled simulations. As mentioned above, the coupled simulations feature a 1 in. wide compliant panel that does not fit in the PnG2 domain. To allow for the increased spanwise domain while keeping the simulation size manageable, the Reynolds number was dropped by a factor of four; the impact of this changes is given in Section 9.1.4. Furthermore, the coupled simulations are run on two different grids to test the solution dependence on the streamwise domain length. The two domains differ in that one has twice the streamwise extent of the other. They are referred to as the long and short domains with their dimensions given in Tab. 8.4. The resolution of the two domains is the same. Due to the periodicity of the domains, the simulation can be visualized as an array of panels. The domains and corresponding domain arrays for the long and short domains are shown in Fig. 8.3 and Fig. 8.4, respectively.

Table 8.4: Long and short domains for the coupled simulation. The viscous-length normalized values are valid at the time of comparison with the reference solution (Section 9.1.4).

Domain	Total Points	$N_x \times N_y \times N_z$	$L_x \times L_y \times L_z$ mm×mm×mm	$\Delta x^+ \times \Delta y^+_{wall} \times \Delta z^+$
Long	24,107,580	$477 \times 140 \times 361$	$142.800 \times 12.700 \times 25.400$	$36.32 \times 0.79 \times 8.57$
Short	12,079,060	$239 \times 140 \times 361$	$71.400 \times 12.700 \times 25.400$	$36.32 \times 0.79 \times 8.57$

Apart from the domain lengths, the fluid simulations run in the two domains differ in one important way: the compliant panel is “inserted” under boundary layers at different stages. In the long domain, the panel is compliant from time $t = 0$, under a laminar boundary layer entering the transitional stage. In the short domain, the panel is made compliant after the boundary layer has become fully turbulent.

Table 8.5: Dimensions in the panel and number of quadratic elements in the discretization.

# Elements	$N_x \times N_y \times N_z$	$L_x \times \tau \times L_z$ mm×μm×mm	E Pa	ρ kg/m^3	ν
30,600	$85 \times 2 \times 180$	$51.000 \times 15.000 \times 25.400$	200×10^9	8000	0.27

Table 8.6: First 9 modes of a 50.1 mm × 25.4 mm clamped panel with 15 μm thickness and material properties comparable to steel ($E = 200 \times 10^9$ Pa, $\rho = 8000$ kg/m^3, and $\nu = 0.27$).

Mode	(1,1)	(2,1)	(3,1)	(4,1)	(1,2)	(2,2)	(3,2)	(5,1)	(4,2)
Frequency (Hz)	136.6	176.7	248.3	351.1	355.8	395.7	462.8	483.4	559.7
Period (ms)	7.32	5.66	4.03	2.84	2.81	2.52	2.16	2.06	1.78

8.2.2 Solid domain

The fluid simulation is coupled with a structurally compliant, 50.1 mm (~ 2 in.) × 25.4 mm (1 in.) panel a thickness of $\tau = 15$ mm and with clamped boundary conditions (Fig. 8.5). The panel is clamped at the streamwise and spanwise boundaries while the top of the panel is loaded by the fluid tractions. The back of the panel is subject to a pressure equal to the time-varying mean pressure on top of the panel. The thickness and material properties are selected to produce a panel that will be excited by the energy containing eddies of the TBL. The panel dimensions, discretization, and material properties are given in Tab. 8.5. The steel panel with the above dimensions has the natural vibrational frequencies listed in Tab. 8.6. An estimation of the power spectra over the panel based on dynamic pressure, Mach number, and wall temperature ratio is shown in Fig. 8.6. The estimation method is based on the Houbolt algorithm [10] and is described by Blevins et al. [**?**]. It is shown that the panel modes in Tab. 8.6 lie in the low frequency, energy containing range of the spectra.

In the coupled simulations to follow, the panel is discretized with two quadratic elements through the thickness. In an identical simulation with three quadratic elements through the thickness, the maximum panel deflection into and out of the flow, after 78,000 time steps, differed from the baseline case by 0.5% and 1.1%, respectively, indicating that the spatial resolution in the baseline discretization of panel is sufficient. The solid grid resolution is assessed in the streamwise and spanwise directions by comparing the baseline grid with a coarse grid containing half as many elements in the streamwise and spanwise directions, shown in Tab. 8.7. Due to the matching node spatial coupling utilized in this study, streamwise and spanwise discretization of the panel cannot be changed in the coupled simulation and therefore the

Table 8.7: Dimensions in the panel and number of quadratic elements in the discretization.

Grid	# Elements	$N_x \times N_y \times N_z$	$L_x \times \tau \times L_z$ mm×μm×mm
Baseline	30,600	$85 \times 2 \times 180$	$51.000 \times 15.000 \times 25.400$
Coarse	7,740	$43 \times 2 \times 90$	$51.000 \times 15.000 \times 25.400$

coarse grid cannot be used in a coupled simulation with the TBL. The baseline and coarse grids are compared in simulations using third-order piston theory (Appendix B) to model the fluid dynamic loads. The baseline and coarse grid panels are initially excited in the (1,1) panel mode. The evolution of the panel solutions under piston theory loading are compared in Fig. 8.7. The agreement shows that the panel solution is converged on the coarse grid and therefore that the solid discretization used in the following coupled simulations is more than sufficient.

Figures for Chapter 8

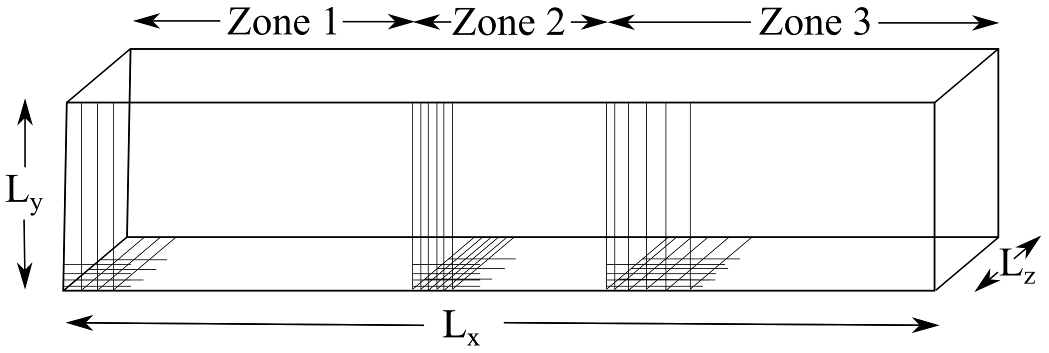

Figure 8.1: Simulation domain from Pirozzoli and Grasso [3]. Domain lengths are $L_x \times L_y \times L_z = 439.420$ mm $\times$ 12.700 mm $\times$ 4.445 mm. Zone lengths 1, 2, and 3 are 76.2 mm, 50.8 mm, and 312.42 mm, respectively.

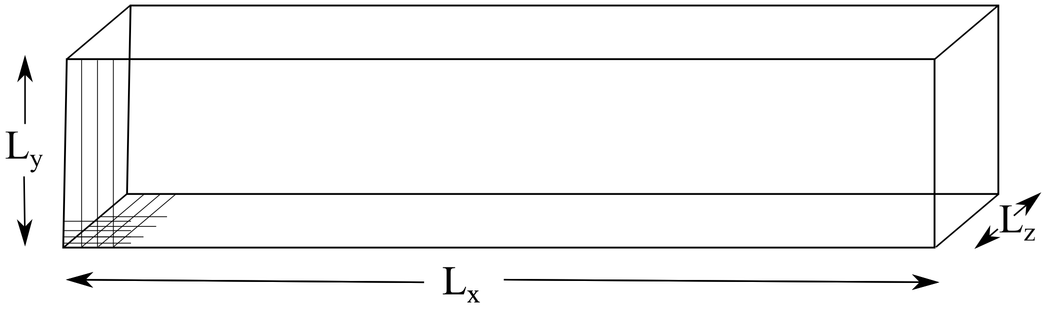

Figure 8.2: Simulation domain of the present work for comparison with Pirozzoli and Grasso [3]. Domain lengths are $L_x \times L_y \times L_z = 142.800$ mm $\times$ 12.700 mm $\times$ 4.445 mm and the grid is uniform in the streamwise and spanwise directions.

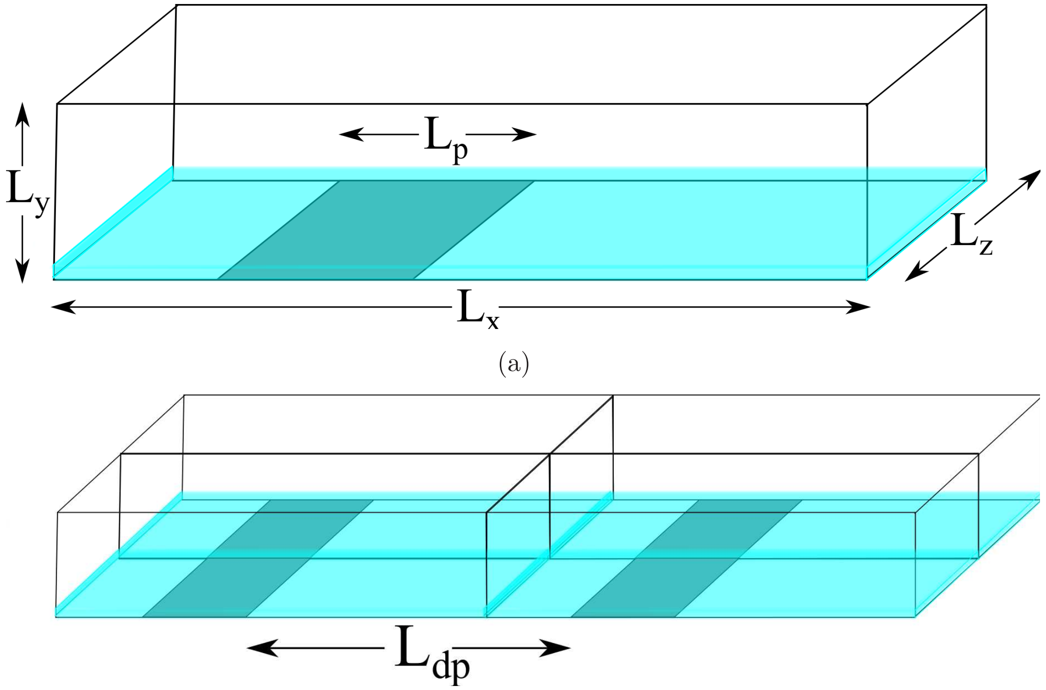

(a)

(b)

Figure 8.3: (a) Long domain for coupled simulation and (b) array of domains. Domain lengths are $L_x \times L_y \times L_z = 142.800$ mm $\times$ 12.700 mm $\times$ 25.400 mm, the panel length is $L_p = 51.000$ mm and the distance between panels is $L_{dp} = 97.200$ mm. The translucent layer represents the TBL and the gray region represents the flexible panel.

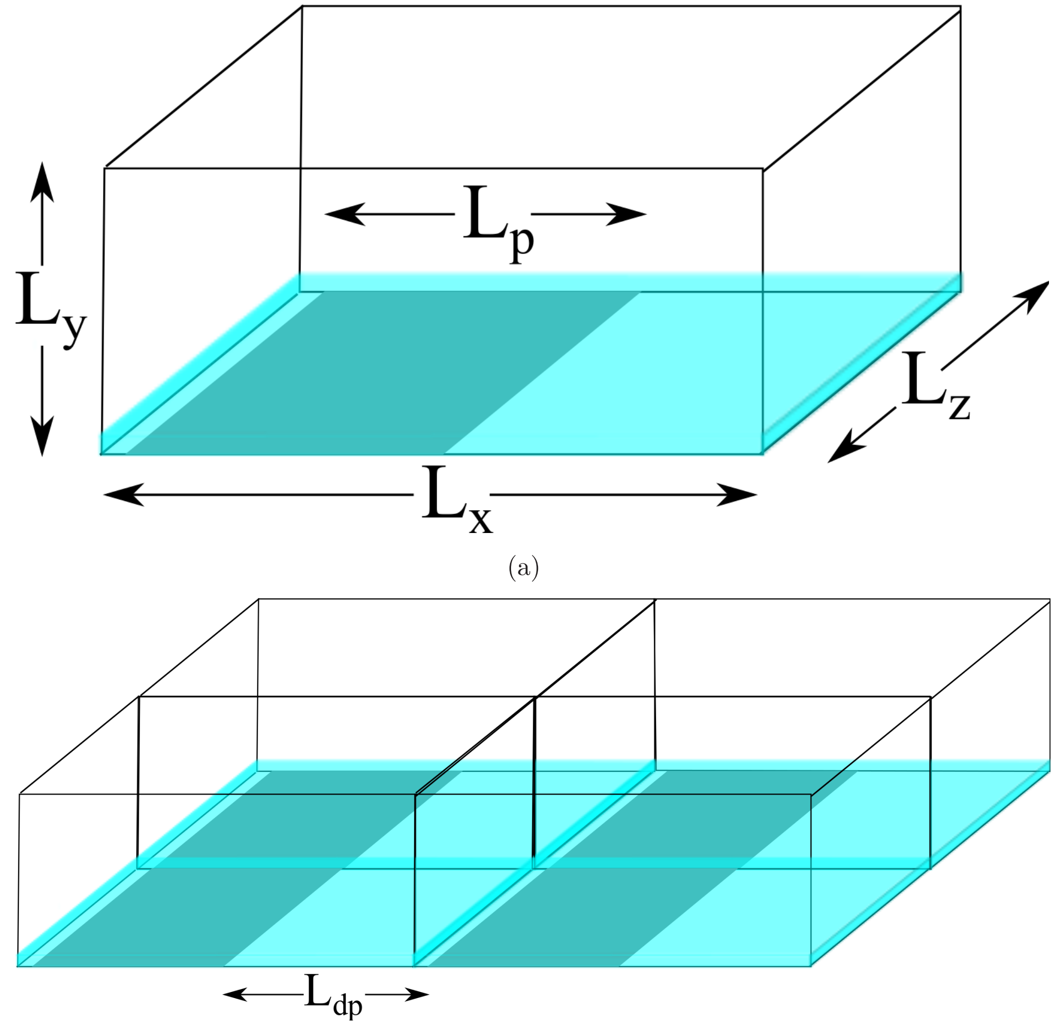

(a)

(b)

Figure 8.4: (a) Short domain for coupled simulation and (b) array of domains. Domain lengths are $L_x \times L_y \times L_z = 71.400$ mm $\times$ 12.700 mm $\times$ 25.400 mm, the panel length is $L_p = 51.000$ mm and the distance between panels is $L_{dp} = 20.400$ mm

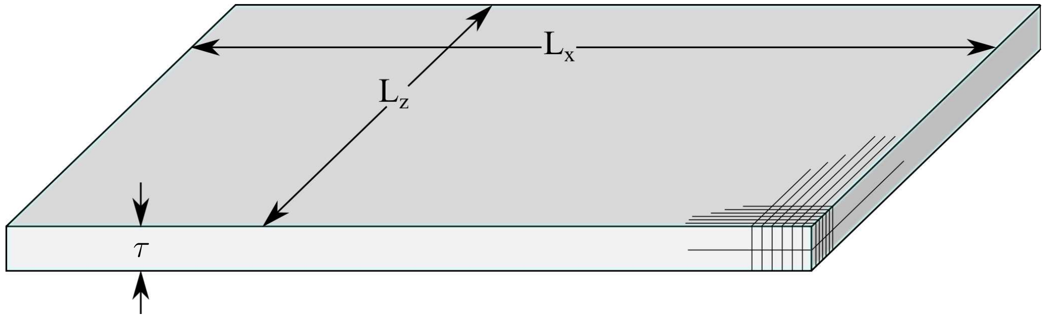

Figure 8.5: Geometry of compliant panel. The back pressure is equal to the mean pressure from the fluid domain. The sides are clamped.

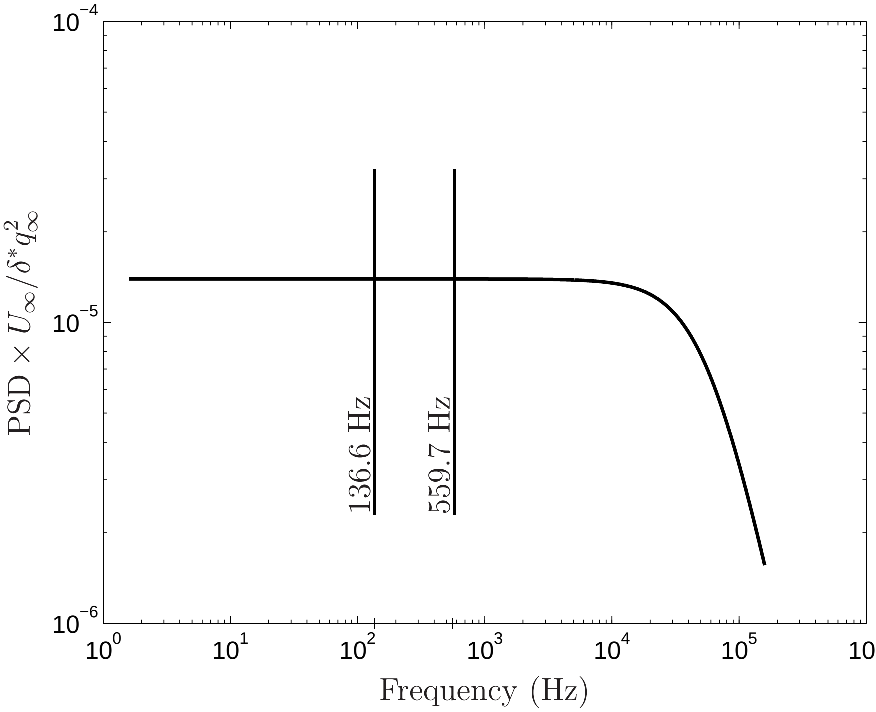

Figure 8.6: Estimate of TBL power spectral density based on dynamic pressure, Mach number, and displacement thickness [10]. The first 9 plate modes in Tab. 8.6 lie within the energy containing frequencies.

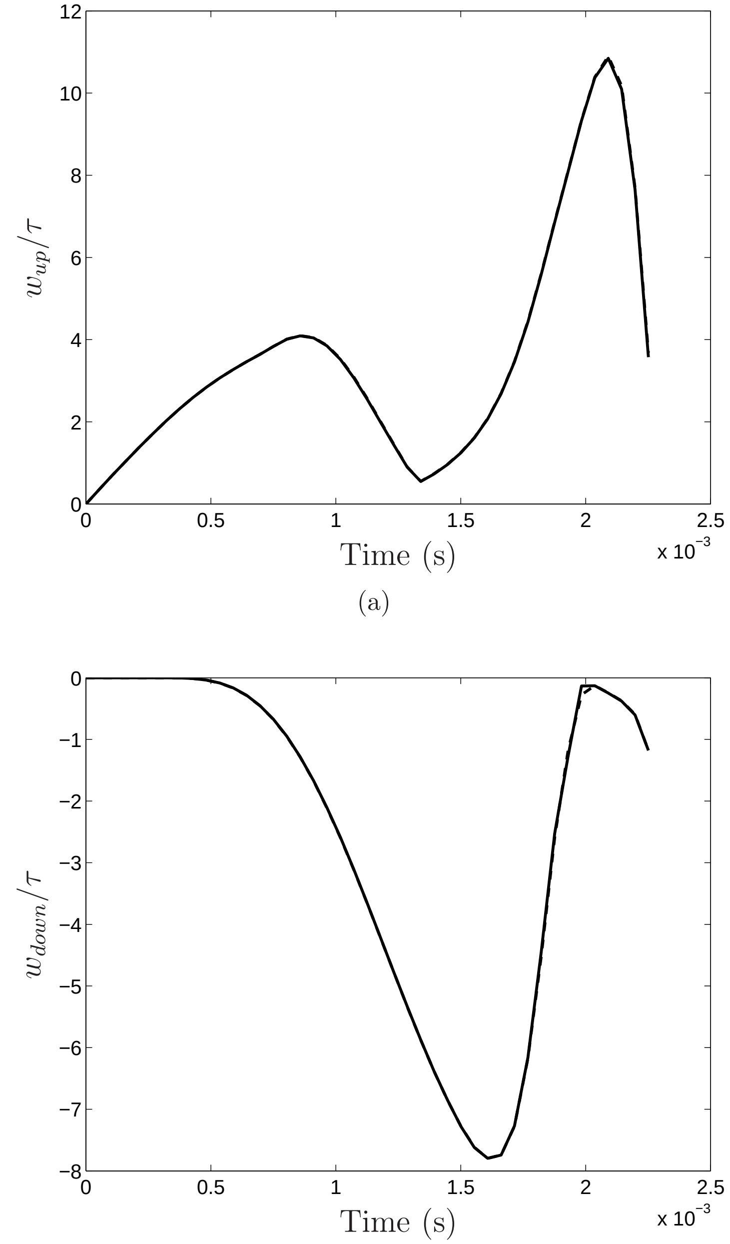

(a)

(b)

Figure 8.7: Maximum panel deflection with time into (a) and out of (b) the flow using the baseline solid grid (solid), and the coarse solid grid (dashed). The baseline and coarse grids are discretized by $N_x \times N_y \times N_z = 85 \times 2 \times 180 = 30,600$ and $N_x \times N_y \times N_z = 43 \times 2 \times 90 = 7,740$ quadratic elements, respectively.

Chapter 9

TDNS of a Turbulent Boundary Layer

9.1 Turbulent boundary layer generation

For the simulation of a turbulent boundary layer over a compliant panel, an initial condition must be chosen such that turbulence will be achieved. To accomplish this, several methods have been used in the past such as using a periodic blowing/suction strip to create instabilities [3, 17] and using a synthetic boundary layer prescribed at the inflow [91]. The approach chosen in this work is to find the temporally unstable eigenmodes to the linear stability equations for a compressible boundary layer [4].

9.1.1 Boundary layer stability

A system's stability is defined as its ability to wisthand a disturbance and return to its original state. A classical example is given in Fig. 9.1, where in Fig. 9.1(a), the ball will remain in the same state when perturbed and is therefore in a stable state. In contrast, Fig. 9.1(b) shows a ball, whose state will change when subjected to a disturbance, and is therefore in an unstable state. When discussing the boundary layer that develops between a moving fluid and a rigid surface, stability refers to the boundary layer's tendency to remain in a laminar state. A boundary layer may experience many kinds of disturbances (acoustic waves, surface roughness, thermal pulses, etc.) and remain laminar, in which case it is stable with respect to those disturbances. If the boundary layer is unstable with respect to one of the disturbances, then the disturbance will grow and may lead to transition of the boundary layer from its laminar state to a turbulent state.

Linear stability theory

The investigation of fluid flow stability is accomplished by decomposing each flow variable into mean and fluctuating parts,

$$\phi(x, y, z, t) = \bar{\phi}(x, y, z) + \hat{\phi}(x, y, z, t), \tag{9.1}$$

where ϕ is a flow variable (e.g. density, ρ, velocity, $\boldsymbol{u}$, etc.) and $\bar{(\ )}$ and $\hat{(\ )}$ specify the mean and fluctuating parts, respectively. Expressing the Navier-Stokes equations in terms of variables as in Eq. (9.1) and then subtracting the mean (which identically satisfies the Navier-Stokes equations), results in equations for the disturbances, $\hat{\phi}$. Additionally, if disturbances are assumed to be infinitesimal so that quadratic and higher terms can be neglected, the linearized disturbance equations result. In the case of a flat plate boundary layer, it is reasonable to make the parallel flow assumption, ($\bar{u} = \bar{u}(y)$, $\bar{w} = \bar{w}(y)$, and $\bar{v} \approx 0$), which reduces the complexity of the problem. Also assuming a 2D mean flow, $\bar{w} = 0$, the disturbance equations become

$$
\begin{aligned}
\left(\frac{\partial \hat{u}}{\partial t} + \bar{u}\frac{\partial \hat{u}}{\partial x} + \hat{v}\frac{\partial \bar{u}}{\partial y}\right)\frac{1}{\bar{T}} =& -\frac{\partial \hat{p}}{\partial x} + \frac{\bar{\mu}}{R}\left[l_2\frac{\partial^2 \hat{u}}{\partial x^2} + l_1\left(\frac{\partial^2 \hat{v}}{\partial x \partial y} + \frac{\partial^2 \hat{w}}{\partial x \partial z}\right)\right. \\
&+\frac{\partial^2 \hat{u}}{\partial y^2} + \frac{\partial^2 \hat{u}}{\partial z^2} + \frac{1}{\bar{\mu}}\frac{d\bar{\mu}}{d\bar{T}}\frac{d\bar{T}}{dy}\left(\frac{\partial \hat{u}}{\partial y} + \frac{\partial \hat{v}}{\partial x}\right) \\
&\left.+\frac{1}{\bar{\mu}}\frac{d\bar{\mu}}{d\bar{T}}\left(\frac{d^2\bar{u}}{dy^2}\hat{T} + \frac{d\bar{u}}{dy}\frac{\partial \hat{T}}{\partial y}\right) + \frac{1}{\mu}\frac{d^2\mu}{d\bar{T}^2}\frac{dT}{dy}\frac{d\bar{u}}{dy}\hat{T}\right] \\
\left(\frac{\partial \hat{v}}{\partial t} + \bar{u}\frac{\partial \hat{v}}{\partial x}\right)\frac{1}{\bar{T}} =& -\frac{\partial \hat{p}}{\partial y} + \frac{\bar{\mu}}{R}\left[\frac{\partial^2 \hat{v}}{\partial x^2} + l_1\left(\frac{\partial^2 \hat{u}}{\partial x \partial y} + \frac{\partial^2 \hat{w}}{\partial x \partial z}\right)\right. \\
&+l_2\frac{\partial \hat{v}}{\partial y} + \frac{\partial^2 \hat{v}}{\partial z^2} + \frac{1}{\bar{\mu}}\frac{d\bar{\mu}}{d\bar{T}}\frac{\partial \hat{T}}{\partial x}\frac{d\bar{u}}{dy} \\
&\left.+\frac{1}{\bar{\mu}}\frac{d\bar{\mu}}{d\bar{T}}\frac{d\bar{T}}{dy}\left\{l_0\left(\frac{\partial \hat{u}}{\partial x} + \frac{\partial \hat{w}}{\partial z}\right) + l_2\frac{\partial \hat{v}}{\partial y}\right\}\right] \\
\left(\frac{\partial \hat{w}}{\partial t} + \bar{u}\frac{\partial \hat{w}}{\partial x}\right)\frac{1}{\bar{T}} =& -\frac{\partial \hat{p}}{\partial z} + \frac{\bar{\mu}}{R}\left[\frac{\partial^2 \hat{w}}{\partial x^2} + l_1\left(\frac{\partial^2 \hat{u}}{\partial x \partial z} + \frac{\partial^2 \hat{v}}{\partial y \partial z}\right)\right. \\
&\left.+\frac{\partial^2 \hat{w}}{\partial y^2} + l_2\frac{\partial^2 \hat{w}}{\partial z^2} + \frac{1}{\bar{\mu}}\frac{d\bar{\mu}}{d\bar{T}}\frac{d\bar{T}}{dy}\left(\frac{\partial \hat{v}}{\partial z} + \frac{\partial \hat{w}}{\partial y}\right)\right] \\
\frac{\gamma M^2}{\bar{T}}\frac{\partial \hat{p}}{\partial t} - \frac{1}{\bar{T}^2}\frac{d\hat{T}}{dt} + \frac{1}{\bar{T}}\frac{\partial \hat{u}}{\partial x} &+ \bar{u}\left(\frac{\gamma M^2}{\bar{T}}\frac{\partial \hat{p}}{\partial x} - \frac{1}{\hat{T}^2}\frac{\partial \hat{T}}{\partial x}\right) + \frac{1}{\bar{T}}\frac{\partial \hat{v}}{\partial y} \qquad (9.2) \\
&- \frac{1}{\bar{T}^2}\frac{d\bar{T}}{dy}\hat{v} + \frac{1}{T}\frac{\partial \hat{w}}{\partial z} \\
\left(\frac{\partial \hat{T}}{\partial t} + \bar{u}\frac{\partial \hat{T}}{\partial x} + \hat{v}\frac{\partial \bar{T}}{\partial y}\right)\frac{1}{\bar{T}} =&(\gamma - 1)M^2\left[\frac{\partial \hat{p}}{\partial t} + \bar{u}\frac{\partial \hat{p}}{\partial x}\right] + \frac{\bar{\mu}}{R\mathrm{Pr}}\left[\frac{\partial^2 \hat{T}}{\partial x^2} + \frac{\partial^2 \hat{T}}{\partial y^2}\right. \\
&\left.+\frac{\partial^2 \hat{T}}{\partial z^2} + \frac{2}{\bar{k}}\frac{d\bar{k}}{d\bar{T}}\frac{d\bar{T}}{dy} + \left(\frac{1}{\bar{k}}\frac{d\bar{k}}{d\bar{T}}\frac{d^2\bar{T}}{dy^2} + \frac{1}{\bar{k}}\frac{d^2\bar{k}}{dT^2}\left(\frac{d\bar{T}}{dy}\right)^2\right)\hat{T}\right] \\
&+ (\gamma - 1)M^2\frac{\bar{\mu}}{R}\left[2\frac{d\bar{u}}{dy}\left(\frac{\partial \hat{u}}{\partial y} + \frac{\partial \hat{v}}{\partial x}\right) + \frac{1}{\bar{\mu}}\frac{d\bar{\mu}}{d\hat{T}}\left(\frac{d\bar{u}}{dy}\right)^2\right],
\end{aligned}
$$

where all variables are non-dimensionalized by their freestream values (Ex. $u = \tilde{u}/\tilde{U}_\infty$, $T = \tilde{T}/\tilde{T}_\infty$, etc.; tilde denotes dimensional quantities), M, μ, R, k, C_p, and $\mathrm{Pr} = \mu C_p/k$ are the Mach number, viscosity, specific gas constant, thermal conductivity, specific heat at constant pressure, and the Prandtl number, respectively. Also, the short hand notation, $l_i = i + \lambda/\mu$, where λ is the bulk viscosity, is used. A useful consequence of the parallel flow assumption is that the flow is homogenous in x and z. The flow variables can therefore be decomposed into their modal components which are inhomogeneous only in y

$$\hat{\phi} = \phi'(y) \exp[i(\alpha x + \beta z - \omega t)], \tag{9.3}$$

where $i = \sqrt{-1}$, and $\phi'(y)$ is a mode shape for a given combination of streamwise and spanwise wavenumbers (α and β, respectively), and mode frequency, ω. In this work, we are concerned with disturbances that grow in time, or temporally unstable disturbances that occur when ω has a positive imaginary part, $\Im[\omega] > 0$. Only streamwise and spanwise periodic flows are considered, and therefore only real α and β are explored. Substituting Eq. (9.3) into Eq. (9.2) yields a five-equation eigenvalue problem, the solutions of which are the eigenfunctions ($\phi'(y)$ profiles) which either decay ($\Im[\omega] < 0$) or grow ($\Im[\omega] > 0$) in time. Given a base flow of a Blasius boundary layer (Appendix E), the developed linear stability theory (LST) solver finds the solutions to Eq. (9.2).

Verification of the compressible LST solver

To thoroughly verify the compressible LST solver described above, the three different approaches were taken. The first verification exercise involved the comparison of the results of the compressible solver with an incompressible formulation. Second, results from the solver were compared with results from the literature [4]. Third, growth rates from the linear stability solver are compared with DNS results.

Comparison with Incompressible LST Generally, flows less than Mach 0.3 are considered incompressible, where the dilatation is assumed to be negligible, $\nabla \cdot \boldsymbol{u} \approx 0$, and the density, ρ, is constant. In these flows the viscosity, μ, is commonly assumed to be constant. The consequence of this is that the continuity and momentum equations are decoupled from the energy equation, and can be solved independently of the thermal state of the fluid. Furthermore, in the incompressible regime, Squire's theorem [95] states (Taken from [11]):

> “For a two-dimensional parallel flow $\bar{u}(y)$, the minimum critical unstable Reynolds number occurs for a two-dimensional disturbance propagating in the same direction ($\beta = 0$),"

which asserts that only streamwise disturbances ($\beta = 0$) need be considered when investigating the stability limits of incompressible flows. The above simplifications significantly reduce the complexity of the problem, reducing the above mentioned eigenvalue problem to a single equation named the Orr-Sommerfeld equation [11]

$$(\bar{u}-c)\left(\frac{d^2\hat{v}}{dy^2} - \alpha_{\delta^*}^2\hat{v}\right) - \frac{d^2\bar{u}}{dy^2}\hat{v} + \frac{i}{\alpha_{\delta^*}Re_{\delta^*}}\left(\frac{d^4\hat{v}}{dy^4} - 2\alpha_{\delta^*}^2\frac{d^2\hat{v}}{dy^2} + \alpha_{\delta^*}^4\hat{v}\right) = 0, \quad (9.4)$$

where $\alpha_{\delta^*} = \tilde{\alpha}\tilde{\delta}^*$ is the streamwise wavenumber non-dimensionalized by the displacement thickness δ^*, $c = \alpha/\omega$ is the phase speed, and $Re_{\tilde{\delta}^*} = \tilde{U}_e\tilde{\delta}^*/\tilde{\nu}$ is the displacement thickness Reynolds number. In the temporal problem, complex eigenvalues, $c = c_r + ic_i$, are found where $\Im(c) > 0$ are indicative of an unstable mode. Solutions to Eq. (9.4) have been extensively studied since 1929 [96], as the majority of technologically relevant flows have historically been in the low-speed regime.

The compressible LST equations are valid in both the compressible and incompressible regimes, and therefore the solution to Eq. (9.2) is required to match the solution obtained by Eq. (9.4) in the incompressible regime. Solutions to either of the equations are used to produce a neutral stability curve, which, in the temporal stability case, outlines the region in $Re - \alpha$ space in which disturbances are predicted to grow. The neutral stability curve for a Mach 0.005 BL is calculated with the compressible LST solver and compared with White [11] in Fig. 9.2.

The neutral stability curve requires only the accurate calculation of the eigenvalues of the LST equations. To verify the eigenfunctions calculated by the compressible LST solver in the incompressible regime, Eq. (9.4) is solved and the eigenfunctions are compared between the solutions from the two solvers. The solution to Eq. (9.4) is obtained by the compound matrix method which is discussed in detail by Ng & Reid [97, 98]. The streamwise and pressure perturbations are calculated from the transverse velocity perturbation solutions of Eq. (9.4) as

$$\hat{u} = -\frac{\hat{v}}{i\alpha}$$

and

$$\hat{p} = \left[\left(\frac{d^2 \hat{u}}{dy^2} - \alpha^2 \hat{u} - i\alpha Re(\bar{u} - c)\hat{u} \right) - Re \frac{d\bar{u}}{dy} \hat{v} \right] \frac{1}{i\alpha Re}.$$

A Blasius boundary layer is calculated for the same Mach 0.005 flow as studied in Fig. 9.2. The eigenmodes at the displacement thickness Reynolds number of $Re_{\delta^*} = 700$ and wavenumber $\alpha\delta^* = 0.25$ (predicted to be unstable as shown in Fig. 9.2) are calculated independently in both the compressible LST solver and the Orr-Sommerfeld solver. The eigenvalues found by the the compressible LST and Orr-Sommerfeld solvers converged to $c = \omega/\alpha = 0.3670 + 5.14 \times 10^{-3} i$. The eigenfunctions, shown in Fig. 9.3, indicate that the two solvers are in good agreement, and verify that the formulation of the compressible LST solver is valid in incompressible flow.

Comparison with Literature In order to assess the performance of the LST solver in the compressible regime, results from the LST solver are also compared with the results from Malik [4] in several flow speed regimes. All comparisons are made with the most accurate results from Malik's 2nd order finite difference solver. Comparisons of predictions of temporal eigenvalues are given in Tab. 9.1. In all cases, $T_w/T_{adb} = 1.0$. It was assumed that $T_{adb}/T_\infty = 1 + (\gamma - 1)/2 \cdot rM^2$, where the recovery factor, r, is defined as $r = Pr^{1/3}$.

M_∞	Re_l	α	β	δ^*/l	(c_r, c_i)	$(c_r, c_i)_{Malik}$
Incompresible $(M_{Malik} = 10^{-6})$ $(M = .005)$	580	0.179	0.0	1.7208	(0.3622, 0.0080) (0.4777, -0.1885) (0.2855, -0.2748)	(0.3641, 0.0079) (0.4839, -0.1921) (0.2897, -0.2768)
					(ω_r, ω_i)	$(\omega_r, \omega_i)_{Malik}$
$M = 0.5$	2000	0.1	0.0	1.8236	(0.0288, 0.0023)	(0.0291, 0.0022)
$M = 2.5$	3000	0.06	0.1	4.2578	(0.0365, 5.745×10^{-4})	(0.0368, 5.733×10^{-4})
$M = 10.0$	1000	0.12	0.0	31.674	(0.1156, 4.704×10^{-4})	(0.1159, 3.251×10^{-4})

Table 9.1: Comparison of temporal eigenvalues with those given by Malik [4]. α and β non-dimensionalized by $1/l$ and ω is non-dimensionalized by u_∞/l as done by Malik [4]. $c = \omega/\alpha$ is the phase velocity.

The comparison generally shows good agreement. However, the Mach 10 case shows a larger difference. At this Mach number, the boundary layer state is influenced by the high temperatures that are present. The eigenvalue is sensitive to the plate temperature as well as the viscous model used. All results presented in Tab. 9.1 use the Sutherland's law viscous model,

$$\mu = 1.0869 \times 10^{-6} \frac{(1.8T)^{3/2}}{1.8T + 198.6} \frac{kg}{m \cdot s},$$

which is the model also used by Malik [4]. The sensitivity of the calculation in the high Mach number case is demonstrated by the difference resulting from the use of the power law viscous model,

$$\frac{\mu}{\mu_\infty} = \left(\frac{T}{T_\infty}\right)^{.666},$$

which yielded the result, $\omega = 0.1156 + 3.044 \times 10^{-4} i$. Comparisons with Malik [4] of the eigenfunctions for the incompressible and Mach 10.0 cases are given in Fig. 9.4(a) and (b) and Fig. 9.5, respectively. Figure 9.4(a) shows the first mode eigenfunctions for the streamwise and wall normal velocity perturbations. These perturbations are temporally unstable with a corresponding eigenvalue of $\omega = 0.3622 + 0.0080i$.

Comparison with DNS Results The solutions satisfying the linearized Navier-Stokes equations should, while perturbations remain sufficiently small, agree with solutions to the full, non-linear Navier-Stokes equations. Any single unstable eigenfunction to Eq. (9.2), when added to the laminar base flow and integrated through time according to the Navier-Stokes equations, is expected to grow at the rate indicated by $\Im[\omega]$ as the flow is advanced in time. However, this expectation is dependent on two assumptions: (1) that the perturbation, while growing, will remain small enough in amplitude that non-linear effects are negligible and (2) that the base flow is a solution to the Navier-Stokes equations. While the parallel flow assumption ($\bar{u} = \bar{u}(y)$, $\bar{w} = \bar{w}(y)$, and $\bar{v} \approx 0$) allows for several useful simplifications in the above derivations, it results in a base flow that does not satisfy the Navier-Stokes equations.

The eigenfunctions found by the LST solver are computed on a parallel base flow and the eigenfunction growth is affected by the temporal evolu-

M_∞	(ω_r, ω_i)
$M = 0.05$	$(3.299 \times 10^{-3}, 2.070 \times 10^{-4})$
$M = 5.8$	$(0.1159, 3.251 \times 10^{-4})$

Table 9.2: LST growth rate predictions for comparison with DNS. In both cases, the displacement thickness Reynolds number, $Re_{\delta^*} = 2000$. α and β, non-dimensionalized by δ^*, are 0.25 and 0.0, respectively. ω is non-dimensionalized by a_∞/δ^*, where a_∞ is the freestream speed of sound.

tion of the base flow to satisfy the Navier-Stokes equations. The growth rates are studied in low (Mach 0.05) and high-speed (Mach 5.8) cases, and the severity of the effect of the base flow adjustment on the growth rate is seen to increase with Mach number. Both cases are run at the boundary layer displacement thickness Reynolds number, $Re_{\delta^*} = 2000$, and are seeded with a single Tollmien-Schlicting (TS) wave with streamwise wavenumber, $\alpha = L_x/2\pi$ so that L_x, streamwise dimension of the domain, is equal to one wavelength, and periodic boundaries can be used. The LST predictions are given in Tab. 9.2, where the imaginary parts, ω_i, are the predicted growth rates. The growth of the perturbations in the DNS are tracked by selecting the Fourier amplitude of the perturbations at a given wall normal coordinate,

$$|F(\alpha_1, y)| = \left| \frac{2}{L_x} \int_0^{L_x} f(x, y) e^{-i\alpha_1 x} dx \right|. \tag{9.5}$$

Results for the Mach 0.05 case are presented from from locations inside ($y = 0.53\delta^*$) and outside ($y = 12.2\delta^*$) the boundary layer in Fig. 9.6 and Fig. 9.7, respectively. In the Mach 5.8 case, the base flow adjustment is large enough that the growth of the eigenfunctions is severely altered. The adjusted base flow may not be unstable with respect to the previously found eigenfunctions. To combat this effect, the wall normal diffusion of streamwise momentum and energy are removed by adding the source terms shown in Eq. (9.6) to the right hand side of the compressible Navier-Stokes equations [99],

$$\boldsymbol{S} = \begin{pmatrix} 0 \\ -\dfrac{\partial}{\partial y}\dfrac{\bar{\mu}}{Re}\dfrac{\partial \bar{u}}{\partial y} \\ 0 \\ 0 \\ -\dfrac{\partial}{\partial y}\dfrac{\bar{\mu}}{Re}\bar{u}\dfrac{\partial \bar{u}}{\partial y} - \dfrac{\partial}{\partial y}\dfrac{\bar{\mu}}{RePr}\dfrac{\partial \bar{T}}{\partial y} \end{pmatrix}. \tag{9.6}$$

This modification suppresses the growth of the velocity and thermal boundary layers and, therefore, the adjustment from the mismatch in the mean initial condition and governing equations. Figure 9.8 exhibits the suppression of the boundary layer adjustment by the use of Eq. (9.6). Negative effects associated with the application of Eq. (9.6) require that it be removed after the transition period. Such effects are shown in Appendix F.

9.1.2 Transition to turbulence

The unstable eigenvalues found following the procedure in Section 9.1.1, when superposed onto a laminar boundary layer solution, grow in time. An example mean profile and corresponding unstable perturbations to the primative variables are shown in Fig. 9.9.

The transition to turbulence from the seeded laminar flow is composed of several stages. Though the specific path is dependent on the initial disturbances, boundary layer transition generally involves the amplification of disturbances to a saturation point, followed by a break down process. For example, in the case of the simulation for comparison with Pirozzoli and Grasso, the transition process is shown in Fig. 9.10(a)-(c). The 3D boundary layer, initially very similar to a 2D flow, begins to develop noticeable spanwise variations, which, in this example, organize into Λ waves, as can be seen in Fig. 9.10(a). After a period of amplification, the disturbances break down into smaller spatial and temporal scales, forming turbulent spots (Fig. 9.10(b)). The initially sporadic spots of turbulence continue to spread and eventually coalesce, finally resulting in a fully turbulent boundary layer flow (Fig. 9.10(c)).

9.1.3 Grid assessment

Having generated the TBL, the suitability of the chosen grid dimensions and grid point densities are assessed.

Domain length and width

The use of periodicity requires that the grid be sufficiently large in the homogeneous directions that the turbulent flow is decorrelated over half the length of that dimension. If the flow is not sufficiently decorrelated, the dynamics of the TBL are affected. To determine the correlation distance, 1D two-point autocorrelations are performed on all variables in the periodic (streamwise and spanwise) directions, were the discrete two-point correlation is defined as

$$R_{uu}(i) = \frac{\sum_{j}^{N_{perp.}-1} \sum_{l}^{N-1} (u(l,j)u(l+i,j))}{(N_{perp.}-1)(N-1)}, \tag{9.7}$$

where N is the number of points in the direction in which the autocorrelation is taken and $N_{perp.}$ is the number of points in the perpendicular periodic direction, resulting in the average two-point autocorrelation over the domain.

Figure 9.11 and Fig. 9.12 show the 1D correlations in the streamwise and spanwise directions, respectively. For each, the correlation is shown at three different wall normal locations: $y^+ = 2.1$, $y^+ = 73.9$, and $y^+ = 151.3$, corresponding to the viscous sublayer, the log-law layer, and the outer layer, respectively. All flow variables appear to be decorrelated in the distance $r_z/\delta^{99} = 3$ in both directions. The streamwise length of the domain is $L_x \delta^{99} = 64.6$, so all variables are easily decorrelated over half the length of the domain. The spanwise length of the domain is $L_z \delta^{99} = 11.5$, so Fig. 9.12 confirms that the flow is decorrelated over the width of the domain.

Energy spectra

The 1D energy spectra give a measure of how well the turbulent structures are resolved on the current grid. As famously proposed by Richardson [100], kinetic energy enters the boundary layer from the freestream into the largest turbulent scales. That energy is then transferred through a cascade of smaller scales until it reaches the smallest (Kolmogorov) scale, at which point it is dissipated by viscosity, resulting in the production of thermal energy. The grid should be fine enough to resolve the smallest scales and represent the energy cascade in the TBL. The energy spectrum function, $E(\kappa)$ is calculated by twice the Fourier transform of the two-point correlation (Eq. (9.7))

$$E_{uu}(\kappa) = \frac{2}{N-1}\sum_{i}^{N-1} R_{uu}(i)e^{-i\kappa r_i}, \tag{9.8}$$

where,

$$r_i = \frac{(i-1)L}{N-1}.$$

Figure 9.13 and Fig. 9.14 show the 1D energy spectra in the streamwise and spanwise directions, respectively. As in the case of the two-point autocorrelations, the spectra are shown at three different wall normal locations: $y^+ = 2.1$, $y^+ = 73.9$, and $y^+ = 151.3$. In addition, the wavenumber range below the cutoff frequency of the implicit filter (shown in Fig. 7.2) are demarcated by vertical dashed lines. In Fig. 9.13 all spectra drop between 3 and 4 decades from their peak values, the exception being the pressure fluctuations in the log-law layer. In Fig. 9.14 all spectra again drop between 3 and 4 decades from their peak values. The pressure fluctuations exhibit a small turn-up at the highest wavenumbers, indicating a small aliasing error.

Kolmogorov's first similarity hypothesis states that in locally isotropic flow, which exists on the small length scales in the universal equilibrium range of a TBL, velocity statistics have a universal form which is solely dependent on the dissipation, ϵ, and kinematic viscosity, ν. Considering the first similarity hypothesis, dimensional analysis gives $E(\kappa)$ as

$$E(\kappa) = \epsilon^{2/3}\kappa^{-5/3}\Psi(\kappa\eta), \tag{9.9}$$

where the $\eta = (\nu^3/\epsilon)^{1/4}$ is the Kolmogorov length scale and Ψ is a the non-dimensional compensated Kolmogorov spectrum function. According to the second similarity hypothesis, in the inertial subrange velocity statistics are only dependent on ϵ, and are independent of ν, requiring $\Psi = C$, where C is constant. In the inertial subrange, Eq. (9.9) then becomes

$$E(\kappa) = C\epsilon^{2/3}\kappa^{-5/3},$$

giving rise to the Kolmogorov -5/3 spectrum. A dashed line with $-5/3$ slope is shown in Fig. 9.13(b)-(c) and Fig. 9.14(b)-(c), where the data is taken from the log-law and outer layers and are independent of viscosity. While the Reynolds number is relatively low, the energy spectra in Fig. 9.13 verify that the TBL is healthy.

Turbulent boundary layer grid convergence

To ensure grid independence of the Mach 2.25 turbulent boundary layer, a grid convergence study was done. The study involved three grids: a baseline grid whose grid point spacing was equal to that shown in Fig. 9.17(a), a grid in which the number of points were doubled in the x and z directions, and one in which the number of points were doubled in the y direction. The details are given in Tab. 9.3. A comparison of the mean velocity profiles (Fig. 9.15) confirms that the baseline grid is sufficiently converged and is very well resolved in the wall normal direction.

Table 9.3: Grid data for convergence study. All grids have phsyical lengths $L_x \times L_y \times L_z = 71.4\text{mm} \times 12.7\text{mm} \times 25.4\text{mm}$

Grid	$N_x \times N_y \times N_z$	$\Delta x^+ \times \Delta y^+_{wall} \times \Delta z^+$	δ_ν μm
A (baseline)	$239 \times 140 \times 361$	$33.36 \times 0.72 \times 7.85$	8.992
B	$239 \times 279 \times 361$	$33.42 \times 0.36 \times 7.86$	8.997
C	$477 \times 140 \times 721$	$16.60 \times 0.72 \times 3.93$	9.039

9.1.4 Turbulent boundary layer verification

As the computational cost associated with DNS of a turbulent boundary layer can be staggering (proportional to Re^3 [101]), the Reynolds number of the flow in the coupled simulation is chosen to be relatively low in order to balance the costs between the two solve stages involved in the multiphysics simulation. The boundary layer has a Reynolds number based on momentum thickness of $\text{Re}_\theta = 1196$. A second turbulent boundary layer simulation at a higher Reynolds number, $\text{Re}_\theta \approx 4000$ was also run for the purpose of verification by comparison with previous work. Simulation conditions were chosen to be similar to a reference solution from Pirozzoli & Grasso [3]. One main difference exists between the current work and that of Pirozzoli & Grasso. Their work featured a spatially developing turbulent boundary layer, or SDNS, which requires a domain with a large streamwise extent, and is therefore generally more costly. In an effort to save on the fluid simulation in the current coupled multiphysics simulation, the current work uses a temporal DNS approach (TDNS) to model the fluid solution. This assumes periodicity in the streamwise direction, and results in a boundary layer thickness that increases in time and not space.

The quantities compared were mean profile and normal Reynolds stresses. As can be seen in Fig. 9.16(a), the Van Driest transformed mean velocity profile satisfies $u_c^+ = y^+$ in the viscous sublayer, and obeys the log law, $1/k \log(y^+) + C$, in the log-law region, where $k = 0.41$ and $C = 5.20$. The comparison with the reference solution is also in agreement. Shown in Fig. 9.16(b) are the normalized, normal components of the Reynolds stresses, which are also in agreement with the reference solution.

Also shown are comparisons between the reference solution and the lower Reynolds number solution planned for the coupled simulation. The two solutions are compared at a time during the TDNS when the momentum thicknesses are similar. The momentum thickness at the time corresponding to $Re_\theta = 1196$ is $\theta = 1.88 \times 10^{-4}$ m, compared to the reference solution [3] at the streamwise location where the momentum thickness was $\theta = 1.69 \times 10^{-4}$ m. Figure 9.17(a) shows that the Van Driest scaled mean velocity profile still follows the same trends, obeying $u_c^+ = y^+$ and the log law in the viscous subregion and log-law region, respectively. The effect of the lower Reynolds number produces a shorter boundary layer and a less pronounced wake at the boundary layer edge. The comparison between the normalized, normal components of the Reynolds stresses (Fig. 9.17(b)) shows that the peaks of the respective quantities occur in the same wall normal locations and that the profiles are similar from the wall into the buffer layer ($y^+ < 30$). The differences highlight the Reynolds number dependence of the Reynolds stresses in the outer layer as documented by DeGraaff & Eaton [102], and indicate that, in the higher Reynolds number TBL, the range of length scales extends to larger structures.

Figures for Chapter 9

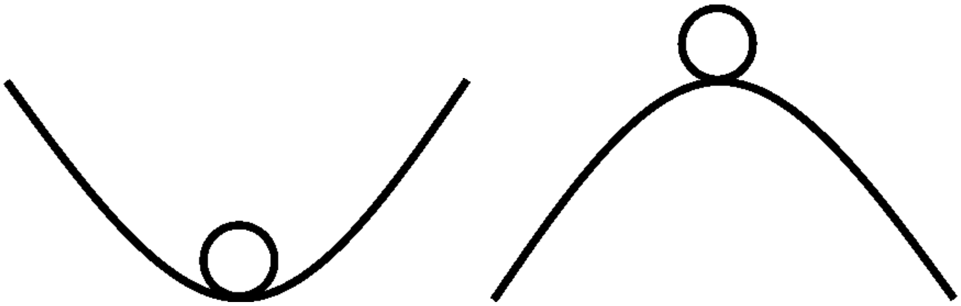

(a)

(b)

Figure 9.1: (a) A ball in stable state, and (b) a ball in an unstable state.

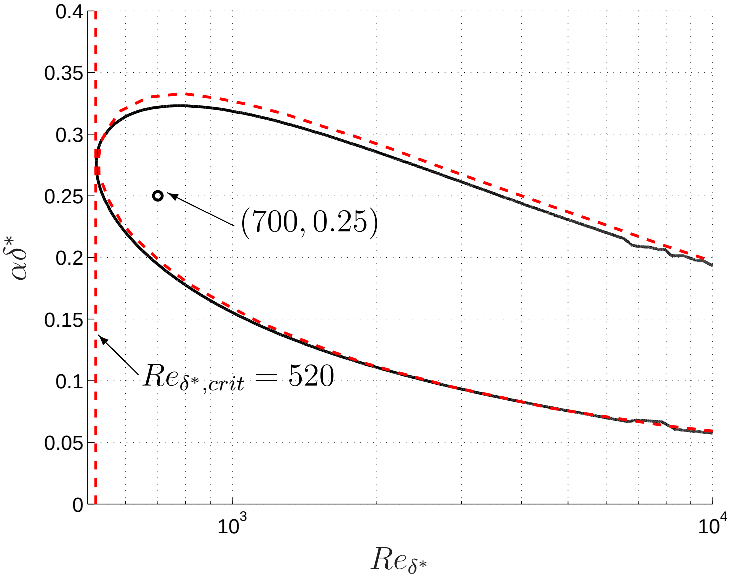

Figure 9.2: Neutral stability "thumb" curve of an incompressible boundary layer created with the compressible linear stability solver (black line) and as published in White [11] (red dashed). The vertical dashed line represents $Re_{\delta^*,crit} = 520$ and the black circle is the $(Re_{\delta^*}, \alpha\delta^*)$ coordinate for the comparison in Fig. 9.3

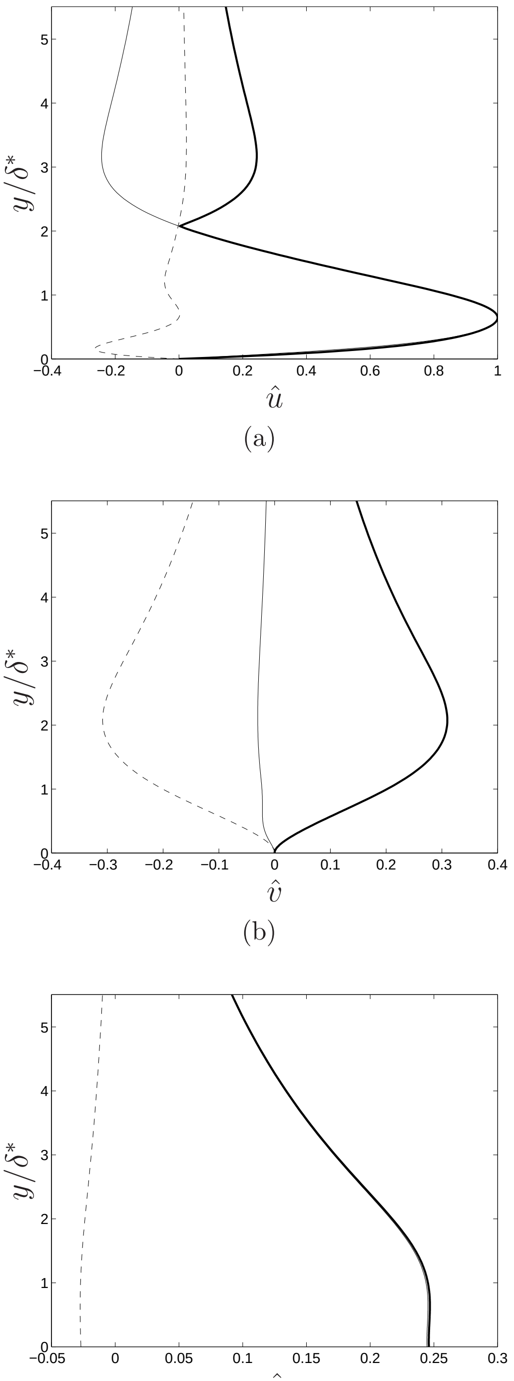

(a)

(b)

(c)

Figure 9.3: Eigenfunctions found by the Orr-Sommerfeld and compressible LST equations for the Mach 0.005 Blasius boundary layer. The real part (solid), imaginary part (dashed), and magnitude (bold) of the (a) streamwise velocity, (b) transverse velocity, and (c) pressure eigenfunctions are shown. The curves lie on top of each other, and therefore only the LST results are shown.

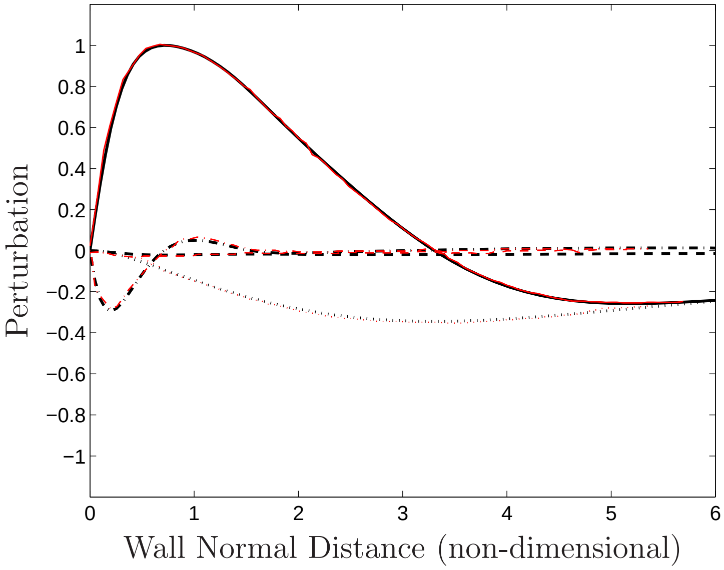

(a)

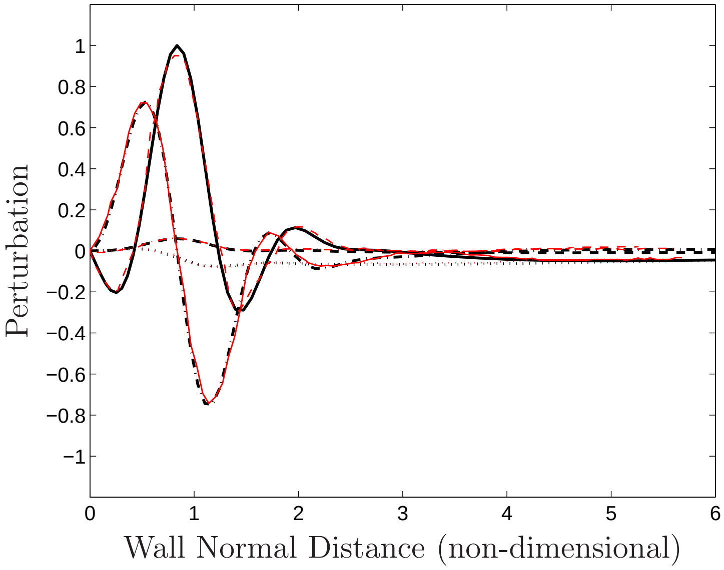

(b)

Figure 9.4: Eigenfunction comparison with Malik [4] for the incompressible $\text{Re}_l = 580$ boundary layer. (a) First mode and (b) third mode. Malik (red), present work (black).

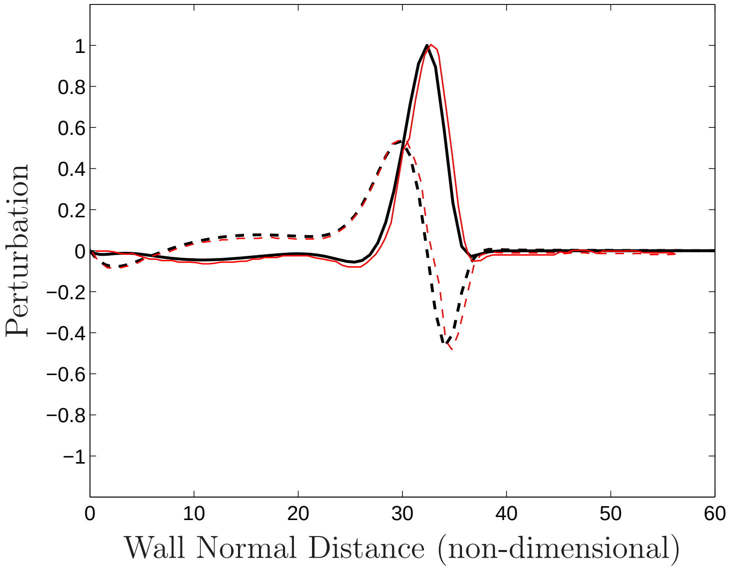

Figure 9.5: Eigenfunction comparison with Malik [4] for the Mach 10 $\mathrm{Re}_l =$ 1000 boundary layer. Malik (red), present work (black).

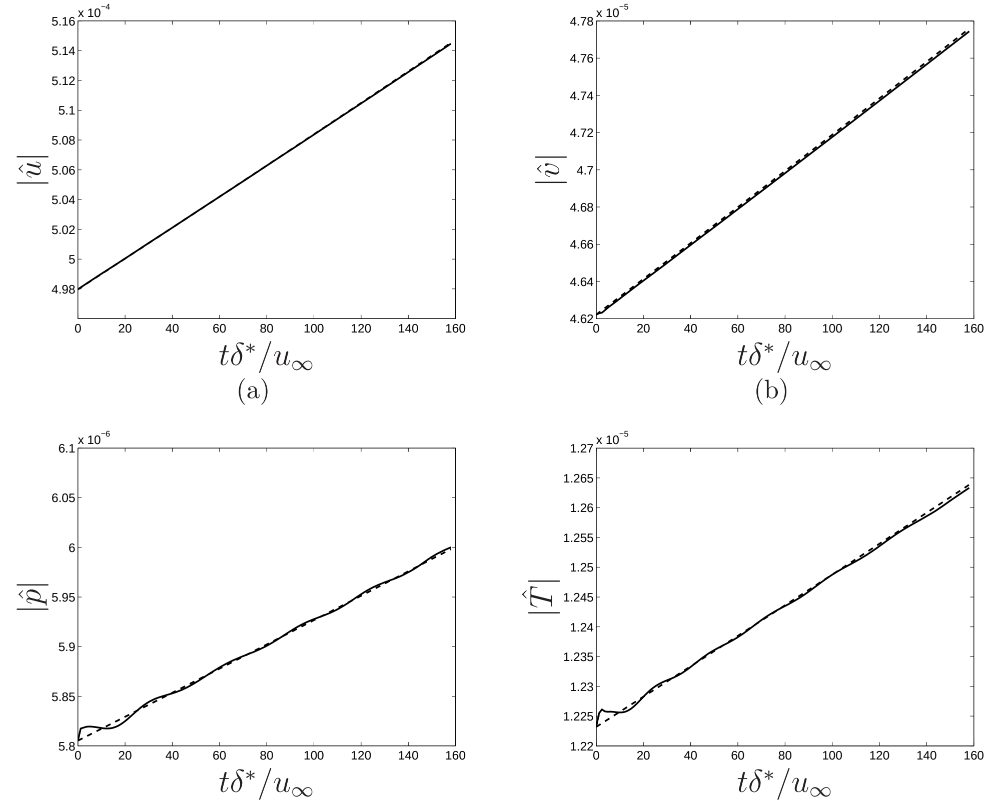

(a) (b)

(c) (d)

Figure 9.6: Growth of perturbations in Mach 0.05 DNS (solid) compared with $e^{\omega_r t}$ predicted by linear stability theory (dashed) for (a) $|\hat{u}|$, (b) $|\hat{v}|$, (c) $|\hat{p}|$, and (d) $|\hat{T}|$. Data taken at the wall normal location $y = 0.53\delta^*$.

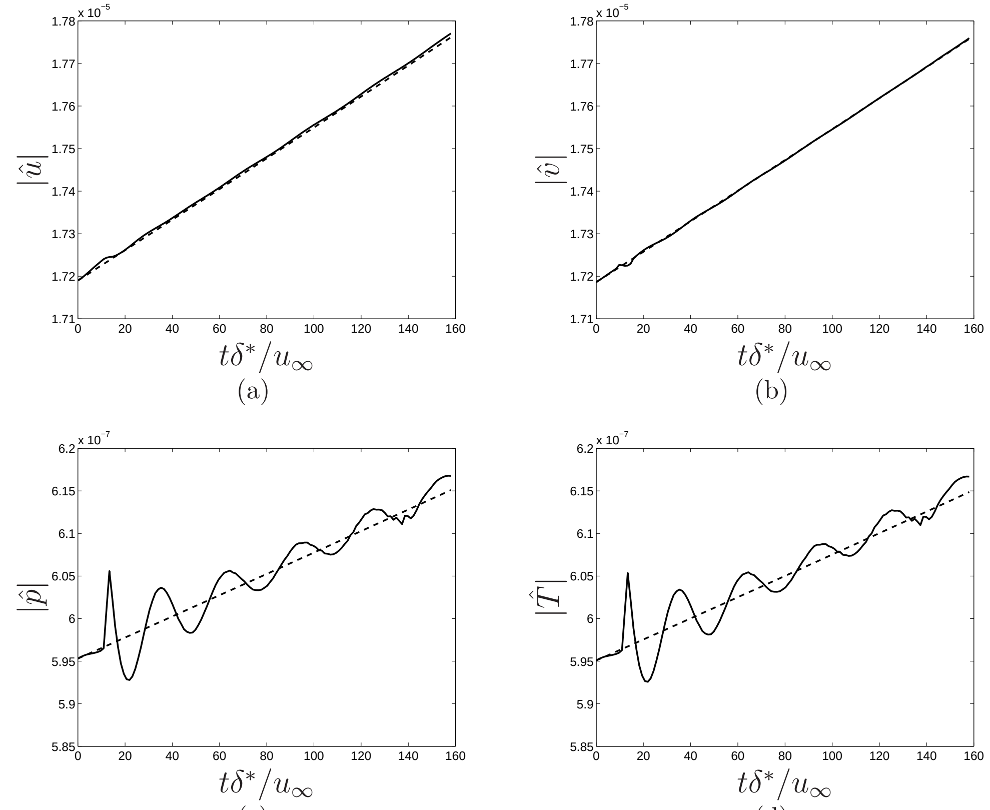

(a) (b)

(c) (d)

Figure 9.7: Growth of perturbations in Mach 0.05 DNS (solid) compared with $e^{\omega_r t}$ predicted by linear stability theory (dashed) for (a) $|\hat{u}|$, (b) $|\hat{v}|$, (c) $|\hat{p}|$, and (d) $|\hat{T}|$. Data taken at the wall normal location $y = 12.2\delta^*$.

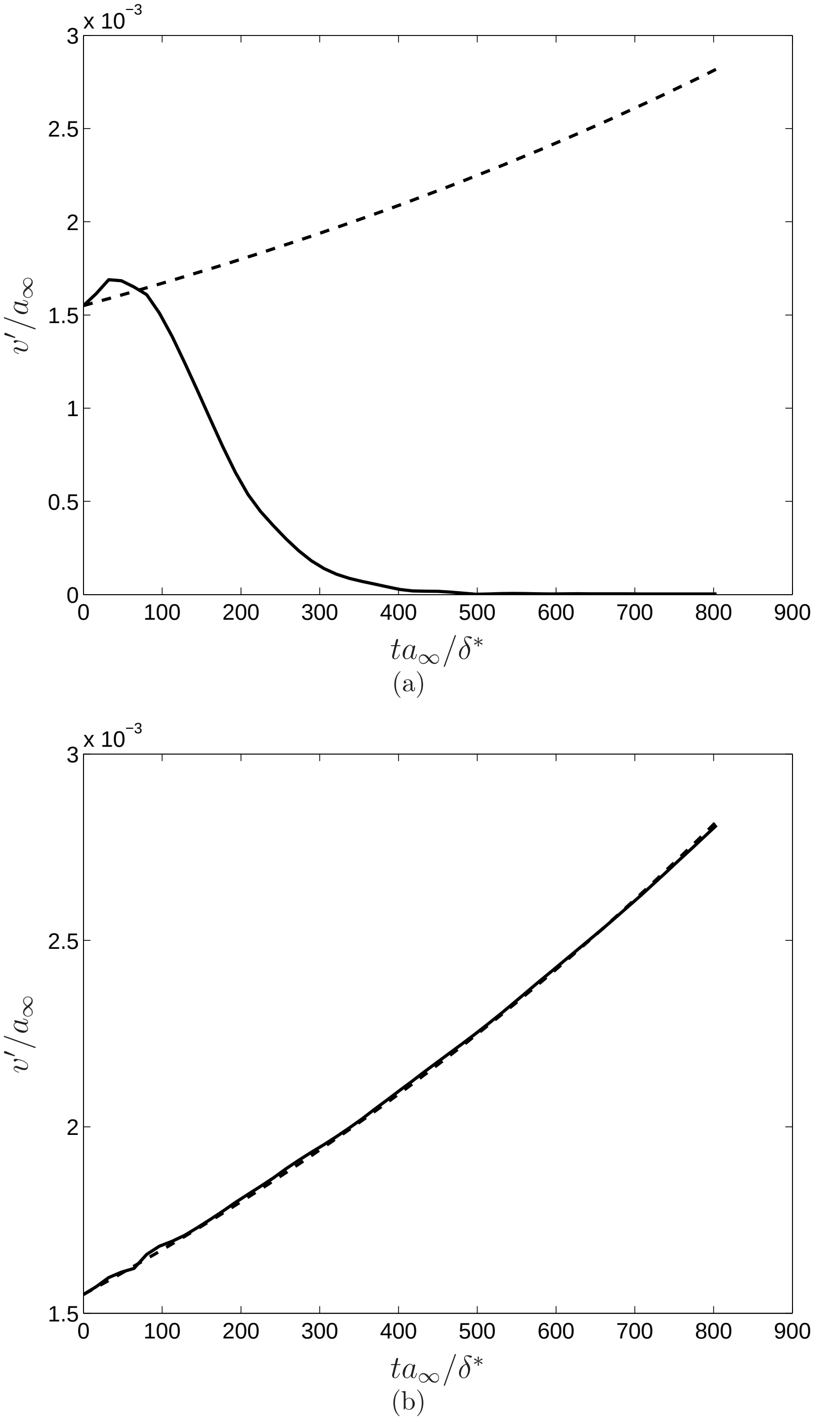

(a)

(b)

Figure 9.8: Growth of v' perturbations in TDNS at $y/\delta^* = 50$ above the wall. TDNS data from simulations (a) without and (b) with the application of Eq. (9.6). The TDNS data (solid) plotted with LST predicted growth rate (dashed), $v'_0 \exp[\omega_i t]$, where $\omega_i = 3.31 \times 10^{-4} \delta^*/a_\infty$.

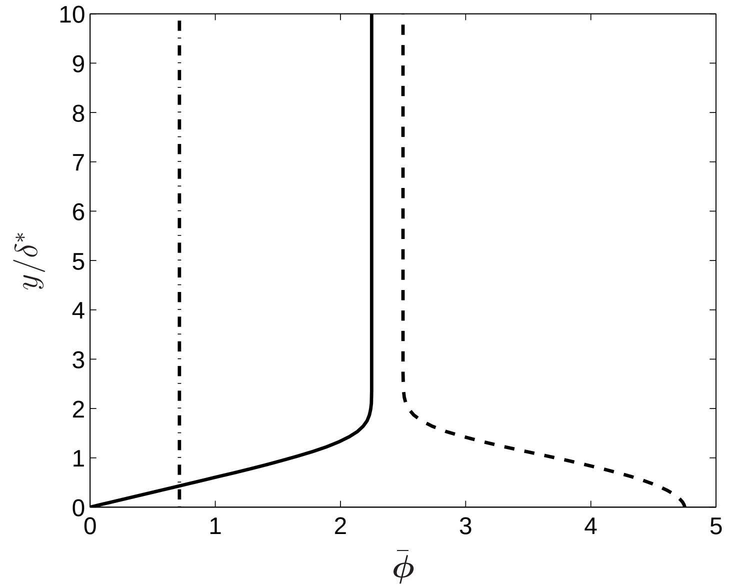

(a)

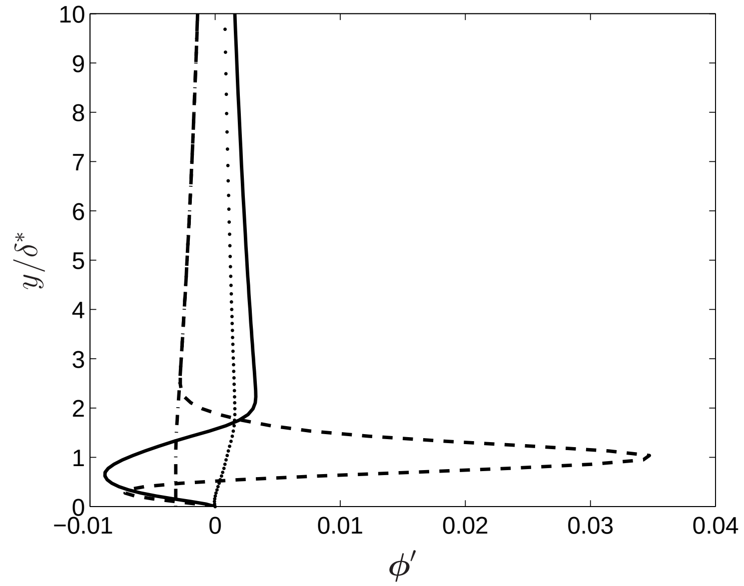

(b)

Figure 9.9: (a) $Re_{\delta^*} = 2000$, Mach 2.25 laminar boundary layer base flow and (b) temporally unstable eigenvectors for the stream wise and spanwise wavenumbers, $\alpha\delta^* = 0.2$, $\beta\delta^* = 0.0$. u (solid), v (dotted), p, (dash dot), T (dashed).

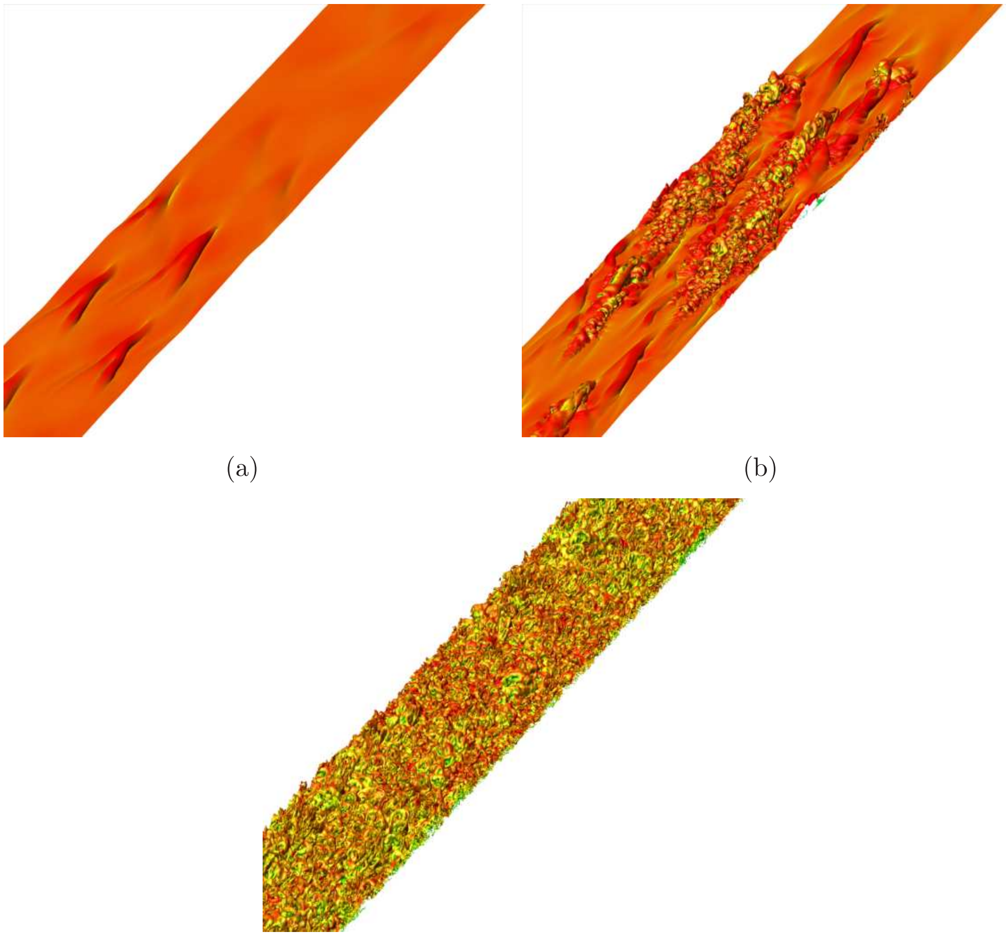

(a)

(b)

(c)

Figure 9.10: Stages of laminar to turbulent boundary layer transition. (a) Staggered Λ waves. (b) The breakdown of amplified disturbances into turbulent spots. (c) The final stage of transition: fully turbulent flow.

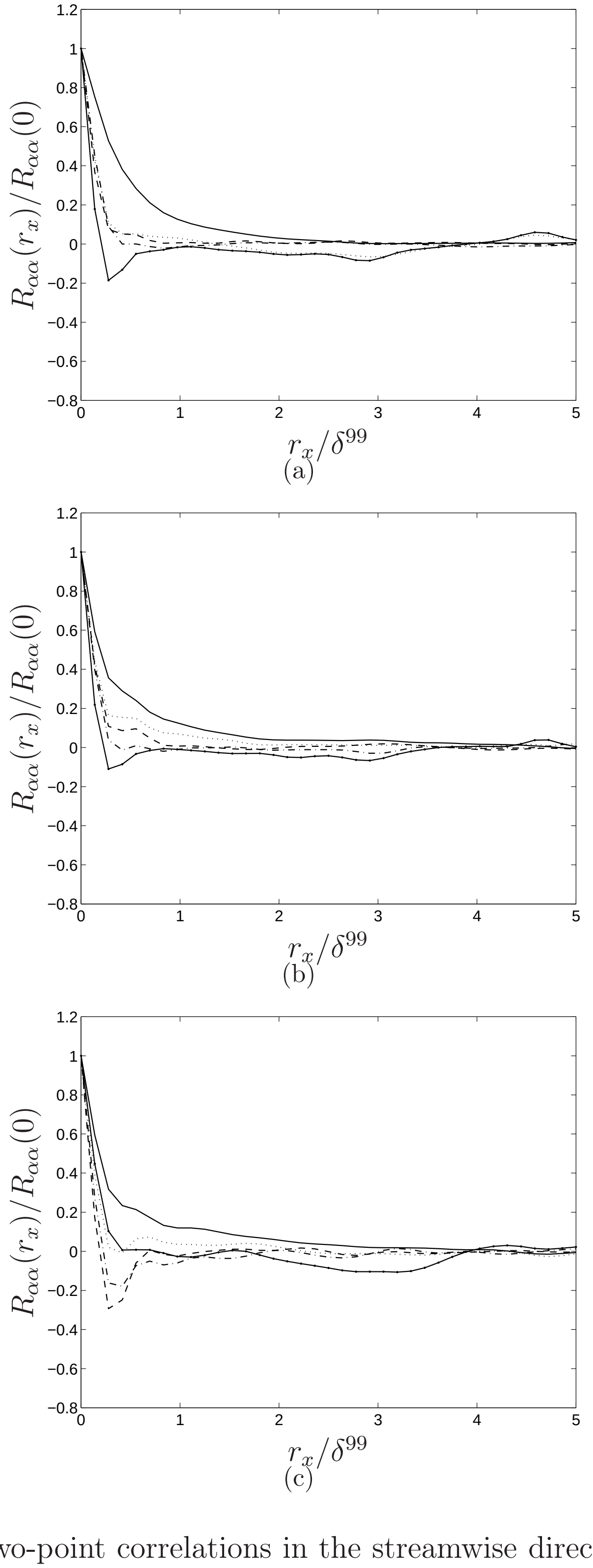

Figure 9.11: Two-point correlations in the streamwise direction at (a) $y^+ = 2.1$, (b) $y^+ = 73.9$, and (c) $y^+ = 151.3$. $R_{\rho'\rho'}$ (dotted), $R_{u'u'}$ (solid), $R_{v'v'}$ (dashed), $R_{w'w'}$ (dash-dot), $R_{p'p'}$ (solid with dots).

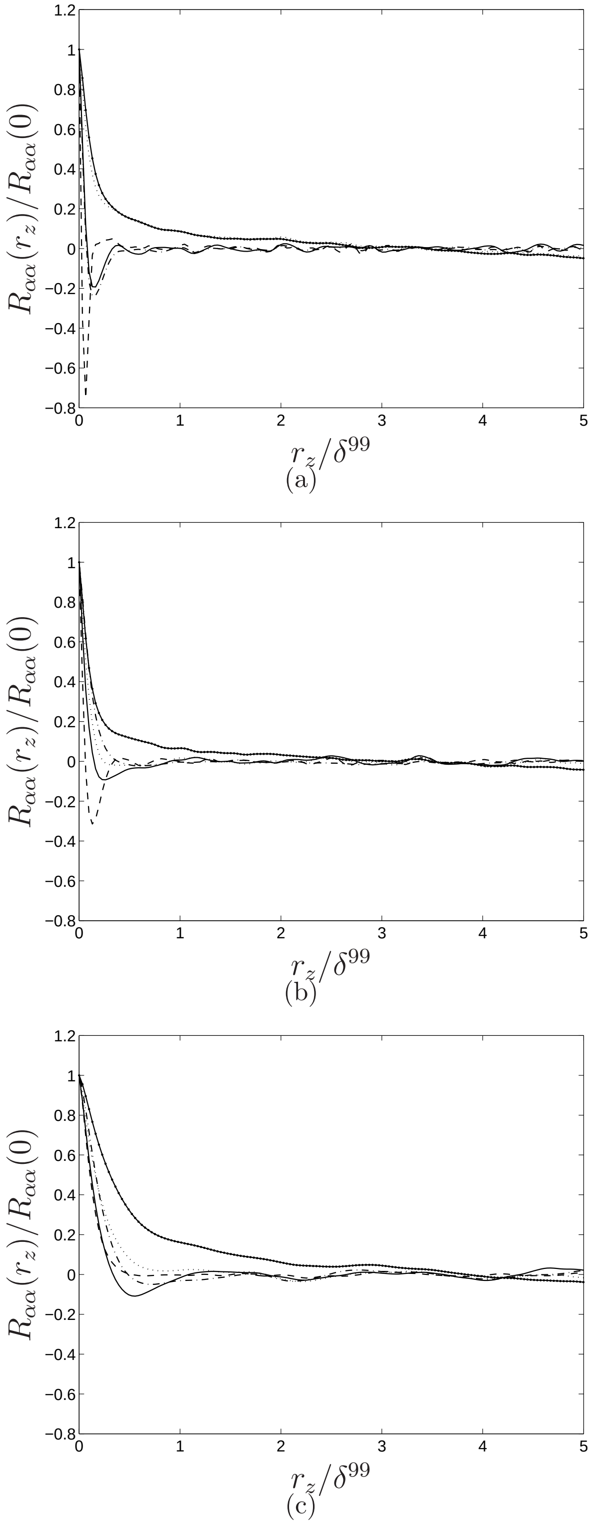

(a)

(b)

(c)

Figure 9.12: Two-point correlations in the spanwise direction at (a) $y^+ = 2.1$, (b) $y^+ = 73.9$, and (c) $y^+ = 151.3$. $R_{\rho'\rho'}$ (dotted), $R_{u'u'}$ (solid), $R_{v'v'}$ (dashed), $R_{w'w'}$ (dash-dot), $R_{p'p'}$ (solid with dots).

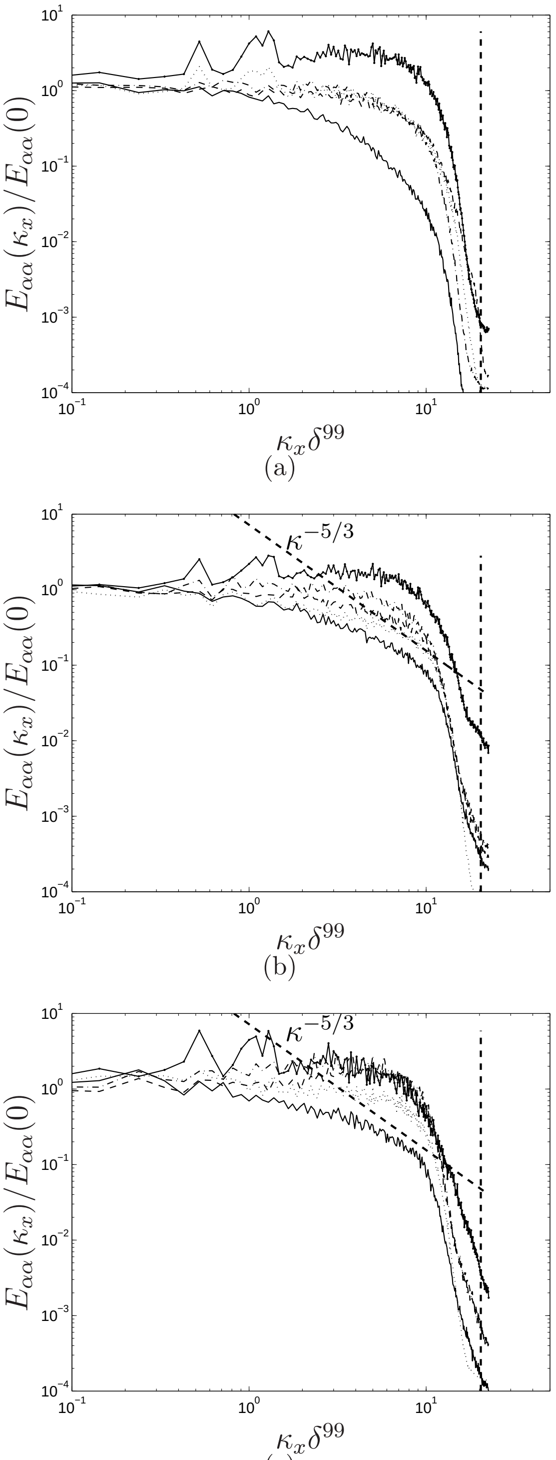

(a)

(b)

(c)

Figure 9.13: Energy spectra in the streamwise direction at (a) $y^+ = 2.1$, (b) $y^+ = 73.9$, and (c) $y^+ = 151.3$. $E_{\rho'\rho'}$ (dotted), $E_{u'u'}$ (solid), $E_{v'v'}$ (dashed), $E_{w'w'}$ (dash-dot), $E_{p'p'}$ (solid with dots). The filter cutoff frequency (refer to Fig. 7.2) is shown by the dashed vertical line. Kolmogorov's $-5/3$ energy spectra is shown in (b) and (c).

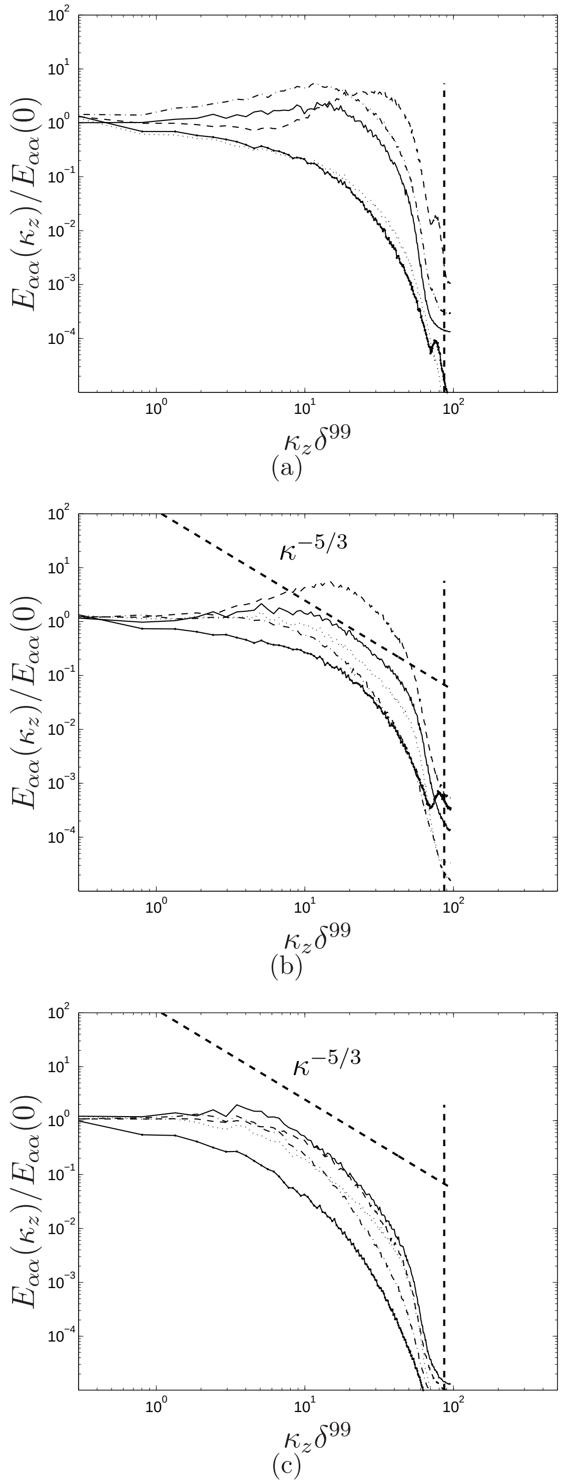

(a)

(b)

(c)

Figure 9.14: Energy spectra in the spanwise direction at (a) $y^+ = 2.1$, (b) $y^+ = 73.9$, and (c) $y^+ = 151.3$. $E_{\rho'\rho'}$ (dotted), $E_{u'u'}$ (solid), $E_{v'v'}$ (dashed), $E_{w'w'}$ (dash-dot), $E_{p'p'}$ (solid with dots). The filter cutoff frequency (refer to Fig. 7.2) is shown by the dashed vertical line. Kolmogorov's $-5/3$ energy spectra is shown in (b) and (c).

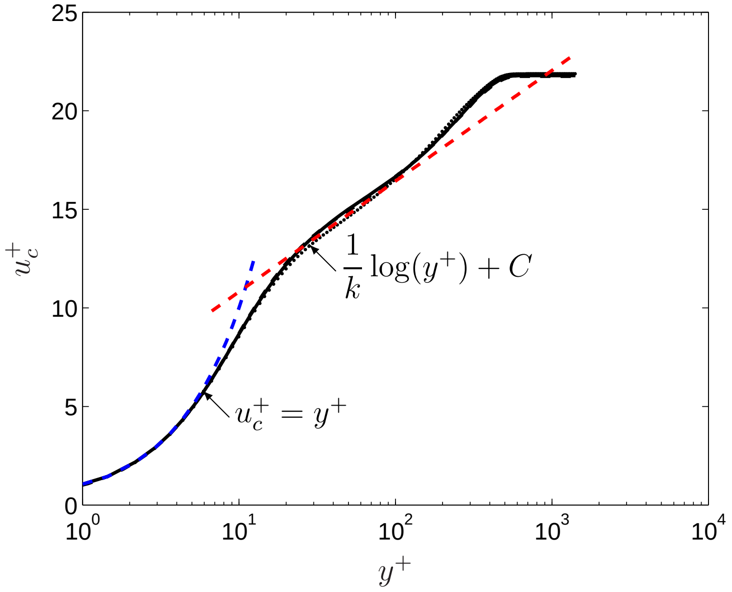

Figure 9.15: Grid convergence study using three grids: A (baseline, solid), B (dashed), and C (dotted).

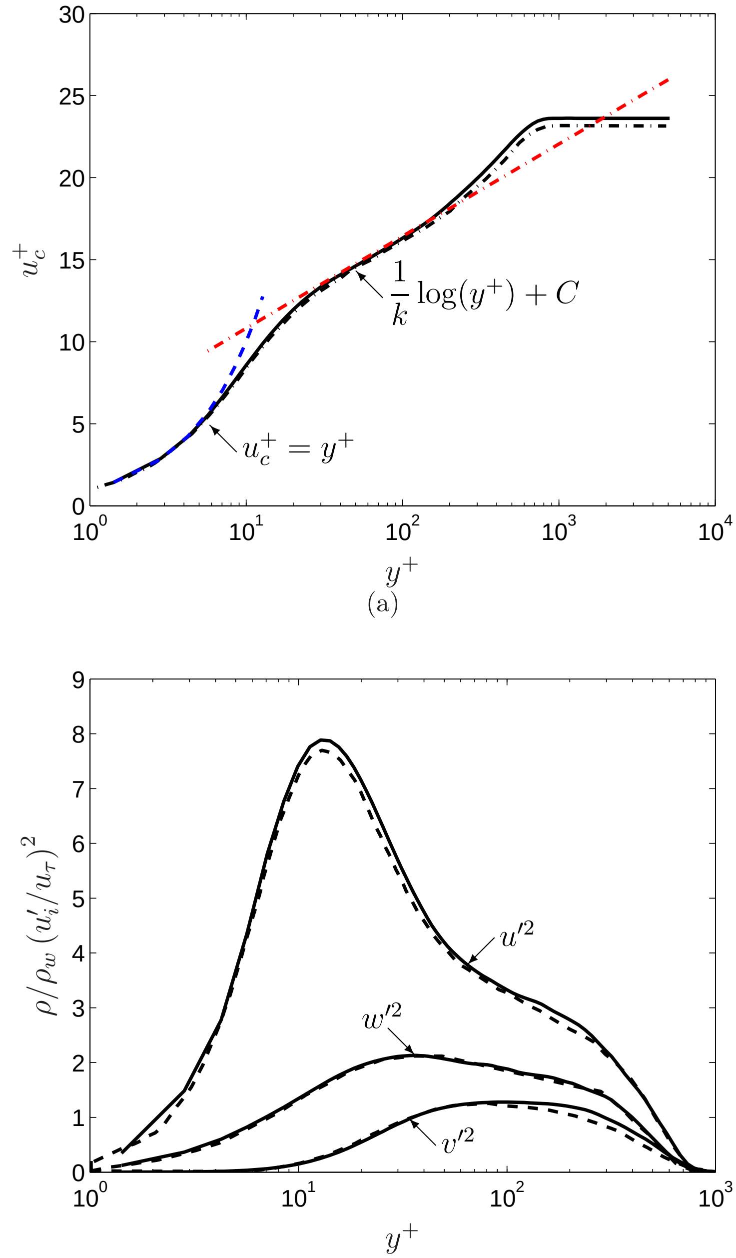

(a)

(b)

Figure 9.16: (a) Van Driest scaled mean velocity profile and (b) normalized normal components of the Reynolds stresses for the current $\mathrm{Re}_\theta \approx 4000$ TBL (solid) and that of Pirozzoli & Grasso [3](dash-dot).

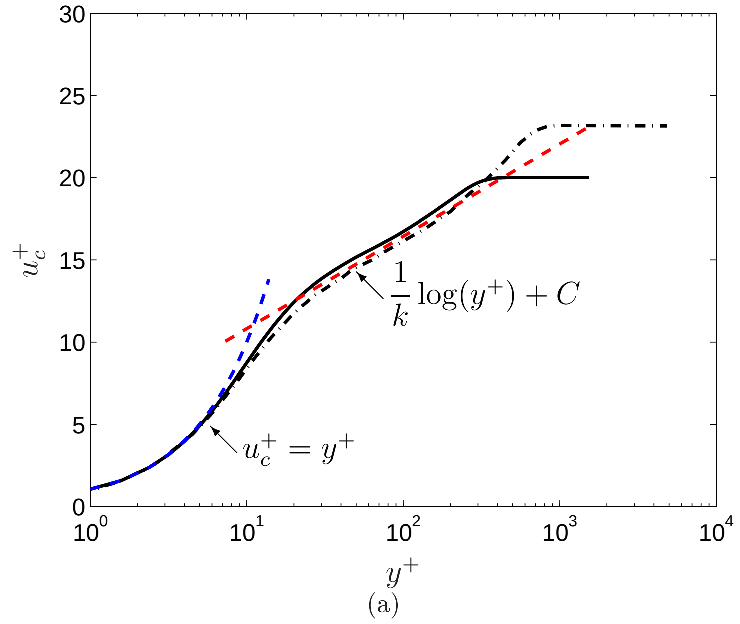

(a)

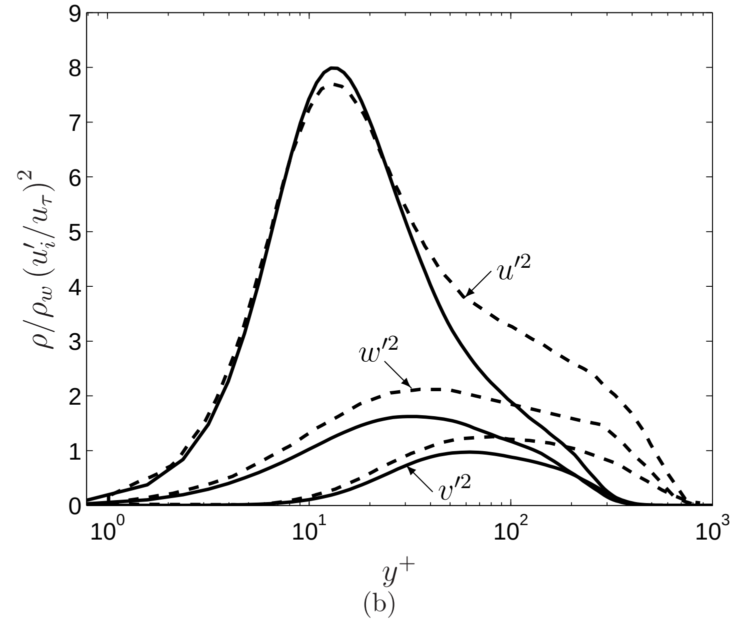

(b)

Figure 9.17: (a) Van Driest scaled mean velocity profile and (b) normalized normal components of the Reynolds stresses for the current $\mathrm{Re}_\theta = 1196$ TBL (solid) and that of Pirozzoli & Grasso [3](dash-dot).

Chapter 10

Aeroelastic Investigation Results

This chapter documents the interaction of the Mach 2.25 turbulent boundary layer (TBL) discussed in Chapter 9 with the compliant panel described in Section 8.2.2. Unless stated, results are from the long domain simulation (Refer to Section 8.2.1).

10.1 Panel solution evolution

The effect of fluid-structure interaction is seen in the evolution of the panel state, immediately departing from its initial flat-plate configuration under the loading from the TBL. Panel deformations are shown at four different instances in time in Fig. 10.1(a)-(d). Figure 10.1(a) shows that, at initial times, panel deformations are small and are in an unorganized dimpled pattern. As shown in Fig. 10.1(b) the panel deflections at $t = 0.79$ ms are made up of higher-mode bending waves which travel down the panel in the streamwise direction. The maximum panel deflections into and out of the boundary layer at this time are $w_{up} = 0.136$ mm $(0.070\delta^*,\ 9.06\tau)$ and $w_{down} = 0.102$ mm $(0.053\delta^*,\ 6.8\tau)$, respectively. Panel deflections normalized by current displacement thickness, δ^*, and panel thickness, τ, are given in parentheses. An x-t diagram of the panel deformations is shown in Fig. 10.2. The slopes of the deformation contours, which are further from zero at earlier times, correspond to the phase velocities of the panel bending waves. The peak which exists at the downstream extent of the panel in Fig. 10.1(b) is seen in Fig. 10.2 to grow and accelerate as it progresses down the panel. At later times, Fig. 10.1(c) and Fig. 10.1(d) show that the panel deformations are characterized by larger amplitude, low spatial mode standing waves. At $t = 1.60$ ms, the maximum panel deflections into and out of the boundary layer are $w_{up} = 0.080$ mm $(0.024\delta^*,\ 5.3\tau)$ and $w_{down} = 0.239$ mm $(0.072\delta^*,\ 15.9\tau)$, respectively. At $t = 1.90$ ms, the maximum panel deflections into and out of the boundary layer are $w_{up} = 0.240$ mm ($0.064\delta^*$, 16.0τ) and $w_{down} = 0.048$ mm ($0.013\delta^*$, 3.2τ), respectively. The stationary nature of these waves is evidenced by the almost zero slope of the associated deflection contours shown in Fig. 10.2 at $t = 1.60$ ms and $t = 1.90$ ms.

10.1.1 Modal decomposition of panel state

The linear mode shapes for a clamped-clamped panel are given in Seodel [103] as

$$\phi_j(x) = \cosh(\lambda_j x) - \cos(\lambda_j x) - \frac{\cosh(\lambda_j L) - \cos(\lambda_j L)}{\sinh(\lambda_j L) - \sin(\lambda_j L)} \left(\sinh(\lambda_j x) - \sin(\lambda_j x)\right), \tag{10.1}$$

where λ_j is the j^{th} solution to the transcendental equation $\cosh(\lambda_j L)\cos(\lambda_j L) = 1$. The first six ($j = 0$ to 5) solutions are given in Tab. 10.1 and the associated mode shapes are shown in Fig. 10.3. While the panel response is non-linear and therefore exhibit slightly different mode shapes [104], the linear shapes are a useful approximation to investigate the modal content of the panel state. Since the panel displacement is dominated by the vertical component, the simplification made by this analysis of only considering wall normal deflections is justified. The displacement of the neutral plane can be represented as the sum of N_x and N_z modes in the streamwise and spanwise directions, respectively, as

Table 10.1: First six solutions to the equation for λ_j, $\cosh(\lambda_j L)\cos(\lambda_j L) = 1$.

j	0	1	2	3	4	5
$\lambda_j L$	0.000000	4.730041	7.853205	10.995608	14.137165	17.278760

$$\eta(x, z, t) = \sum_{m}^{N_x} \sum_{n}^{N_z} A_{mn}(t)\phi_m(x)\phi_n(z). \tag{10.2}$$

Taking advantage of the orthogonality of ϕ_n,

$$\int_0^L \phi_n(x)\phi_m(x)dx = 0 \quad \text{for } m \neq n,$$

the modal coefficients $A_{mn}(t)$ are found by

$$A_{mn}(t) = \frac{1}{C_m D_n} \int_0^{L_x} \int_0^{L_z} \eta(x, z, t)\phi_m(x)\phi_n(z) dx dz, \tag{10.3}$$

where

$$C_m = \int_0^{L_x} \phi_m(x)^2 dx, \quad \text{and} \quad D_n = \int_0^{L_z} \phi_n(z)^2 dz.$$

The temporal evolution of the modal content of the panel solution is shown in Fig. 10.4. At earlier times, such as $t = 0.79$ ms, there exist a variety of low and high modes with similar amplitudes. However, it is seen that at later times the lower modes (mostly (2,1)), clearly dominate.

10.1.2 Power balance in the panel

The power into the panel from the fluid is calculated by evaluating the integral

$$\dot{W} = \int_{\partial B_i} \boldsymbol{u} \cdot (\boldsymbol{\tau} \cdot \hat{\boldsymbol{n}})\, d\partial B, \tag{10.4}$$

where $\hat{\boldsymbol{n}}$ is the unit normal, $\boldsymbol{u}$ is the velocity, and $\boldsymbol{\tau}$ fluid stress tensor at the interacting surface, ∂B_i. The evolution of $\dot{W}$ is shown in Fig. 10.5. Before $t = 0.5$ ms the power into the panel is relatively small. During this time the panel is nominally flat (Fig. 10.1(a)) and, since the mean pressure above and below the panel are equal, only the local TBL pressure fluctuations and viscous stresses contribute to the power into the panel. This result suggests that their contributions to the panel response are small compared to the loading due to the aerodynamic pressure created on the deflected panel. The role of viscous loading is addressed again below. Over the whole time record, the power directed into the panel from the fluid has both positive and negative values corresponding to instants at which the panel is moving with the fluid loading and against it, respectively. The kinetic energy of the panel is given by

$$KE = \int_B \frac{1}{2} \rho_s \left(\boldsymbol{u} \cdot \boldsymbol{u}\right) dB,$$

where ρ_s denotes the panel density. The evolution of the kinetic energy in the panel is shown in Fig. 10.6. The kinetic energy is always positive due to the presence of many panel modes of different frequencies and phases. The low frequency periodicity in the evolution of the kinetic energy lags that of the power into the panel by 90°, with peaks occurring at points in time just before the panel loses power back to the fluid. The total energy transferred to the panel from the fluid is obtained by integrating the power in Eq. (10.4) over time from the beginning of the simulation

$$E_{tot.}(t) = \int_0^t \dot{W}(t')dt'.$$

Since no structural damping is used, all energy that is passed to the panel is either pumped back into the fluid or stored in the panel in the form of kinetic and strain energy. Consequently, the strain energy in the panel can be found by the difference between the total energy and kinetic energy

$$SE(t) = E_{tot.}(t) - KE(t).$$

The strain energy over time is shown in Fig. 10.7. Naturally, peaks in the strain energy coincide with valleys in the kinetic energy and vice-versa.

In aeroelastic studies, the inviscid assumption is commonly made to calculate the fluid loading using both reduced-order models [105, 106] or the Euler equations [82]. This assumption reduces the computational cost both directly, by removing the viscous terms from the computation, and indirectly, by relaxing the stability requirements therefore allowing larger time steps. The quality of this assumption in transmitting forces to the panel is assessed here by comparing the power resulting from the inviscid loading on the panel with the full power calculation in Eq. (10.4). Given the geometry, velocity and surface pressure on the panel, the inviscid contribution to the fluid power into the panel is

$$\dot{W}_{inv.} = \int_{\partial B_i} -p\left(\boldsymbol{u} \cdot \hat{\boldsymbol{n}}\right) d\partial B. \tag{10.5}$$

The results of this calculation are compared with the total power (Eq. (10.4)) to assess the amount of power into the panel that results from viscous loading, shown in Fig. 10.8. The viscous loads, at their peak, contribute less than 2% of the total power exchanged between the fluid and the panel. Additionally, in this study, the panel deflections are small so that a further assumption that the rotation of the surface normal due to the deflection of the panel is negligible may be valid. The inviscid power into the flat panel geometry is calculated by assuming a vertical normal as

$$\dot{W}_{inv.,flat} = \int_{\partial B_i} -p \left(\boldsymbol{u} \cdot \hat{\boldsymbol{e}}_2 \right) d\partial B.$$

The result of this is again compared with the full power. Figure 10.9 shows that this assumption is justified, as the consideration of the surface normal's deviation from vertical in the power calculation is less the 0.8% of the total power. However, this does not mean that panel deflection can be neglected. In a later section it will be shown that the panel cannot be approximated to be flat as panel deflections significantly affect the coupled solution.

10.1.3 Deflection into the boundary layer

The evolution of the panel's maximum deflections both into and out of the the flow are plotted in Fig. 10.10(a) and Fig. 10.10(b), respectively. The panel deflections approach 20 times the panel thickness, putting them well into the non-linear regime. The panel deforms 7% though the boundary layer displacement thickness at initial times. At $t = 1.60$ ms and $t = 1.90$ ms, the panel deflection out of and into the boundary layer are around $k^+ = 25$, where $k^+ = w/\delta_v$ and δ_v is the viscous length. Deflections into the boundary layer extend through the viscous subregion and into the buffer region.

Robustness to domain size and initial conditions

In a second set of fluid-only and coupled simulations, the fluid solution is found in a domain with half the streamwise extent of the first set of simulations. The simulations on the two different domains will be referred to as the long and short domain simulations. The short domain effectively reduces the distance between the panels in the periodic simulation (Fig. 8.4(b)). Whether the panel response is significantly altered by the coupling of more closely spaced panels through the boundary layer is of interest, and can be assessed by comparing the results between the long and short domain simulations. A second difference is that the short domain coupled simulation does not start until the boundary layer becomes fully turbulent. Therefore initial loads experienced by the panel are different between the two simulations. The panel in the long domain is initially subject to the larger spatial and temporal scales of the unsteady eigenmodes, while the short domain panel is subject to the small scale turbulent fluctuations for the duration of the simulation. The panel dimensions are kept the same. One final difference between the two simulations is that the freestream densities differ by $\sim 2\%$, where in the long domain, $\rho_\infty = .4893$ kg/m^3, and in the short domain, $\rho_\infty = .4981$ kg/m^3. Deformations into and out of the boundary layer in the second case are shown in Fig. 10.11(a) and Fig. 10.11(b), respectively. A comparison of Fig. 10.10 with Fig. 10.11 shows that, while the initial loading on the panel was different, the large amplitude, long time, panel response is very similar.

Effect of panel thickness

A simulation featuring a panel with a thickness of $\tau = 150\mu m$, ten times the thickness of the original panel, was run in the long domain to compare the effect of panel thickness on the coupled solution. The simulation was run for 1.33 ms over which time the panel deformation remained well below one panel thickness as shown in Fig. 10.12. Based on an analysis by Degundji [70], this higher panel thickness and the dynamic pressure of the flow place the thick panel well inside the flutter boundary.

10.2 One-way vs. two-way coupling

It has been standard analysis and design practice to compute the fluid loads around a vehicle body and then pass those loads to structural models to determine the structural response. Here the role of communication from the structure back to the fluid is assessed in order to study the significance of full coupling in the panel response. Two coupled simulations are run on the short domain from the same initial state, with zero deflection and velocity under the already fully developed TBL. The simulations differ in that one of them uses the same two-way coupling as used in the above simulations while the other only employs one-way coupling. One-way coupling is defined here as passing fluid loads to the structure while not communicating the structural solution to the fluid.

Figure 10.13(a) and (b) show the one-way and two-way coupled panel solutions, respectively, at $t = 1.34$ ms (0.21 ms after they were “inserted” into the flow). At this initial time the panel responses are very similar, as highlighted by the tight contour limits in the figure. However, after another 0.27 ms, Fig. 10.14 shows that the solutions quickly diverge. There is a striking qualitative difference in the panel response between the two solutions which suggests that the fluid response to the panel geometry, which is neglected in the one-way coupled solutions, has a significant effect on the panel response. The panel motion in the two-way coupled simulation has developed into a wave like response, while the one-way coupled simulation produces panel deformations in a dimpled pattern similar to that in Fig. 10.13. Quantitatively, the panel states are also very different. The one-way coupled panel has maximum in/out deflections of $16.9\ \mu\text{m}/-11.8\ \mu\text{m}$ $(8.32 \times 10^{-3}\delta^*,\ 1.1\tau/{-5.81} \times 10^{-3}\delta^*,\ \ -0.8\tau)$ while the two-way coupled panel deflections are over three times as large, $150.2\ \mu\text{m}/-97.5\ \mu\text{m}$ $(3.05 \times 10^{-2}\delta^*,\ 4.03\tau/{-1.81}\times 10^{-2}\delta^*,\ -2.5\tau)$. At a time 0.27 ms later (Fig. 10.15), the disparity in the two solutions grows larger. In the two-way coupled case, the waves have begun to interact with the clamped BC. A positive wave crest has reflected off of the downstream boundary, producing a large negative deflection. Figure 10.16 shows that, 1.07 ms later, there is almost an order of magnitude difference in the response amplitudes. Furthermore, the two-way coupled response has achieved the standing wave state observed in the earlier simulation (Fig. 10.1(d)).

The *x*-*t* diagram shown in Fig. 10.17 gives spatio-temporal information about the differences in the panel responses between the one- and two-way coupled cases. It is shown that the panel response in the one-way coupled case is made up of seemingly random fluctuations about zero in space and time. In contrast, the two-way coupled simulation produces a panel response with an *x*-*t* diagram exhibiting ordered patterns; at earlier times the accelerating wave patterns are again seen while the two-state standing wave pattern is observed at later times. The modal decomposition (refer to Section 10.1.1) shown in Fig. 10.18 supports the statement that the one-way coupled response is much less ordered, remaining broadband and low amplitude over time. At later times, there is an emergence of a slightly dominant $(1,1)$ mode. The two-way coupled response again evolves from an initially low amplitude, broadband nature to being dominated by large amplitude $(2,1)$ waves.

In Fig. 10.19, the maximum amplitudes of the deflections into and out of the boundary layer are compared. The maximum deformations from the two cases follow the same trajectory initially. However, there is a point where the panel deformations both into and out of the boundary layer quickly amplify in the two-way coupled case. Figure 10.20 compares the maximum amplitudes of the deflections normalized by the boundary layer displacement thickness. It appears that the panel deflects slightly more than $0.005\delta^*$ before the two solutions diverge. The displacement thickness represents the effective shape of the panel to the inviscid free stream flow, and therefore changes to the displacement thickness govern the aerodynamic pressure felt by the panel.

A one-way coupled simulation over the thick panel in Section 10.1.3 shows negligible differences from the two-way coupled case, as shown in Fig. 10.21. This suggests that, in the absence of panel flutter, two-way coupling is less important.

10.2.1 Panel response frequency

The Fourier transform of the maximum panel deformations into and out of the boundary layer highlight the dominant panel response frequency, shown in Fig. 10.22 and Fig. 10.23 for the long and short domain simulations, respectively. The dominant response frequencies are 1822 ± 114 Hz in the long domain simulation and 2028 ± 206 Hz in the short domain simulation. Additionally, in each domain there are well defined peaks at harmonics of the primary frequencies, 3654 ± 114 Hz and 4056 ± 128 Hz in the long domain and short domain simulations, respectively. To investigate the relation between the pressure fluctuations under the TBL and the dominant panel response, the spectral content of the pressure at a point on the plate surface downstream of the panel is shown in Fig. 10.24 and Fig. 10.25. Pressure traces from both the rigid and compliant cases are investigated. If the turbulent fluctuations contributed significantly to the response of the panel, it would be expected that there would be peaks in the rigid panel simulation pressure spectra at the panel response frequencies. The absence of such peaks suggests that the turbulent fluctuations are not a driver of the panel response. Rather, the panel motion induces pressure fluctuations that can be seen under the TBL, as evidenced by the 141.8 dB spike in the pressure spectra at 1860 ± 85 Hz in the long domain and the 141.8 dB spike at 2054 ± 93 Hz in the short domain post-panel pressure spectra. The observation that the turbulent fluctuations are not a driver of the panel solution is supported by the results presented in Section 10.2. The one-way coupled panel was subject only to the turbulent fluctuations and did not exhibit large amplitude responses at discrete frequencies.

10.3 Influence of panel motion on fluid solution

Figure 10.26 shows the coupled solution at $t = 0.98$ ms. Constant vorticity magnitude surfaces exhibit the turbulent structures present in the boundary layer and constant pressure surfaces representing compression waves are shown in gray. The panel is outlined and deformations are shown. The deformations are shallow and are emphasized with blue and red contours to indicate negative and positive deflections, respectively. The effect of the turbulent boundary layer on the panel is easily seen, as shown in Fig. 10.10(a)-(d). However, changes to the fluid solution due to the panel motion are more subtle. Figure 10.26 shows the relationship between the fluid and panel states, and illustrates the significant effect the panel has on the flow solution. As shown in Fig. 10.27(a)-(d), the bending waves propagating through the panel cause compression and expansion waves to oscillate back and forth. In the conditions studied, the compression waves are relatively weak. The normal Mach number to the waves does not become subsonic, indicating that they are not sufficiently strong to be considered shock waves. Oscillations of compression/expansion wave patterns is a potential cause for concern in internal flow applications where unsteady loading on an opposite wall may be an issue.

The flux of power through the top surface of the fluid domain is calculated at every fluid time step by evaluating the integral

$$\dot{W}_{top} = \int_s (\boldsymbol{u}(\rho E + p) + \boldsymbol{q} - \boldsymbol{\tau u}) \cdot \hat{\boldsymbol{n}} \, ds,$$

where $\hat{\boldsymbol{n}}$ is the outward pointing normal on a surface, s, in the x-z plane positioned below the sponge region in the fluid domain, and the total energy per unit volume is $\rho E = p/(\gamma - 1) + \frac{1}{2}\rho \boldsymbol{u} \cdot \boldsymbol{u}$. The evolution of the power with time in the long domain rigid and compliant panel simulations is shown in Fig. 10.28. The average trend of the both power evolutions are influenced by the vertical velocity induced by the temporal boundary layer. The time derivative of the displacement thickness, shown in Fig. 10.29, provides evidence supporting this claim. The presence of the compliant panel fluttering under the boundary layer produces fluctuations in the power flux through the top of the fluid domain as seen in Fig. 10.28. The difference in the power evolution between the rigid and the compliant panel is shown in Fig. 10.30(a) to highlight the power modification due to the panel motion. The peak to peak oscillation amplitude is $\sim 1.4\%$ of the inflow power and makes a negligible contribution to the power balance in the fluid domain. The Fourier transform of the power difference shown in Fig. 10.30(b) indicates that the power out of the top of the compliant panel simulation fluctuates with a frequency of 1860 ± 85 Hz, which correlates well with the large amplitude panel response frequency of 1822 ± 114 Hz in the long domain simulation (Fig. 10.22). Results are similar in the short domain simulations, where the power out fluctuation frequency is 2054 ± 93 Hz (Fig. 10.31) corresponding to the panel fluctuation frequency of 2028 ± 206 Hz.

Temporal averages of the wall normal flow were taken over 0.1 ms centered around $t = 1.56$ ms (panel down position in Fig. 10.20(b)) and $t = 1.86$ ms (panel up position in Fig. 10.20(a)) to investigate the effect of the panel deformations on relevant turbulence statistics. In order to ensure the independence of the samples, the sample frequency was chosen so that they were spaced by the integral timescale, δt, given by

$$\delta t = \int_0^{0.1\text{ms}} \frac{\langle u(t)u(t+s)\rangle}{\langle u(t)u(t)\rangle} ds.$$

The Reynolds shear stresses, $\langle u'v'\rangle$, were compared over the same time intervals between the compliant and rigid panel (fluid only) simulations to determine the effect that the compliant panel state had on the shear stress. The Reynolds shear stress profiles above the panel from the time interval surrounding $t = 1.56$ ms (panel down position) are compared in Fig. 10.32. When compared to the rigid panel case, $-\langle u'v'\rangle$ is reduced in the log-law region. The Reynolds shear stress profiles above the panel from the time interval surrounding $t = 1.86$ ms (panel up position) are compared in Fig. 10.33. As compared to the rigid panel case, there appears to be a deficiency in $-\langle u'v'\rangle$ towards the boundary layer edge surrounded by large spikes. Values taken by $-\langle u'v'\rangle$ in all cases differ from previous work [102], which may be due to the non-trivial task of taking flow statistics over a moving surface.

The compressible turbulent kinetic energy (TKE) equation is written as

$$\bar{\rho}\frac{\partial k}{\partial t} + \bar{\rho}\tilde{u}_j\frac{\partial k}{\partial x_j} = P + D + T_{u'} + T_{p'} + \Pi - \rho\epsilon - ST_1 - ST_2, \tag{10.6}$$

where explanations of the individual terms are given in Appendix G. The effect on the turbulence downstream of the panel is examined by averaging over sections in the post-panel domain and comparing the turbulent kinetic energy (TKE, $k = 1/2\overline{\rho u_i'' u_i''}$) budget computed from both the rigid and compliant panel cases in that region (Eq. (10.6)). Three post-panel sections, shown in Fig. 10.34, are studied. Each section is one integral length long, based on the initial state of the TBL, which as shown in Fig. 9.11, is $\approx 0.5\delta_0^{99}$, where δ_0^{99} is the initial boundary layer thickness. For the comparison, TKE budget terms were averaged over one panel cycle over a period shown in Fig. 10.35(a). Differences in the temporal averages of all terms between the rigid and compliant panel cases are small and are not noticeable in Fig. 10.35(b). Detailed plots of the comparisons of P and $-\rho\epsilon$ in post-panel sections one, two, and three are shown in Fig. 10.36, Fig. 10.37, and Fig. 10.38, respectively. Error bars represent ± one standard deviation. The results indicate that there is no statistical difference in the temporal means of any of the TKE budget terms between the rigid and compliant panel cases in the post-panel region. However, the fluctuations in P and $-\rho\epsilon$ due to the panel movement are seen in the increased deviations from the mean in section one (Fig. 10.36). By sections two and three (Fig. 10.36 and Fig. 10.36) the deviations in P and $-\rho\epsilon$ are similar between the rigid and compliant panel cases. This result suggests that any local effects on the turbulence statistics (Fig. 10.32 and Fig. 10.33) are forgotten by the TBL within one integral length downstream of the compliant panel.

10.4 Comparison with piston theory

To assess the performance of a popular ROM the panel response is solved under the loading provided from first order piston theory, which computes the pressure at a point on the panel as a function of freestream dynamic pressure, Mach number, streamwise slope and vertical velocity of the panel surface and is given as

$$p - p_\infty = \frac{\rho_\infty U_\infty^2}{M_\infty}\left(\frac{\partial w}{\partial x} + \frac{1}{U_\infty}\frac{\partial w}{\partial t}\right). \tag{10.7}$$

The panel solution is determined by the current non-linear solver, and only the fluid model is changed. The freestream conditions are identical to those in the short domain simulations, with $\rho_\infty = 0.4981$ kg/m^3. Since Eq. (10.7) will not provide any loading over a flat panel at rest, the (1,1) mode of the panel, given by Eq. (10.1), is given an initial velocity of 0.1 m/s. The evolution of the panel subject to the piston theory loading is qualitatively similar to the response in the fully coupled simulations utilizing the Navier-Stokes solver. The panel reaches a state exhibiting a standing wave response with states shown in Fig. 10.39. Quantitatively, there are differences between the simulations using the two different methods. Maximum deformations into and out of the flow are 0.163 mm (10.9τ) and 0.177 mm (11.8τ), respectively. The response frequency, which due to non-linear stiffening is dependent on the magnitude of the deformations, also has a reduced value compared to the high-fidelity simulations, 761.5 ± 63 Hz. Third-order piston theory, while not shown, gives nearly identical results. Differences in the panel response to piston theory loading and to the Navier-Stokes loads are evidence of a possible deficiency in piston theory under these conditions.

10.5 Effect of domain height on solution

One negative feature of the TDNS approach is that the boundary layer grows in time, which places a finite limit on the length of time a simulation can run before the boundary layer outgrows the fluid domain. Figure 10.40 shows the evolution of the boundary layer visual (δ^{99}), displacement (δ^*), and momentum (θ) thickness over time in the short domain rigid panel simulation. The visual boundary layer thickness hits the top of the domain relatively early in the simulation, but the displacement and momentum thicknesses appear to remain undisturbed. To assess the effect, if any, of the domain height on the panel response, a simulation featuring a compliant panel in a domain twice the height of the previous simulations is run. The new fluid domain was created by adding 39 uniformly spaced grid points to the top of the short domain to extend it to twice the height of the previous simulation. The initial condition in the fluid was set equal to the fluid solution from which the short domain compliant panel simulation was started, but the freestream flow was extended upwards to the top of the domain. The fluid initial condition is shown in Fig. 10.41. The flow solution in the initial condition above the previous domain height is not consistent with the Navier-Stokes equations and causes as small adjustment at the beginning of the coupled simulation. The maximum deflections of the panel into and out of the flow are compared to the panel response in the short domain simulation in Fig. 10.42. The Fourier transform of the maximum deflections into and out of the boundary layer in Fig. 10.43 indicate that the large amplitude fluctuations occur at a frequency of 1895 ± 316 Hz and the lower amplitude response occurs at 3790 ± 316 Hz. The uncertainties overlap in the response frequencies of the short and tall domains, indicating that there is no statistical difference between the two.

10.6 Summary of Part II

A high-accuracy, high-fidelity methodology for the simulation of coupled fluid-structural problems has been developed for the purpose of predicting the structural response of a panel on an aerospace vehicle in extreme conditions. Few assumptions are made about the physical properties or solution geometry in order to achieve accurate predictions in situations where simplified approaches may be invalid and experiments may be extremely difficult. In particular, no turbulence model was used and all turbulent scales were resolved. The formulation of the coupled solver was presented. Details about the method for generation of the turbulent boundary layer in a temporal direct numerical simulation were discussed and it was shown that, in high-speed flows, the growth of the mean flow needs to be suppressed in order for linear stability theory to hold. The effect of coupling on both the fluid and structural response were studied.

Results showed that panel deformations, in the form of traveling bending waves, amplify when they interact with the clamped panel boundaries. At later times, the deformations exhibit a standing wave behavior which is dominated by the (2,1) panel mode at a frequency around 2000 Hz. In all cases, a second, lower amplitude panel response occurs at the next harmonic of the primary response frequency. The deformation approached 20 panel thicknesses, and extended into the boundary layer a distance of 25 wall units. Differences were small between short and long domain simulations, suggesting that, in the conditions studied the distance between successive panels did not affect the panel response. Changes in surface topology led to the generation of oscillating compression and expansion waves, which may cause localized unsteady loads on an opposing wall in internal flow applications. The large amplitude panel response produces pressure fluctuations that radiate into the fluid and are seen in at the top of the domain as well as under the turbulent boundary layer downstream. Turbulence statistics show that the Reynolds shear stress profiles may be modified on the compliant panel, but results were not conclusive. The effect of the interaction with the panel on the turbulence can be seen in the downstream turbulent kinetic energy budget close to the panel and suggest that panel compliance effects on turbulence are forgotten after one integral length. In comparing results from a simulation where structural deformations are not communicated to the fluid solution with the standard two-way coupled results, a large difference is seen. Two-way coupling is shown to be very important in response prediction of a panel interacting with a compressible turbulent boundary layer in situations where the panel flutter may occur.

Figures for Chapter 10

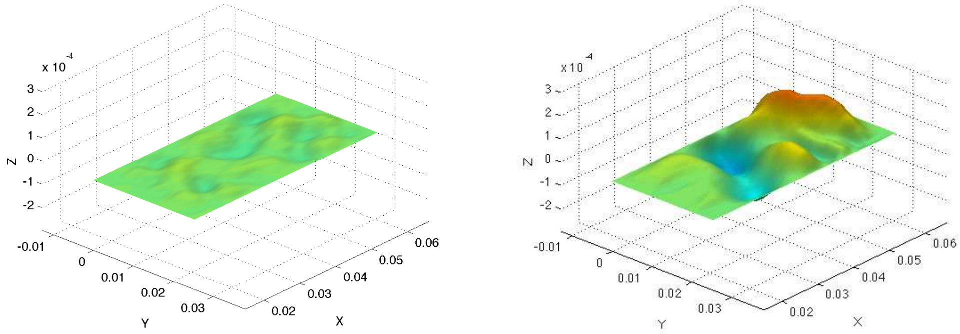

(a) $t = 0.27$ ms (b) $t = 0.79$ ms

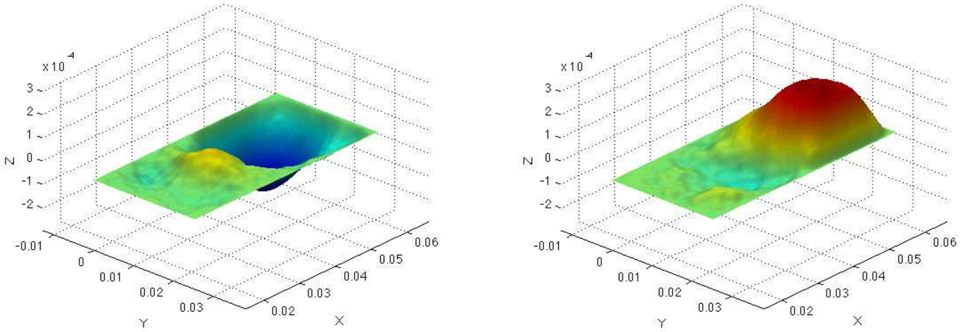

(c) $t = 1.60$ ms (d) $t = 1.90$ ms

Figure 10.1: Panel deformation at (a) $t = 0.27$ ms, (b) $t = 0.79$ ms , (c) $t = 1.60$ ms , and (d) $t = 1.90$ ms. Red and blue indicate deflection into and out of the boundary layer, respectively. Units are in meters.

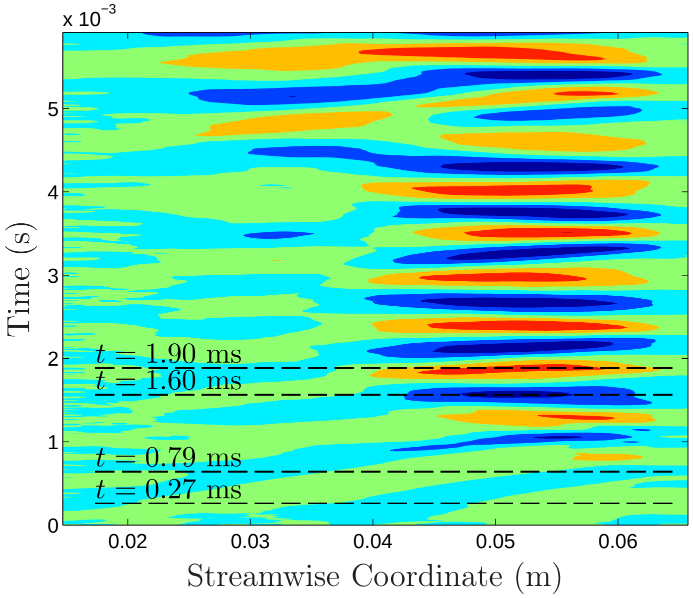

Figure 10.2: x-t diagram of panel deflections along the centerline of the panel ($z = .0127$ m). The times $t = 0.27$, 0.79, 1.60, and $t = 1.90$ ms corresponding to Fig. 10.1(a)-(d) are marked with dashed lines.

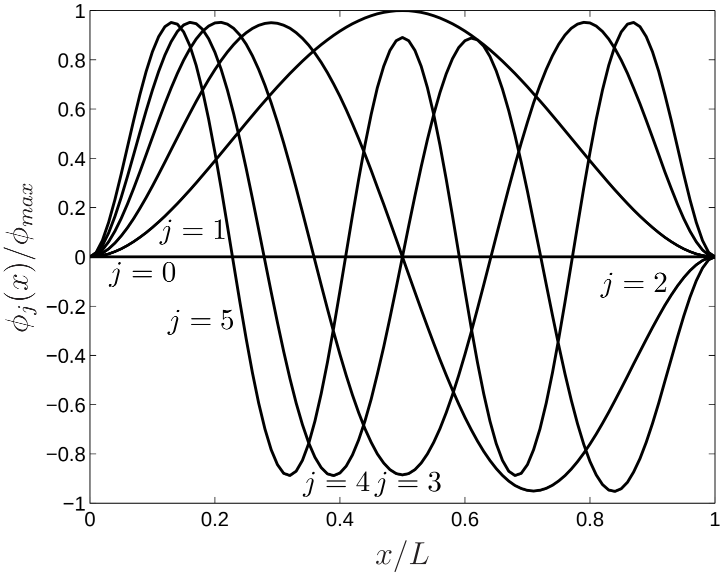

Figure 10.3: First six clamped-clamped beam modes.

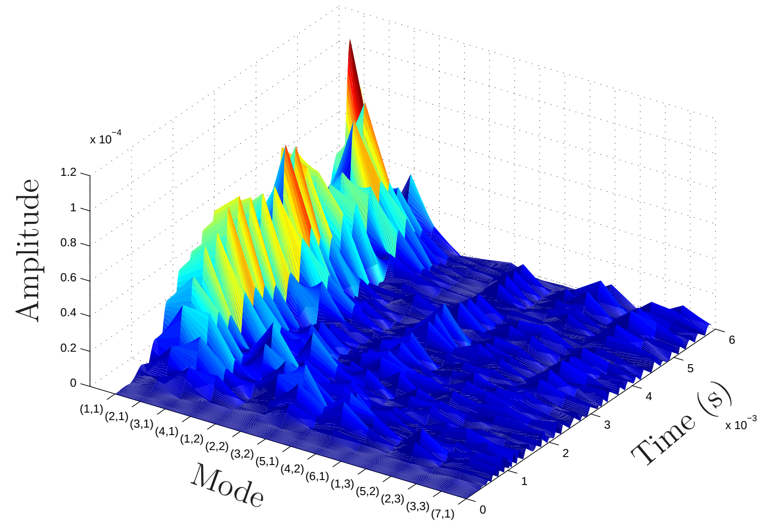

Figure 10.4: Evolution of the first 15 spatial modes of the bending waves in the panel solution.

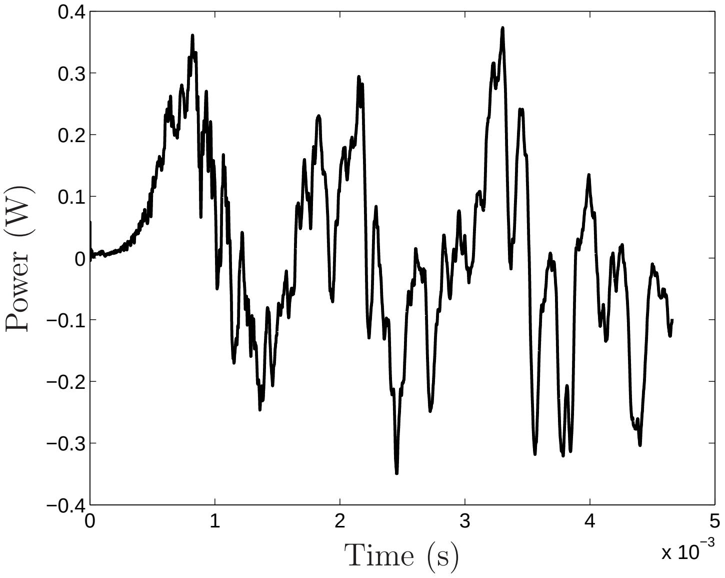

Figure 10.5: Power into the panel from the fluid, as defined by Eq. (10.4).

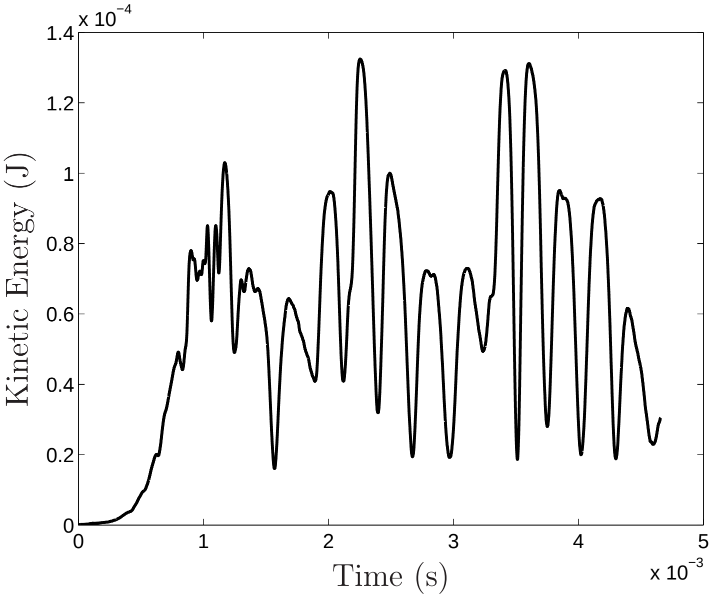

Figure 10.6: Kinetic energy of the panel.

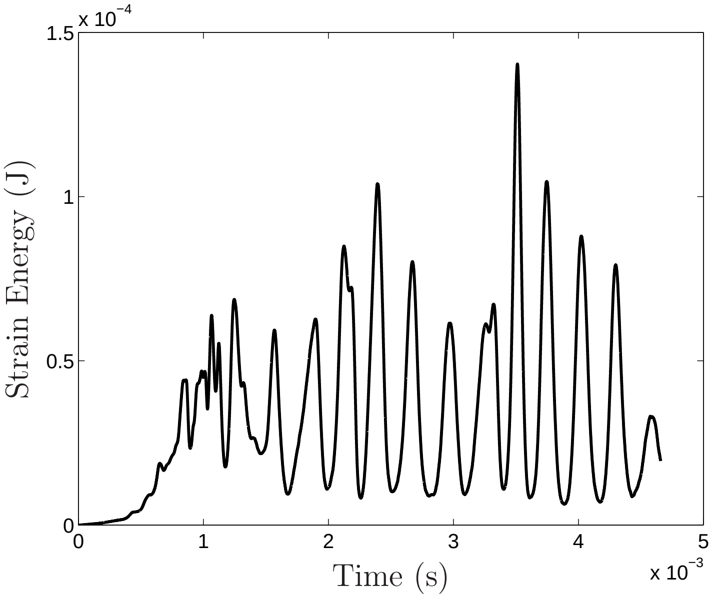

Figure 10.7: Strain energy of the panel.

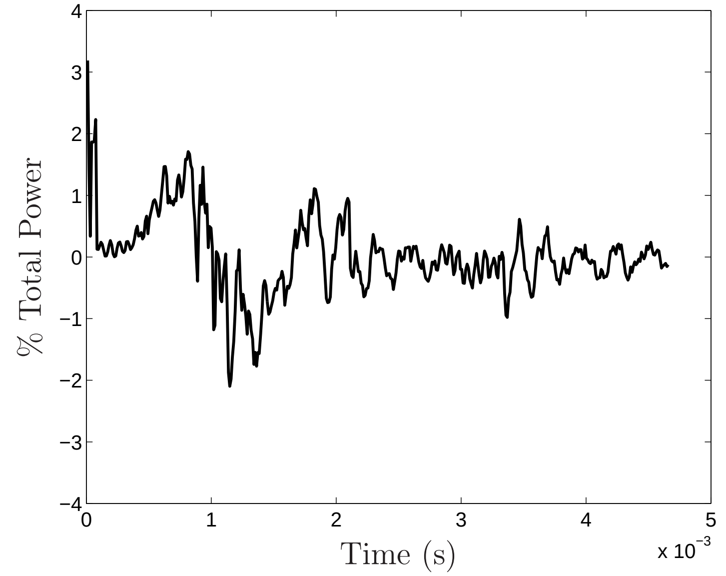

Figure 10.8: Percentage of power resulting from viscous effects, $\frac{\dot{W}-\dot{W}_{inv.}}{max(\dot{W})} \times$ 100%.

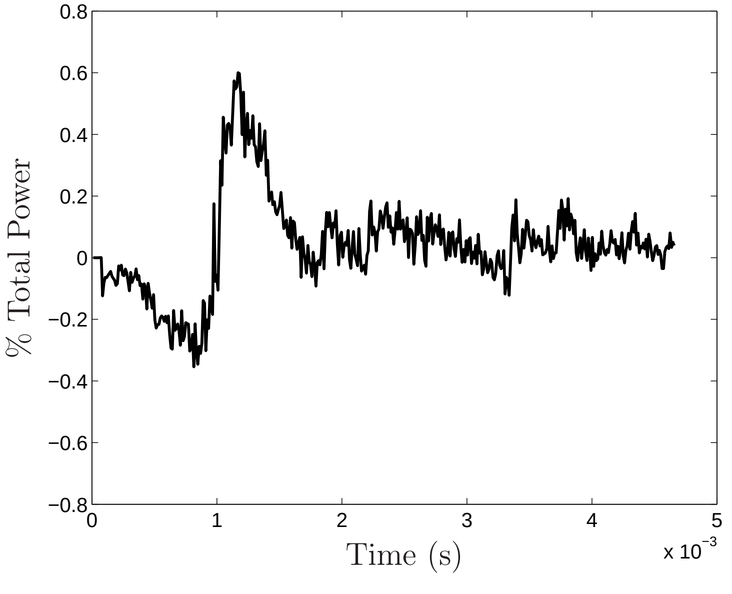

Figure 10.9: Percentage of power resulting from a non-vertical panel surface normal, $\frac{\dot{W}_{inv.}-\dot{W}_{inv.,flat}}{max(\dot{W})} \times 100\%$.

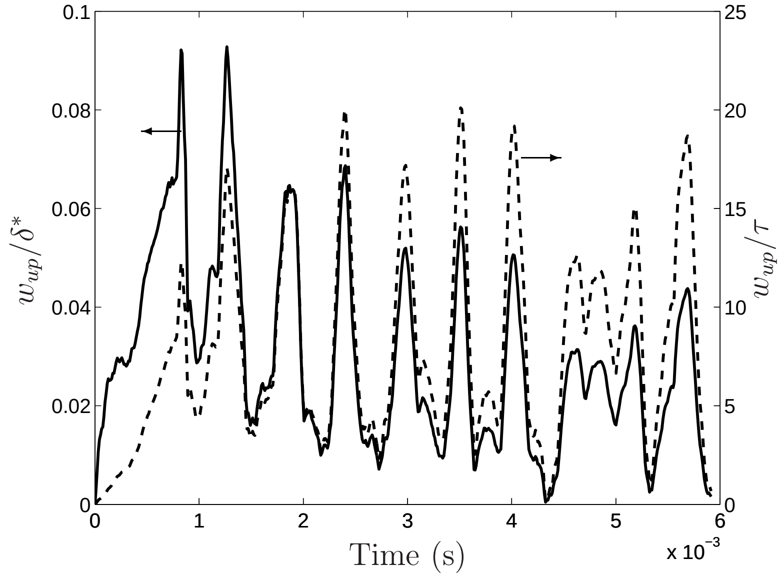

(a)

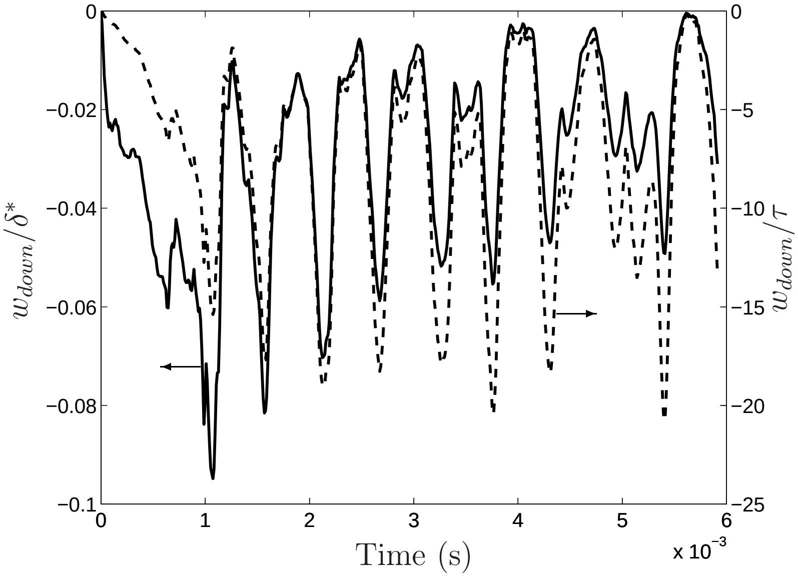

(b)

Figure 10.10: Maximum panel deflection with time into (a) and out of (b) the flow in the long domain simulation. The deflections are normalized by the boundary layer displacement thickness, δ^* (solid), and panel thickness, τ (dashed).

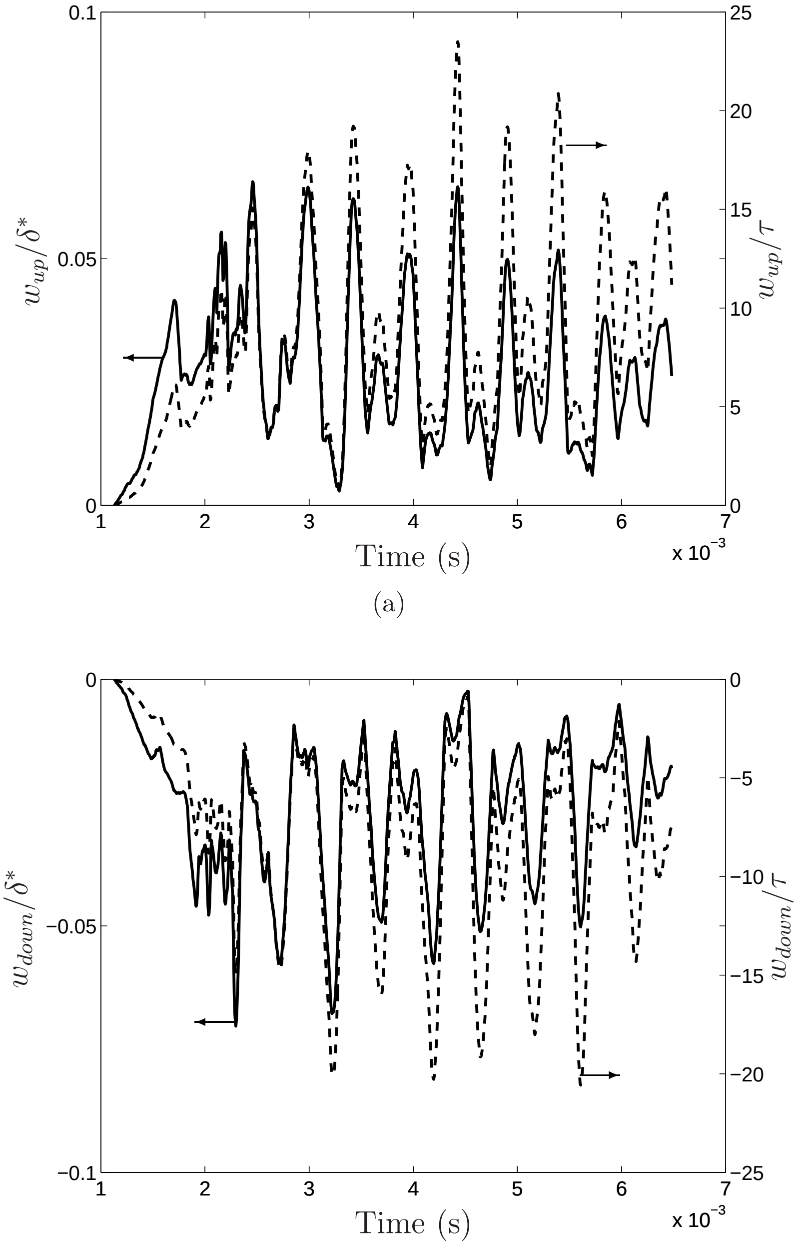

(a)

(b)

Figure 10.11: Maximum panel deflections with time into (a) and out of (b) the flow in the short domain simulation. The deflections are normalized by the boundary layer displacement thickness, δ^* (solid), and panel thickness, τ (dashed). Note that the time starts at $t = 1.13$ ms, when the compliant panel section is "inserted" into wall.

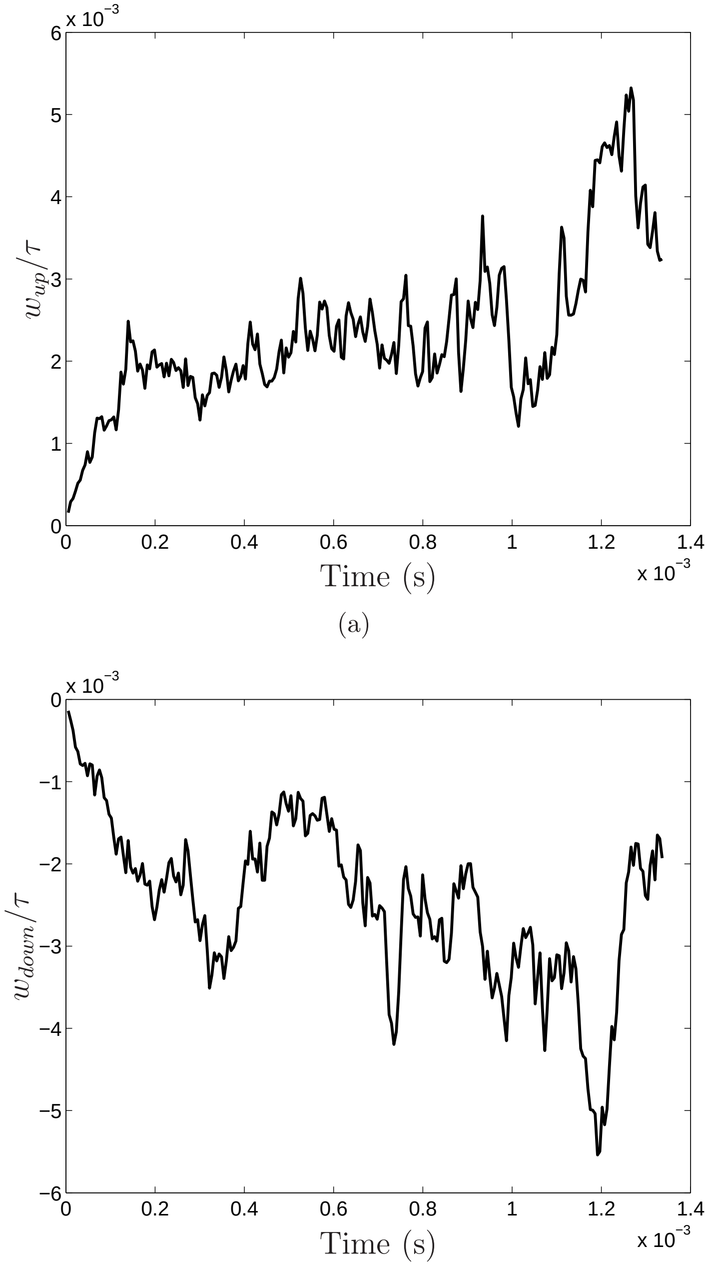

(a)

(b)

Figure 10.12: Maximum deformation of the thick panel with time into (a) and out of (b) the flow. Deformations are normalized by the panel thickness, $\tau = 150\ \mu$m.

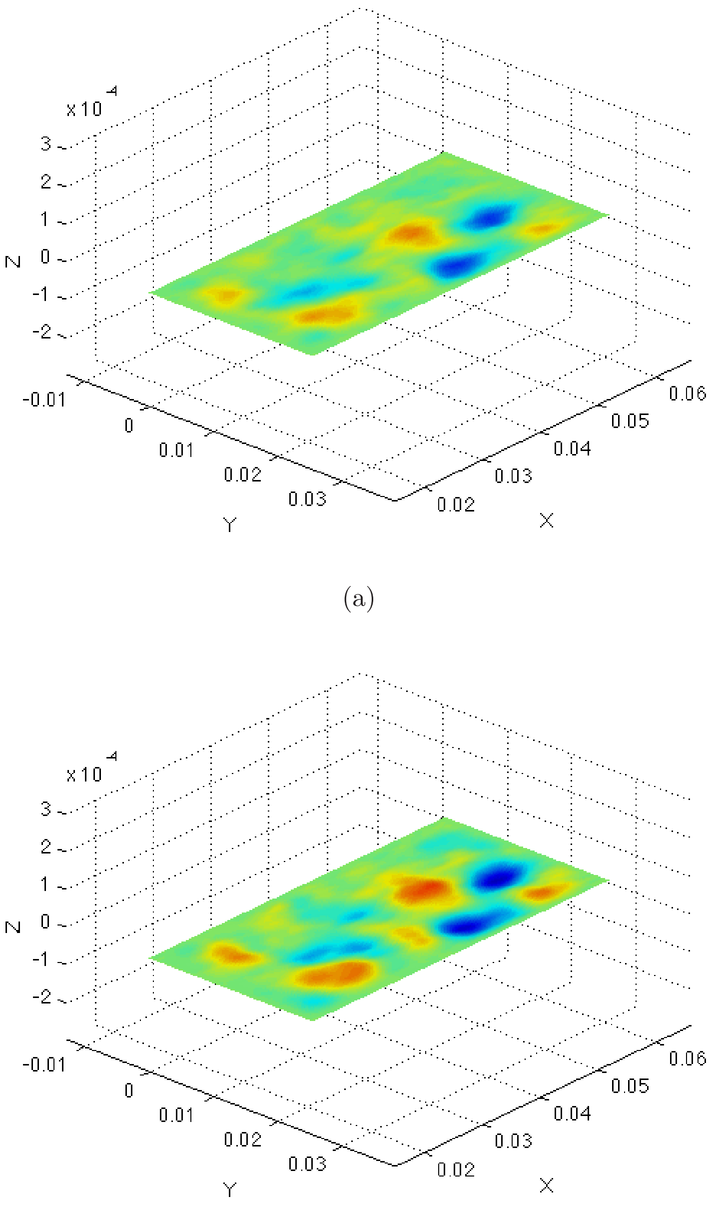

(a)

(b)

Figure 10.13: Panel solutions from the (a) one-way coupled and (b) two-way coupled simulations at $t = 1.34$ ms. Maximum panel deflections in/out of the TBL are (a) 7.7 μm$/-10.9$ μm ($5.05\times10^{-3}\delta^*,\ 0.5\tau/{-7.15}\times10^{-3}\delta^*,\ -0.7\tau$) and 10.0 μm$/-13.9$ μm ($6.56\times10^{-3}\delta^*,\ 0.7\tau/{-9.12}\times10^{-3}\delta^*,\ -0.9\tau$), Contour limits are ($-16.3$ μm$, 16.3$ μm) to highlight solution similarities.

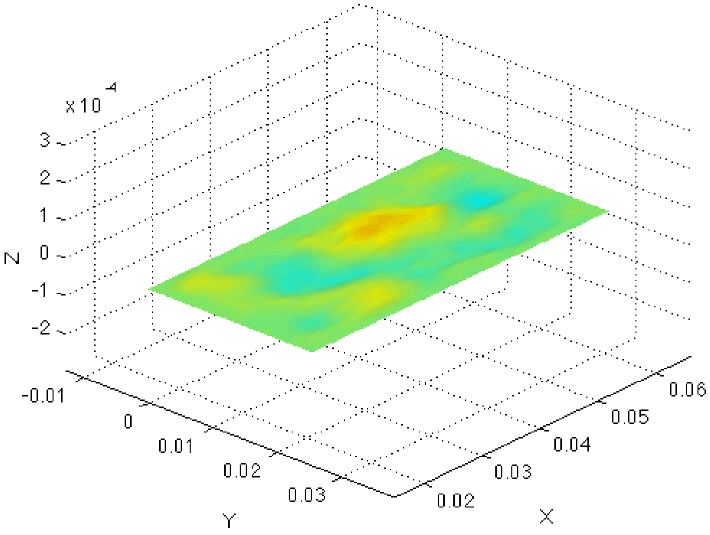

(a)

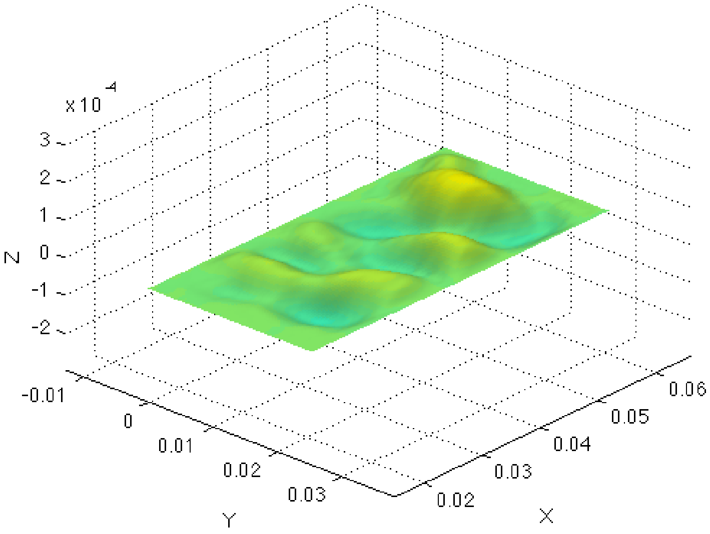

(b)

Figure 10.14: At $t = 1.61$ ms, the panel solutions from the (a) one-way coupled and (b) two-way coupled simulations show significant differences. Maximum panel deflections in/out of the TBL are (a) 16.9 μm/ $-$ 11.8 μm ($8.32 \times 10^{-3}\delta^*,\ 1.1\tau/{-5.81} \times 10^{-3}\delta^*,\ -0.8\tau$) and b) 62.0 μm/ $-$ 36.8 μm ($3.05 \times 10^{-2}\delta^*,\ 4.1\tau/{-1.81} \times 10^{-2}\delta^*,\ -2.5\tau$). Contour limits (a) ($-48.8\ \mu$m$, 48.8\ \mu$m) and (b) ($-270.6\ \mu$m$, 270.6\ \mu$m) are held constant through Fig. 10.14-Fig. 10.16 to display panel state evolution.

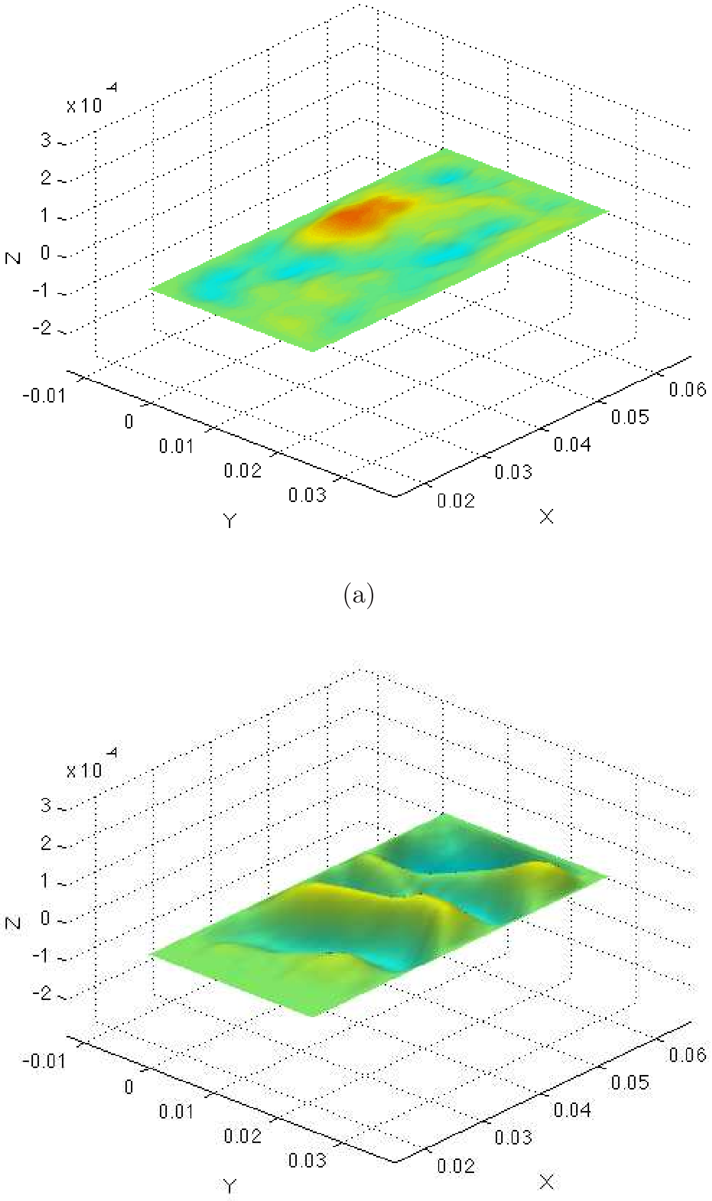

(a)

(b)

Figure 10.15: At $t = 1.88$ ms, the panel solutions continue to diverge between the (a) one-way coupled and (b) two-way coupled simulations. Maximum panel deflections in/out of the TBL are (a) $25.6\ \mu\text{m}/-13.5\ \mu\text{m}$ ($1.02 \times 10^{-2}\delta^*,\ 1.7\tau/{-5.37} \times 10^{-3}\delta^*,\ \ -0.9\tau$) and $62.2\ \mu\text{m}/-97.5\ \mu\text{m}$ ($2.48 \times 10^{-2}\delta^*,\ 4.2\tau/{-3.88} \times 10^{-2}\delta^*,\ \ -6.5\tau$). Contour limits (a) $(-48.8\ \mu\text{m}, 48.8\ \mu\text{m})$ and (b) $(-270.6\ \mu\text{m}, 270.6\ \mu\text{m})$ are held constant through Fig. 10.14-Fig. 10.16 to display panel state evolution.

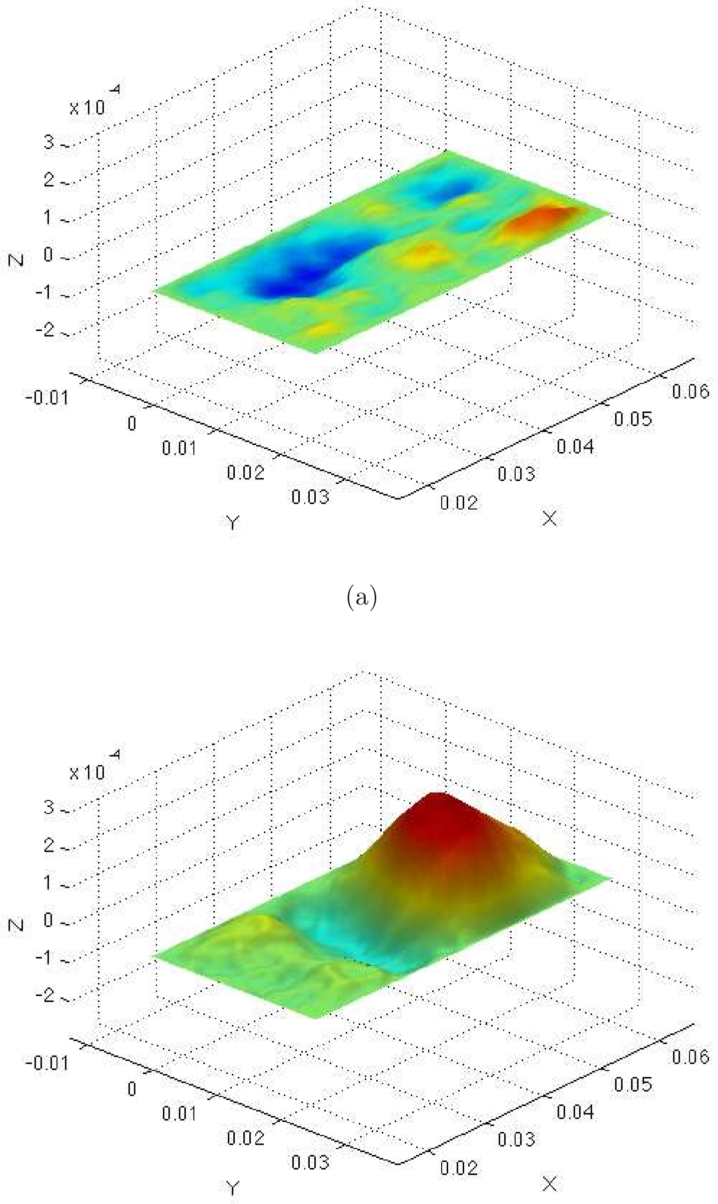

(b)

Figure 10.16: By $t = 2.95$ ms, the panel solutions from the (a) one-way coupled and (b) two-way coupled simulations differ substatially. Maximum panel deflections in/out of the TBL are (a) 29.6 μm/ − 36.4 μm ($7.17 \times 10^{-3}\delta^*$, $2.0\tau/{-8.81} \times 10^{-3}\delta^*$, -2.4τ) and 245.2 μm/ − 61.1 μm ($5.94 \times 10^{-2}\delta^*$, $16.3\tau/{-1.48} \times 10^{-2}\delta^*$, -4.0τ). Contour limits (a) (-48.8 μm, 48.8 μm) and (b) (-270.6 μm, 270.6 μm) are held constant through Fig. 10.14-Fig. 10.16 to display panel state evolution.

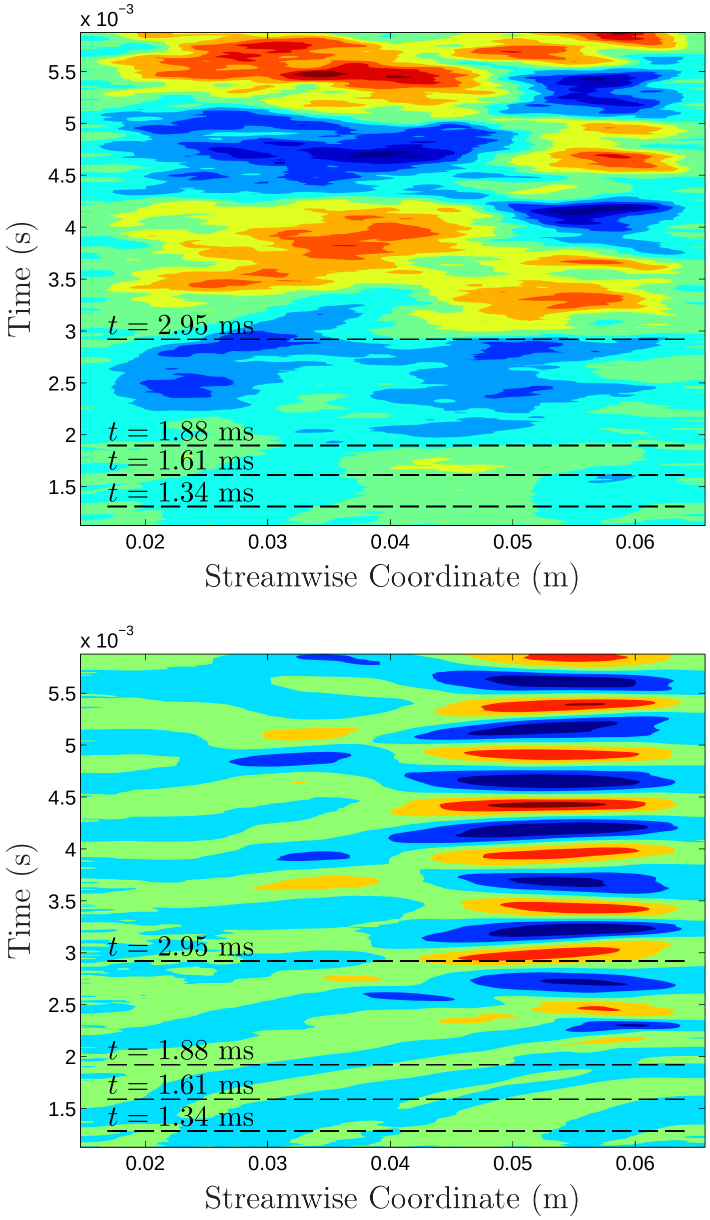

Figure 10.17: x-t diagram of panel deflections along the centerline of the panel ($z = .0127$ m) in the (a) one-way coupled and (b) two-way coupled cases. The times $t = 1.34,\ 1.61,\ 1.88$, and 2.95 ms corresponding to Fig. 10.13-Fig. 10.16 are marked with dashed lines.

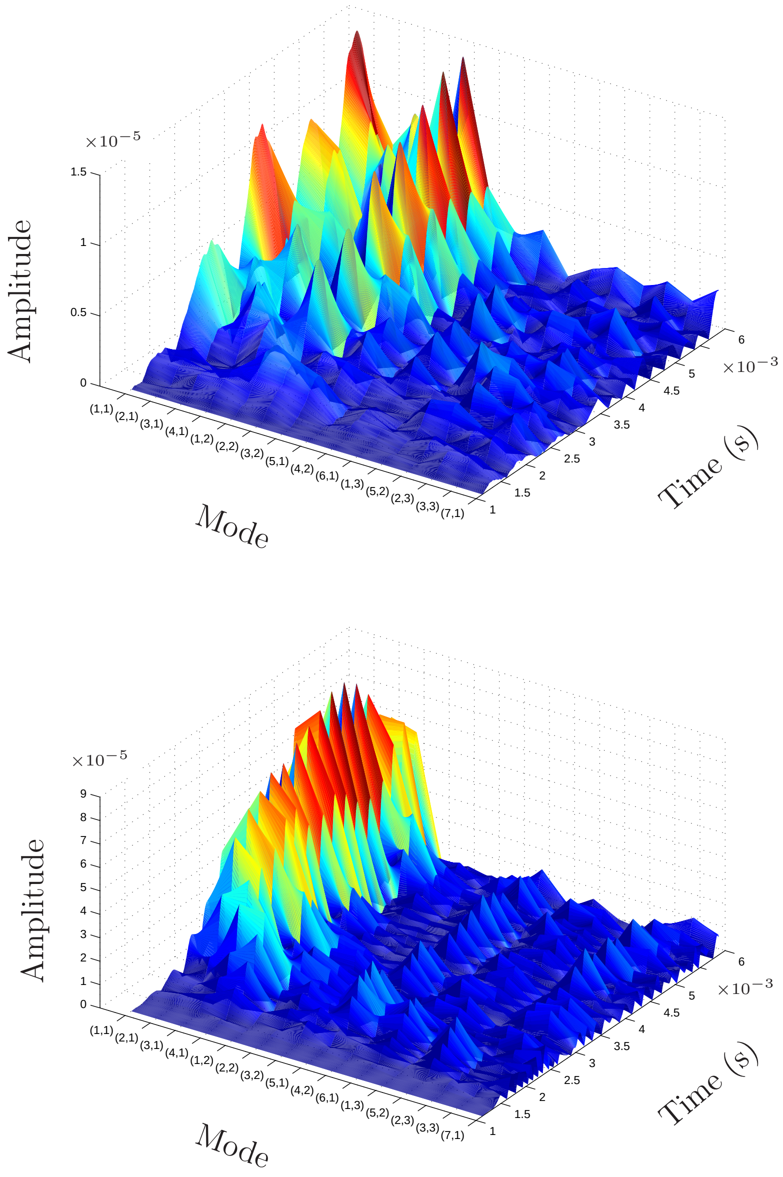

Figure 10.18: Evolution of the first 15 spatial modes of the in the (a) one-way and (b) two-way coupled panel response. Note the substantial difference in amplitude.

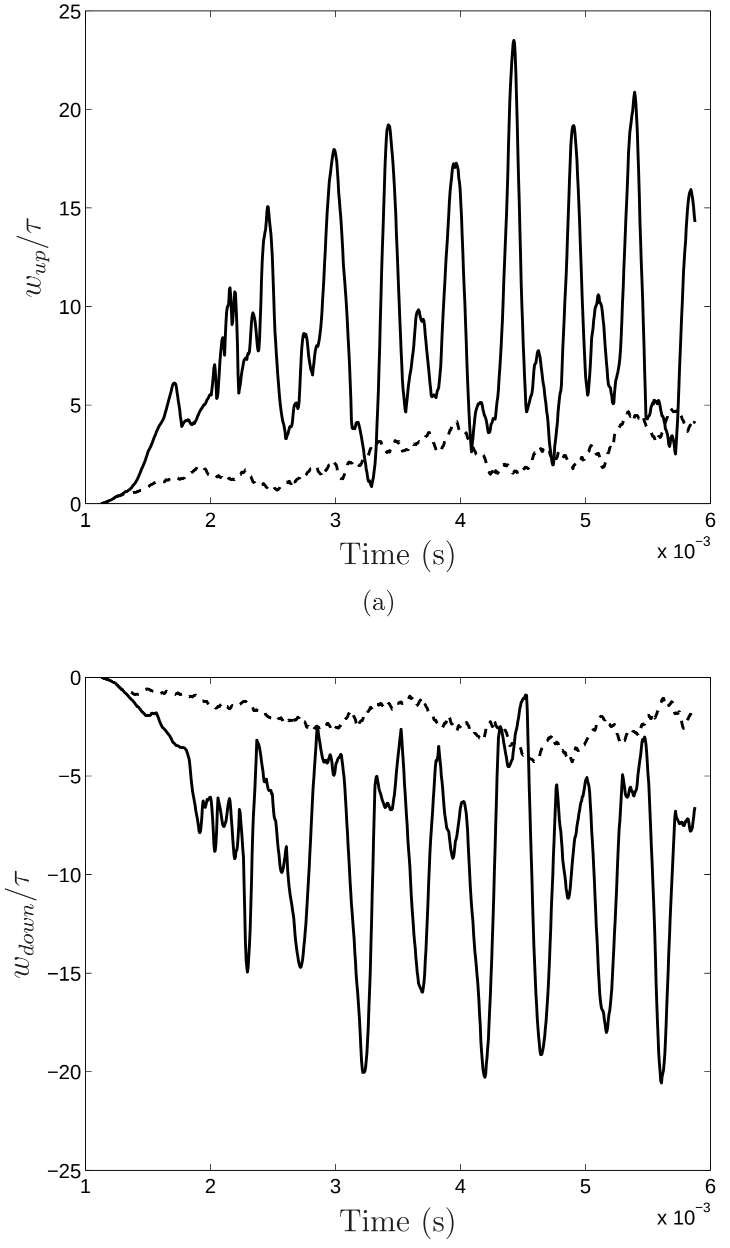

(a)

(b)

Figure 10.19: Evolution of the maximum panel deflection (a) into and (b) out of the flow obtained for the one-way (dashed) and two-way coupled (solid) simulations. The deflections are normalized by panel thickness, τ.

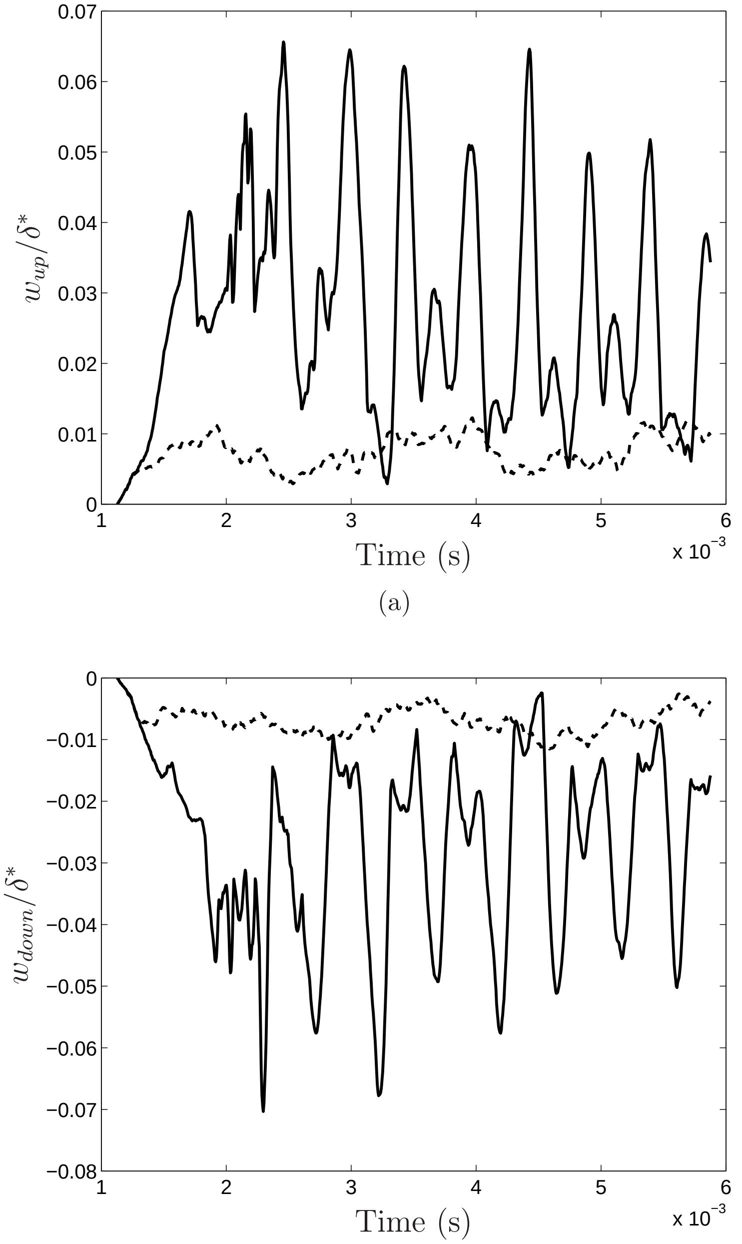

(a)

(b)

Figure 10.20: Evolution of the maximum panel deflections (a) into and (b) out of the flow comparing the one-way (dashed) and two-way coupled (solid) solutions. The deflections are normalized by the rigid panel boundary layer displacement thickness, δ^*.

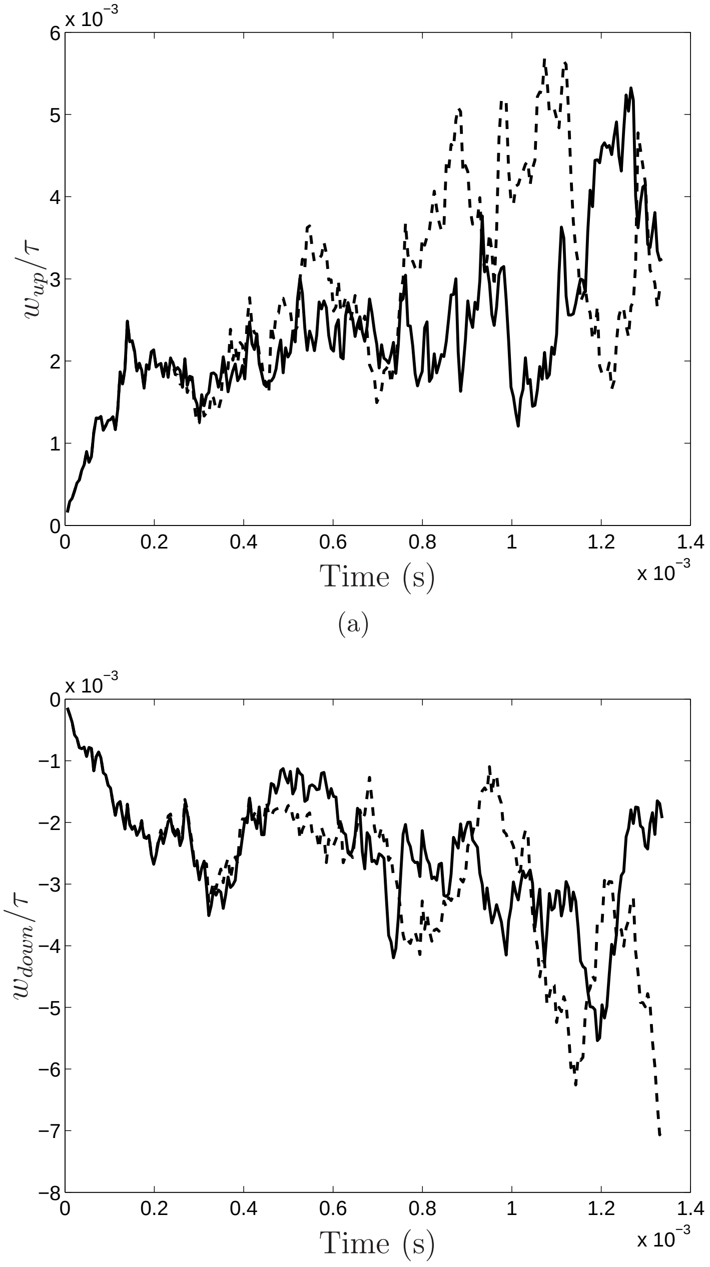

(a)

(b)

Figure 10.21: Maximum deformation of the thick panel with time into (a) and out of (b) the flow in two-way (solid) and one-way (dashed) coupled simulations. Deformations are normalized by the panel thickness, $\tau = 150\ \mu$m.

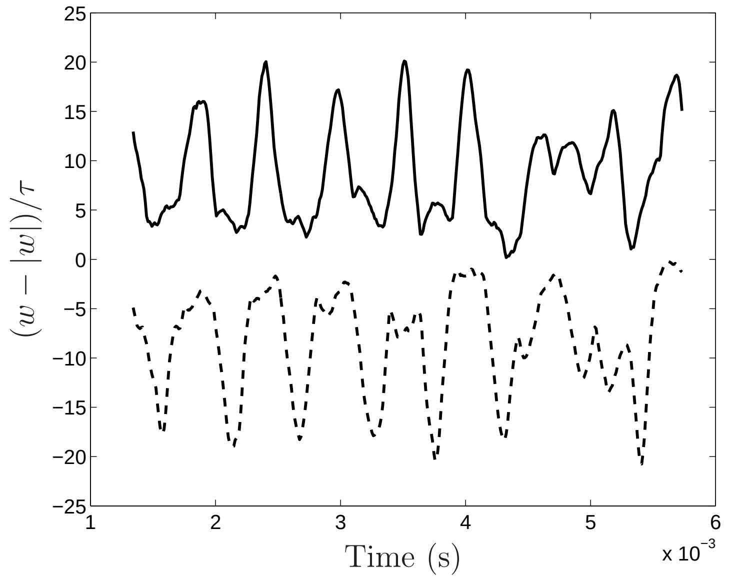

(a)

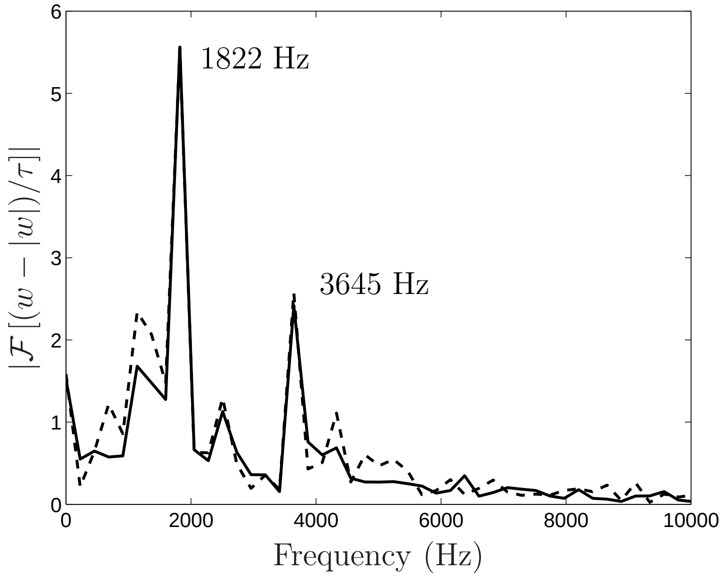

(b)

Figure 10.22: (a) Panel deformation into (solid) and out of (dash) the boundary layer over a truncated window for long domain length simulation. (b) Corresponding Fourier transform of data over that data.

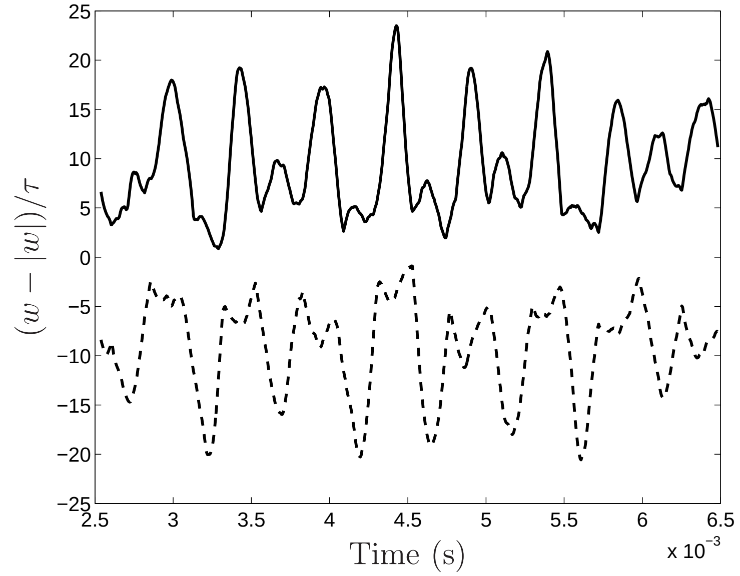

(a)

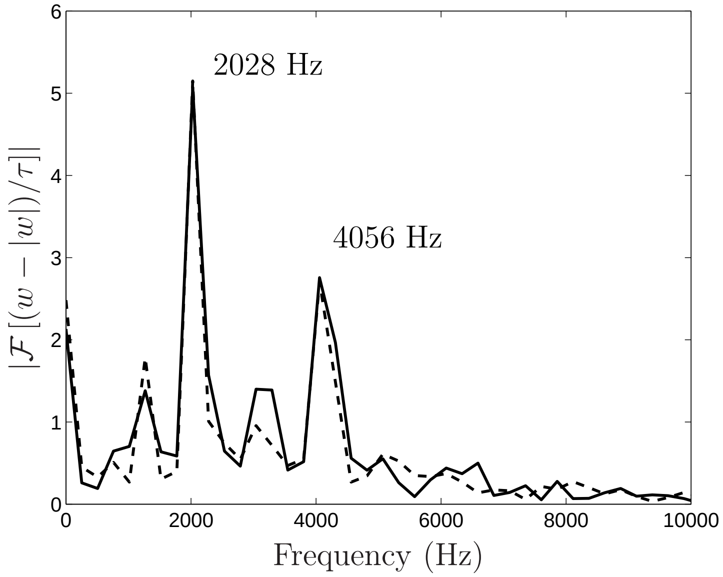

(b)

Figure 10.23: Same as Fig. 10.22 for the short domain simulation.

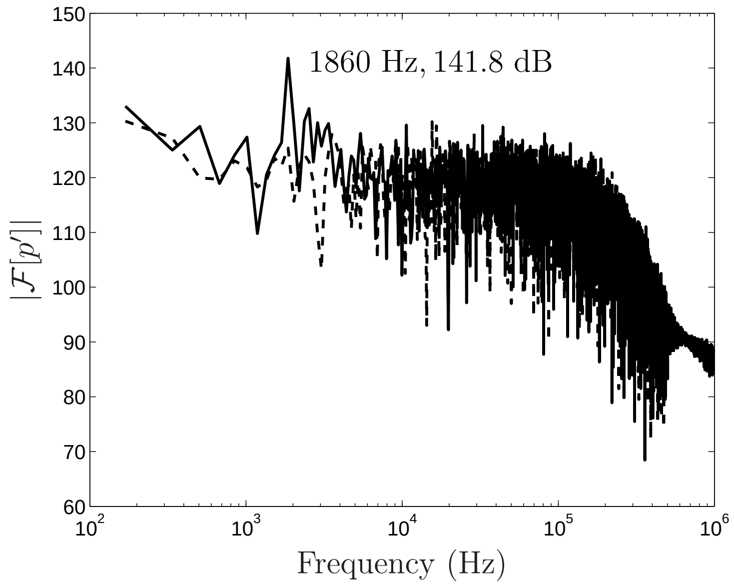

Figure 10.24: Pressure spectra exhibiting the difference in the post-panel pressure fluctuations between the rigid (dashed) and compliant (solid) panel cases in the long domain simulations.

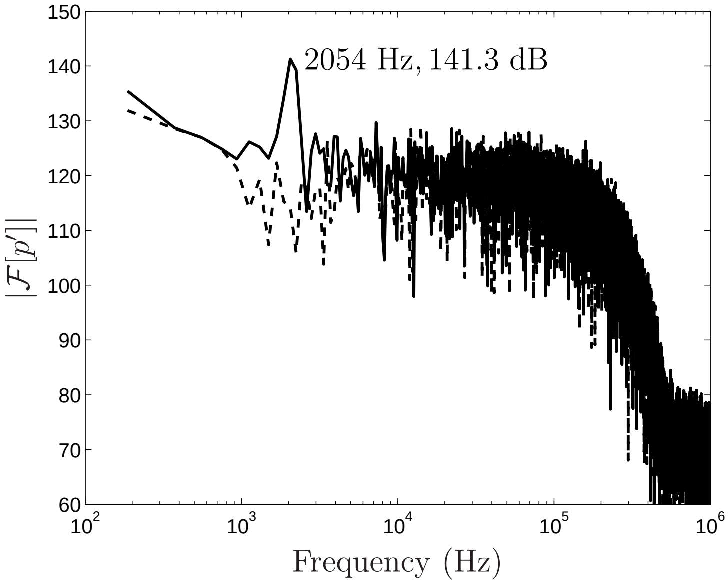

Figure 10.25: Same as Fig. 10.24 for the short domain simulations.

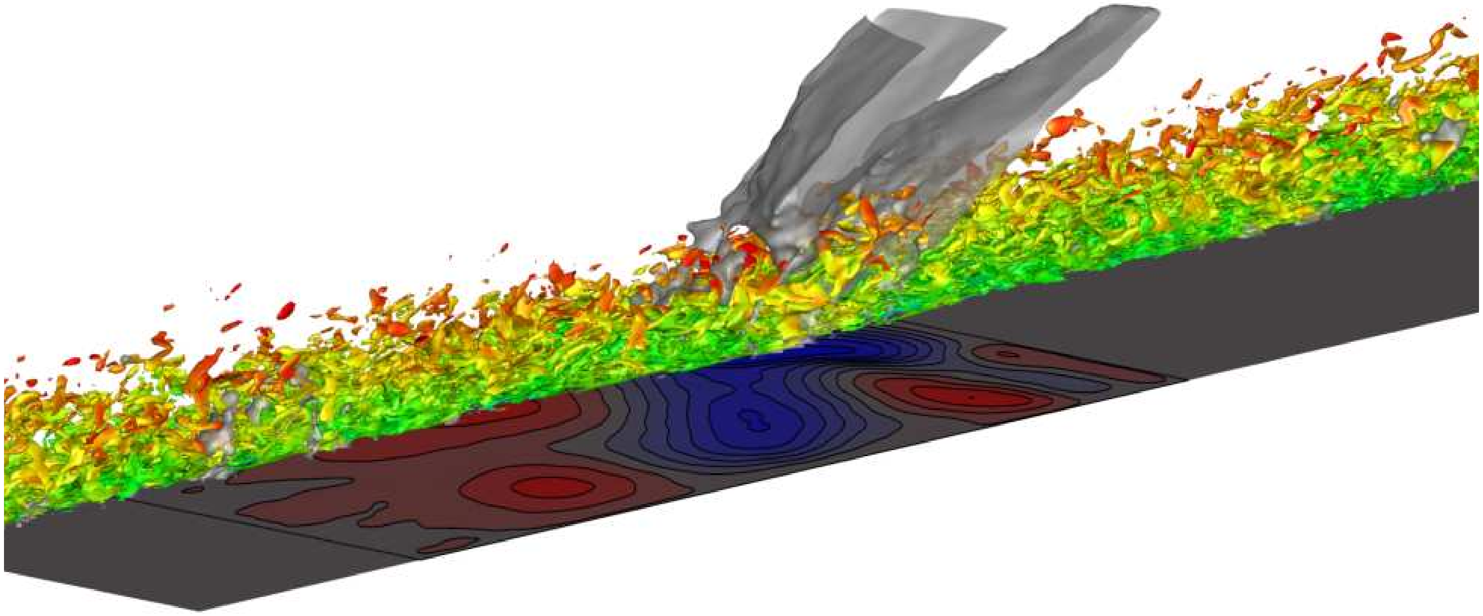

Figure 10.26: Fluid and panel state at $t = 0.98$ ms. The panel deformations are emphasized with blue (negative) and red (positive) contours. Turbulent structures are presented as constant scalar vorticity surfaces and are colored by streamwise velocity. Compression waves resulting from panel deformations are shown in gray.

(a) $t = 0.85$ ms

(b) $t = 1.07$ ms

(c) $t = 1.29$ ms

(d) $t = 1.47$ ms

Figure 10.27: Compression wave locations due to panel deformations at (a) $t = 0.85$ ms, (b) $t = 1.07$ ms, (c) $t = 1.29$ ms, and (d) $t = 1.47$ ms. Pressure isosurfaces representing compression waves colored by streamwise velocity contours. Pressure contours on the extreme spanwise boundary are also shown.

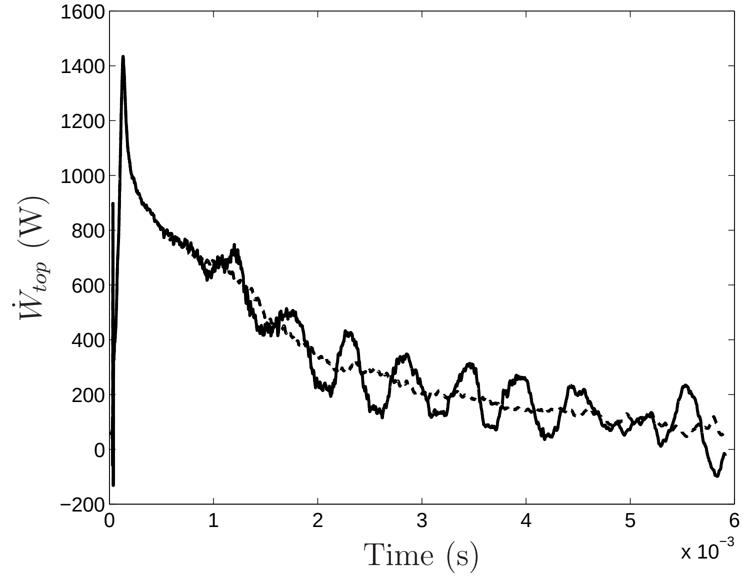

Figure 10.28: Power out of the top of the fluid domain in the rigid (dashed) and compliant (solid) panel simulations.

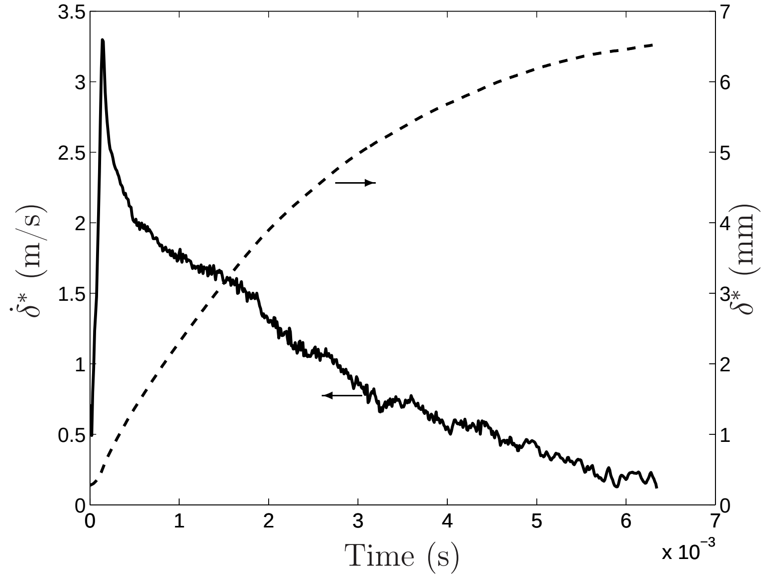

Figure 10.29: Displacement thickness, δ^*, (dashed) and time derivative of displacement thickness, $\dot{\delta}^*$ (solid) in the rigid panel simulation.

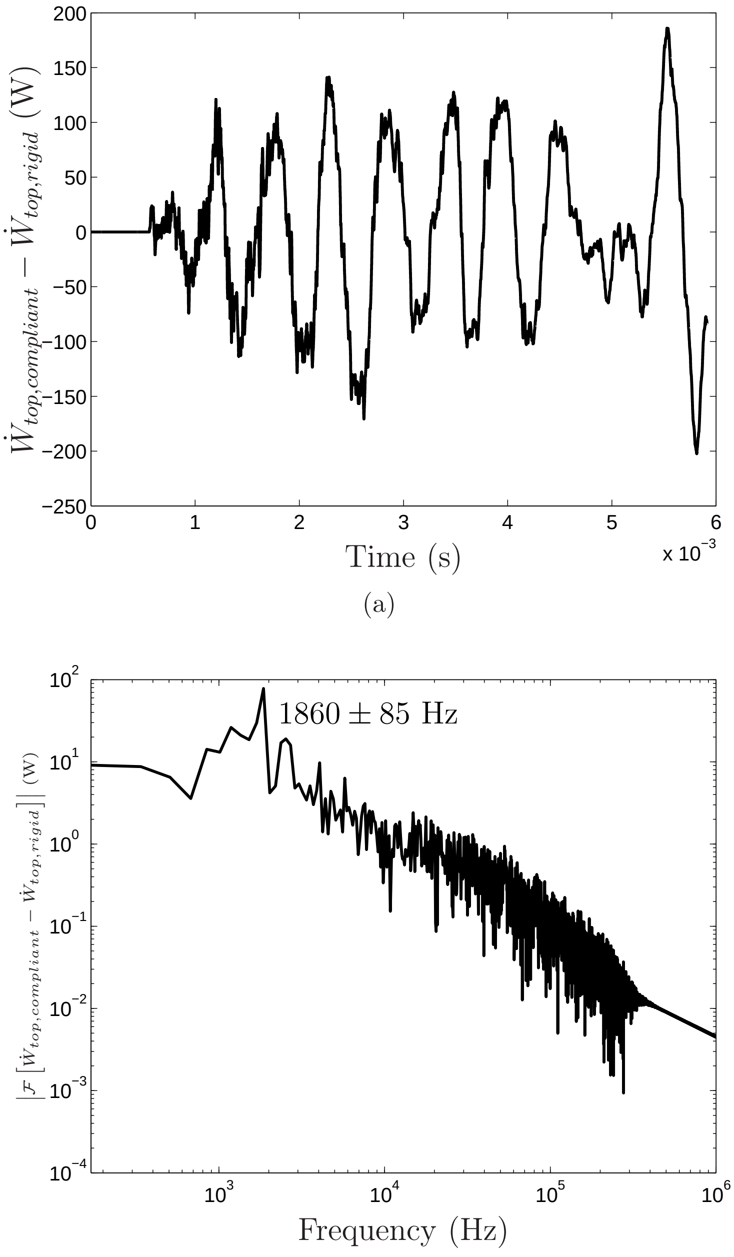

(a)

(b)

Figure 10.30: (a) Difference in the power out of the top of the fluid domain between the rigid and compliant panel cases in the long domain simulation. (b) Fourier transform of the power difference.

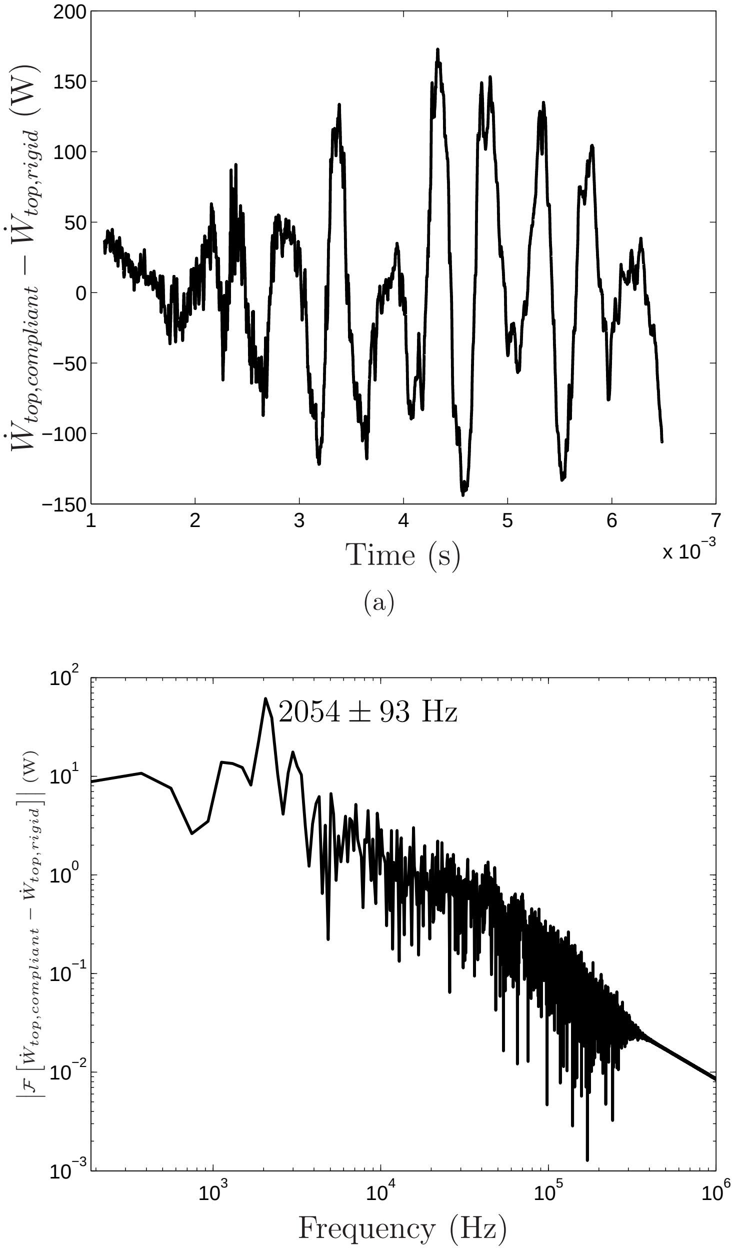

(a)

(b)

Figure 10.31: (a) Difference in the power out of the top of the fluid domain between the rigid and compliant panel cases in the short domain simulation. (b) Fourier transform of the power difference.

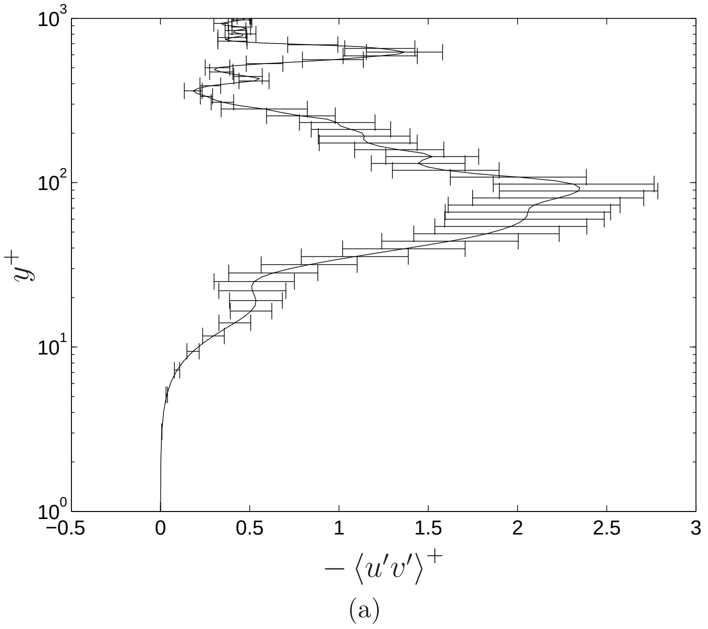

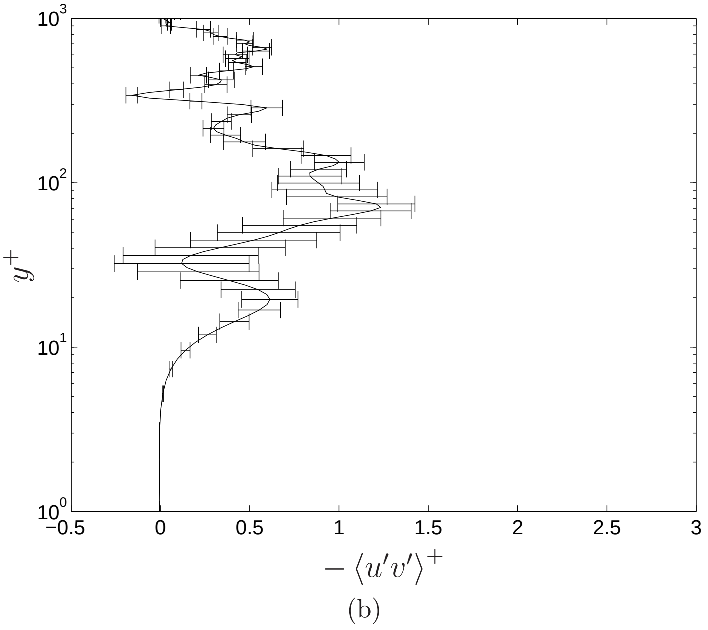

Figure 10.32: Reynolds shear stress profile above (a) rigid and (b) compliant panel for $t = 1.56 \pm 0.05$ ms corresponding to the time when the panel is deflected out of the boundary layer. Error bars represent 95% confidence intervals.

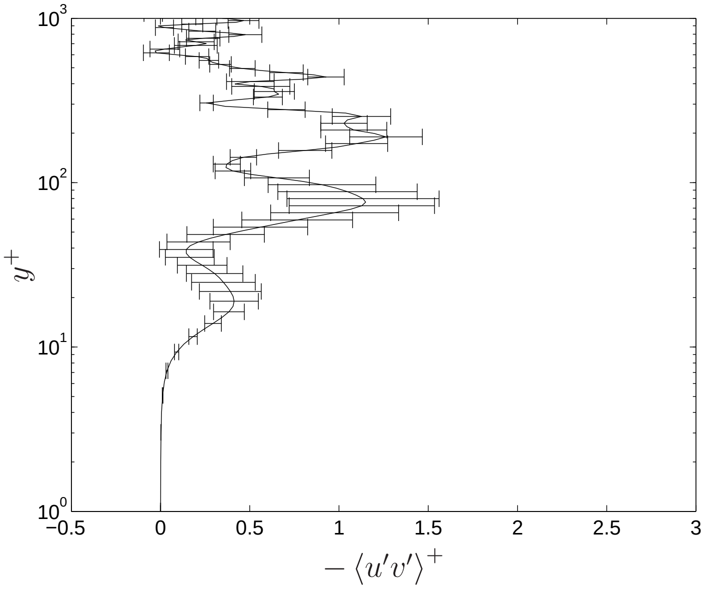

(a)

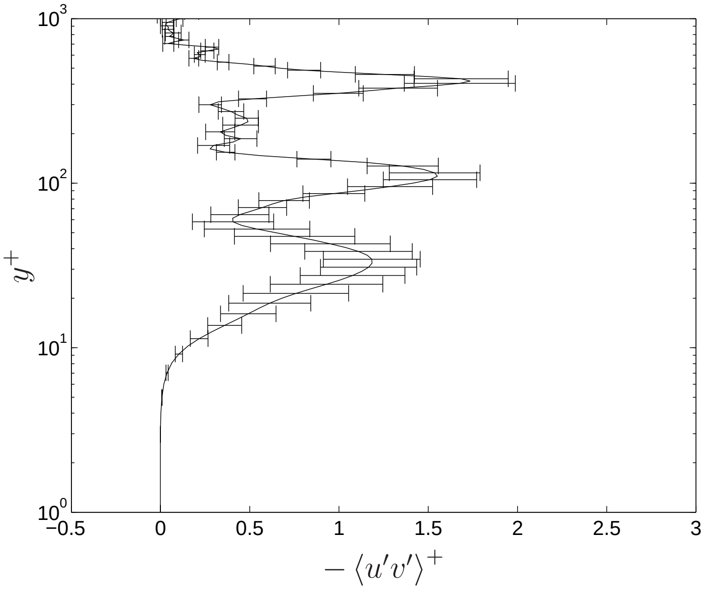

(b)

Figure 10.33: Reynolds shear stress profile above (a) rigid and (b) compliant panel for $t = 1.86 \pm 0.05$ ms corresponding to the time when the panel is deflected out of the boundary layer. Error bars represent 95% confidence intervals.

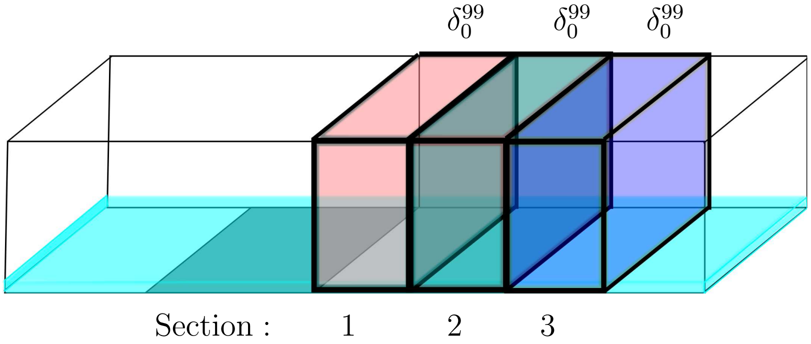

Figure 10.34: Post-panel regions over which TKE budget terms (Eq. (G.2)) are compared between rigid and compliant panel simulations. Each section is $1/2\delta_0^{99} \approx 1$ integral length scale, where δ_0^{99} is the initial boundary layer thickness .

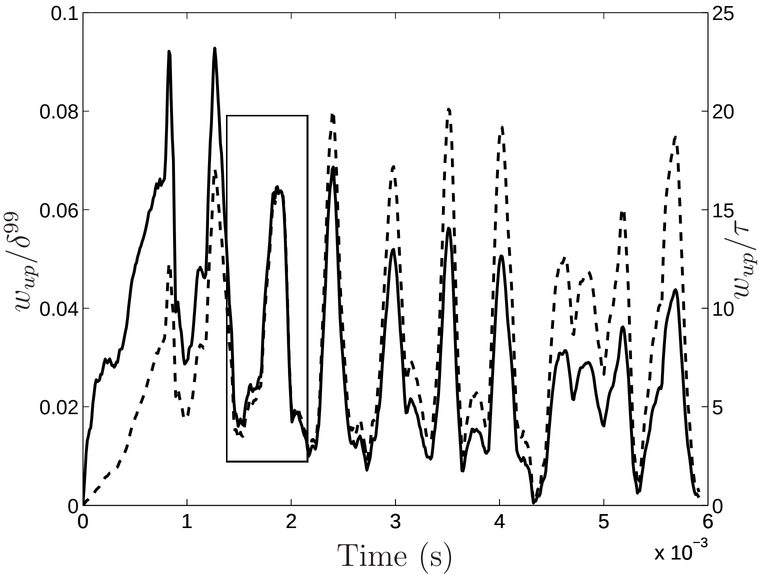

(a)

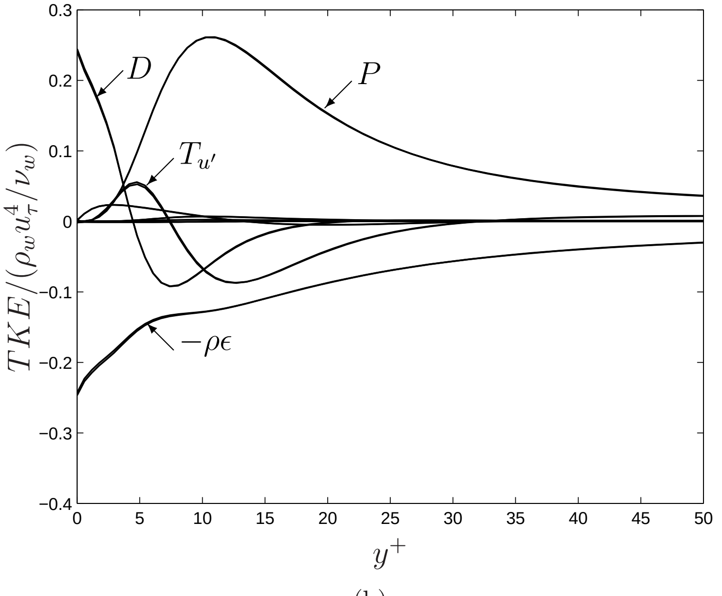

(b)

Figure 10.35: (a) Time period over which the TKE budget is averaged for comparison of post-panel statistics between the rigid and compliant panel cases. (b) Rigid and compliant panel TKE budget terms averaged over the time period shown in (a). The viscous diffusion, D, production, P, turbulent transport, $T_{u'}$, and viscous dissipation, $-\rho\epsilon$, are the dominant terms and are given by Eq. (G.2)

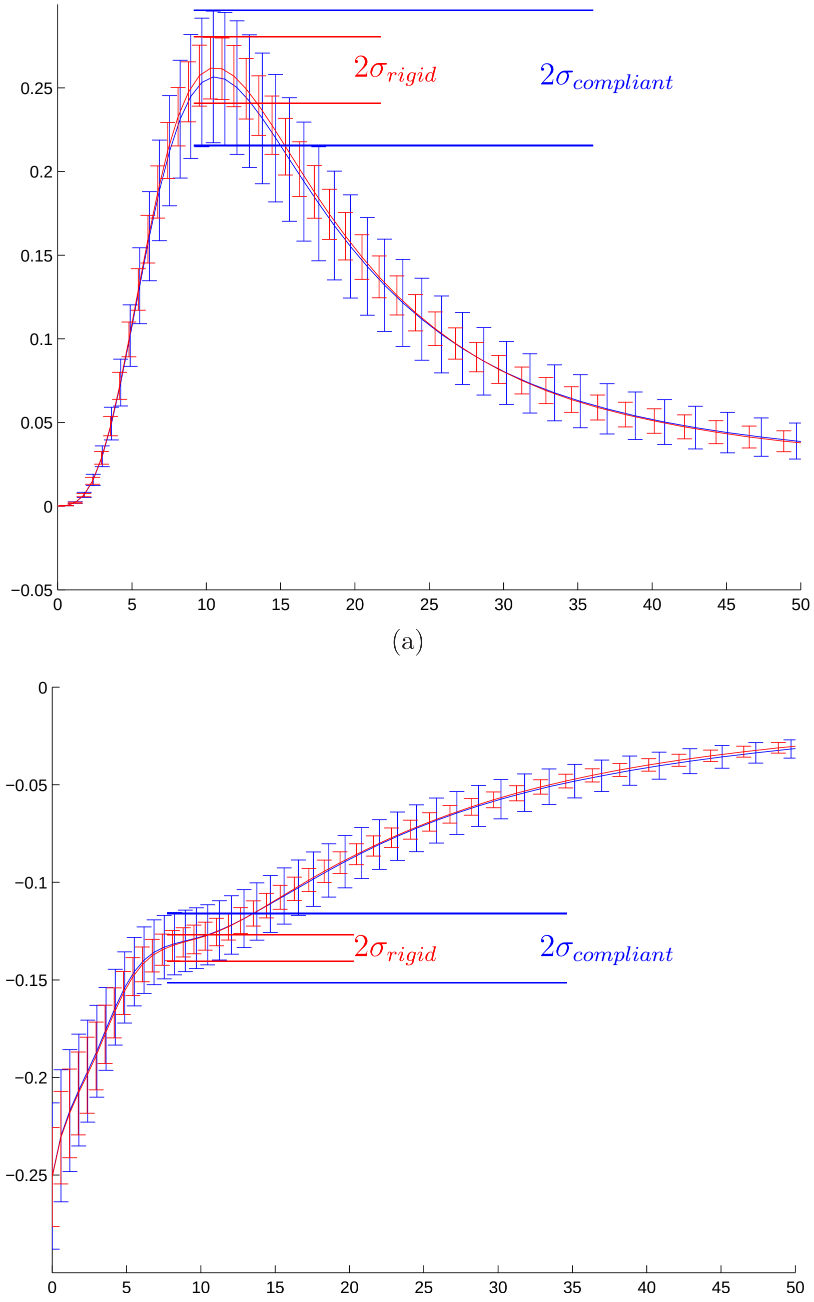

(a)

(b)

Figure 10.36: Comparison of TKE budget terms (a) production (P) and (b) viscous dissipation ($-\rho\epsilon$) between the rigid and compliant panel cases with error bars of ± one standard deviation. The deviations in the compliant panel case are larger than those in the rigid panel case, indicating that the fluctuations in P and $-\rho\epsilon$ due to the panel motion still exist in station 1.

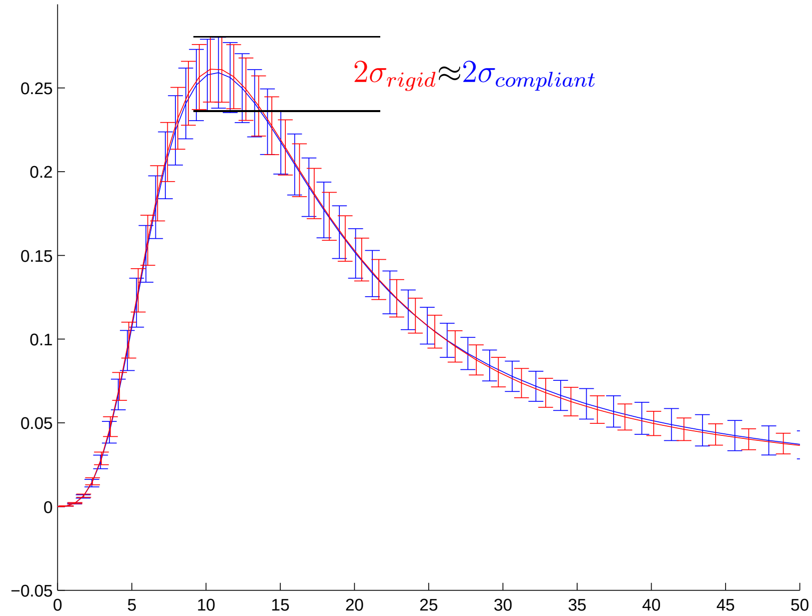

(a)

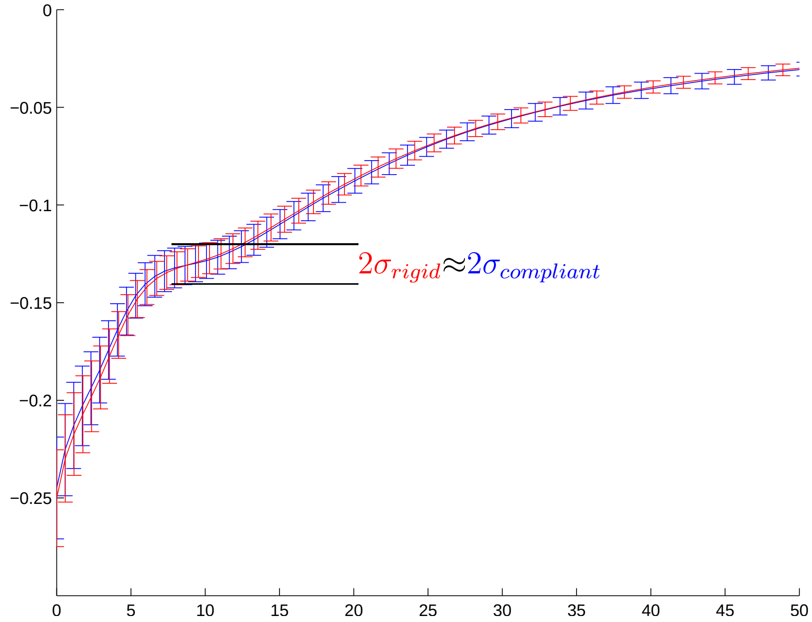

(b)

Figure 10.37: Comparison of TKE budget terms (a) production (P) and (b) viscous dissipation ($-\rho\epsilon$) between the rigid and compliant panel cases with error bars of ± one standard deviation. The standard deviations in the terms between the rigid panel and compliant panel cases are similar, indicating that the effect of the panel motion has been forgotten by section 2.

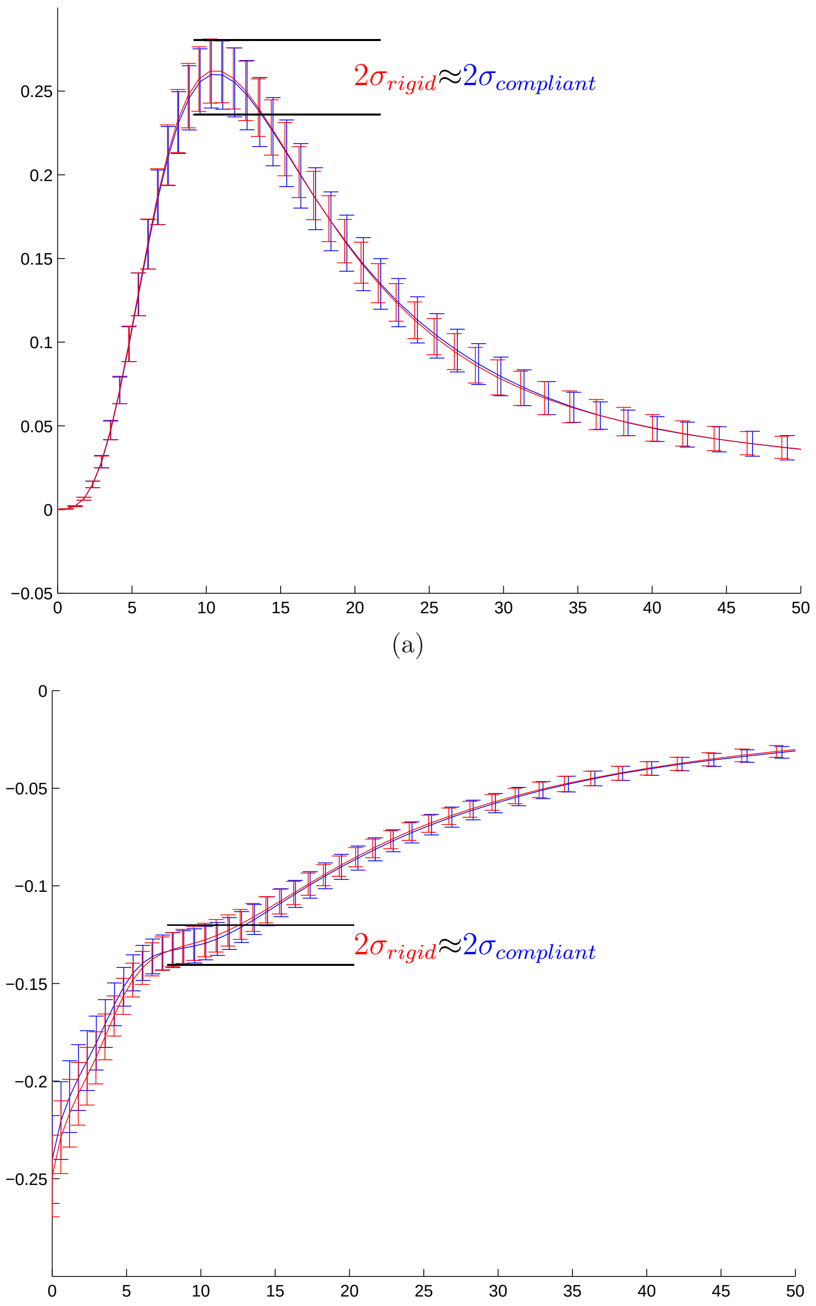

(a)

(b)

Figure 10.38: Comparison of TKE budget terms (a) production (P) and (b) viscous dissipation ($-\rho\epsilon$) between the rigid and compliant panel cases with error bars of ± one standard deviation. Deviations in the terms between the rigid panel and compliant panel cases are similar.

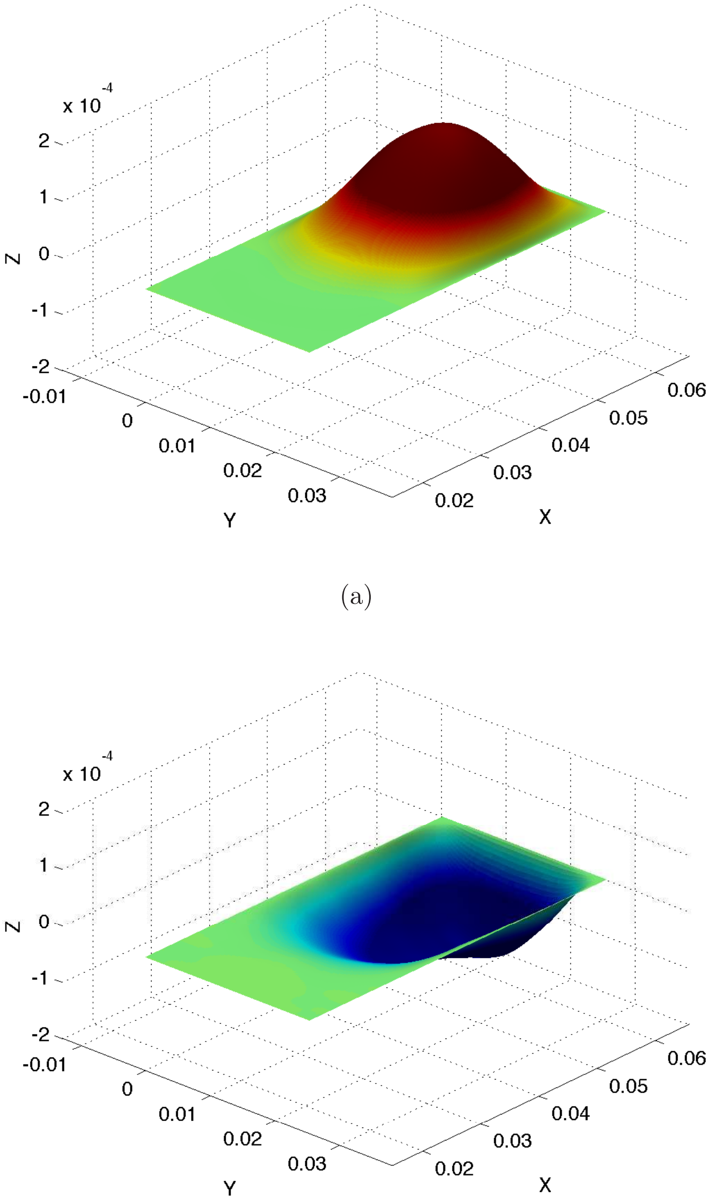

(a)

(b)

Figure 10.39: (a) Up and (b) down states of the panel response under aerodynamic loading provided by piston theory.

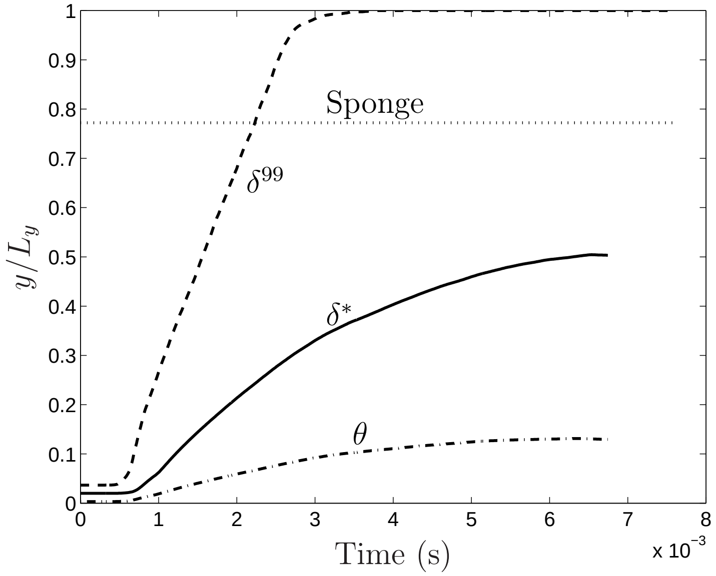

Figure 10.40: Boundary layer thickness, δ^{99} (dashed), displacement thickness δ^*, (solid), and momentum thickness, θ (dash-dot) in the short domain rigid panel simulation. The beginning of the sponge region is shown by a dotted line.

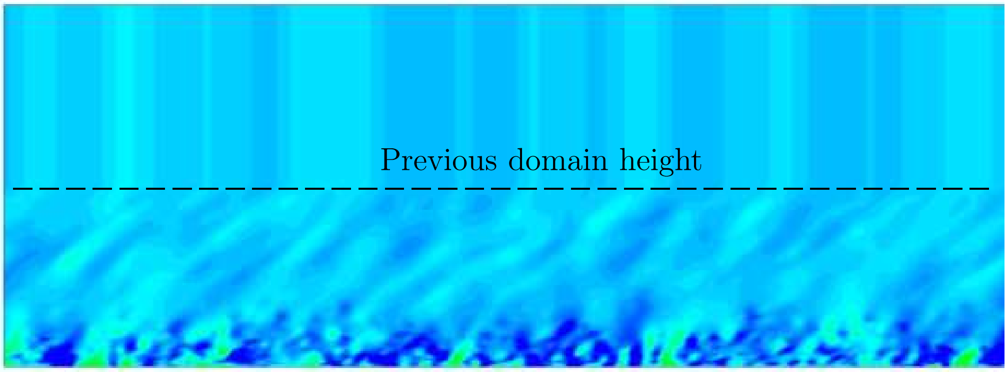

Figure 10.41: Boundary layer thickness, δ^{99} (dashed), displacement thickness δ^*, (solid), and momentum thickness, θ (dash-dot) in the short domain rigid panel simulation. The beginning of the sponge region is shown by a dotted line.

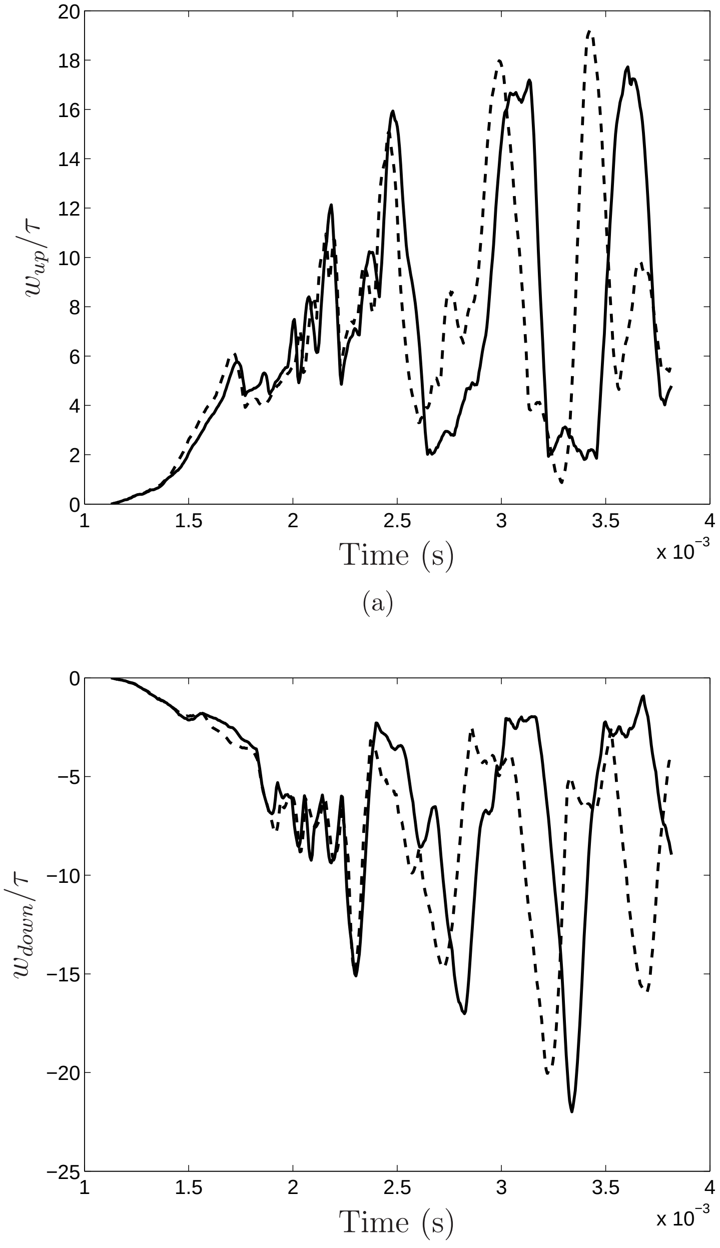

(a)

(b)

Figure 10.42: Comparison between short domain and tall domain simulation maximum panel deformations with time (a) into and (b) out of the flow. Deformations normalized by panel thickness, τ.

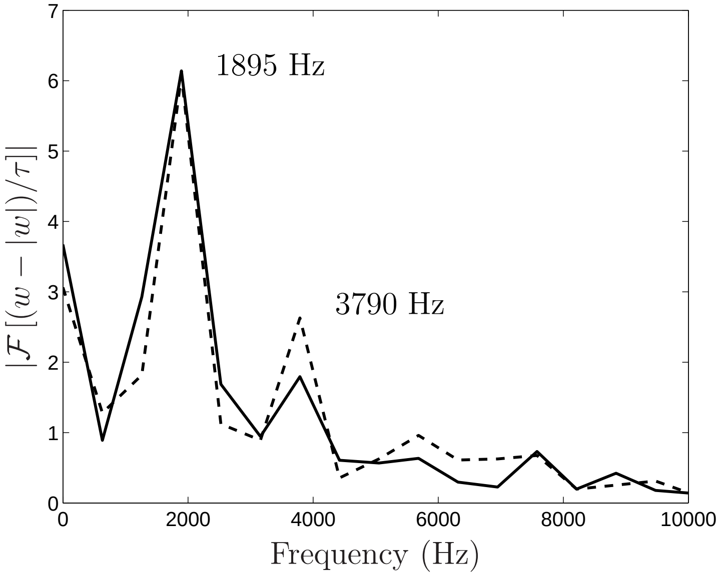

Figure 10.43: Fourier transform of maximum panel deformations into (solid) and out of (dashed) the boundary layer in the tall domain simulation.

Chapter 11

Conclusions and Future Work

11.1 Conclusions

Future high performance vehicles are desired to be lightweight, flexible, and reusable. Structures satisfying these requirements are subject to complex fluid-structure interactions at the desired extreme flight conditions. To better understand the interactions between a fluid and a solid in high-speed flows, a high-fidelity, coupled, numerical approach to structural response prediction was taken. The work presented was composed of two parts including coupled fluid-thermal and fluid-structural studies.

In Part I, the fluid-thermal problem was motivated by a phenomena observed when thin National Aerospace Plane (NASP) thermal protection system (TPS) panels bowed into the flow field due to thermal gradients. The resulting modified geometry produced changes in the thermal and mechanical loading both on the TPS panel and surrounding area. A finite-element thermal solver was developed and coupled with an existing finite difference Navier-Stokes solver to investigate the effects of fluid-thermal coupling in this scenario. In addition to the validation of the coupled solver by comparison with experimental results, the following conclusions resulted from Part I:

1. Reynolds analogy provides a fair relation between surface shear stress and heat flux over a flat plate, but fails in the presence of geometry changes and pressure gradients.

2. Semi-analytical and reduced-order models based on inviscid aerodynamics reproduce some qualitative trends but significantly overpredict quantitatively the heat loads on the deformed geometry. Additionally, significant features in the heat flux, such as those due to vortex shedding, are completely missed by the inviscid approach.

3. To accurately predict the thermal solution, thermal loading, geometrical features, and material properties must be accounted for.

4. In flows that contain regions of extreme temperatures, the calorically perfect assumption may not be justified and the use of more general gas models are required to make accurate predictions.

5. The high temperatures of the solid domain that resulted from an extended period of time in hypersonic flow led to changes in the flow solution, decreasing the drag and heat load on the structure.

In Part II, the response of a thin metallic panel under a fully turbulent supersonic boundary layer was studied. The fluid solution incorporated no turbulence model and all turbulent scales were resolved. The structural solution of the panel state required the development of a non-linear finite-element formulation, which was coupled with the flow solver at the fluid-solid interface. The effect of coupling on both the fluid and structural response were studied. The study in Part II yielded the following results:

1. The panel response is initially broadband and low amplitude under the turbulent fluctuations, but at later times under aerodynamic pressure, the response is dominated by high amplitude low mode waves.

2. Changes in surface topology lead to the generation of oscillating compression and expansion waves, which may cause localized unsteady loads on an opposing wall in internal flow applications.

3. Fluctuations generated by the fluttering panel modify the power out of the top of the fluid domain, but make a negligible contribution to the overall power balance in the flow.

4. Significant panel response is due to an aeroelastic instability and is not driven by turbulent loading.

5. Viscous loading on the panel does not contribute significantly to the power balance in the panel.

6. Two-way coupling is shown to be very important in response prediction of a panel interacting with a compressible turbulent boundary layer in conditions where panel flutter is expected.

7. Under the conditions studied, the panel motion may effect turbulence statistics locally, but the effect of the interaction with the panel on the turbulence is forgotten within one integral length downstream.

11.2 Future work

This work has presented results from high-fidelity fluid-thermal and fluid-structural coupled simulations in high-speed flows. A natural progression suggests a study involving fluid-thermal-structural interaction. However, several incremental steps are necessary to advance the application of the high-fidelity, high-accuracy approach developed here to a realistic, high-speed aerothermoelastic problem, which would likely involve a turbulent boundary layer.

In the work presented in Part II of this thesis, significant difficulties and limitations were imposed by the use of temporally developing boundary layer. While the TDNS approach allowed for the use of a smaller computational fluid domain, the following three drawbacks are sufficient evidence that the approach should be changed in future studies. First, the generation of the TBL involved the use of non-physical suppression of the boundary layer growth in order for the unstable perturbations to amplify to the point where the laminar boundary layer began to transition. A second, more detrimental feature is that the temporal growth limited the time record of the simulation as the boundary layer outgrew the height of the computational domain. A third, equally severe limitation of the TDNS approach is that the growing boundary layer made difficult the analysis of turbulence statistics. The short domain afforded by the TDNS in this study allowed for a relatively large streamwise extent which could accommodate a wide compliant panel. Even so, the panel dimensions were unrealistic. A next iteration in the high-fidelity structural response prediction should involve a spatially developing boundary layer over a more realistic sized panel. The computational investment in such a study would be significantly larger

Another advancement is needed in the algorithms applied to these problems. Both the spatial and temporal coupling strategies used in this work can be improved. In Part I, the common refinement based load transfer scheme allowed for conservative load transfer between non-matching meshes, but was cumbersome in its implementation. In Part II, the use of matching nodes at the interface required the structural mesh to have the same level of refinement as the fluid mesh. The TBL resolution requirements led to unnecessary computational effort on the structural problem. Due to the highly disparate time scales involved in fluid turbulence, structural, and thermal physics, aerothermoelastic computations are required to be temporally resolved with regard to turbulence but long enough to capture the evolution of the thermal solution. Temporal coupling schemes need to be developed for accurate yet efficient communication between the three solutions.

Continued collaboration between experimental and numerical approaches is needed for the purpose of validation. The above mentioned advances need to be made to simulate realistic geometries used in experiments.

Chapter 12

References

[1] CE Glass and LR Hunt. Aerothermal tests of spherical dome protuberances on a flat plate at a Mach number of 6.5. *NASA STI/Recon Technical Report N*, 87, 1986.

[2] G. Cheng and C. Mei. Finite element modal formulation for hypersonic panel flutter analysis with thermal effects. *AIAA J.*, 42(4):687–695, April 2004.

[3] S. Pirozzoli, F. Grasso, and TB Gatski. Direct numerical simulation and analysis of a spatially evolving supersonic turbulent boundary layer at M= 2.25. *Phys. Fluids*, 16:530, 2004.

[4] M. R. Malik. Numerical methods for hypersonic boundary-layer stability. *J. Comp. Phys.*, 86:376–413, 1990.

[5] DARPA/TTO. Blackswift program solicitation 08-02. Technical report, 2008.

[6] DreamSaver Enterprises, LLC, 2013.

[7] Third Army/U.S. Army Central. Defense video and imagery distribution system, 2013.

[8] C. Campbell. Sts-128 boundary layer transition-hythirm briefing materials, 2013.

[9] C.E. Glass and L.R. Hunt. Aerothermal tests of quilted dome models on a flat plate at a Mach number of 6.5. *NASA STI/Recon Technical Report N*, 88, 1988.

[10] J.D. Houbolt. On the estimation of pressure fluctuations in boundary layers and wakes. TIS 662SD296, GE, April 1966.

[11] F. M. White. *Viscous Fluid Flow*. McGraw-Hill, Inc., U. S. A., 2nd edition, 1991.

[12] R. D. Blevins, I. Holehouse, and K. R. Wentz. Thermoacoustic loads and fatigue of hypersonic vehicle skin panels. *J. Aircraft*, 30(6):971–978, 1993.

[13] P. Pozefsky, R. D. Blevins, and A. L. Laganelli. Thermo-vibro-acoustic loads and fatigue of hypersonic flight vehicle structure. Technical Report AFWAL-TR-89-3014, Flight Dynamics Laboratory, AFRL, 1989.

[14] J.J. Bertin and R.M. Cummings. Fifty years of hypersonics: where we've been, where we're going. *Progress in Aerospace Sciences*, 39(6-7):511–536, 2003.

[15] A. J. Culler and J. J. McNamara. Studies on fluid-thermal-structural coupling for aerothermoelasticity in hypersonic flow. *AIAA J.*, 48(8):1721–1738, 2010.

[16] National Research Council. Review and evaluation of the air force hypersonic technology program. Technical Report AFSB-J-97-01-A, 1998.

[17] S. Pirozzoli and F. Grasso. Direct numerical simulation of impinging shock wave/turbulent boundary layer interaction at M= 2.25. *Phys. Fluids*, 18, 2006.

[18] A.J. Culler and J.J. McNamara. Impact of fluid-thermal-structural coupling on response prediction of hypersonic skin panels. *AIAA J.*, 49(11):2393–2406, 2011.

[19] M. J. Lighthill. Oscillating airfoils at high mach numbers. *Journal of the Aeronautical Sciences*, 20(6):402–406, June 1953.

[20] ERG Eckert. Engineering relations for heat transfer and friction in high-velocity laminar and turbulent boundary-layer flow over surfaces with constant pressure and temperature. *J. Aero. Sci.*, 22(8):585–587, 1955.

[21] A.R. Crowell and J.J. McNamara. Model reduction of computational aerothermodynamics for hypersonic aerothermoelasticity. *AIAA J.*, 50(1):74 – 84, 2012.

[22] N.J. Falkiewicz and C.E.S. Cesnik. Proper orthogonal decomposition for reduced-order thermal solution in hypersonic aerothermoelastic simulations. *AIAA J.*, 49:994–1009, 2011.

[23] P. Dechaumphai, A. Wieting, and E. Thornton. Flow-thermal-structural study of aerodynamically heated leading edges. *Journal of Spacecraft and Rockets*, 26:201–209, 1989.

[24] P. Dechaumphai, P., A. Wieting, A., and A. Pandey. Fluid-thermal-structural interaction of aerodynamically heated leading edges. In *AIAA, ASME, ASCE, AHS, and ASC, Structures, Structural Dynamics and Materials Conference, 30 th, Mobile, AL*, pages 621–631. AIAA, 1989.

[25] E.A. Thornton and P. Dechaumphai. Coupled flow, thermal, and structural analysis of aerodynamically heated panels. *J. Aircraft*, 25(11):1052–1059, 1988.

[26] D. Kontinos and G. Palmer. Numerical simulation of metallic tps panel bowing. *J. Spacecraft and Rockets*, 36(6):842–849, 1997.

[27] A.J. Culler and J.J. McNamara. Coupled flow-thermal-structural analysis for response prediction of hypersonic vehicle skin panels. volume AIAA-2010-2965 of *51st AIAA/ASME/ASCE/AHS/ASC Structures, Structural Dynamics, and Materials Conference*. AIAA, April 2010.

[28] B. Hassan, D.W. Kuntz, D.E. Salguero, and D.L. Potter. A coupled fluid/thermal/flight dynamics approach for predicting hypersonic vehicle performance. Number AIAA-2001-2903, 2001.

[29] A.R. Crowell, B.A. Miller, and J.J. McNamara. Computational modeling for conjugate heat transfer of shock-surface interactions on compliant skin panels. Number AIAA-2011-2017. 52nd AIAA/ASME/ASCE/AHS/ASC Structures, Structural Dynamics and Materials Conference, Denver, Colorado, Apr. 4-7, 2011.

[30] X. Zhao, Z. Sun, L. Teng, and G. Zheng. Coupled flow-thermal-structural analysis of hypersonic aerodynamically heated cylindrical leading edge. *Eng. Appl. Comp. Fl. Mech.*, 5(2):170–179, June 2011.

[31] M. Vinokur. Conservation equations of gasdynamics in curvilinear coordinate systems. *J. Comp. Phys.*, 14:105–125, 1974.

[32] B. Strand. Summation by parts for finite difference approximations for d/dx. *J. Comp. Phys.*, 110:47–67, 1994.

[33] K. Mattsson, M. Svärd, and J. Nordström. Stable and accurate artificial dissipation. *J. Sci. Comput.*, 21(1):57–79, 2004.

[34] M. H. Carpenter, D. Gottlieb, and S. Abarbenel. Time-stable boundary conditions for finite difference schemes involving hyperbolic systems: Methodology and application for high-order compact schemes. *J. Comp. Phys.*, 111:220–236, 1994.

[35] M. Svärd, M. H. Carpenter, and J. Nordström. A stable high-order finite difference scheme for the compressible navier-stokes equations, far-field boundary conditions. *J. Comp. Phys.*, 225:1020–1038, 2007.

[36] M. Svärd and J. Nordström. A stable high-order finite difference scheme for the compresible Navier-Stokes equations: No-slip wall boundary conditions. *J. Comp. Phys.*, 227:4805–4824, 2008.

[37] J. Nordström, J. Gong, E. Van der Weide, and M. Svärd. A stable and conservative high order multi-block method for the compressible navier-stokes equations. *J. Comp. Phys.*, 228:9020–9035, 2009.

[38] D. J. Bodony. Accuracy of the simultaneous-approximation-term boundary condition for time-dependent problems. *J. Sci. Comput.*, 43(1):118–133, 2010.

[39] T. H. Pulliam and D. S. Chaussee. A diagonal form of an an implicit approximate-factorization algorithm. *J. Comp. Phys.*, 43:357–372, 1981.

[40] D. J. Bodony. Analysis of sponge zones for computational fluid mechanics. *J. Comp. Phys.*, 212:681–702, 2006.

[41] S. K. Lele. Compact finite difference schemes with spectral-like resolution. *J. Comp. Phys.*, 103:16–42, 1992.

[42] S. Kawai, SK Shankar, and SK Lele. Les of compressible turbulent flows: assessment of compact differencing with localized artificial diffusivity scheme, 2009.

[43] E.W. Leyhe and R.R. Howell. *Calculation Procedure for Thermodynamic, Transport, and Flow Properties of the Combustion Products of a Hydrocarbon Fuel Mixture Burned in Air with Results for Ethylene-Air and Methane-Air Mixtures.* National Aeronautics and Space Administration, 1962.

[44] J. Kim, D. J. Bodony, and J. B. Freund. LES investigation of a mach 1.3 jet with and without plasma actuators. AIAA Paper 2009-0290, Presented at the 47th Aerospace Sciences Meeting & Exhibit, January 2009.

[45] D. J. Bodony. Heating effects on the structure of noise sources of high-speed jets. AIAA Paper 2009-0291, Presented at the 47th Aerospace Sciences Meeting & Exhibit, Orlando, Florida, Jan. 5-8, 2009.

[46] M. Sucheendran, D. J. Bodony, and P. H. Geubelle. Structural-acoustic interaction of a cavity-backed, clamped, elastic plate with sound in a duct. *Bull. Am. Phys. Soc.*, 54(19), 2009.

[47] G. Zagaris, D. J. Bodony, M. Brandyberry, M. T. Campbell, E. G. Shaffer, and J. B. Freund. A collision detection approach to chimera grid assembly for high fidelity simulations of turbofan noise. In *48th AIAA Aerospace Sciences Meeting*, number 2010–836. AIAA, AIAA, January 2010.

[48] J. Kim, M. Natarajan, D. J. Bodony, and J. B. Freund. A high-order, overset mesh algorithm for adjoint-based optimization for aeroacoustics control. AIAA Paper 2010-3818, Presented at the 16th AIAA/CEAS Aeroacoustics Conference, June 2010.

[49] D. J. Bodony, G. Zagaris, A. Reichert, and Q. Zhang. Aeroacoustic predictions in complex geometries. In R. J. Astley and G. Gabard, editors, *IUTAM Symposium on Computational Aero-Acoustics for Aircraft Noise Prediction*, volume 6, pages 234–243. Procedia Engineering, 2010.

[50] M. Plesha M. Cook, D. Malkus. *Concepts and Applications of Finite Element Analysis*. Wiley, 1974.

[51] Schultz M. Saad, Y. Gmres: A generalized minimal residual algorithm for solving nonsymmetric linear systems. *SIAM J. Sci. Stat. Comp.*, 7(3):856 – 869, July 1986.

[52] ACTS (Advanced CompuTational Software Collection). http://acts.nersc.gov/hypre/.

[53] R.K. Jaiman, X. Jiao, P.H. Geubelle, and E. Loth. Assessment of conservative load transfer for fluid-solid interface with non-matching meshes. *Int. J. Num. Meth. Engng*, 64:2014 – 2038, 2005.

[54] R.K. Jaiman, X. Jiao, P.H. Geubelle, and E. Loth. Conservative load transfer along curved fluid-solid interface with non-matching meshes. *J. Comp. Phys.*, 218:372 – 397, 2006.

[55] M. B. Giles. Stability analysis of numerical interface conditions in fluid-structure thermal analysis. *Int. J. Num. Methods. Fluids*, 25(8):421–436, 1997.

[56] B. Roe, A. Haselbacher, and P. H. Geubelle. Stability of fluid-structure thermal simulations on moving grids. *Int. J. Num. Methods. Fluids*, 54:1097–1117, 2007.

[57] C. Ostoich, D. J. Bodony, and P. H. Geubelle. Thermal loads on a domed protuberance under a mach 5.7 boundary layer. In *Bulletin of the American Physical Society*, volume 56(18), 2011.

[58] A. Jameson. Transonic flow calculations for aircraft. In F. Brezzi, editor, *Numerical Methods in Fluid Dynamics. Lecture Notes in Mathematics Volume 1127*. Springer-Verlag, 1985.

[59] R. C. Swanson and E. Turkel. Multistage schemes with multigrid for euler and navier-stokes equations. Technical Report 3631, NASA, August 1997.

[60] J.S. Hodge and S.F. Harvin. Test capabilities and recent experiences in the nasa langley 8-foot high temperature tunnel. volume AIAA 2000-2646. 21st AIAA Advanced Measurement Technology and Ground Testing Converence, June 2000.

[61] Colorado State Universiy, Bioanalytical Microfluidics Program. Chemical equilibrium calculation, 2012.

[62] L.D. Huebner, K.E. Rock, R.T. Voland, and A.R. Wieting. Calibration of the langley 8-foot high temperature tunnel for hypersonic airbreathing propulsion testing. Number 96–2197. AIAA, NASA Langley Technical Report Server, June 17–20 1996.

[63] JE Harris and DK Blanchard. Computer program for solving laminar, transitional, or turbulent compressible boundary-layer equations for two-dimensional and axisymmetric flow. *NASA STI/Recon Technical Report N*, 83, 1982.

[64] C. Ostoich, D. J. Bodony, and P. H. Geubelle. Development and validation of a first principles fluid-thermal multi-physics solver for hypersonic boundary layer heat transfer problems. *13th AIAA Dynamic Specialists Conference, Denver, Colorado, 4–7 April*, AIAA Paper 2011-1964, 2011.

[65] Omega Engineering, Inc. Reference tables for standard type k thermocouples. *http://www.omega.com/temperature/Z/pdf/z204-206.pdf*, Accessed: January 30, 2012.

[66] GM Corcos and H.W. Liepmann. On the contribution of turbulent boundary layers to the noise inside a fuselage. 1956.

[67] J. E. Ffowcs Williams. Sound radiation from turbulent boundary layers formed on compliant surfaces. *J. Fluid Mech.*, 22(2):347–358, 1965.

[68] S.F. Wu and L. Maestrello. Responses of a finite baffled plate subject to turbulent and mean flow excitations. Technical report, DTIC Document, 1993.

[69] E.H. Dowell. Panel flutter-a review of the aeroelastic stability of plates and shells. *AIAA Journal*, 8(3), March 1970.

[70] J. Dugundji. Theoretical considerations of panel flutter at high supersonic mach numbers. Technical report, DTIC Document, 1965.

[71] E.H. Dowell. Nonlinear flutter of curved plates, part 2. 1969.

[72] J.C. Houbolt. *A study of several aerothermoelastic problems of aircraft structures in high-speed flight*. PhD thesis, Diss. Techn. Wiss. ETH Zürich, Nr. 2760, 0000. Ref.: Rauscher, M.; Korref.: Stiefel, E., 1958.

[73] M.A. Hopkins and E.H. Dowell. Limited amplitude panel flutter with a temperature differential. In *Proceedings of the AIAA/ASME/ASCE/AHS/ASC 35th Structures, Structural Dynamics and Materials Conference*, 1994.

[74] A.J. Culler. *Coupled fluid-thermal-structural modeling and analysis of hypersonic flight vehicle structures*. PhD thesis, Ohio State University, 2012.

[75] C. Mei, K. Abdel-Motagaly, and R. Chen. Review of nonlinear panel flutter at supersonic and hypersonic speeds. In *NASA CONFERENCE PUBLICATION*, pages 171–188. NASA, 1999.

[76] HP Kappus, CE Lemley, and NH Zimmerman. An experimental investigation of high amplitude panel flutter. 1971.

[77] Michael Spottswood, Thomas Eason, and Timothy Beberniss. Influence of shock-boundary layer interactions on the dynamic response of a flexible panel. In *proceedings of the International Conference on Noise and Vibration Engineering*, Leuven, Belgium 2012.

[78] Timothy Beberniss, Michael Spottswood, and Thomas Eason. High-speed digital image correlation measurements of random nonlinear dynamic response. In Tom Proulx, editor, *Experimental and Applied Mechanics, Volume 6*, volume 9999 of *Conference Proceedings of the Society for Experimental Mechanics Series*, pages 171–186. Springer New York, 2011.

[79] Timothy Beberniss, Thomas Eason, and Michael Spottswood. High-speed 3d digital image correlation measurement of long-duration random vibration; recent advancements and noted limitations. In *proceedings of the International Conference on Noise and Vibration Engineering*, Leuven, Belgium 2012.

[80] R.E. Gordnier and M.R. Visbal. Computation of three-dimensional nonlinear panel flutter. *J. Aero. Eng.*, 16:155, 2003.

[81] M. R. Visbal and R. E. Gordnier. Numerical simulation of the interaction of a transitional boundary layer with a 2-d flexible panel in the subsonic region. *J. Fluids Structures*, 19:881–903, 2004.

[82] M.R. Visbal. On the interaction of an oblique shock with a flexible panel. *Journal of Fluids and Structures*, 30(0):219 – 225, 2012.

[83] F. Schäfer, S. Müller, T. Uffinger, S. Becker, J. Grabinger, M. Kaltenbacher, S. Rienstra, C.D. Munz, and H. Boden. Fluid-structure-acoustics interaction of the flow past a thin flexible structure. *AIAA journal*, 48(4):738, 2010.

[84] S.P. Spekreijse, B.B. Prananta, and J.C. Kok. A simple, robust and fast algorithm to compute deformations of multi-block structured grids. Report TP-2002-105, National Aerospace Laboratory NLR, February 2002.

[85] L. Vujošević and VA Lubarda. Finite-strain thermoelasticity based on multiplicative decomposition of deformation gradient. *Theoretical and applied mechanics*, (28-29), 2002.

[86] J. Bonet and R.D. Wood. *Nonlinear continuum mechanics for finite element analysis*. Cambridge university press, 1997.

[87] K.R. Srinivasan. *Thermomechanical meso-scale modeling of combustion of heterogeneous solid propellants*. PhD thesis, University of Illinois at Urbana-Champaign, 2008.

[88] I. Doghri. *Mechanics of deformable solids: linear, nonlinear, analytical, and computational aspects*. Springer Verlag, 2000.

[89] Dassault Systèmes Simulia Corporation. http://www.3ds.com/.

[90] N.A. Adams. Direct simulation of the turbulent boundary layer along a compression ramp at m= 3 and re θ= 1685. *Journal of Fluid Mechanics*, 420:47–83, 2000.

[91] N. D. Sandham, Y. F. Yao, and A. A. Lawal. Large-eddy simulation of transonic turbulent flow over a bump. *Int. J. Heat and Fluid Flow*, 24:584–595, 2003.

[92] S. Pirozzoli and M. Bernardini. Direct numerical simulation database for impinging shock wave/turbulent boundary-layer interaction. *AIAA J.*, 49:1307–1312, 2011.

[93] S. Xu and M.P. Martin. Assessment of inflow boundary conditions for compressible turbulent boundary layers. *Physics of Fluids*, 16:2623, 2004.

[94] T. Maeder, N.A. Adams, and L. Kleiser. Direct simulation of turbulent supersonic boundary layers by an extended temporal approach. *Journal of Fluid Mechanics*, 429(1):187–216, 2001.

[95] H.B. Squire. On the stability of three-dimensional viscous fluid between parallel walls. *Proc. Roy. Soc. Lond., Series A*, 142:621–628, 1933.

[96] W. Tollmien. The origin of turbulence. Technical Memorandum 609, NACA, 1929.

[97] BS Ng and WH Reid. An initial value method for eigenvalue problems using compound matrices. *Journal of Computational Physics*, 30(1):125–136, 1979.

[98] BS Ng and WH Reid. On the numerical solution of the orr-sommerfeld problem: asymptotic initial conditions for shooting methods. *Journal of Computational Physics*, 38(3):275–293, 1980.

[99] NA Adams and L. Kleiser. Subharmonic transition to turbulence in a flat-plate boundary layer at mach number 4.5. *Journal of Fluid Mechanics*, 317(1):301–335, 1996.

[100] L. F. Richardson. *Weather Prediction by Numerical Process.* Cambridge University Press, Cambridge, U.K., 1922.

[101] S. B. Pope. *Turbulent Flows.* Cambridge University Press, Cambridge, U.K., 2000.

[102] D.B. DeGraaff and J.K. Eaton. Reynolds-number scaling of the flat-plate turbulent boundary layer. *Journal of Fluid Mechanics*, 422(1):319–346, 2000.

[103] W. Soedel. *Vibrations of shells and plates*, volume 177. CRC, 2004.

[104] W.C. Xie, H.P. Lee, and S.P. Lim. Normal modes of a non-linear clamped-clamped beam. *Journal of Sound and Vibration*, 250(2):339–349, 2002.

[105] P. P. Friedmann, J. J. McNamara, B. J. Thuruthiamatta, and I. Nydick. Aeroelastic analysis of hypersonic vehicles. *J. Fluids Structures*, 19:681–712, 2004.

[106] J.J. McNamara. *Aeroelastic and Aerothermoelastic Behavior of Two and Three Dimensional Lifting Surfaces in Hypersonic Flow.* PhD thesis, University of Michigan, 2005.

[107] M. J. Lighthill. Oscillating airfoils at high mach numbers. *J. Aero. Sci.*, 20(6):402–406, 1953.

[108] A. J. Culler and J. J. McNamara. Studies of fluid-thermal-structural coupling for aerothermoelasticity in hypersonic flow. *AIAA J.*, 48(8):1721–1738, 2010.

[109] E.H. Dowell. Nonlinear oscillations of a fluttering plate (two- and three-dimensional plates in high supersonic flow undergoing limit cycle oscillations analyzed, using aerodynamic theory and von karman large deflection plate theory). *AIAA J.*, 4:1267–1275, 1966.

[110] Lian Duan, Pino Martin, and I. Beekman. *Direct numerical simulation of hypersonic turbulent boundary layers with varying freestream Mach number*. American Institute of Aeronautics and Astronautics, 2013/01/08 2010.

Appendix A

Thermally Perfect Gas Model Verification

The thermally perfect gas model implementation was verified by numerically solving for the flow field of a Mach 2 expansion fan around a 10° corner and comparing the result with an analytically determined solution. The pre-expansion freestream conditions are shown in Tab. A.1. The analytical solution is found by the following steps. First the sonic conditions, denoted by a superscript $*$, are found iteratively. The calorically perfect sonic conditions are used as an initial guess to the iterative process and are defined as

Table A.1: Pre-expansion fan flow conditions.

M_1	T_1 K	ρ_1 kg/m^3	p_1 kPa	γ_1 $= C_p(T_1)/(C_p(T_1) - R)$
2	1000	1.2	352.38	1.3005

$$T^*_{CP} = T_1 \left(1 + \frac{\gamma_1 - 1}{2} M_1^2\right) \frac{2}{\gamma_1 + 1},$$

and

$$p^*_{CP} = p_1 \left(\frac{T^*_{CP}}{T_1}\right)^{\frac{\gamma_1}{\gamma_1 - 1}}.$$

The sonic enthalpy and temperature, h^* and T^*, respectively, are calculated as

$$h^* = \int_0^{T^*} \frac{R\gamma(T')}{\gamma(T') - 1} dT',$$

and

$$T^* = \left[\left(h_1 + \frac{u_1^2}{2}\right) - h^*\right] \frac{2}{R\gamma(T^*)},$$

respectively, and iterated until convergence. After finding the converged solution the sonic ratio of specific heats is known from the tabulated value at the sonic temperature, $\gamma^* = \gamma(T^*)$. The sonic pressure is found by evaluating the following integral

$$p^* = p_1 \exp\left[\frac{1}{R}\int_{T_1}^{T^*} C_p(T')dT'\right].$$

The Prandtl-Meyer function on in the pre-expansion flow is calculated as

$$\nu_1 = -\int_{p^*}^{p_1} \frac{\sin(2\mu(T))}{2\gamma(T)p'}dp',$$

where the Mach angle, $\mu(T)$, is found using the following expressions:

$$\mu(T) = \sin^{-1}\left(\frac{1}{M(T)}\right),$$

$$M(T) = \sqrt{\frac{2\left(h^* + \gamma^* RT^*/2 - h(T)\right)}{\gamma(T)RT}},$$

and

$$h(T) = \int_0^T \frac{R\gamma(T')}{\gamma(T') - 1}dT'.$$

The post-expansion flow values are found such that the following equation is satisfied,

$$\nu_2 - \nu_1 = \phi = -\int_{p^*}^{p_2} \frac{\sin(2\mu(T))}{2\gamma(T)p'}dp',$$

where ϕ is the expansion angle. In this verification exercise, $\phi = -10° = -\pi/18$ radians. The flow values are propagated along the characteristics, (μ = constant) into the interior of the domain shown in Fig. A.1. The resulting analytical solution and the corresponding numerical solution are compared at the post-expansion reference location shown in Fig. A.1. The comparison is shown in Tab. A.2.

Table A.2: Comparison of post-expansion fan flow conditions between numerical and analytically determined values.

Variable	Analytical	Numerical	% Difference
M_2	2.32990	2.32992	8.58×10^{-4}
T_2, K	878.125	878.120	5.69×10^{-4}

Figures for Appendix A

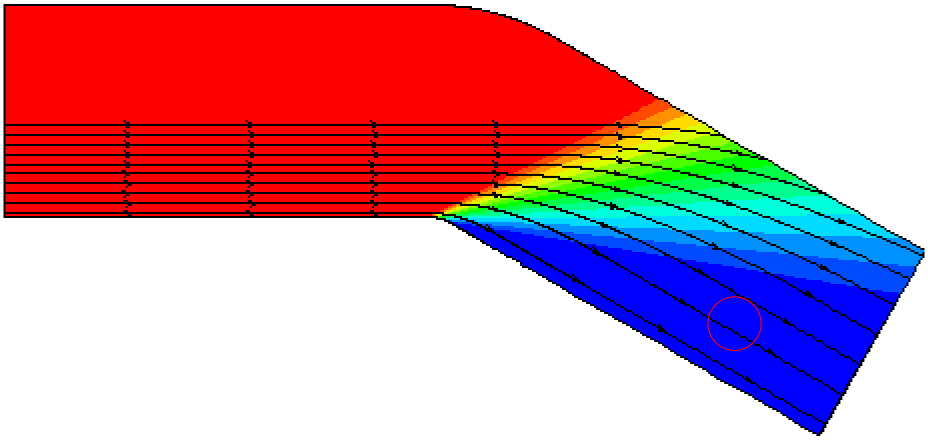

Figure A.1: Expansion fan solution for ρu. The reference location in Tab. A.2 is circled.

Appendix B

Piston Theory and Eckert's Reference Enthalpy

B.1 Piston theory

A popular reduced-order model for calculating unsteady pressure loading over a static or dynamic protrusion is piston theory. Devloped by Lighthill [107], piston theory is a simplistic model that has been heavily utilized since its inception [70, 108, 109]. The model is based on the observation that a slab of fluid moving with a horizontal velocity U_∞ past an inclined surface will rise in a column like it was being forced by a piston with velocity

$$V_p = U_\infty \frac{\partial w}{\partial x} + \frac{\partial w}{\partial t}, \tag{B.1}$$

where w is the vertical coordinate of the surface, as shown in Fig. B.1. If the piston velocity, dependent on the surface inclination, surface motion, and freestream velocity, is low enough that no there are no changes in entropy and only simple waves are created, then the pressure on the surface of the piston, p_s, can be calculated as

$$\frac{p_s}{p_\infty} = \left(1 + \frac{\gamma - 1}{2} \frac{V_p}{c_\infty}\right)^{\frac{2\gamma}{\gamma-1}}, \tag{B.2}$$

where p_∞, c_∞, and γ are the freestream pressure, speed of sound, and ratio of specific heats, respectively. The first-, second-, and third-order binomial expansions of Eq. (B.2) result in

$$p_s - p_\infty = \rho_\infty c_\infty V_p, \tag{B.3}$$

$$p_s - p_\infty = \rho_\infty c_\infty^2 \left[\frac{V_p}{c_\infty} + \frac{\gamma+1}{4} \left(\frac{V_p}{c_\infty} \right)^2 \right], \tag{B.4}$$

$$p_s - p_\infty = \rho_\infty c_\infty^2 \left[\frac{V_p}{c_\infty} + \frac{\gamma+1}{4} \left(\frac{V_p}{c_\infty} \right)^2 + \frac{\gamma+1}{12} \left(\frac{V_p}{c_\infty} \right)^3 \right], \tag{B.5}$$

for the first-, second-, and third-order forms of piston theory, respectively.

B.2 Eckert's reference enthalpy

Using Eckert's reference enthalpy method [20], an approximation for the heat flux under a laminar or turbulent boundary layer can be found. Though there is an analogous reference temperature method, the reference enthalpy method is better suited for flows with large temperature variations where the calorically perfect assumption may not be valid, and is thus described here. The heat flux on a surface is given by

$$q_s = h(i_r - i_w), \tag{B.6}$$

where h, i_r, and i_s are the heat transfer coefficient, recovery enthalpy, and wall enthalpy, respectively. The recovery enthalpy is given by

$$i_r = i_\infty + r\left(\frac{U_\infty^2}{2} \right), \tag{B.7}$$

where r, the recovery factor, is given by

$$r = \sqrt{\mathrm{Pr}^*} \tag{B.8}$$

for a laminar boundary layer, and Pr^* is the Prandtl number evaluated at the reference enthalpy, defined by

$$i^* = i_\infty + 0.5(i_s - i_\infty) + 0.22(i_r - i_\infty). \tag{B.9}$$

The solutions to Eq. (B.7) and Eq. (B.9) are determined iteratively. It remains to determine, h, the heat transfer coefficient, which is related to the coefficient of friction, c_f, through the Stanton number, St. The friction coefficient for a laminar boundary layer is given by

$$c_f = \frac{0.664}{\sqrt{\mathrm{Re}^*}} = \frac{0.664}{\sqrt{\rho^* U_\infty x/\mu^*}}, \tag{B.10}$$

where ρ^* and μ^* are the density and dynamic viscosity evaluated at the reference enthalpy, and x is the distance from the leading edge of the flat plate over which the boundary layer is growing. After the determination of c_f, the Stanton number can be determined by the relation

$$\mathrm{St} = \frac{c_f}{2}(\mathrm{Pr}^*)^{-\frac{2}{3}}. \tag{B.11}$$

The heat transfer coefficient can now be determined by

$$h = \mathrm{St}\rho^* U_e, \tag{B.12}$$

where U_e is the velocity at the edge of the boundary layer, and can be found from its relation to the pressure, p_s, found in Section B.1

$$U_e = c_\infty \sqrt{\frac{2}{\gamma - 1}\left[\left(\frac{\rho_\infty U_\infty^2 + 2p_\infty}{2p_s}\right)^{\frac{\gamma-1}{\gamma}} - 1\right]} \tag{B.13}$$

In the case of a turbulent boundary layer, the the relations given in Eq. (B.8) and Eq. (B.10), are replaced by

$$r = \sqrt[3]{\mathrm{Pr}^*},$$

and

$$c_f = \frac{0.370}{(\log_{10}\mathrm{Re}^*)^{2.584}} = \frac{0.370}{(\log_{10}\rho^* U_\infty x/\mu^*)^{2.584}},$$

respectively.

Figures for Appendix B

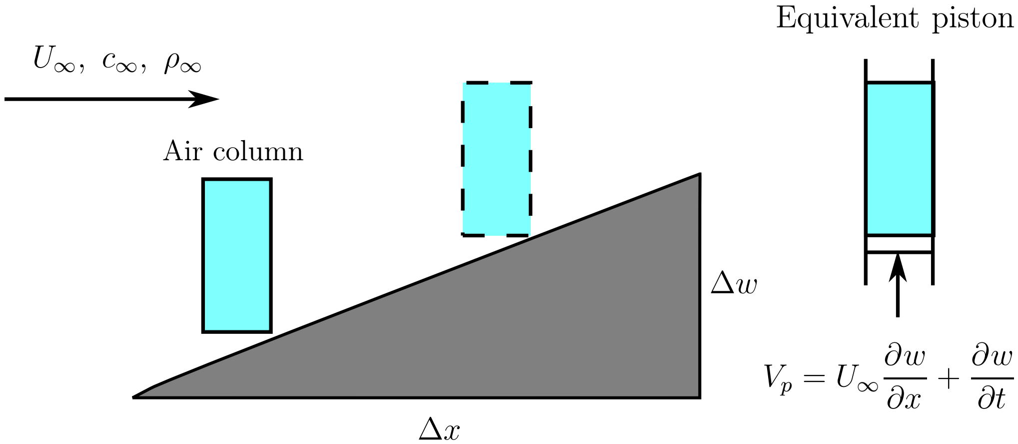

Figure B.1: Piston-like motion of a column of air moving over a sloped surface.

Appendix C

Comparison Between Gas Thermal Models with Equal Freestream Static Temperatures

To determine whether the more complex thermally perfect gas model would be justified if the calorically perfect case were run with freestream static temperature equal to that in the thermally perfect case ($T_\infty = 237.14$ K), an additional 2D ANSYS Fluent simulation is run. The resulting flat plate heat flux and boundary layer profile are compared to those from the thermally perfect case. The calorically perfect and thermally perfect simulations are run on the same grid with the same freestream conditions.

The fluid in close proximity to the stagnation streamline passes through the high temperature region of the flow at the blunt leading edge where the calorically perfect and thermally perfect gas thermal models differ significantly. This is reflected in the surface heat flux at the blunt leading edge of the plate. At the stagnation point, the heat fluxes are 1107.1 kW/m^2 and 1024.1 kW/m^2 for the calorically perfect and thermally perfect cases, respectively. This result owes to the fact that the temperature of the gas in the stagnation region is higher in the calorically perfect case than in the thermally perfect case. The pressure and density are lower leading to a larger shock standoff distance in the calorically perfect case. Accurate prediction of the flow in the stagnation region, heat flux in particular in design contexts, would require use of the more complex thermally perfect gas model.

Figure C.1 shows the boundary layer and temperature profiles at the boundary layer probe location. Inside the boundary layer, Fig. C.1(a) shows that, in the immediate vicinity of the plate, the thermally perfect model captures the near-wall gradients more closely than does the calorically perfect model. However, the differences are minor. It is interesting to note that in Fig. C.1(b) the maximum temperature in the thermally perfect simulation is higher than that in the calorically perfect case.

The heat flux into the flat region of the plate is shown in Fig. C.2. Over the entire length of the plate, the calorically perfect model predicts a higher heat flux into the plate (approximately +500 W/m^2, X = 0.25 m) which decreases with distance (approximately +15 W/m^2, X = 2.5 m). In the calorically perfect case, more energy is lost to the plate over a given distance because of the higher heat flux predicted by the model, which causes a temperature difference between the two models in the boundary layer which becomes larger with distance from the leading edge, as shown in Fig. C.1(b).

Figures for Appendix C

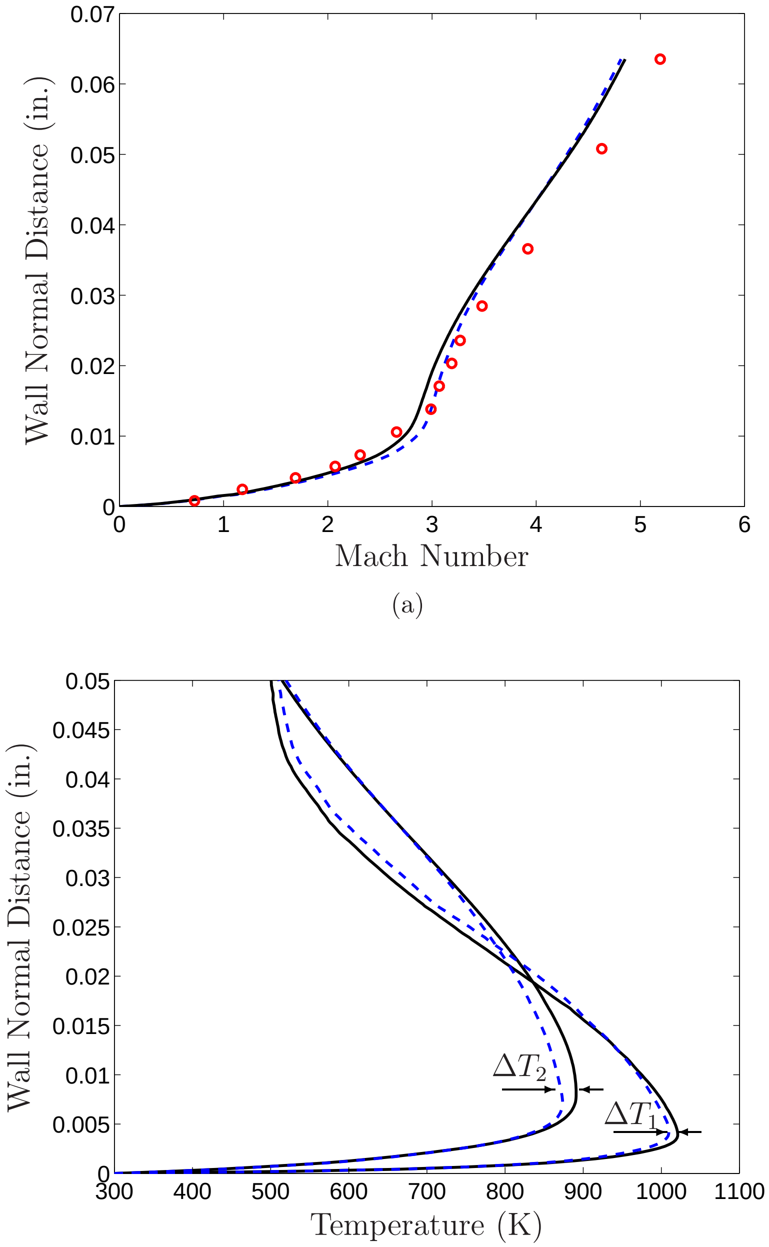

(a)

(b)

Figure C.1: (a) Boundary layer profile at $X = 1.476$ m and (b) temperature profiles at $X_1 = 0.1$ m and $X_2 = 1.476$ m, where $\Delta T_1 = 11$ K and $\Delta T_2 = 17$ K. Calorically perfect (dashed line), thermally perfect (solid line), experiment (circles).

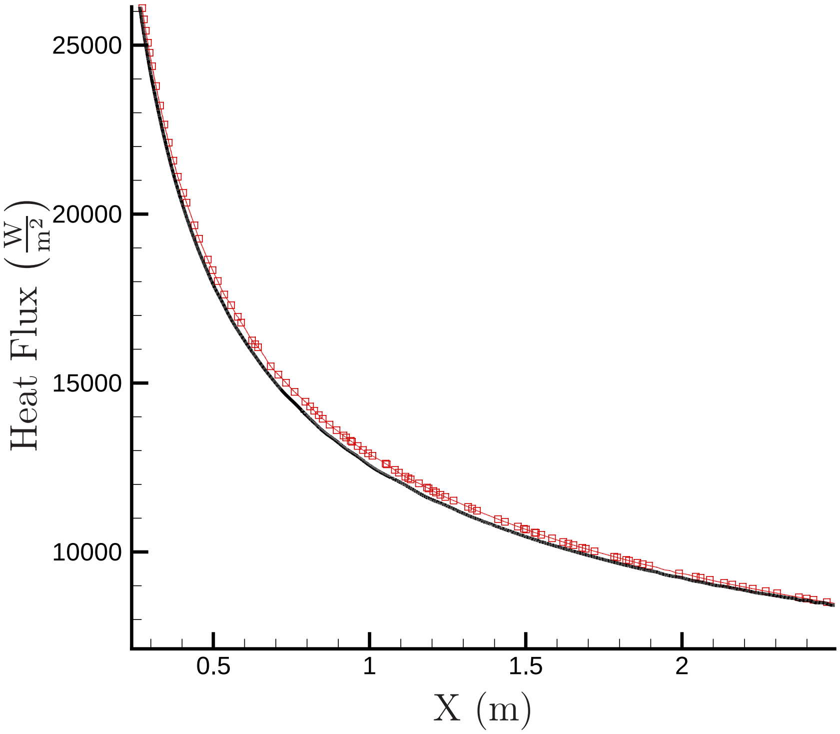

Figure C.2: Heat flux into the flat plate (W/m^2). Calorically perfect (squares), thermally perfect (solid line).

Appendix D

Additional Thermomechanical Formulation Details

D.1 Constitutive models

In the geometrically non-linear regime, a hyperelastic constitutive model is derived from the function $W(\boldsymbol{X}, \boldsymbol{F})$, the stored energy per unit volume in the reference configuration. The stored energy function is often expressed in terms of the right Cauchy-Green strain, $W(\boldsymbol{F}) = \hat{W}(\boldsymbol{C})$, or, in the case of isotropic materials, the the invariants of $\boldsymbol{C}$, $\bar{W}(I_1, I_2, I_3)$. The three invariants are $I_1 = \mathrm{Tr}(\boldsymbol{C})$, $I_2 = 1/2(\mathrm{Tr}(\boldsymbol{C})^2 - \mathrm{Tr}(\boldsymbol{C}^2)$, and $I_3 = det(\boldsymbol{C}) = J^2$. Expressing W in terms of the invariants is useful when taking derivatives of W. For example, the second Piola-Kirchhoff stress tensor is given as

$$\boldsymbol{S} = 2\frac{\partial \hat{W}}{\partial \boldsymbol{C}} = 2\sum_{j=1}^{3} \frac{\partial \bar{W}}{\partial I_j}\frac{\partial I_j}{\partial \boldsymbol{C}}. \tag{D.1}$$

D.1.1 St. Venant-Kirchhoff constitutive model

The St. Venant-Kirchhoff model has the stored energy function

$$\hat{W} = \frac{\mu}{2}\mathrm{Tr}\left(\frac{\boldsymbol{C}-\boldsymbol{I}}{2}\right) + \frac{\lambda}{8}\left(\mathrm{Tr}(\boldsymbol{C}) - 3\right)^2, \tag{D.2}$$

where λ and μ are Lamè's first and second parameters, respectively. From Eq. (D.1), the second Piola-Kirchhoff stress tensor is found to be

$$\boldsymbol{S} = [\lambda \mathrm{Tr}(\boldsymbol{E})\boldsymbol{I} + 2\mu\boldsymbol{E}]. \tag{D.3}$$

The first Piola-Kirchhoff stress tensor can be shown to be $\boldsymbol{P} = \boldsymbol{F}\boldsymbol{S}$. Given an energy functional, W, the first Piola-Kirchhoff stress tensor is defined as

$$P_{iK} = \frac{\partial W}{\partial F_{iK}} = \frac{\partial \hat{W}}{\partial C_{JP}}\frac{\partial C_{JP}}{\partial F_{iK}}, \tag{D.4}$$

where $\boldsymbol{C} = \boldsymbol{F}^T\boldsymbol{F}$ is the right Cauchy-Green tensor and $\boldsymbol{S} = 2\dfrac{\partial W}{\partial \boldsymbol{C}}$. Further manipulation gives

$$\frac{\partial C_{JP}}{\partial F_{iK}} = \frac{\partial}{\partial F_{iK}}(F_{jJ}F_{jP}) = \frac{\partial}{\partial F_{iK}}(\delta_{ij}\delta_{KJ}F_{jP}+\delta_{ij}\delta_{KP}F_{jJ}) = \frac{\partial}{\partial F_{iK}}(\delta_{KJ}F_{iP}+\delta_{KP}F_{iJ}). \tag{D.5}$$

Considering the symmetry of the right Cauchy-Green tensor

$$\begin{aligned} P_{iK} &= \frac{\partial \hat{W}}{\partial C_{JP}}(\delta_{KJ}F_{iP} + \delta_{KP}F_{iJ}) = \frac{\partial \hat{W}}{\partial C_{JP}}\delta_{KJ}F_{iP} + \frac{\partial \hat{W}}{\partial C_{JP}}\delta_{KP}F_{iJ} \quad \text{(D.6)} \\ &= 2F_{iP}\frac{\partial \hat{W}}{\partial C_{KP}} = F_{iP}S_{KP}. \end{aligned}$$

Therefore,

$$\boldsymbol{P} = \boldsymbol{F}[\lambda tr(\boldsymbol{E})\boldsymbol{I} + 2\mu\boldsymbol{E}]. \tag{D.7}$$

D.1.2 Modified Neo-Hookean constitutive model

The stored energy function for the modified Neo-Hookean model is given by

$$\bar{W}(I_1, I_2, I_3) = \frac{G}{2}(\tilde{I}_1 - 3) + \frac{K}{2}(J-1)^2, \tag{D.8}$$

where, $\tilde{I}_1 = I_1/J^{1/3} = I_1/I_3^{2/3}$ is the deviatoric expression of the first invariant of $\boldsymbol{C}$ and

$$G = \frac{E}{2(1-\nu)}$$

and

$$K = \frac{E}{3(1-2\nu)}$$

are the shear and bulk moduli, respectively. For this class of materials, the second Piola-Kirchhoff stress tensor is given by

$$\boldsymbol{S} = 2\frac{\partial \hat{W}}{\partial \boldsymbol{C}} = G\,J^{-2/3}\left(1 - \frac{\mathrm{Tr}(\boldsymbol{C})\boldsymbol{C}^{-1}}{3}\right) + K(J^2 - J)\boldsymbol{C}^{-1} \tag{D.9}$$

D.2 Elasticity tensor, $\mathcal{A}$

The elasticity tensor, $\mathcal{A}$, is defined as $\mathcal{A} = \partial\boldsymbol{P}/\partial\boldsymbol{F}$. Given the result in appendix D.1.1, the elasticity tensor relating changes in the first Piola-Kirchhoff elasticity tensor to changes in the deformation gradient can be found as

$$\begin{aligned}
\mathcal{A}_{KiLj} &= \frac{\partial}{\partial F_{jL}}\left(F_{iP}S_{KP}\right) = \frac{\partial}{\partial F_{jL}}\left(2F_{iP}\frac{\partial W}{\partial C_{KP}}\right) \\
&= 2\delta_{ij}\delta_{LP}\frac{\partial W}{\partial C_{KP}} + 2F_{iP}\frac{\partial^2 W}{\partial C_{KP}\partial C_{MN}}\frac{\partial C_{MN}}{\partial F_{jL}} \\
&= \delta_{ij}S_{KL} + 4F_{iP}F_{jM}\frac{\partial^2 W}{\partial C_{KP}\partial C_{ML}} \\
&= \delta_{ij}S_{KL} + F_{iP}F_{jM}\mathcal{C}_{KPML},
\end{aligned} \tag{D.10}$$

where $\mathcal{C}_{KPML} = 4\frac{\partial^2 \hat{W}}{\partial C_{KP}\partial C_{ML}}$ is the elasticity tensor relating changes in the Green-Lagrange strain tensor, $\boldsymbol{E}$, to the second Piola-Kirchhoff stress tensor, $\boldsymbol{S}$. This result is valid for any isotropic material. For the St. Venant-Kirchhoff model, it is known that

$$\mathcal{C}_{KPML} = \lambda\delta_{KP}\delta_{ML} + \mu(\delta_{KM}\delta_{PL} + \delta_{KL}\delta_{PM}),$$

where λ and μ are the first and second Lamé parameters, respectively. For the modified Neo-Hookean model, following the derivation steps summarized in Doghri [88], the elasticity tensor is found to be

$$\mathcal{C}_{KPML} = \Gamma_1 C^{-1}_{KP}C^{-1}_{ML} + \Gamma_2\left(C^{-1}_{KP}\delta_{ML} + \delta_{KP}C^{-1}_{ML}\right) + \frac{1}{2}\Gamma_8\left(C^{-1}_{KM}C^{-1}_{PL} + C^{-1}_{KL}C^{-1}_{PM}\right),$$

where

$$\Gamma_1 = \frac{2}{9}G\ \mathrm{Tr}(\boldsymbol{C})J^{-2/3} + K(2J^2 - J),$$

$$\Gamma_2 = -\frac{2}{3}G\ J^{-2/3},$$

and

$$\Gamma_8 = \frac{2}{3}G\ \mathrm{Tr}(\boldsymbol{C})J^{-2/3} - 2K(J^2 - J).$$

D.3 External load jacobian, $\mathcal{B}$

The term $\mathcal{B}$ entering Eq. (7.14) is

$$\begin{aligned}
\mathcal{B} &= \frac{\partial}{\partial^e \boldsymbol{F}} \left(\boldsymbol{t}\, {}^e J \sqrt{\boldsymbol{N} \cdot \boldsymbol{C}^{-1} \boldsymbol{N}} \right) \\
&= \frac{\partial \boldsymbol{t}}{\partial^e \boldsymbol{F}} \left({}^e J \sqrt{\boldsymbol{N} \cdot \boldsymbol{C}^{-1} \boldsymbol{N}} \right) + \boldsymbol{t} \frac{\partial}{\partial^e \boldsymbol{F}} \left({}^e J \sqrt{\boldsymbol{N} \cdot \boldsymbol{C}^{-1} \boldsymbol{N}} \right) \\
&= \mathcal{B}_{\boldsymbol{t}} \left({}^e J \sqrt{\boldsymbol{N} \cdot \boldsymbol{C}^{-1} \boldsymbol{N}} \right) + \boldsymbol{t}\, \mathcal{B}_{da},
\end{aligned} \tag{D.11}$$

where $\mathcal{B}_{\boldsymbol{t}}$ and $\mathcal{B}_{da}$ are the Jacobians associated with the change in traction and surface, respectively, This term is derived as follows. The superscript e on the deformation gradient $\boldsymbol{F}$ and Jacobian, J, will be left off for brevity.

$$\begin{aligned}
\mathcal{B}_{da,gG} &= \frac{\partial}{\partial F_{gG}} \left(J \sqrt{\boldsymbol{N} \cdot \boldsymbol{C}^{-1} \boldsymbol{N}} \right) = \frac{\partial J}{\partial F_{gG}} \sqrt{\boldsymbol{N} \cdot \boldsymbol{C}^{-1} \boldsymbol{N}} + J \frac{\partial}{\partial F_{gG}} \left(\sqrt{\boldsymbol{N} \cdot \boldsymbol{C}^{-1} \boldsymbol{N}} \right) \\
&= J F^{-1}_{gG} \sqrt{\boldsymbol{N} \cdot \boldsymbol{C}^{-1} \boldsymbol{N}} + \frac{J}{2} \left(\boldsymbol{N} \cdot \boldsymbol{C}^{-1} \boldsymbol{N} \right)^{-1/2} \frac{\partial}{\partial F_{gG}} \left(\boldsymbol{N} \cdot \boldsymbol{C}^{-1} \boldsymbol{N} \right) \\
&= J \left[F^{-1}_{gG} \sqrt{\boldsymbol{N} \cdot \boldsymbol{C}^{-1} \boldsymbol{N}} + \frac{1}{2} \left(\boldsymbol{N} \cdot \boldsymbol{C}^{-1} \boldsymbol{N} \right)^{-1/2} N_I \frac{\partial C^{-1}_{IJ}}{\partial F_{gG}} N_J \right] \\
&= J \left[F^{-1}_{gG} \sqrt{\boldsymbol{N} \cdot \boldsymbol{C}^{-1} \boldsymbol{N}} + \frac{1}{2} \left(\boldsymbol{N} \cdot \boldsymbol{C}^{-1} \boldsymbol{N} \right)^{-1/2} N_I \frac{\partial}{\partial F_{gG}} \left(F^{-1}_{Ik} F^{-1}_{Jk} \right) N_J \right] \\
&= J \left[F^{-1}_{gG} \sqrt{\boldsymbol{N} \cdot \boldsymbol{C}^{-1} \boldsymbol{N}} \right. \\
&\qquad \left. + \frac{1}{2} \left(\boldsymbol{N} \cdot \boldsymbol{C}^{-1} \boldsymbol{N} \right)^{-1/2} N_I \left(F^{-1}_{Ik} \frac{\partial F^{-1}_{Jk}}{\partial F_{gG}} + F^{-1}_{Jk} \frac{\partial F^{-1}_{Ik}}{\partial F_{gG}} \right) N_J \right]
\end{aligned} \tag{D.12}$$

$$\begin{aligned}
&= J \left[F^{-1}_{gG} \sqrt{\boldsymbol{N} \cdot \boldsymbol{C}^{-1} \boldsymbol{N}} \right. \\
&\qquad \left. + \frac{1}{2} \left(\boldsymbol{N} \cdot \boldsymbol{C}^{-1} \boldsymbol{N} \right)^{-1/2} N_I \left(F^{-1}_{Ik} F^{-1}_{Jg} F^{-1}_{Gk} + F^{-1}_{Jk} F^{-1}_{Ig} F^{-1}_{Gk} \right) N_J \right]
\end{aligned}$$

$$\begin{aligned}
\mathcal{B}_{\boldsymbol{t},gG} = \frac{\partial t_i}{\partial gG} = \sigma_{ij}\frac{\partial n_j}{\partial gG} &= \sigma_{ij}\frac{\partial}{\partial gG}\left(\frac{F^{-1}_{Ii}N_I}{\sqrt{N_I F^{-1}_{Im}F^{-1}_{Km}N_K}}\right) \\
&= \sigma_{ij}\left[\frac{\partial F^{-1}_{Jj}N_J}{\partial F_{gG}}\left(\boldsymbol{N}\boldsymbol{C}^{-1}\boldsymbol{N}\right)^{-1/2} + F^{-1}_{Jj}N_J\frac{\partial}{\partial F_{gG}}\left(\boldsymbol{N}\boldsymbol{C}^{-1}\boldsymbol{N}\right)^{-1/2}\right] \\
&= \sigma_{ij}\Big[N_J F^{-1}_{Jg}F^{-1}_{Gj}\left(\boldsymbol{N}\boldsymbol{C}^{-1}\boldsymbol{N}\right)^{-1/2} - \\
&\qquad \frac{1}{2}F^{-1}_{Jj}N_J\left(\boldsymbol{N}\boldsymbol{C}^{-1}\boldsymbol{N}\right)^{-3/2}N_I\frac{\partial}{\partial F_{gG}}\left(F^{-1}_{Im}F^{-1}_{Km}\right)N_K\Big] \\
&= \sigma_{ij}\Big[N_J F^{-1}_{Jg}F^{-1}_{Gj}\left(\boldsymbol{N}\boldsymbol{C}^{-1}\boldsymbol{N}\right)^{-1/2} - \\
&\qquad \frac{1}{2}F^{-1}_{Jj}N_J\left(\boldsymbol{N}\boldsymbol{C}^{-1}\boldsymbol{N}\right)^{-3/2}N_I\left(\frac{\partial F^{-1}_{Im}}{\partial F_{gG}}F^{-1}_{Km} + F^{-1}_{Im}\frac{\partial F^{-1}_{Km}}{\partial F_{gG}}\right)N_K\Big] \\
&= \sigma_{ij}\Big[N_J F^{-1}_{Jg}F^{-1}_{Gj}\left(\boldsymbol{N}\boldsymbol{C}^{-1}\boldsymbol{N}\right)^{-1/2} - \\
&\qquad \frac{1}{2}F^{-1}_{Jj}N_J\left(\boldsymbol{N}\boldsymbol{C}^{-1}\boldsymbol{N}\right)^{-3/2}N_I\left(F^{-1}_{Ig}F^{-1}_{Gm}F^{-1}_{Km} + F^{-1}_{Im}F^{-1}_{Kg}F^{-1}_{Gm}\right)N_K\Big]
\end{aligned} \tag{D.13}$$

D.3.1 External load from fluid stress tensor, $\boldsymbol{\tau}$

The formulation is simplified if the traction on the boundary is expressed as the product of the Cauchy stress tensor and the current surface normal, $t_j = \tau_{ij}n_i$. The traction load is then calculated as

$$\int_{\partial B}\boldsymbol{\delta u}\cdot\boldsymbol{t}\;da = \int_{\partial B}\boldsymbol{\delta u}\cdot\left(\boldsymbol{\tau}\cdot\boldsymbol{n}\right)\;da = \int_{\partial B_0}\boldsymbol{\delta u}\cdot\left(\boldsymbol{\tau}\cdot\left(J\boldsymbol{F}^{-T}\cdot\boldsymbol{N}\right)\right)\;dA. \tag{D.14}$$

The advantage of this form is that the resulting linearization is simpler:

$$\begin{aligned}
D\int_{\partial B}\delta u_j t_j\;da[\boldsymbol{u}] =& D\int_{\partial B}\delta u\left(\tau_{ij}n_i\right)\;da[\boldsymbol{u}] \\
=& D\int_{\partial B_0}\delta u_j\left(\tau_{ij}\left(JF^{-1}_{Ii}N_I\right)\right)\;dA[\boldsymbol{u}] \\
=& \int_{\partial B_0}\delta u_j\left(\tau_{ij}N_I\;D\left(JF^{-1}_{Ii}\right)[\boldsymbol{u}]\right)\;dA \\
=& \int_{\partial B_0}\delta u_j\left(\tau_{ij}N_I\;\mathcal{B}_{IikK}\frac{\partial u_k}{\partial X_K}\right)\;dA,
\end{aligned} \tag{D.15}$$

where

$$\begin{aligned}\mathcal{B}_{IikK} =& \frac{\partial}{\partial F_{kK}}\left(JF^{-1}_{Ii}\right) = \left(\frac{\partial J}{\partial F_{kK}}F^{-1}_{Ii} + J\frac{\partial F^{-1}_{Ii}}{\partial F_{kK}}\right) \\ =& J\left(F^{-1}_{Kk}F^{-1}_{Ii} - F^{-1}_{Ik}F^{-1}_{Ki}\right).\end{aligned} \tag{D.16}$$

D.4 Spatial discretization of structural equations

Solution values $\boldsymbol{X}$ and $\boldsymbol{u}$ are stored at the n nodal locations per element. Values are interpolated using shape functions N of order n

$$X_d = \sum_{a=1}^{n} N_a \hat{X}_{ad}, \tag{D.17}$$

where d is the direction index, a is the element local node index, and $\hat{(\ )}$ denotes the nodal value of a given quantity. Isoparametric elements are used, so that

$$\int_e \phi(\boldsymbol{x})\ dV = \int_{-1}^{1} \phi'(\boldsymbol{\xi}) J\ d\boldsymbol{\xi}$$

where $J = det\left(\partial \boldsymbol{X}/\partial \boldsymbol{\xi}\right)$. Numerical integration is done using Gauss quadrature, so that (in three dimensions, for example)

$$\int_{-1}^{1}\int_{-1}^{1}\int_{-1}^{1} \phi'(\boldsymbol{\xi})J(\boldsymbol{\xi})\ d\xi d\eta d\zeta \approx \sum_{i=1}^{ng}\sum_{j=1}^{ng}\sum_{k=1}^{ng} \phi'(\xi_{ijk})J(\xi_{ijk})W(\xi_i)W(\eta_j)W(\zeta_k).$$

Discretizing the first term of Eq. (7.15) for each element

$$\begin{aligned}\int_e \beta^2(\Theta)\hat{\boldsymbol{P}} : \boldsymbol{\delta F}\ dV \approx \delta\hat{u}_{ad} \sum_{ijk=1}^{ng} \beta^2(\boldsymbol{\xi}_{ijk}) P_{dK}(\boldsymbol{\xi}_{ijk}) \frac{\partial N_a(\boldsymbol{\xi}_{ijk})}{\partial \xi_l} \frac{\partial \xi_l}{\partial X_K} J(\boldsymbol{\xi}_{ijk}) \\ \times W(\xi_i)W(\eta_j)W(\zeta_k) = \delta\hat{u}_{ad} r^{int}_{ad},\end{aligned}$$

which, when assembled over the entire body, B_0, gives

$$\int_{B_0} \beta^2(\Theta)\hat{\boldsymbol{P}} : \boldsymbol{\delta F}\ dV \approx \boldsymbol{\delta \hat{u}}^T \boldsymbol{R}^{int}.$$

In the latter relation, $\boldsymbol{R}^{int}$ is the internal load vector. The remaining terms are discretized similarly:

The external load due to a body force over an element is given by

$$\int_e \rho_0 \boldsymbol{b} \cdot \boldsymbol{\delta u}\; dV \approx \delta \hat{u}_{ad} \sum_{ijk=1}^{ng} \rho_0(\boldsymbol{\xi}_{ijk}) b(\boldsymbol{\xi}_{ijk}) N_a(\boldsymbol{\xi}_{ijk}) J(\boldsymbol{\xi}_{ijk}) \\ \times W(\xi_i) W(\eta_j) W(\zeta_k) = \delta \hat{u}_{ad} r_{ad}^{body}.$$

When added over B_0, this term yields

$$\int_{B_0} \rho_0 \boldsymbol{b} \cdot \boldsymbol{\delta u}\; dV \approx \boldsymbol{\delta \hat{u}}^T \boldsymbol{R}^{body},$$

where $\boldsymbol{R}^{body}$ is the external load vector due a body force.

The external load due to a traction force over an element takes the form

$$\int_{\partial e} \boldsymbol{t}_0 \cdot \boldsymbol{\delta u}\; dA \approx \delta \hat{u}_{ad} \sum_{ij=1}^{ng} t_{0a}(\boldsymbol{\xi_{2D}}_{ij}) N_a(\boldsymbol{\xi_{2D}}_{ij}) N_b(\boldsymbol{\xi_{2D}}_{ij}) J_{2D}(\boldsymbol{\xi_{2D}}_{ij}) \\ \times W(\xi_i) W(\eta_j) = \delta \hat{u}_{ad} r_{ad}^{tract.}.$$

When assembled over the entire body, B_0, this term gives

$$\int_{\partial B_0} \boldsymbol{t}_0 \cdot \boldsymbol{\delta u}\; dA \approx \boldsymbol{\delta \hat{u}}^T \boldsymbol{R}^{tract.},$$

where $\boldsymbol{R}^{tract.}$ is the external load vector due a body force.

The acceleration term is discretized as follows:

$$\int_e \rho_0 \ddot{\mathbf{u}} \cdot \boldsymbol{\delta u}\; dV \approx \delta \hat{u}_{ad} \sum_{ijk=1}^{ng} \rho_0(\boldsymbol{\xi}_{ijk}) N_a(\boldsymbol{\xi}_{ijk}) N_b(\boldsymbol{\xi}_{ijk}) J(\boldsymbol{\xi}_{ijk}) \\ \times W(\xi_i) W(\eta_j) W(\zeta_k) \ddot{u}_{bd} = \delta \hat{u}_{ad} m_{adbd} \hat{\ddot{u}}_{bd},$$

which, when added over B_0 gives

$$\int_{B_0} \rho_0 \ddot{\mathbf{u}} \cdot \boldsymbol{\delta u}\; dV \approx \boldsymbol{\delta \hat{u}}^T \boldsymbol{M} \hat{\ddot{\mathbf{u}}},$$

where $\boldsymbol{M}$ is the mass matrix.

Finally, the linearized internal work term yields

$$\begin{aligned}\int_e &\beta^2(\Theta)\boldsymbol{\delta F} : \mathcal{A} : \nabla_{\boldsymbol{X}}\Delta\boldsymbol{u}\ dV \\ &\approx \delta\hat{u}_{ad}\sum_{ijk=1}^{ng}\beta^2(\boldsymbol{\xi}_{ijk})\mathcal{A}_{KdLm}(\boldsymbol{\xi}_{ijk})\frac{\partial N_a(\boldsymbol{\xi}_{ijk})}{\partial\xi_l}\frac{\partial\xi_l}{\partial X_K}\frac{\partial N_b(\boldsymbol{\xi}_{ijk})}{\partial\xi_q}\frac{\partial\xi_q}{\partial X_L} \\ &\qquad \times J(\boldsymbol{\xi}_{ijk})W(\xi_i)W(\eta_j)W(\zeta_k)\Delta\hat{u}_{bm} = \delta\hat{u}_{ad}k_{adbm}\Delta\hat{u}_{bm}.\end{aligned}$$

The global form of that term is then

$$\int_{B_0}\beta^2(\Theta)\boldsymbol{\delta F} : \mathcal{A} : \nabla_{\boldsymbol{X}}\boldsymbol{u}dV \approx \boldsymbol{\delta u}^T\boldsymbol{K}\Delta\hat{\boldsymbol{u}},$$

where $\boldsymbol{K}$ is the tangent stiffness matrix. The discretized form of the principle of virtual work is thus

$$\boldsymbol{\delta u}^T\left(\boldsymbol{R}^{int} + \boldsymbol{M}\ddot{\boldsymbol{u}} - \boldsymbol{R}^{tract.} - \boldsymbol{R}^{body} + \boldsymbol{K}\Delta\boldsymbol{u}\right) = \boldsymbol{0}, \tag{D.18}$$

where the $\hat{(\ )}$ on nodal values are assumed.

D.5 Area change

The relation between the areas in the reference (initial) and deformed (current) configurations is derived as follows. We can first start with the relation between two volume elements, dv and dV, in the current and initial configurations, respectively

$$dv = JdV, \tag{D.19}$$

where the Jacobian, $J = det(\boldsymbol{F})$. Each volumes can be decomposed into the product of an area and a length element

$$dv = d\boldsymbol{l}\cdot d\boldsymbol{a},$$

and

$$dV = d\boldsymbol{L}\cdot d\boldsymbol{A},$$

where

$$d\boldsymbol{l} = \boldsymbol{F} d\boldsymbol{L}.$$

Plugging into Eq. (D.19) and multiplying both sides by $\boldsymbol{F}^{-1}$ gives the resulting relation between area vectors

$$d\boldsymbol{a} = J\boldsymbol{F}^{-T} d\boldsymbol{A}. \tag{D.20}$$

This is known as Nanson's relation. To relate the two scalar areas, we use the fact that $da = \sqrt{d\boldsymbol{a} \cdot d\boldsymbol{a}}$. When applied to Eq. (D.20), this results in

$$da = \sqrt{d\boldsymbol{a} \cdot d\boldsymbol{a}} = \sqrt{J\boldsymbol{F}^{-T} d\boldsymbol{A} \cdot J\boldsymbol{F}^{-T} d\boldsymbol{A}} = J\sqrt{[\boldsymbol{N}\boldsymbol{F}^{-1}]^T \boldsymbol{F}^{-T} \boldsymbol{N}} dA$$

$$= J\sqrt{\boldsymbol{N} \cdot \boldsymbol{F}^{-1}\boldsymbol{F}^{-T} \boldsymbol{N}} dA$$

This gives the final relation as

$$da = J\sqrt{\boldsymbol{N} \cdot \boldsymbol{C}^{-1} \boldsymbol{N}} dA.$$

D.6 Spatial discretization of thermal equations

Discretization of Eq. (7.25) on B_0 is similar to the discretization the the structural equations described above except that, in the thermal problem, there is only one degree of freedom per node. The thermal solution, Θ is stored at n nodal locations and interpolated using the same shape functions, N, as those used in the structural problem:

$$\Theta = \sum_{a=1}^{n} N_a \hat{\Theta}_a, \tag{D.21}$$

where, again, a is the element local node index and $\hat{(\;)}$ denotes a nodal quantity. The first term in Eq. (7.20) is discretized as

$$\int_e \rho_0 C\dot{\Theta}\delta\Theta \; dV \approx \delta\hat{\Theta}_a \sum_{ijk=1}^{ng} \rho_0(\boldsymbol{\xi}_{ijk})C(\boldsymbol{\xi}_{ijk})N_a(\boldsymbol{\xi}_{ijk})N_b(\boldsymbol{\xi}_{ijk})J(\boldsymbol{\xi}_{ijk})$$
$$\times W(\xi_i)W(\eta_j)W(\zeta_k)\dot{\hat{\Theta}}_b = \delta\hat{\Theta}_a c_{ab}\dot{\hat{\Theta}}_b,$$

which, when added over B_0, gives

$$\int_{B_0} \rho_0 C\dot{\Theta}\delta\Theta \; dV \approx \delta\hat{\boldsymbol{\Theta}}^T \boldsymbol{C}_{th}\dot{\hat{\boldsymbol{\Theta}}},$$

where $\boldsymbol{C}_{th}$ is the thermal capacitance matrix.

The second term in Eq. (7.25) is discretized as

$$\int_e Jk\boldsymbol{C}^{-1}\nabla_X\Theta \cdot \nabla_X\delta\Theta dV$$
$$\approx \delta\hat{\Theta}_a \sum_{ijk=1}^{ng} k_0(\boldsymbol{\xi}_{ijk})\boldsymbol{C}^{-1}_{PK}(\boldsymbol{\xi}_{ijk})\frac{\partial N_a(\boldsymbol{\xi}_{ijk})}{\partial \xi_l}\frac{\partial \xi_l}{\partial X_P}\frac{\partial N_b(\boldsymbol{\xi}_{ijk})}{\partial \xi_q}\frac{\partial \xi_q}{\partial X_K}J(\boldsymbol{\xi}_{ijk})$$
$$\times W(\xi_i)W(\eta_j)W(\zeta_k)\hat{\Theta}_b = \delta\hat{\Theta}_a k_{ab}\hat{\Theta}_b.$$

Its global (assembled) form is

$$\int_{B_0} Jk\boldsymbol{C}^{-1}\nabla_X\Theta \cdot \nabla_X\delta\Theta dV \approx \delta\hat{\boldsymbol{\Theta}}^T \boldsymbol{K}_{th}\hat{\Theta},$$

where $\boldsymbol{K}_{th}$ is the thermal stiffness matrix and $Jk = k_0$ is the heat conduction coefficient in the reference configuration.

The final term in Eq. (7.25) is discretized as

$$\int_{\partial e} \boldsymbol{Q}\cdot\boldsymbol{N}\delta\Theta \; dA \approx \delta\hat{\Theta}_a \sum_{ij=1}^{ng}(\boldsymbol{Q}\cdot\boldsymbol{N})_b(\boldsymbol{\xi_{2D}}_{ij})N_b(\boldsymbol{\xi_{2D}}_{ij})N_a(\boldsymbol{\xi_{2D}}_{ij})$$
$$\times J_{2D}(\boldsymbol{\xi_{2D}}_{ij})W(\xi_i)W(\eta_j) = \delta\Theta_a r_a^{heat},$$

which when computed over the entire body, B_0, yields

$$\int_{\partial B_0} \boldsymbol{Q} \cdot \boldsymbol{N} \delta\Theta \; dA \approx \delta\hat{\boldsymbol{\Theta}}^T \boldsymbol{R}_{th},$$

where $\boldsymbol{R}_{th}$ is the thermal load vector.

The final semi-discrete thermal equation is thus

$$\boldsymbol{C}_{th}\dot{\boldsymbol{\Theta}} + \boldsymbol{K}_{th}\boldsymbol{\Theta} = \boldsymbol{R}_{th}, \tag{D.22}$$

where the $\hat{(\ )}$ on nodal values are assumed.

Appendix E

Solution of 2D Steady-State Compressible Boundary Layer Equations

E.1 Compressible boundary layer equations

The Navier-Stokes equations are non-linear, non-unique, complex and difficult to solve. In the boundary layer, some approximations can be applied that simplify the Navier-Stokes equations significantly. The approximations are as follows:

- Stream wise gradients are much smaller than transverse gradients, i.e.

  $$u >> v,$$

  and

  $$\frac{\partial^2}{\partial y^2} >> \frac{\partial^2}{\partial x^2}.$$

- Pressure is imposed from the freestream, i.e.

  $$p = p_e(x).$$

- In the case of a flat plate, freestream pressure is constant,

  $$p_e = \text{constant}.$$

- Body forces, such as that due to gravity, are negligible,

  $$\boldsymbol{f} \approx 0.$$

The resulting equations are called the boundary layer equations, and are presented below. The derivation of the boundary layer equations as well as the details of the Howarth transformation to similarity coordinates are presented in the Lui Ph.D. thesis[1]. They are restated below.

E.1.1 Derivation of the boundary layer equations

The 2-dimensional, steady, compressible Navier-Stokes equations are as follows:

$$\begin{aligned} \frac{\partial}{\partial x_i}(\rho u_i) &= 0, \\ \frac{\partial}{\partial x_j}[\rho u_i u_j + p\delta_{ij} - \mu \frac{\partial}{\partial x_j}(u_i)] &= \rho f_i, \\ \frac{\partial}{\partial x_j}[u_j(\rho E + p) + q_j - u_i \mu \frac{\partial}{\partial x_j}(u_i)] &= \rho f_i u_i. \end{aligned} \tag{E.1}$$

The following non-dimensionalizations are applied (the tilde denotes a dimensional quantity):

$$u_i = \frac{\tilde{u}_i}{\tilde{U}_\infty}$$

$$x_i = \frac{\tilde{x}_i}{\tilde{L}}$$

$$\rho = \frac{\tilde{\rho}}{\tilde{\rho}_\infty}$$

$$p = \frac{\tilde{p}}{\tilde{\rho}_\infty \tilde{c}_\infty^2}$$

$$\mu = \frac{\tilde{\mu}}{\tilde{\mu}_\infty}$$

$$T = \frac{\tilde{T}}{\tilde{c}_\infty^2/\tilde{C}_{p,\infty}} = \frac{\tilde{T}}{(\gamma - 1)\tilde{T}_\infty}$$

Additionally, the following non-dimensional groups are defined. The Reynolds number based on freestream quantities is

$$Re = \frac{\tilde{\rho}_\infty \tilde{c}_\infty \tilde{L}}{\tilde{\mu}_\infty},$$

and the Prandtl number is

$$Pr = \frac{\tilde{C}_{p,\infty}\tilde{\mu}_\infty}{\tilde{k}_\infty},$$

where $\tilde{C}_{p,\infty}$, $\tilde{k}_\infty$ and $\tilde{L}$ are the freestream specific heat capacity at constant pressure, the freestream thermal conductivity and a length scale, respectively.

When applied to the Navier-Stokes equations, the non-dimensionalizations and assumptions listed above produce the non-dimensional, steady, compressible boundary layer equations. The conservation of mass, streamwise momentum, and energy, respectfully, are listed as

$$\begin{aligned} \frac{\partial}{\partial x}(\rho u) + \frac{\partial}{\partial y}(\rho v) &= 0, \\ \rho u \frac{\partial u}{\partial x} + \rho v \frac{\partial u}{\partial y} - \frac{1}{Re}\frac{\partial}{\partial y}\left(\mu \frac{\partial u}{\partial y}\right) &= 0, \\ \rho u \frac{\partial T}{\partial x} + \rho v \frac{\partial T}{\partial y} - \frac{1}{Re}\frac{\partial}{\partial y}\left(\frac{\mu}{Pr}\frac{\partial T}{\partial y}\right) - \frac{\mu}{Re}\frac{\partial^2 u}{\partial y^2} &= 0. \end{aligned} \tag{E.2}$$

Additionally, a passive scalar concentration can be modeled as

$$\rho u \frac{\partial c}{\partial x} + \rho v \frac{\partial c}{\partial y} - \frac{1}{Re}\frac{\partial}{\partial y}\left(\frac{\mu}{Sc}\frac{\partial c}{\partial y}\right) = 0. \tag{E.3}$$

The four equations above contain the five unknowns: u, v, T, ρ and c. The non-dimensionalized ideal gas law,

$$T = \frac{1}{(\gamma - 1)\rho},$$

is used to close the system of equations. Note that pressure does not appear in the above expression. Due to the assumption of constant pressure, the non-dimensionalized quantity is equal to the inverse of the ratio of specific heats

$$p = \frac{1}{\gamma}.$$

The first coefficient of viscosity, μ, is modeled using the power law,

$$\mu = ((\gamma - 1)T)^n,$$

where n is a fluid-specific constant and is taken as $n = 0.666$ for air [11].

E.1.2 The Howarth transformation

The Howarth transformation alters the coordinates in Eq. (E.2) making it more tractable for an analytical solution. The transformation is outlined below. A new set of cartesian coordinates, X and Y, are defined as

$$X = x,$$

and

$$Y = \int_0^y \rho dy',$$

where the density variations are integrated into the new Y coordinate. This results in the following coordinate stretching factors:

$$\frac{\partial X}{\partial x} = 1$$

$$\frac{\partial Y}{\partial x} = \int_0^y \frac{\partial \rho}{\partial x}, dy'$$

$$\frac{\partial X}{\partial y} = 0$$

$$\frac{\partial Y}{\partial y} = \rho$$

Substituting the stretching factors into the boundary layer equations produces the following:

$$\begin{aligned} \frac{\partial u}{\partial X} + \frac{\partial V}{\partial Y} &= 0, \\ u\frac{\partial u}{\partial X} + V\frac{\partial u}{\partial Y} - \frac{1}{Re}\frac{1}{\gamma - 1}\frac{\partial}{\partial Y}\left(\frac{\mu}{T}\frac{\partial u}{\partial Y}\right) &= 0, \\ u\frac{\partial T}{\partial X} + V\frac{\partial T}{\partial Y} - \frac{1}{Re}\frac{1}{Pr}\frac{1}{\gamma - 1}\frac{\partial}{\partial Y}\left(\frac{\mu}{T}\frac{\partial T}{\partial Y}\right) - \frac{\mu}{Re}\frac{\partial^2 u}{\partial Y^2} &= 0, \\ u\frac{\partial c}{\partial X} + V\frac{\partial c}{\partial Y} - \frac{1}{Re}\frac{1}{Pr}\frac{1}{\gamma - 1}\frac{\partial}{\partial Y}\left(\frac{\mu}{T}\frac{\partial c}{\partial Y}\right) &= 0, \end{aligned} \tag{E.4}$$

and the equation of state

$$\rho = \frac{\gamma}{(\gamma - 1)T}.$$

By the Howarth transformation, the first three equations contain only three unknowns: u, V and T. These three equations are decoupled from the equation of state and can be solved without knowledge of the density. The density and passive scalar can be solved for after the quantities u, V and T are found.

A boundary layer over a flat plate has no intrinsic length scale, and the problem can be further simplified by treating it as self-similar. The similarity variable, η, is introduced as

$$\eta(X,Y) = Y\sqrt{\frac{Re}{X}},$$

the following coordinate stretching factors are obtained.

$$\frac{\partial\eta}{\partial X} = -\frac{1}{2}\frac{\eta}{X},$$

and

$$\frac{\partial\eta}{\partial Y} = \sqrt{\frac{Re}{X}},$$

and the unknown variables are redefined as

$$u = f'(\eta),$$

$$V = \frac{1}{2\sqrt{ReX}}(f'(\eta)\eta - f(\eta)),$$

$$T = g(\eta),$$

and

$$c = h(\eta).$$

One consequence of this transformation is that the continuity equation is satisfied identically. These definitions transform the boundary layer equations into the following:

$$\begin{aligned} ff'' + 2(\gamma-1)^{n-1}[f''' + (n-1)\frac{g'}{g}f'']g^{n-1} &= 0, \\ \frac{2}{Pr}(\gamma-1)^{n-1}g^{n-1}[g'' + (n-1)\frac{g'^2}{g}] + fg' + 2(\gamma-1)^{n-1}g^{n-1}f''^2 &= 0, \quad \text{(E.5)} \\ \frac{2}{Sc}(\gamma-1)^{n-1}g^{n-1}[h'' + (n-1)\frac{g'h'}{g}] + fh' &= 0. \end{aligned}$$

The first two equations represent a system of two, non-linear, third order ordinary differential equations. The solution of the equations is obtained by a shooting method.

E.1.3 Backwards transformation

Once the transformed boundary layer equations are solved, the variables $f(\eta)$, $f'(\eta)$, $g(\eta)$ and $h(\eta)$ are known. The task still remains to recover the variables $\rho(x,y)$, $u(x,y)$, $v(x,y)$, $T(x,y)$ and $c(x,y)$. Since the solution variables are functions of η, the first step in the backwards transformation is to determine the values $\eta(x,y)$. This is accomplished with the relation,

$$y = (\gamma - 1)\sqrt{\frac{Re}{x}} \int g(\eta')d\eta'. \tag{E.6}$$

Once the values of $\eta(x,y)$ are found, it is trivial to assign

$$u(x,y) = f'(\eta(x,y)),$$

$$T(x,y) = g(\eta(x,y)),$$

$$\rho(x,y) = \frac{1}{(\gamma-1)g(\eta(x,y))},$$

and

$$c(x,y) = h(\eta(x,y)).$$

The transverse specific momentum, ρv, is found by

$$\rho v = \frac{1}{2\sqrt{Rex}}(\eta f' - f) - f' \int_0^y \frac{\partial \rho}{\partial x} dy'. \tag{E.7}$$

Appendix F

Effect of Boundary Layer Forcing Terms on Mean Profile

The forcing terms (Eq. (9.6)), while preserving the boundary layer mean flow prior to transition, leave a noticeable effect on the turbulent boundary layer after transition. In order to obtain a the expected turbulent boundary layer statistics, the forcing is removed after transition is complete. The plateau of the shape factor, $H = \theta/\delta^*$, is taken to indicate the end of the transition period (Fig. F.1(c)). The forcing is then removed and the boundary layer relaxes to its expected profile, as shown in Fig. F.1(a) and (b), which occurs over $ta_\infty/\delta^{99} = 12$.

Figures for Appendix F

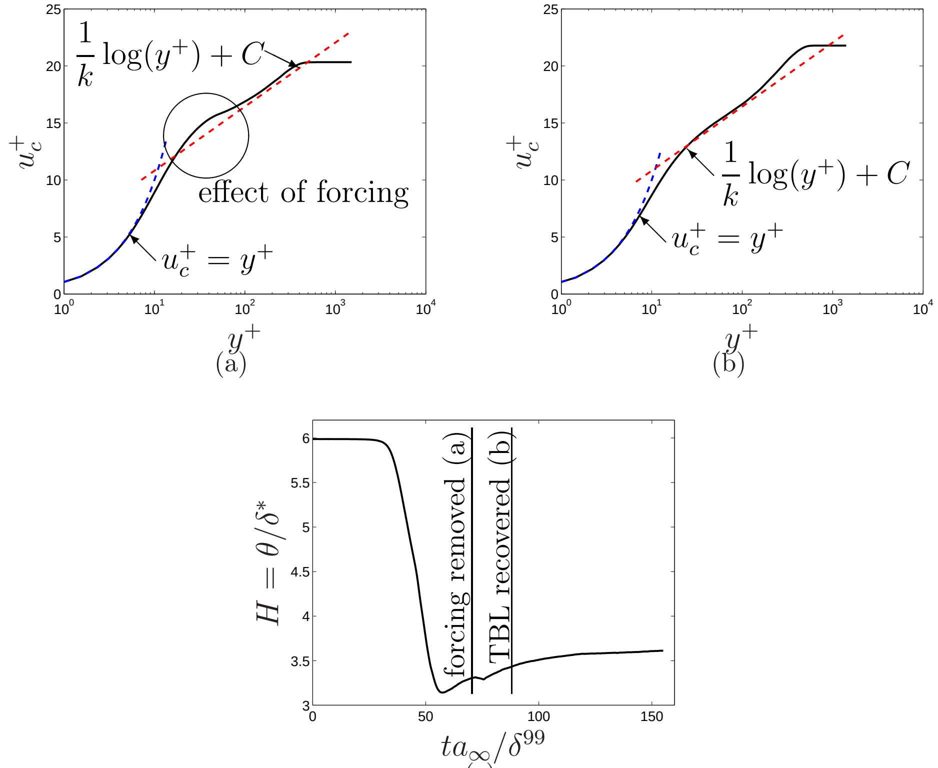

(a) (b)

(c)

Figure F.1: (a) Effect of forcing seen in TBL mean profile at $ta_\infty/\delta^{99} = 0.25$. (b) TBL mean profile recovered $ta_\infty/\delta^{99} = 0.05$ after forcing is removed. (c) Evolution of the shape factor up to and after forcing is removed.

Appendix G

Turbulent Kinetic Energy Budget

The compressible turbulent kinetic energy (TKE) equation is written as

$$\bar{\rho}\frac{\partial k}{\partial t} + \bar{\rho}\tilde{u}_j\frac{\partial k}{\partial x_j} = P + D + T_{u'} + T_{p'} + \Pi - \rho\epsilon - ST_1 - ST_2, \tag{G.1}$$

where

$$\begin{aligned}
P =& -\overline{\rho u_i'' u_j''}\frac{\partial \tilde{u}}{\partial x_j}, && \text{(Production)}\\
D =& \frac{\partial}{\partial x_j}\overline{\tau_{ij}' u_i''}, && \text{(Viscous Diffusion)}\\
T_{u'} =& -\frac{1}{2}\frac{\partial}{\partial x_j}\overline{\rho u_j'' u_i'' u_i''}, && \text{(Turbulent Transport)}\\
T_{p'} =& -\frac{\partial}{\partial x_j}\overline{p' u_j''}, && \text{(Pressure Diffusion)}\\
\Pi =& \overline{p'\frac{\partial u_j''}{\partial x_j}}, && \text{(Pressure Dilatation)}\\
\rho\epsilon =& -\overline{\tau_{ij}'\frac{\partial u_j''}{\partial x_j}}, && \text{(Viscous Dissipation)}\\
ST_1 =& -\overline{u''}_j\frac{\partial \bar{p}}{\partial x_j}, && \text{(Pressure Work)}\\
ST_2 =& \overline{u''}_j\frac{\partial \bar{\tau}_{ij}}{\partial x_j}. && \text{(Additional Compressibility Term)}
\end{aligned} \tag{G.2}$$

The terms above utilize Favre averaging, where

$$\tilde{u} = \frac{\overline{\rho u}}{\overline{\rho}},$$

and

$$u'' = u - \tilde{u},$$

are the Farve average of velocity and the fluctuations about the Favre average, respectively. Additionally, $k = 1/2\overline{\rho u_i'' u_i''}$ is the compressible TKE and $\overline{\tau}_{ij}$ and τ_{ij}' are the Reynolds averaged mean and fluctuating parts of the viscous stress tensor. Favre averaging is a mathematical simplification, yielding Favre averaged equations (ex. Eq. (G.1)) that are similar to their incompressible, Reynolds averaged counterparts. The pressure dilatation term, Π, in Eq. (G.1) becomes zero in an incompressible flow ($\partial u_j''/\partial x_j = 0$). Additionally, the terms ST_1 and ST_2 (as they are referred to in [110]) are a direct consequence of Favre averaging, where

$$\overline{u''} = -\frac{\overline{\rho' u'}}{\overline{\rho}} \neq 0.$$

Those terms, therefore, also vanish in the incompressible limit. The terms on the right hand side of Eq. (G.1) are shown for the rigid panel, Mach 2.25, $\mathrm{Re}_\theta = 1196$ boundary layer (Section 9.1.4) in Fig. G.1(a). At the modest Mach number of 2.25, the terms arising from compressibility are relatively small. The pressure dilatation, Π, is very small, and appears to zero in Fig. G.1(a). The net change in TKE is given by the sum of those terms, and it is shown in Fig. G.1(b) that there is small net production of TKE in the TBL.

Figures for Appendix G

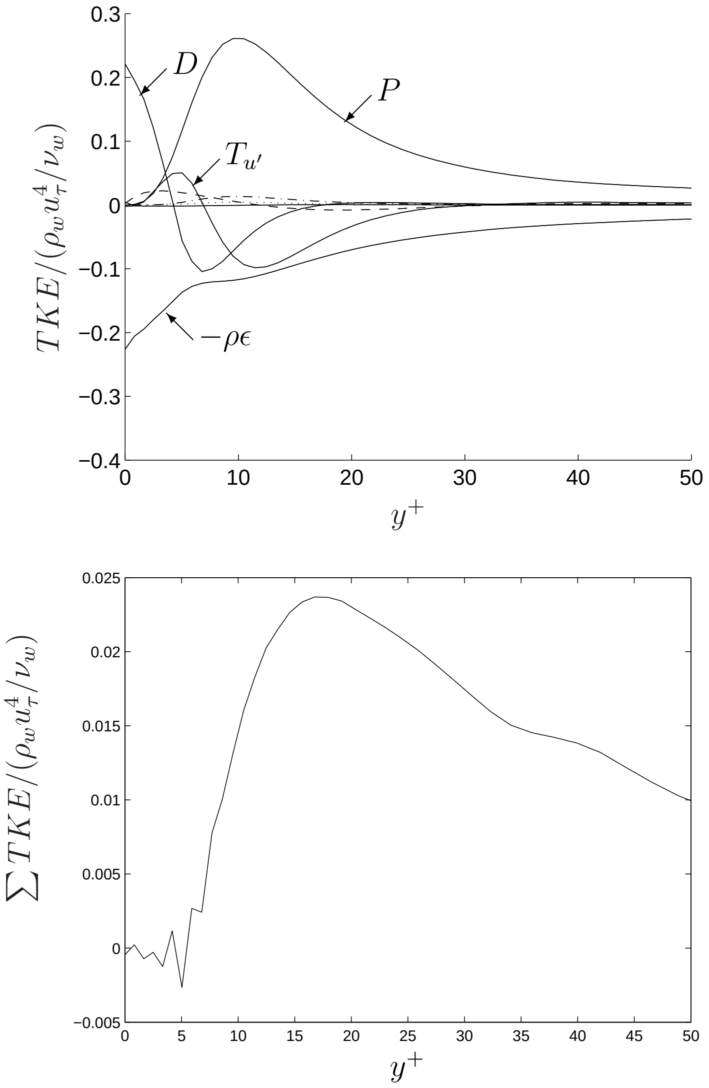

Figure G.1: (a) TKE budget terms. P, D, $-\rho\epsilon$, and $T_{u'}$ are noted on the figure. Less significant terms are shown with different line types for clarity: $T_{p'}$ (dashed), ST_1 (dash-dot), and ST_2 (dotted). Π is the solid line on on the x-axis. (b) Sum of the TKE budget terms.